Multiple Radar Target Tracking in Environments with High Noise and Clutter

by

Samuel P. Ebenezer

A Dissertation Presented in Partial Fulfillment
of the Requirement for the Degree
Doctor of Philosophy

Approved December 2014 by the
Graduate Supervisory Committee:

Antonia Papandreou-Suppappola, Chair
Chaitali Chakrabarti
Daniel Bliss
Narayan Kovvali

ARIZONA STATE UNIVERSITY

May 2015

ABSTRACT

Tracking a time-varying number of targets is a challenging dynamic state estimation problem whose complexity is intensified under low signal-to-noise ratio (SNR) or high clutter conditions. This is important, for example, when tracking multiple, closely spaced targets moving in the same direction such as a convoy of low observable vehicles moving through a forest or multiple targets moving in a crisscross pattern. The SNR in these applications is usually low as the reflected signals from the targets are weak or the noise level is very high. An effective approach for detecting and tracking a single target under low SNR conditions is the track-before-detect filter (TBDF) that uses unthresholded measurements. However, the TBDF has only been used to track a small fixed number of targets at low SNR.

This work proposes a new multiple target TBDF approach to track a dynamically varying number of targets under the recursive Bayesian framework. For a given maximum number of targets, the state estimates are obtained by estimating the joint multiple target posterior probability density function under all possible target existence combinations. The estimation of the corresponding target existence combination probabilities and the target existence probabilities are also derived. A feasible sequential Monte Carlo (SMC) based implementation algorithm is proposed. The approximation accuracy of the SMC method with a reduced number of particles is improved by an efficient proposal density function that partitions the multiple target space into a single target space.

The proposed multiple target TBDF method is extended to track targets in sea clutter using highly time-varying radar measurements. A generalized likelihood function for closely spaced multiple targets in compound Gaussian sea clutter is derived together with the maximum likelihood estimate of the model parameters using an iterative fixed point algorithm. The TBDF performance is improved by proposing a computationally feasible method to estimate the space-time covariance matrix of rapidly-varying sea clutter. The method applies the Kronecker product approximation to the covariance matrix and uses particle filtering to solve the resulting dynamic state space model formulation.

To my forebearing wife Bernice and my loving daughters Anya and Neha

ACKNOWLEDGEMENTS

I would like to express my utmost gratitude to my advisor Prof.Antonia Papandreou-Suppappola, for graciously agreeing to be my PhD thesis advisor despite knowing that this academic process is going to be a part-time endeavor. She made the entire process stimulating by directing me with challenging research topics. She was also patient and kind during the arduous journey by nudging me in the right direction to achieve the end goal even though sometimes it seemed unattainable. I can never forget her burning the midnight oil many times while writing various research papers pertaining to this work and teaching me how to write a precise and technically rigorous research paper. I would also like to thank my committee members, Prof.Chaitali Chakrabarti, Prof.Daniel Bliss and Dr.Narayan Kovvali for agreeing to be in the committee despite their busy schedules. I am thankful for their constructive and relevant feedback and also reviewing this thesis. I am especially grateful to Dr.Narayan Kovvali for many stimulating and thought provoking discussions that motivated me to approach the problems in a fundamentally sound manner. I would also like to thank Dr.Seth Suppappola and Mr.Doug Olsen at Cirrus Logic Inc., for allowing me to embark on this parallel journey and being flexible during the seemingly never ending process. I am also thankful to my sister Ms.Geetha Andrew for carefully reviewing this thesis. I am indebted to my mother for everything she has done for me through all my years. Finally, none of this would have happened without the constant encouragement and prayers of my patient wife Bernice and I am blessed to have her at my side.

TABLE OF CONTENTS

Page

CHAPTER

APPENDIX

LIST OF TABLES

LIST OF FIGURES

Figure Page

Chapter 1

INTRODUCTION

1.1 Motivation

The development of radar tracking systems for defense applications started as early as 1930 and became an active research topic with the development of the Kalman filter (KF) in 1960 [1]. Initially, the research was primarily focused on target tracking for air and maritime defense and guidance radar systems. With new advancements in computational and embedded processing capabilities, radar technology is now penetrating into many other areas such as air-traffic control for commercial air travel, weather surveillance radar for locating precipitation [2], vehicle collision avoidance radar systems [3], talker tracking in speech processing [4], image processing [5], robotics [6], remote sensing [7], and biomedical research [8]. All these diverse applications are driving the need to improve the robustness of target tracking algorithms under various environmental conditions.

1.1.1 Target Tracking

Historically, Bayesian techniques have been used to track targets in noise following the state space model formulation [9]. The KF provides an optimal state parameter estimate for linear state space models in which the measurement and modeling error random processes are assumed Gaussian [10]. The alpha-beta filter is a computationally simple derivative of the KF that was successfully used to estimate a moving target's position and velocity [11–13]. Since the KF is optimal only for linear and Gaussian state space models, the tracking performance of the KF and the alpha-beta filters is not optimal for nonlinear and non-Gaussian models. With the extended KF (EKF), the state transition and observation models do not need to be linear functions of the target state but, differentiable, so that they can be linearized at the current estimate using Taylor series approximations [14]. A new class of simulation based algorithms including the particle filter (PF) or sequential Monte Carlo (SMC) methods [15–17] have evolved in the late 1990s that can be used for nonlinear and non-Gaussian distributed state space models.

1.1.2 Target Tracking in Clutter

Target tracking is a complex problem that requires the consideration of many signal and environmental conditions for practical solutions [9, 18, 19]. For example, the typical reflected radar signal level from a low observable target is very low. Under low signal-to-noise ratio (SNR) conditions, it is possible to miss detecting valid measurements originating from existing targets. However, a tracking system should still be able to estimate the target's state parameters when a measurement that originated from a true target is weak. False alarms such as clutter, which are common in real systems, can further complicate processing. The clutter in a realistic measurement space can cause uncertainty in the origin of the measurement. This is a data association problem as the uncertainty makes it difficult to associate the measurement corresponding to the true target. The measurement origin uncertainty is further increased by the presence of multiple targets. In this scenario, it is imperative that measurements from all possible targets are associated with the corresponding targets in addition to pruning the measurements originated from clutter. Furthermore, in many real-life practical cases, the number of targets that are present in the measurement space of a tracking system is not known *a priori*. Thus, a target tracking system should not only be able to track the trajectory of moving targets but also estimate the number of targets that are present at each time step. Moreover, the number of measurements is usually not the same as the number of targets that are present in the field of view (FOV). In addition to these problems, at each time step, a tracker must also determine if a particular target has left the FOV and if a new target has entered the FOV.

The tracking performance of the classical detect-before-track algorithms is acceptable when tracking a single target in high SNR. However, these algorithms do not perform well under low SNR conditions or when the measurements also originate from clutter. At each time step, multiple measurements are available, and the tracker must identify the measurement associated with the target from all the measurements. In real-life target tracking applications, the source of a measurement is usually not known by a tracking system. Hence, the tracker needs to first associate each measurement with its corresponding source. This data association process is a very critical step in a practical target tracking system and as a result, many data association techniques have been proposed in the literature [18, 20]. One of the simplest data association techniques is the nearest neighbour method, which selects the measurement closest to the predicted track to update the target state [21]. Even if the state space model is assumed linear and Gaussian, the estimated target states are not optimal because the selected measurement need not originate from a target. Track and split is an optimal data association technique in which all measurements are assumed to be valid and a new track is initiated for every measurement [22]. However, as the computational complexity of this technique increases very fast with time because of the exponential growth of the tree structure, it is not feasible for real-time applications. A probability based method to track a target in clutter was proposed in [23]. In this probabilistic data association (PDA) method, the target states for all the measurements are estimated separately in addition to computing the measurement-to-target association probability. The approach estimates the final target state by combining all the possible target states weighted by the corresponding measurement-to-target association probability [20, 24, 25]. A PF based method to track a target in clutter was also proposed in [26] for nonlinear/non-Gaussian state space models.

1.1.3 Multiple Target Tracking

The aforementioned tracking problem in clutter becomes extremely complicated when there is a multiple number of targets to track simultaneously. A comprehensive list of different multiple target tracking techniques together with a comparison of their performance and computational complexity is presented in [27]. Multiple hypothesis tracking (MHT) [28], [29] is a popular multiple target measurement oriented technique in which each established target or a new target that gives rise to a measurement sequence is obtained. This technique is similar to the track and split technique used for single target tracking in clutter. Using the MHT, different possible track hypotheses are generated when a new measurement set is received. The hypothesis tracking enables the tracking system to detect when a new target enters or a target leaves the FOV. The target states for each hypothesis are estimated using a KF, EKF or PF tracker, depending on the state space model assumptions. The probability of occurrence of each track hypothesis is computed and their probabilities are used to compute the weighted average estimate of a target state. Since this algorithm maintains the track hypothesis based on the current and past measurements, the validated target states are available only after some delay. The computational complexity of this algorithm can grow exponentially as the number of track hypotheses increases. One could use hypothesis reduction techniques such as zero scan clustering or hypothesis elimination to increase the computational feasibility of this algorithm. The joint probabilistic data association (JPDA) filter [30] is another popular algorithm that extends the PDA filter for multiple target tracking. This is a zero scan algorithm in which all the current measurement sets are combined immediately to provide a target state estimate. In the JPDA filter, given all the measurement data and a known number of targets, all possible measurement-to-target combinations (hypothesis) are formed. The state vectors corresponding to all targets are estimated for each hypothesis along with their hypothesis probabilities. Finally, the target state estimates are combined to obtain the final target estimate. One of the drawbacks of the JPDA filter is that it assumes that the number of targets present in the measurement space is known. Hence, this algorithm cannot be used when the number of targets in the FOV is time-varying. When the JPDA algorithm was originally proposed, it used the KF to estimate the target state under different hypotheses. In the early 2000s, the JPDA was often integrated with the PF to track multiple targets for nonlinear/non-Gaussian state space models [31–34].

Recently, the optimal Bayesian multiple target probability density function (PDF) estimation approach was proposed using random finite set (RFS) statistics [35–37]. This approach keeps track of the varying number of targets to estimate their state vectors. However, a feasible implementation of the optimal Bayesian multiple target PDF estimation does not exist in the literature. Nevertheless, two popular approximation techniques with feasible implementations have been proposed that approximate the multiple target PDF by either Poisson [38, 39] or multiple Bernoulli distributions [36, 40]. The probability hypothesis density filter (PHDF) [38, 39] that approximates the multiple target PDF by a Poisson distribution has gained popularity in tracking a varying number of targets with a non-zero probability of detection in the presence of clutter. The PHDF recursively tracks the intensity function of a Poisson process that models the number of existing targets in any given range of the single target state space. In the multiple Bernoulli filtering approach, the posterior PDF is approximated by a multiple Bernoulli distribution and the parameters of this distribution are updated in each time step [36, 40]. The PHDF can be implemented using closed form versions by approximating the posterior intensity function by a Gaussian mixture model under linear and Gaussian assumption for the target motion and measurement models [41–43]. The SMC version of the PHDF for nonlinear and non-Gaussian models was originally proposed in [37, 44].

1.1.4 Track-before-detect Filter

In conventional radar systems, tracking moving targets in low SNR using constant false alarm rate (CFAR) detectors [45, 46] can result in poor performance. Since the detection threshold for a CFAR detector dynamically increases under low SNR conditions, the probability of target detection is low for a target with small radar cross section [47]. If the threshold is raised to increase the probability of detection, then more measurements are needed as input to a tracking algorithm due to the increased number of false alarms. This increased number of measurements can exponentially increase the computational complexity of multiple target tracking algorithms such as JPDA and MHT. To improve the tracking performance under low SNR conditions, the track-before-detect filter (TBDF) method was proposed that uses unthresholded measurements. TBDF algorithms based on the Hough transform [48], dynamic programming [49] or maximum likelihood methods [50] are generally computationally intensive [17]. With recent advancement in SMC techniques, TBDF algorithms implemented using PF are now computationally feasible [51–56].

1.1.5 Multiple Target Track-before-detect Filtering

Tracking multiple targets under low SNR or high clutter conditions is a difficult problem. For example, in maritime surveillance applications, it is critical to track small-sized intruder boats under turbulent sea conditions or in an early warning defense system, it is imperative to detect targets farther away from the radar system. In these applications, the SNR is usually low as the reflected signal from the target is weak or the noise level is very high. Tracking multiple targets in such poor conditions is an extremely challenging problem since the tracking problem is complicated by many factors such as measurement origin uncertainty, unknown number of targets, and computational feasibility.

Different TBDF algorithms were considered for tracking a time-varying/fixed number of multiple targets under varying conditions. The single target PF based TBDF in [51] was extended to track two targets in [57] by replacing the binary state target existence variable with a three state mode variable. The particles corresponding to this mode variable is also propagated during the tracking process and the method was illustrated using a restrictive example by tracking a second target that spawns from the first target [57]. Moreover, in this method the target state vector dimension is set to the maximum number of targets and the state vector dimension is not accounted for varying number of targets. In addition, this method does not entirely cover all possible target death and birth combinations. For example, there is no unambiguous mechanism to track the trajectory of the remaining target after one of the target has disappeared. The authors in [58] have used the single target TBDF in [51] to track multiple targets by keeping track of the number of peaks in the estimated posterior PDF. The authors have exploited the fact that the likelihood function is typically high in the vicinity of different target's state vector and this will cause the estimated posterior PDF to become a multi-modal distribution function with each peak corresponding to different targets. A separate clustering method was used to associate the particle clusters with different targets. However, clustering based methods can lead to inaccurate estimates when the number of clusters exceeds the actual number of targets. Moreover, the joint multi-target state PDF is also not estimated, instead a multi-modal PDF in single target space is estimated. A generalized likelihood ratio test based multi-target TBDF and a multi-hypothesis test strategy for a known and unknown number of targets, respectively, were presented in [59]. These methods were demonstrated for two targets at medium range SNR conditions (8-24 dB). A multi-target acoustic source tracking TBDF for two known fixed targets was discussed in [60]. Multiple speech sources were tracked in [61] by detecting and removing each source with a likelihood ratio computed from particle weights from microphone pair phase differences. Multi-target TBDF for a passive radar was used in [62] by extending the single target recursive TBDF to each range-Doppler bin with a target existence probability and PDF conditioned on target existence in each bin.

The RFS based methods were originally introduced for detect-before-track applications and they are expected to perform poorly under low SNR/SCR conditions. For example, the multiple Bernoulli approximation is acceptable only when the clutter rate is low since it introduces cardinality bias in high clutter situations [63]. Moreover, the SMC implementations of PHDF based multiple target tracking methods [37, 44, 64, 65] to support non-linear/non-Gaussian models, require a clustering step to estimate the number of existing targets. Many PHDF based TBDF (PHDF-TBD) methods for non-linear measurement models exist in literature. A SMC based PHDF-TBD for image applications was introduced in [66] and demonstrated by tracking three targets. In [67], the poor performance of one such PHDF-TBD was reported when tracking three well-separated targets and the performance was improved by using measurements from multiple sensors. In [68, 69], the PHDF-TBD was used to track two targets using range, Doppler and bearing angle measurements. An improved PHDF-TBD was also used in [70] following the multiple model PHDF [71] to track three maneuvering targets. In the SNR-PHDF [72], the SNR is also tracked and a detection step is included in the tracking method by using the measurement only if the estimated SNR exceeds certain threshold. The mathematical equivalence of the SNR-PHDF with the threshold set to zero and the single target TBDF [51] is shown in [73]. All these SMC based methods require the clustering step. Moreover, in all the above mentioned RFS based methods, track management is an additional required step, since the target state estimates from these methods are not distinguishable from each other. Only recently, a new subset of RFS approach called as labeled multiple Bernoulli filter [74] are beginning to emerge to accommodate target tracks under low SNR conditions. A multiple Bernoulli based TBDF with a separate label based track management step was proposed in [75] and illustrated using image measurement to track up to 4 targets under high SNR conditions. A multi-target label based RFS TBDF implemented using SMC method was proposed in [63] and illustrated using 3-D radar (range, Doppler, azimuth) measurement at 10 and 13 dB SNR to track up to 4 targets.

Most of the aforementioned techniques are implemented using SMC methods, and they do not track the multiple target PDF. Moreover, many of the RFS based methods require a separate track management step since they do not associate the estimates with the target identity. Therefore, the problem of tracking a time-varying number of multiple targets under severe conditions of low SNR and high clutter is still an active research topic.

1.2 Summary of Proposed Thesis Work

1.2.1 Multiple Mode Multiple Target Track-before-detect Filter

We propose a multiple target TBDF method to track a varying number of targets by estimating the target states under all possible target existence combinations

[76, 77]. We derive a set of multiple target joint posterior PDFs corresponding to all possible target existence combinations under the recursive Bayesian framework. The track management of multiple targets is achieved by tracking all possible target existence combinations in which the identity of targets are dynamically maintained as the targets enter and leave the FOV. We propose a feasible implementation of the algorithm using SMC techniques through three layers of particle filter sets. Thus, the proposed algorithm is developed by integrating three main concepts: (i) estimating the PDF of target states under multiple hypotheses [29] in order to consider all possible target existence combinations at each time step; (ii) multiple particle filtering [78] in order to have multiple PFs for each hypothesis and then optimally combining each PF output, weighted by a posterior transition probability; and (iii) a parallel PF architecture [79] in order to attack the computational complexity problem using distributed processing.

1.2.2 Partition Based Proposal Density Function for Multiple Mode Multiple Target Track-before-detect Filter

In general, the number of particles necessary to accurately estimate the target state vector can grow exponentially as a function of the state vector dimension [80]. Therefore, the proposed SMC implementation needs a large number of particles when the number of targets to be tracked is increased. To mitigate this curse of dimensionality problem, we propose a partition based particle proposal generation method [77, 81] in which the particles are sampled from a single target space instead of a higher dimensional multi-target state space. The single target measurement likelihood function is used to prune the proposal particles selected from the single target space. The Metropolis-Hastings Markov chain Monte Carlo (MCMC) [17] based method is also integrated into our SMC method to improve the sample impoverishment problem typically encountered at low state modeling error variances. We have demonstrated the feasibility of this algorithm to track multiple targets under low SNR conditions for various simulation test cases such as SNR, inter-target proximity, number of targets, and number of particles. The newly proposed TBDF algorithm was also shown to work under different measurement models such as image and range/range-rate/azimuthal-direction measurements. The computational complexity of this algorithm is also investigated and a simple decision-directed scheme is introduced to dynamically adjust the number of active PF sets, thereby reducing the peak and average computational requirement of the algorithm. Using this approach, we empirically show that the computational requirement of the proposed algorithm is a linear function, instead of an exponential function, of the maximum number of targets.

1.2.3 Multiple Target TBDF in Compound Gaussian Sea Clutter

The proposed multiple target TBDF algorithm is extended to track multiple targets in the presence of high clutter [82]. Specifically, the complex Gaussian model is used to model the clutter measurements from a low resolution radar and the compound Gaussian model is used to model the clutter measurement from a high resolution radar. In the proposed TBDF framework, the generalized likelihood functions developed in the classical detection methods are used in the PF weight update step. A new theoretically optimal generalized likelihood function for closely spaced multiple targets is also derived in the compound Gaussian case with the known model parameters. For the case of unknown model parameters, the maximum likelihood estimate of the clutter statistics is also derived and the estimator is implemented using an iterative fixed-point method [83, 84]. The tracking error using this newly proposed generalized likelihood function is compared with the classical sub-optimal adaptive generalized likelihood function [85, 86] and the relation between the newly derived optimal likelihood function and the sub-optimal likelihood function is also derived. A recently proposed Doppler spectrum model for sea clutter [87, 88] is used to simulate the fast time radar measurements. In this method, the sea clutter is modeled as a combination of slow moving Bragg scattering and fast moving sea swells that are typically observed in real life sea clutters [89].

1.2.4 Estimation of Sea Clutter Space-Time Covariance Matrix Using Kronecker Product Approximation

Tracking a target in sea clutter is a challenging problem due to the dynamic nature of sea clutter. The efficacy of the tracking algorithm depends on the accurate estimation of the clutter statistics. Although, most classical methods rely only on the temporal correlation of sea clutter, various studies have shown strong spatial correlation in sea clutter [89]. In this thesis, we propose a method to estimate the space-time covariance matrix of rapidly varying sea clutter [90, 91]. The method first develops a dynamic state space representation for the covariance matrix and then approximates the covariance matrix using the Kronecker product to reduce computational complexity. Particle filtering is then applied to estimate the dynamic elements of the covariance matrix. The validity of the Kronecker product approximation is also investigated by analyzing real sea clutter measurements. We further demonstrate the use of the estimated space-time covariance matrix in the track-before-detect filter to track a low observable target in sea clutter.

1.3 Thesis Organization

This thesis is organized as follows. In Chapter 2, we provide a summary on the state space model for tracking a single target and discuss various approaches to estimate the target state parameters such as Kalman and particle filtering. We extend the state space formulation to multiple targets, and we review the joint probabilistic data association approach and its sequential Monte Carlo version for tracking multiple targets under low probability of detection conditions. In Chapter 3, we discuss track-before-detect particle filtering for tracking a single target in low SNR. In Chapter 4, we propose a generalization of the single target track-before-detect filter to track a varying number of targets by estimating the joint multi-target posterior density for different target existence combinations. In this chapter, we also derive a particle filtering based implementation of the proposed generalized approach. In Chapter 5, we propose an efficient proposal density function through partitioning of the multiple target space into a single target space to improve the approximation accuracy of the particle filter. In Chapter 6, the generalized track-before-detect filter framework is extended for tracking multiple targets under different clutter model assumptions such as complex Gaussian and compound Gaussian sea clutter. Finally, in Chapter 7, we propose an approach to increase the multiple target tracking performance by efficiently estimating the space-time covariance matrix of rapidly-varying sea clutter using a Kronecker product (KP) covariance matrix approximation and a corresponding dynamic state space formulation.

A list of acronyms used in the thesis is provided in Table 1.1.

Table 1.1: List of Acronyms

Acronym	**Description**
AML	approximate maximum likelihood
CFAR	constant false alarm rate
CG	compound Gaussian
DFT	discrete Fourier transform
DOA	direction of arrival
EKF	Extended Kalman filter
FISST	finite set statistics
FOV	field of view
GLRT	generalized likelihood ratio test
IMM	interacting multiple model
IP	independent partition
JPDA	joint probabilistic data association
KF	Kalman filter
KP	Kronecker product
LFM	linear frequency modulated
LQ	linear quadratic
M-ANMF	M-adaptive normalized matched filter
MCJPDA	Monte Carlo based JPDA
MCMC	Markov chain Monte Carlo
MHT	multiple hypothesis tracking
ML	maximum likelihood
MLE	maximum likelihood estimate

Continued on next page

Table 1.1 – *Continued from previous page*

Acronym	**Description**
MM-MT-TBDF	Multiple mode multiple target TBDF
MM-MT-TBDF-IP	Independent partition based MM-MT-TBDF
MM-MT-TBDF-IP-MCMC	Independent partition and MCMC based MM-MT-TBDF
MM-MT-TBDF-PF	Particle filter implementation of MM-MT-TBDF
MMSE	Minimum mean-squared error
MSE	Mean-squared error
NKPA	nearest Kronecker product approximation
NMF	Normalized matched filter
OHGR	Osborne Head Gunnery Range
OSPA	Optimal sub-pattern assignment
PCA	Principal component analysis
PDA	probabilistic data association
PDF	probability density function
PF	particle filter
PF-TBDF	particle filter based TBDF
PHDF	probability hypothesis density filter
PHDF-TBDF	track-before-detect using PHDF
RCS	Radar cross section
RFS	Random finite set
RMSE	Root mean-squared error
Σ-ANMF	Σ-adaptive normalized matched filter

Continued on next page

Table 1.1 – *Continued from previous page*

Acronym	**Description**
SCR	signal-to-clutter ratio
SIR	sampling importance resampling filter
SMC	Sequential Monte Carlo
SNR	signal-to-noise ratio
TBDF	track-before-detect filter

Chapter 2

REVIEW ON TARGET TRACKING

2.1 Single Target Tracking

2.1.1 State Space Model Formulation

Target tracking is the problem of estimating the state parameters of a target such as the target's position, velocity or bearing angle, given a set of noisy measurements. In most cases, the measurements are related to the target state by either a linear or a nonlinear function. The first step in estimating the state parameters is to identify a model that closely matches the underlying physical motion characteristics of the target. State space modeling is a widely accepted approach to model dynamic systems such as moving targets. The state space model [1] is a set of equations that specify the input-output relation of a system under consideration at each time step based on some initial conditions.

The state space model consists of two main equations. The first equation describes the process or state transition model; it provides the relationship between the state at time step k and the state at time step $k-1$. Specifically, given a state parameter vector $\mathbf{x}_k$ at time step k, the process model is given by, [2]

$$\mathbf{x}_k = \mathbf{f}_k(\mathbf{x}_{k-1}) + \mathbf{v}_k, \tag{2.1}$$

where $\mathbf{f}_k(\mathbf{x}_k)$ is a possibly time-varying function of the state and $\mathbf{v}_k$ is the modeling error random process with covariance matrix $\mathbf{Q}$. The main aim is to estimate the

---

[1] Unless otherwise stated, this thesis only considers state space models at discrete time steps.

[2] In this thesis, vectors are represented by bold lower case letters and matrices are represented by bold upper case letters. Vector and matrix transpose is represented by superscripted `T`.

state vector from a set of measurements $\mathbf{z}_k$. The measurement model for the state equation is given by

$$\mathbf{z}_k = \mathbf{h}_k(\mathbf{x}_k) + \ \mathbf{w}_k, \tag{2.2}$$

where $\mathbf{h}_k(\mathbf{z}_k)$ is a possibly time-varying function of the current state $\mathbf{x}_k$ at time k, and $\mathbf{w}_k$ is the measurement noise random process with covariance matrix $\mathbf{R}$. In general, the nonlinear state estimation problem involves estimating the current state at time instant k, from all available measurements until the current time instant k, $\mathbf{Z}_k = \{\mathbf{z}_1, \mathbf{z}_2, \ldots, \mathbf{z}_k\}$.

2.1.2 Bayesian Filtering Framework

Given the state space model in Equations (2.1) and (2.2), the next step is to estimate the state parameters. Since the state parameter has to be estimated from noisy measurements, it's estimate is a random vector and, as a result may take many values. In other words, given all measurements up to time k, we have to estimate all possible target states with an associated probability. In theory, one can estimate the target states when the posterior probability density function (PDF) of the target states is available. For example, given all measurements, the minimum mean-squared error (MMSE) estimate of the target state is derived by computing the conditional mean of the posterior PDF. Thus, the optimal solution to the nonlinear state estimation problem involves estimating the posterior PDF of the target states. The classical Bayes theorem can be used to provide a framework for estimating this posterior PDF of the states in a recursive manner. The recursive solution consists of two stages: prediction and update. During the prediction stage, the current state PDF is predicted from past state estimates using the process model. During the update stage, the predicted state PDF at time state k is updated based on current measurements. If we assume that the initial posterior PDF $p(\mathbf{x}_{k-1}|\mathbf{Z}_{k-1})$ is known, then the prior

PDF (predicted) is given by [3]

$$\begin{aligned} p(\mathbf{x}_k|\mathbf{Z}_{k-1}) &= \int p(\mathbf{x}_k, \mathbf{x}_{k-1}|\mathbf{Z}_{k-1}) d\mathbf{x}_{k-1} \\ &= \int p(\mathbf{x}_k|\mathbf{x}_{k-1}, \mathbf{Z}_{k-1}) p(\mathbf{x}_{k-1}|\mathbf{Z}_{k-1}) d\mathbf{x}_{k-1} \\ &= \int p(\mathbf{x}_k|\mathbf{x}_{k-1}) p(\mathbf{x}_{k-1}|\mathbf{Z}_{k-1}) d\mathbf{x}_{k-1} \qquad (2.3) \end{aligned}$$

The PDF of the first order Markov process $p(\mathbf{x}_k|\mathbf{x}_{k-1})$ is defined by the process model in Equation ((2.1)). Given the prior PDF and measurements at time k, we can update the estimated prior PDF to obtain the posterior PDF using Bayes theorem. The posterior PDF is given by

$$p(\mathbf{x}_k|\mathbf{Z}_k) = \frac{p(\mathbf{z}_k|\mathbf{x}_k) p(\mathbf{x}_k|\mathbf{Z}_{k-1})}{p(\mathbf{z}_k|\mathbf{Z}_{k-1})}$$

where $p(\mathbf{z}_k|\mathbf{Z}_{k-1})$ is given by

$$p(\mathbf{z}_k|\mathbf{Z}_{k-1}) = \int p(\mathbf{z}_k|\mathbf{x}_k) p(\mathbf{x}_k|\mathbf{Z}_{k-1}) d\mathbf{x}_k$$

and $p(\mathbf{z}_k|\mathbf{x}_k)$ is the likelihood function defined by the measurement equation. The above recursive solution provides only a theoretical framework. This is because, in most cases, it is not feasible to compute the aforementioned integrals. Hence, in those cases, it is not possible to derive a closed form solution for the above recursive equations.

2.2 Kalman Filtering for Single Target Tracking

2.2.1 Algorithm Description

An analytical Bayesian solution for linear models in additive Gaussian noise was derived by Kalman in the early 1970s [1]. Using the linearity and Gaussian assumption, it can be shown that the posterior PDF of the target states is also Gaussian [92].

---

[3] Unless otherwise indicated, all integrals in this thesis range from $-\infty$ to ∞.

Kalman derived a recursive solution in estimating the posterior PDF of a Gaussian process. Specifically, if we assume that the functions $\mathbf{f}_k(\mathbf{x}_k)$ and $\mathbf{h}_k(\mathbf{z}_k)$ in Equations (2.1) and (2.2), respectively, are linear and the state modeling error and measurement noise processes $\mathbf{v}_k$ and $\mathbf{w}_k$, respectively, are Gaussian, we can use basic probability theory to derive an analytic solution for the posterior PDF $p(\mathbf{x}_k|\mathbf{Z}_k)$. Following the aforementioned assumptions, we can re-write the state space model as

$$\mathbf{x}_k = \mathbf{F}_k\mathbf{x}_{k-1} + \mathbf{v}_k, \tag{2.4}$$

$$\mathbf{z}_k = \mathbf{H}_k\mathbf{x}_k + \mathbf{w}_k, \tag{2.5}$$

where $\mathbf{F}_k$ and $\mathbf{H}_k$ are matrices. For this simplified state space model, it can be shown that when the posterior density $p(\mathbf{x}_{k-1}|\mathbf{Z}_{k-1})$ is Gaussian, then $p(\mathbf{x}_k|\mathbf{Z}_k)$ is also Gaussian [92]. If we know that the posterior PDF is Gaussian, then the state estimation problem is much simplified, since a Gaussian PDF is completely characterized by its mean and covariance. The recursive solution derived under this assumption is the KF; this is an optimal solution as it minimizes the mean-squared error of the estimated state parameter vector, and it is given by [1, 10, 15]

$$\begin{aligned} p(\mathbf{x}_{k-1}|\mathbf{Z}_{k-1}) &\sim \mathcal{N}(\mathbf{x}_{k-1}; \mathbf{m}_{k-1|k-1}, \mathbf{P}_{k-1|k-1}) \\ p(\mathbf{x}_k|\mathbf{Z}_{k-1}) &\sim \mathcal{N}(\mathbf{x}_k; \mathbf{m}_{k|k-1}, \mathbf{P}_{k|k-1}) \\ p(\mathbf{x}_k|\mathbf{Z}_k) &\sim \mathcal{N}(\mathbf{x}_k; \mathbf{m}_{k|k}, \mathbf{P}_{k|k}) \end{aligned}$$

where $\mathcal{N}(\mathbf{x}_{k-1}; \mathbf{m}_{k-1|k-1}, \mathbf{P}_{k-1|k-1})$ indicates that the vector $\mathbf{x}_{k-1}$ is a Gaussian random vector with mean $\mathbf{m}_{k-1|k-1}$ and covariance matrix $\mathbf{P}_{k-1|k-1}$, and

$$\begin{aligned} \mathbf{m}_{k|k-1} &= \mathbf{F}_k\mathbf{m}_{k-1|k-1} \\ \mathbf{P}_{k|k-1} &= \mathbf{Q}_{k-1} + \mathbf{F}_k\mathbf{P}_{k-1|k-1}\mathbf{F}_k^{\mathtt{T}} \\ \mathbf{m}_{k|k} &= \mathbf{m}_{k|k-1} + \mathbf{K}_k(\mathbf{z}_k - \mathbf{H}_k\mathbf{m}_{k|k-1}) \\ \mathbf{P}_{k|k} &= \mathbf{P}_{k|k-1} - \mathbf{K}_k\mathbf{H}_k\mathbf{P}_{k|k-1} \end{aligned}$$

where $\mathbf{z}_k - \mathbf{H}_k \mathbf{m}_{k|k-1}$ is the mean of the difference between the predicted and the actual measurement vector, referred to as innovation vector. The covariance of the innovation vector is given by

$$\mathbf{S}_k = \mathbf{H}_k \mathbf{P}_{k|k-1} \mathbf{H}_k^{\mathtt{T}} + \mathbf{R}_k.$$

The Kalman gain $\mathbf{K}_k$ is given by

$$\mathbf{K}_k = \mathbf{P}_{k|k-1} \mathbf{H}_k^{\mathtt{T}} \mathbf{S}_k^{-1}.$$

The Kalman gain is a scaling factor for the correction amount or the innovation vector applied to the predicted state. This amount is directly proportional to the measurement prediction error. Specifically, if the latest measurement has new information that is not possible to predict, then this new information is used to update the current states.

2.2.2 Kalman Filter Simulations for Two-dimensional Tracking

We have implemented the KF in MATLAB to perform target tracking using range and range-rate measurements in the two-dimensional (2-D) plane. Unless otherwise stated, we use a constant velocity dynamic model [93] to simulate non-maneuvering target tracking. For a moving target, the state vector is given by $\mathbf{x}_k = [x_k, \dot{x}_k, y_k, \dot{y}_k]$ in Cartesian coordinates, where (x_k, y_k) are the target position coordinates and $(\dot{x}_k, \dot{y}_k)$ are the corresponding velocity coordinates. In the constant velocity model, the modeling error due to turbulence, thrust, etc., is modeled by white acceleration noise [93]. Since we assume a non-maneuvering dynamic model, the matrix $\mathbf{F}_k = \mathbf{F}$ in the process model of the state equation is time invariant and is given by

$$\mathbf{F} = \begin{bmatrix} 1 & \Delta T & 0 & 0 \\ 0 & 1 & 0 & 0 \\ 0 & 0 & 1 & \Delta T \\ 0 & 0 & 0 & 1 \end{bmatrix} \tag{2.6}$$

where ΔT is the time in seconds between time steps (k-1) and k. The covariance matrix for the constant velocity target motion model is [93]

$$\mathbf{Q} = \begin{bmatrix} \frac{q\Delta T^4}{4} & \frac{q\Delta T^3}{2} & 0 & 0 \\ \frac{q\Delta T^3}{2} & q\Delta T^2 & 0 & 0 \\ 0 & 0 & \frac{q\Delta T^4}{4} & \frac{q\Delta T^3}{2} \\ 0 & 0 & \frac{q\Delta T^3}{2} & q\Delta T^2 \end{bmatrix}$$

where q is a constant. The tracking system is assumed to measure the target position (x, y). The matrix in the measurement model in Equation (2.5) of the state equation is given by

$$\mathbf{H} = \begin{bmatrix} 1 & 0 & 0 & 0 \\ 0 & 0 & 1 & 0 \end{bmatrix}.$$

The measurement noise is modeled as white Gaussian noise with covariance matrix $\mathbf{R}$. The measurement noise is assumed to be independent of the modeling error process. In our simulations, we assumed that the initial position and velocity of the target is (1,10) m and (0.5,0.5) m/s, respectively; thus, the initial state vector is $\mathbf{x}_0 = [1\ 0.5\ 10\ 0.5]^{\mathrm{T}}$. The initial states were obtained from a Gaussian distribution with mean equal to the true initial state of the target. The process noise parameter q is set to 0.0001 and the measurement noise variances for the measurement vector is set at 25 for both measurements. Figure 2.1 shows the true and estimated target position. As seen from the figure, the variance of the estimated target position is much lower than the original measurement, and it also closely follows the target's true trajectory.

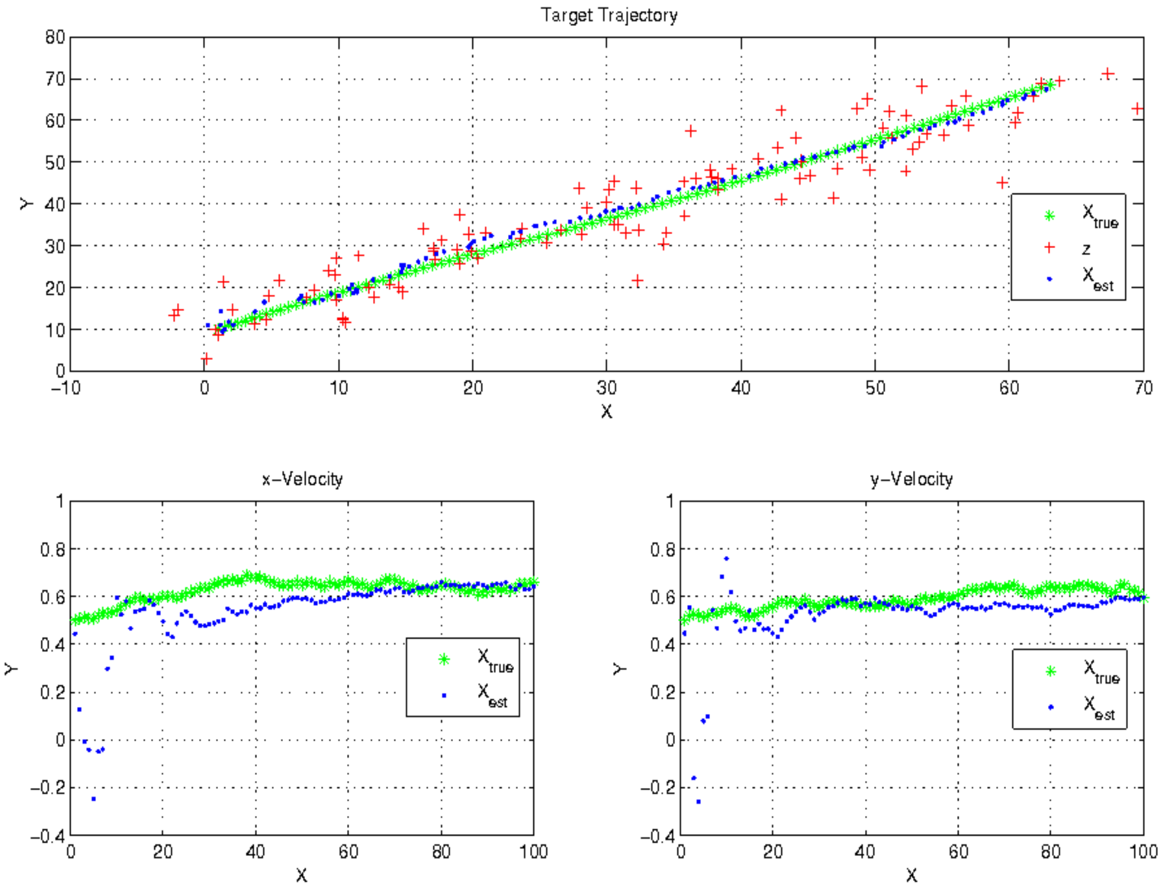

Figure 2.1: True and Estimated Target Trajectory (Top); Velocity in the y-direction (Bottom Right); and Velocity in the x-direction (Bottom Left). In the Top Plot, the Measurements are Represented by Crosses.

2.3 Sequential Monte Carlo Methods for Single Target Tracking

If the actual physical system that is modeled using the state space model deviates from the linearity and Gaussian assumptions, then the KF solution is no longer optimal. For example, if the provided measurement consists of the range and range-rate of the target, then the relationship between the unknown target position and the range measurement is nonlinear. The extended Kalman filter (EKF) is a method that is used to linearize state space functions using Taylor series approximations. As the EKF always approximates the posterior PDF as Gaussian, if the true posterior PDF is a multi-modal distribution, then the EKF is not expected to provide accurate results. Note, however, that in spite of its non-optimal solution, this technique is the standard technique used in many nonlinear state estimation problems owing to its relative computational simplicity.

Different simulation based Monte Carlo methods have emerged to solve the nonlinear and non-Gaussian state estimation problem [15]. The main idea of Monte Carlo methods is to represent the posterior density function by a set of random numbers. Each random number is assigned a weight value. If the random numbers and their associated weights are used to characterize the posterior PDF, then the states can be estimated using Monte Carlo integration in which the integral is replaced by a summation operator. This discrete representation of the posterior density can be used to approximate the continuous function of the PDF when a large number of random numbers or particles are used. The resulting solution derived from these particles is known as particle filter. The main task of the particle filter is to device a scheme to generate the random particles and determine their weights such that the discrete representation closely matches the true posterior PDF. The discrete equivalence of the continuous function PDF depends heavily on how the random numbers are generated.

2.3.1 Monte Carlo Integration

The term "Monte Carlo" was possibly first used by nuclear scientists in Los Alamos laboratories for random simulations to build atomic bombs. Their method uses law of chances and was aptly named after the international gambling destination Monte

Carlo. The author in [94] defined the Monte Carlo method as “the art of approximating an expectation by the sample mean of a function of simulated random variables”. This method can be used to compute the integrals of a function of random variables. For example, if we wish to find the integral [92],

$$I = \int_0^1 g(u)\ du.$$

we first introduce a random variable u that is uniformly distributed in the interval (0, 1) and generate another random variable $y = g(u)$. We can write the mean of y as

$$E[y = g(u)] = \int_0^1 g(u)p(u)\ du = \int_0^1 g(u)\ du = I$$

where $E[\cdot]$ is statistical expectation and $p(u)$ is the PDF of the random variable u. Since u is uniformly distributed in (0,1), $f_u(u) = 1$. From the above relation, we can see that the integral I can be evaluated as the expected value of the random variable y. If we have N samples $u^{(n)}$ of the random variable u that are generated by a random process, then we can compute the corresponding values of $y^{(n)} = g(u^{(n)})$. From $y^{(n)}$ we can evaluate I by computing its sample mean, which is given by

$$I = E[y = g(u)] \approx \frac{1}{N}\sum_{n=1}^{N} g(u^{(n)}).$$

2.3.2 Importance Sampling

In the above example, we can approximate I using the sample mean based on the assumption that the PDF of the random variable u is available. This may not be true in many cases. In this case, to generate N samples, we have to first identify the PDF that best fits the true PDF. Importance sampling is a statistical technique used to estimate the properties of a distribution from a set of samples generated from a distribution different from the true distribution. Using the above example, we can write I as,

$$I = E[y = g(u)] = E\Big[\frac{g(u)}{q(u)}\Big] \approx \frac{1}{N}\sum_{n=1}^{N}\frac{g(u^{(n)})}{q(u^{(n)})}$$

where $q(u)$ is called the importance sampling distribution or proposal density with $q(u) \neq 0$ for any values of $u \in A$, where A is the range of u, and $u^{(n)}$ is distributed according to $q(u)$. It can be shown that the variance of the Monte Carlo estimate of I is minimized when $q(u)$ is proportional to $|g(u)|$ [95]. A good importance sampling function should have the following properties [94]: $q(u)$ must be greater than zero whenever $g(u) \neq 0$, $q(u)$ should be proportional to $|g(u)|$, it should be easy to generate samples from $q(u)$, and it should be easy to evaluate $q(u)$ for any values of u.

2.3.3 Particle Filtering

Using the principle of importance sampling, the numerator of the prior density defined in Equation (2.3) can be written as

$$\begin{aligned}
p(\mathbf{x}_k|\mathbf{Z}_{k-1}) &\propto \int p(\mathbf{x}_k|\mathbf{x}_{k-1})p(\mathbf{x}_{k-1}|\mathbf{Z}_{k-1})d\mathbf{x}_{k-1} \\
&\propto \int \frac{p(\mathbf{x}_k|\mathbf{x}_{k-1})p(\mathbf{x}_{k-1}|\mathbf{Z}_{k-1})q(\mathbf{x}_{k-1}|\mathbf{Z}_{k-1})}{q(\mathbf{x}_{k-1}|\mathbf{Z}_{k-1})}d\mathbf{x}_{k-1} \\
&\propto \frac{1}{N}\sum_{n=1}^{N}\frac{p(\mathbf{x}_k|\mathbf{x}_{k-1}^{(n)})p(\mathbf{x}_{k-1}^{(n)}|\mathbf{Z}_{k-1})}{q(\mathbf{x}_{k-1}^{(n)}|\mathbf{Z}_{k-1})} \\
&\propto \frac{1}{N}\sum_{n=1}^{N} w_{k-1}^{(n)}p(\mathbf{x}_k|\mathbf{x}_{k-1}^{(n)}).
\end{aligned}$$

Comparing the arguments of the integral and summation terms, we can see that the sample estimate of the posterior density at time k is proportional to

$$p(\mathbf{x}_k|\mathbf{Z}_k) \propto \frac{1}{N}\sum_{n=1}^{N} w_k^{(n)}\delta(x_k - x_k^{(n)}) \tag{2.7}$$

where $\delta(\cdot)$ is the Dirac delta function. It can be shown that as N tends to ∞, the discrete representation in Equation (2.7) approaches the actual posterior density, and

$$w_k^{(n)} \propto \frac{p(\mathbf{x}_k|\mathbf{Z}_k)}{q(\mathbf{x}_k^{(n)}|\mathbf{Z}_k)}.$$

The weights can be computed in a sequential manner and the corresponding recursive weight equation is given by [15]

$$w_k^{(n)} \propto w_{k-1}^{(n)} \frac{p(\mathbf{z}_k|\mathbf{x}_k^{(n)})p(\mathbf{x}_k^{(n)}|\mathbf{x}_{k-1}^{(n)})}{q(\mathbf{x}_k^{(n)}|\mathbf{x}_{k-1}^{(n)}, \mathbf{z}_k)}. \tag{2.8}$$

One of the major problems with the particle filter is the degeneracy condition in which only a few particles have appreciable weight values after a few recursions. The weight value for the remaining particles becomes close to zero and their contribution to the posterior PDF approximation is negligible. When the degeneracy problem occurs, it becomes a waste of resource to compute the weights for all particles whose contribution to PDF approximation is negligible. One of the methods to mitigate the degeneracy problem is resampling. In the resampling technique, the particles with negligible weights are removed and the particles with significant weights are replenished by duplicating them. Many different techniques are being developed [16] to reduce the computational cost of the resampling process. In almost all cases, the weights are normalized to one before the resampling step. Although the resampling technique mitigates the degeneracy problem, it creates other problems such as sample impoverishment since it results in loss of particle diversity due to sample repetition. For example, if the process noise is very small, all the particles degenerate to a single sample after a few iterations. The degeneracy problem can also be mitigated if one knows the optimal importance density function. However, in most applications it is not possible to derive a closed form importance density function and hence the resampling technique is the most prevalent technique used to mitigate the degeneracy problem.

2.3.4 Sampling Importance Resampling Filter

The sampling importance resampling filter (SIR) is one of the most popular particle filter methods [16], [15] when the optimal importance density is not available. The weights calculation in SIR is inexpensive and the importance density can also be easily sampled by using the state space model. The SIR filter can be derived from the generic particle filter formulation in Equation (2.7) by assuming $q(\mathbf{x}_k|\mathbf{x}_{k-1}^{(n)}, \mathbf{z}_k)$ to be the prior PDF $p(\mathbf{x}_k|\mathbf{x}_{k-1}^{(n)})$ and executing the resampling process in every recursion. Under this assumption, the SIR weight recursion equation is given by,

$$w_k^{(n)} \propto w_{k-1}^{(n)} p(\mathbf{z}_k|\mathbf{x}_k^{(n)}). \tag{2.9}$$

However, during the resampling stage, all the particles are assigned to 1/N reducing the above recursion equation to,

$$w_k^{(n)} \propto p(\mathbf{z}_k|\mathbf{x}_k^{(n)}).$$

The importance density $p(\mathbf{x}_k|\mathbf{x}_{k-1}^{(n)})$ uses the process equation of the state space model to generate random samples and the likelihood function $p(\mathbf{z}_k|\mathbf{x}_k^{(n)})$ is evaluated using the measurement equation of the state space model. Since the importance density does not depend on the measurements, the SIR filter can become inefficient and sensitive to outliers. Nevertheless, SIR is the most widely method in target tracking due to its computational simplicity.

2.4 Multiple Target Tracking

2.4.1 State Space Model Formulation

In the multiple target tracking problem, the state vector of individual targets are augmented to form the multiple target state vector as

$$\mathbf{x}_k = [\mathbf{x}_{k,1}^{\mathtt{T}}\ \mathbf{x}_{k,2}^{\mathtt{T}}\ \ldots \mathbf{x}_{k,\mathscr{L}}^{\mathtt{T}}]^{\mathtt{T}}$$

where $\mathscr{L}$ is the number of targets and $\mathbf{x}_{k,\ell}$ is the state vector corresponding to the ℓth target. The state space model can be defined as in Equation (2.1), with the kinematic motion of each target separately provided. For example, the multiple target linear state space model can be defined as

$$\mathbf{x}_k = \begin{bmatrix} \mathbf{F}_{k,1} & \mathbf{0} & \dots & \mathbf{0} \\ \mathbf{0} & \mathbf{F}_{k,2} & \dots & \mathbf{0} \\ \vdots & \vdots & \vdots & \vdots \\ \mathbf{0} & \mathbf{0} & \dots & \mathbf{F}_{k,\mathscr{L}} \end{bmatrix} \mathbf{x}_{k-1} + \mathbf{v}_k \tag{2.10}$$

where $\mathbf{F}_{k,\ell}$ governs the kinematic state of the ℓth target, $\ell = 1, \dots, \mathscr{L}$, and $\mathbf{v}_k$ is the corresponding multiple target state modeling error. As there are multiple targets present at time step k, it is assumed that the number of received measurements at time step k is $N_{k,m}$. Then the set of all measurements received at time step k is given by $\mathbf{z}_k = \{\mathbf{z}_{k,1}, \mathbf{z}_{k,2}, \dots \mathbf{z}_{k,N_{k,m}}\}$ and it is related to the multiple state vector as in Equation (2.2). The set of all measurements up to time step k is given by $\mathbf{Z}_k = \{\mathbf{z}_1, \mathbf{z}_2, \dots, \mathbf{z}_k\}$.

2.4.2 Joint Probabilistic Data Association Filter

In this multiple target problem, the received measurement and its association with the corresponding target or clutter is not known *a priori*. To track multiple targets, one could use multiple probabilistic data association (PDA) filters (one each for each target) and consider the measurement associated with other targets as clutter. However, in the PDA filter, it is assumed that the spatial distribution of clutter is a random process with uniform distribution and the clutter measurements are independent in time. In the multiple target scenario, measurements from other targets cannot be assumed as independent and uniformly distributed in measurement space.

The classical PDA filter was designed to track a single target in clutter [20, 23, 24].

It is a sub-optimal data association technique in which all the measurements are used in the target state update step. Specifically, the target states are first independently computed for all measurements and then the final target states are estimated by taking the weighted average of the independent target state estimates. The weights represent the probability that the corresponding measurement is associated with the target. The following assumptions were made to derive the PDA filter: (a) only one target is present in the measurement space; (b) the track of the target has been initialized; (c) the clutter is uniformly distributed in the FOV; (d) the clutter and target associated measurements are independent and the clutter measurements are independent in time; (e) the number of clutter measurements at each time instant are Poisson distributed; (h) at most one measurement is originated from the target at a given time instant; (i) the innovation vector is assumed to be Gaussian; and (j) the measurement detections are made independently over time with a known probability of detection P_d.

In the JPDA filter, given a set of measurements and a known number of targets, a set of exhaustive measurement to target hypothesis set is formed [30]. The innovation vector for each target is computed for all measurements. The innovation vectors are then combined to estimate the target states. The weighted average of the innovation vector for each target is computed based on the probability of occurrence of each hypothesis. In addition to the assumptions mentioned for deriving the PDA filter, the following additional assumptions were made to derive the JPDA filter: (a) the number of targets present in the measurement space is known and their initial tracks are initialized; (b) no more than one measurement can originate from a target at time step k; (c) a measurement can have only one source (d) no back scanning; (e) unlike the PDA filter, every measurement is assumed validated (i.e., the validation gate coincides with the entire measurement space). Given $N_{k,m}$ measurements and

$\mathscr{L}$ targets, the first step is to define a set of hypothesis that contains all possible combinations of target and clutter measurements. Note that the number of possible hypothesis varies with the number of measurements. Using the total probability theorem, the minimum mean-squared error (MMSE) estimate of the ℓth target state vector is given by

$$\hat{\mathbf{x}}_{k|k,\ell} = \sum_{i=0}^{N_{k,m}} E[\mathbf{x}_{k,\ell} | i\text{th measurement belongs to } \ell\text{th target}, \mathbf{Z}_k] \beta^i_{k,\ell}$$

where the data association probability $\beta^i_{k,\ell}$ is the probability that the ith measurement belongs to the ℓth target and $N_{k,m}$ is the number of measurements at time k. This probability is obtained by summing the probability of all hypothesis that has the ith measurement associated with the ℓth target.

We have implemented the JPDA filter in MATLAB for tracking multiple targets in a 2-D plane using range and range-rate measurements. We have simulated the JPDA performance for different number of targets, and various clutter density and probability of detection. In the simulations, the matrix in Equation (2.10) is $\mathbf{F}_{k,\ell} = \mathbf{F}$ for all ℓ, $\ell = 1, 2, 3, 4$. Similarly, all targets use the same matrix in the measurement equation. In our simulations, we assumed that the initial positions and velocities of the four targets are (-50,50), (-50,0), (-50,-50) and (0,50) m and (1,-1.5), (1,0), (1,0.75) and (0,-1.5) m/s, respectively. The initial target states were set to the same values used in [33]. The FOV for the target in the x and y directions are [-50 50] m and [-100 50] m. The initial states for all targets were obtained using a Gaussian random variable with mean equal to the true initial state of the target. The process noise parameter q was set to 10^{-6} and the measurement noise variance for the measurement vector was set at 25 for all measurements. The average number of clutters per measurement was set at 2 (clutter spatial density $\lambda = 0.002924$). The probability of target detection P_d was 0.9. The top figure in Figure 2.2 shows the original clutter measurement dis-

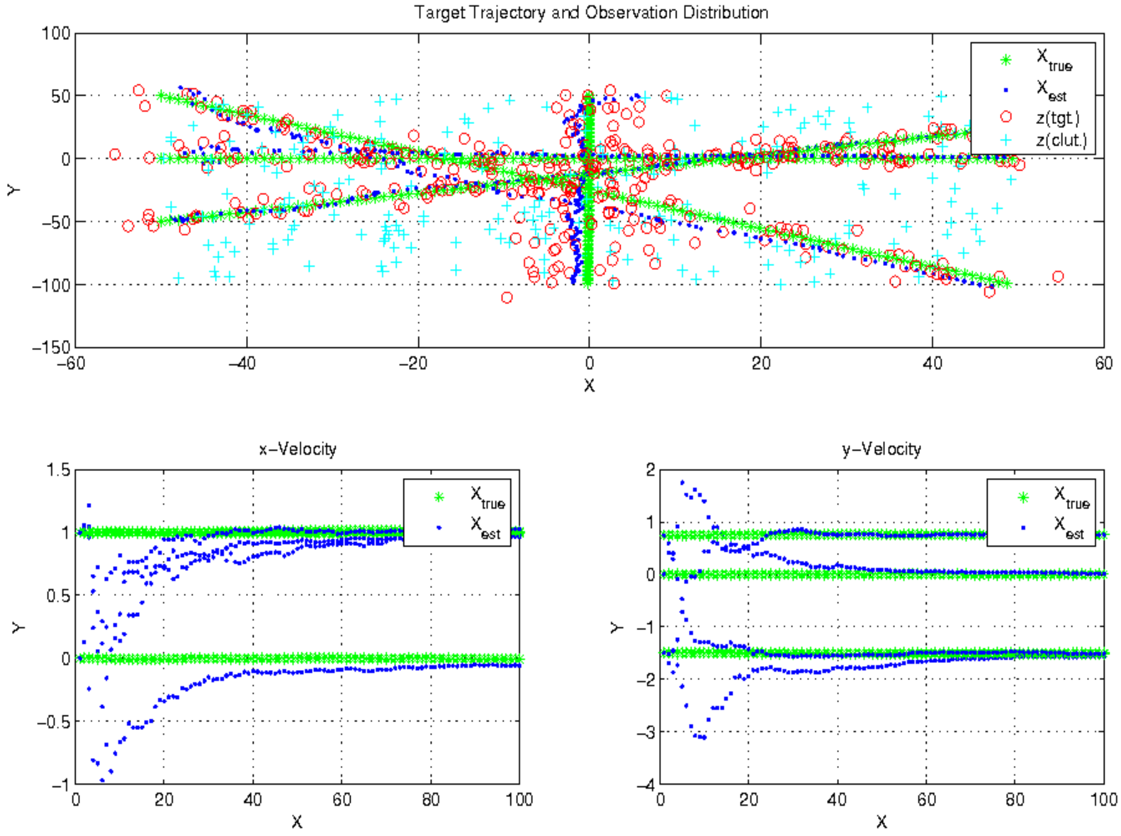

Figure 2.2: True and Estimated Trajectories for Four Targets (Top); Velocity in the y-direction (Bottom Right); and Velocity in the x-direction (Bottom Left). The Top Plot Also Shows the Target and Clutter Associated Measurements Represented by Circles and Crosses, respectively.

tribution at all times and the target associated measurement distribution. The same figure also shows the true and estimated target position for all four targets. As it can be seen, the SNR of the measurement vector is poor as the measurement is spread around the true target positions with high variance.

Figure 2.3 shows the performance of the JPDA filter under different environmental conditions. Specifically, we compared the root mean-squared error (RMSE) for differ-

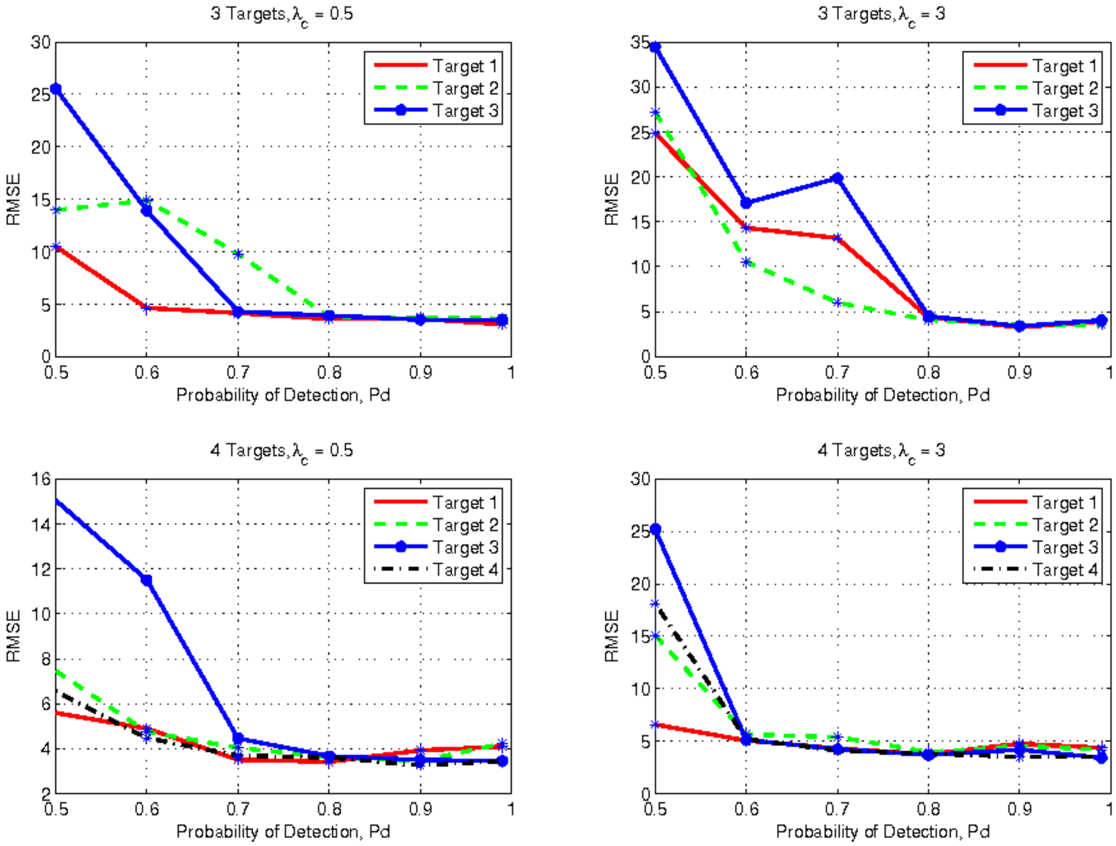

Figure 2.3: Tracking Performance of JPDA Filter for Various Values of Clutter Density, Number of Targets and Probability of Detection: RMSE at 0.5 Clutters Per Measurement Time with $\mathscr{L} = 3$ Targets (Top Left); RMSE at 3 Clutters Per Measurement Time with $\mathscr{L} = 3$ Targets (Top Right); RMSE at 3 Clutters Per Measurement Time with $\mathscr{L} = 4$ Targets (Bottom Right); and RMSE at 0.5 Clutters Per Measurement Time with $\mathscr{L} = 4$ Targets (Bottom Left).

ent values of average number of clutters per measurement (0.5 and 3), P_d (0.5-1) and number of targets (3 and 4). The RMSE was obtained by running 50 Monte Carlo simulations. As shown in Figure 2.3, the RMSE increases as the clutter density is increased for both 3 or 4 targets. Similarly, the RMSE increases as the P_d decreases.

This is expected because, when the probability of detection is low, the JPDA filter can use a fewer number of correct measurements for target tracking. The RMSE for all targets reaches a steady state condition when the P_d is greater than 0.8. Thus, at higher P_d values, the JPDA is able to track multiple targets without being drastically influenced by the presence of multiple targets. However, the tracking performance begins to degrade when the probability of detection decreases.

2.5 Sequential Monte Carlo Based Joint Probabilistic Data Association

The JPDA discussed in Section 2.4.2 assumed linear and Gaussian state space models. If the model is nonlinear, then the JPDA filter equations derived using the KF can be extended to support nonlinear models by using the EKF. However, if the state space model is not Gaussian, then, the EKF based JPDA filter's tracking performance will not be satisfactory. A particle filter (PF) based JPDA technique to track multiple targets in clutter environment was considered in [31, 32]. Since then, different PF based techniques [33, 34, 96] have been developed to track multiple targets in clutter environments for nonlinear and non-Gaussian state space models. For example, a PF based technique was used in [34] by combining PFs with the multiple hypothesis tracking method. The computational cost involved with this method is very expensive. To reduce the computational cost, the authors proposed to use KF or EKF to track the actual target states and PF to track different target hypothesis. The target states and the track hypothesis distribution estimate were then combined using the Rao-Blackwellization technique [97].

2.5.1 Monte Carlo Based JPDA Filter

A generalized Monte Carlo based JPDA (MCJPDA) framework for multiple target and multiple sensor tracking with data association was presented in [33], with two possible extensions to reduce computational complexity. This MCPJDA method closely follows the KF based JPDA filter as it uses the same hypothesis probability calculation method. The main difference is in the estimation of the posterior PDF for each target. The JPDA filter tries to collapse the posterior PDF into a single Gaussian distribution, whereas, in the MCJPDA filter, the posterior PDF is approximated by particles. Hence, if the importance distribution is selected appropriately, then the MCJPDA can approximate any multi-modal distribution without any significant loss of information.

2.5.2 Data Association and Sequential Monte Carlo

All the assumptions made for JPDA is valid for MCJPDA except for the Gaussian assumptions. The prediction equation for each target in the optimal Bayesian framework is given by

$$p(\mathbf{x}_{k,\ell}|\mathbf{z}_{k-1}) = \int p(\mathbf{x}_{k,\ell}|\mathbf{x}_{k-1,\ell})p(\mathbf{x}_{k-1,\ell}|\mathbf{z}_{k-1})d\mathbf{x}_{k-1,\ell} \tag{2.11}$$

where $\mathbf{z}_{k-1}$ is the set of all measurement vectors at time step $k-1$. As the MCJPDA is assumed to be a zero scan algorithm, we substitute $\mathbf{z}_k$ (only the current measurement) for all $\mathbf{Z}_k$. Due to measurement origin uncertainty, the update step cannot be performed independently for each target. In order to solve this data association problem, the JPDA concept is used to assign measurement-to-target probabilities such that all measurements are used to update the ℓth target state. Specifically, the measurement-to-target probabilities are used as weights to obtain the weighted likelihood function for the ℓth target. The weighted likelihood function is given by

$$p(\mathbf{z}_k|\mathbf{x}_{k,\ell}) = \beta^0_{k,\ell} + \sum_{i=1}^{N_{k,m}} \beta^i_{k,\ell}p(\mathbf{z}^i_k|\mathbf{x}_{k,\ell}) \tag{2.12}$$

where $\mathbf{z}^i_k$ is the ith measurement vector at time k, and $\beta^i_{k,\ell}$ is the probability that the ith measurement is associated with the ℓth target. Based on the modified definition of the likelihood function, the update equation for the optimal Bayesian solution is given by

$$p(\mathbf{x}_{k,\ell}|\mathbf{z}_k) \propto p(\mathbf{z}_k|\mathbf{x}_{k,\ell})p(\mathbf{x}_{k,\ell}|\mathbf{z}_{k-1}). \tag{2.13}$$

The PDF of the predicted measurement can be calculated as

$$p(\mathbf{z}_k|\mathbf{z}_{k-1}) = \int p(\mathbf{z}_k|\mathbf{x}_{k,\ell})p(\mathbf{x}_{k,\ell}|\mathbf{z}_{k-1})d\mathbf{x}_{k,\ell}. \tag{2.14}$$

The calculation of the hypothesis probability is exactly the same as for the JPDA. The recursive Equations (2.11), (2.12) and (2.13) provide a theoretical framework for tracking multiple targets with measurement origin uncertainty.

2.5.3 Particle Filter Implementation of MCJPDA

In most cases, it is very difficult to derive a closed form solution for a given dynamic state and measurement model. Hence, we have to resort to particle filters to approximate the posterior PDF of the target states. For the ℓth target, if we assume that the approximate posterior PDF is available and it is parameterized as $\{\mathbf{x}^{(n)}_{k-1,\ell}, w^{(n)}_{k-1,\ell}\}_{n=1}^{N}$, where N is the number of particles, then the particle filter steps are given as follows.

- At time step k, generate new samples that are distributed according to the importance density $q_\ell(\mathbf{x}_{k,\ell}|\mathbf{x}^{(n)}_{k-1,\ell}, \mathbf{z}_k)$,

$$\mathbf{x}^{(n)}_{k,\ell} \approx q_\ell(\mathbf{x}_{k,\ell}|\mathbf{x}^{(n)}_{k-1,\ell}, \mathbf{z}_k)$$

- Compute the particle filter approximation of the predicted measurement likelihood as

$$p(\mathbf{z}_k|\mathbf{z}_{k-1}) \approx \sum_{n=1}^{N} \alpha^{(n)}_{k,\ell} p(\mathbf{z}_k|\mathbf{x}^{(n)}_{k,\ell})$$

where the predictive weights $\alpha_{k,\ell}^{(n)}$ are calculated by applying Monte Carlo integration on Equation (2.14),

$$\alpha_{k,\ell}^{(n)} \approx w_{k-1,\ell}^{(n)} \frac{p(\mathbf{x}_{k,\ell}^{(n)}|\mathbf{x}_{k-1,\ell}^{(n)})}{q_\ell(\mathbf{x}_{k,\ell}^{(n)}|\mathbf{x}_{k-1,\ell}^{(n)}, \mathbf{z}_k)}, \sum_{n=1}^{N} \alpha_{k,\ell}^{(n)} = 1$$

- Enumerate all possible hypothesis and compute their corresponding probabilities.

- Calculate the measurement-to-target data association probability using the predicted measurement likelihood and the hypothesis probability.

- Compute the target likelihood PDF in Equation (2.13) based on the computed data association probability.

- Compute the particle weights for approximating the posterior PDF,

$$w_{k,\ell}^{(n)} \approx w_{k-1,\ell}^{(n)} \frac{p(\mathbf{z}_k|\mathbf{x}_{k,\ell}^{(n)})p(\mathbf{x}_{k,\ell}^{(n)}|\mathbf{x}_{k-1,\ell}^{(n)})}{q_\ell(\mathbf{x}_{k,\ell}^{(n)}|\mathbf{x}_{k-1,\ell}^{(n)}, \mathbf{z}_k)}$$

- Normalize the weights and resample the particles to avoid sample degeneration.

2.5.4 MCJPDA Using SIR particle filter

Using the aforementioned PF implementation, to generate the particles requires the importance density and the tracking performance is highly dependent on the choice of importance density. One simple choice is to use the state transition distribution as the importance density [31],

$$q_\ell(\mathbf{x}_{k,\ell}^{(n)}|\mathbf{x}_{k-1,\ell}^{(n)}, \mathbf{z}_k) \approx p(\mathbf{x}_{k,\ell}^{(n)}|\mathbf{x}_{k-1,\ell}^{(n)}).$$

If the state transition distribution is used, then the measurement likelihood becomes

$$p(\mathbf{z}_k|\mathbf{z}_{k-1}) \approx \frac{1}{N} \sum_{n=1}^{N} p(\mathbf{z}_k|\mathbf{x}_{k,\ell}^{(n)})$$

and the particle filter weights depend only on the measurement likelihood,

$$w_{k,\ell}^{(n)} \approx w_{k-1,\ell}^{(n)} p(\mathbf{z}_k|\mathbf{x}_{k,\ell}^{(n)}).$$

We have implemented the MCJPDA filter using the SIR particle filter in MATLAB for tracking multiple targets in the 2-D plane. Unlike previous examples, we used nonlinear measurement functions to track multiple targets. We used the same process model as before with the matrix $\mathbf{F}$ for all targets as in Equation (2.6). The measurement vector consists of range $r_{k,\ell}$ and range-rate $\dot{r}_{k,\ell}$. The nonlinear relation between the measurements and target states are given by

$$r_{k,\ell} = \sqrt{(x_{k,\ell} - x_o)^2 + (y_{k,\ell} - y_o)^2} \tag{2.15}$$

$$\dot{r}_{k,\ell} = \frac{\dot{x}_{k,\ell}(x_{k,\ell} - x_o) + \dot{y}_{k,\ell}(y_{k,\ell} - y_o)}{\sqrt{(x_{k,\ell} - x_o)^2 + (y_{k,\ell} - y_o)^2}} \tag{2.16}$$

where (x_o, y_o) is the stationary sensor location coordinates. In our simulations, we assumed Gaussian noise for both the measurement noise and the modeling error process. We used four targets, whose initial target states are same as the ones used in the JPDA illustration in Figure 2.2. The process noise parameter q was set to 10^{-6} and the measurement noise variance for the measurement vector was set at 25 for range and 1 for range-rate measurements. The average number of clutters per measurement was set at 2, (clutter spatial density $\lambda = 0.002924$). The probability of target detection P_d was set at 0.9 and 300 particle were used to approximate the posterior PDF. Figure 2.4 shows the original clutter measurement distribution at all times and also the target associated measurement distribution. From the figure, it is not possible to visually separate the clutter associated measurements from the target associated measurements. Figure 2.4 also shows the true and estimated target position for all four targets and the MCJPDA filter is able to accurately estimate the state vectors. The estimated trajectory deviates from the true trajectory when the targets came close to each other. However, the MCJPDA filter was able converge back to the true trajectory after the targets had moved away from each other.

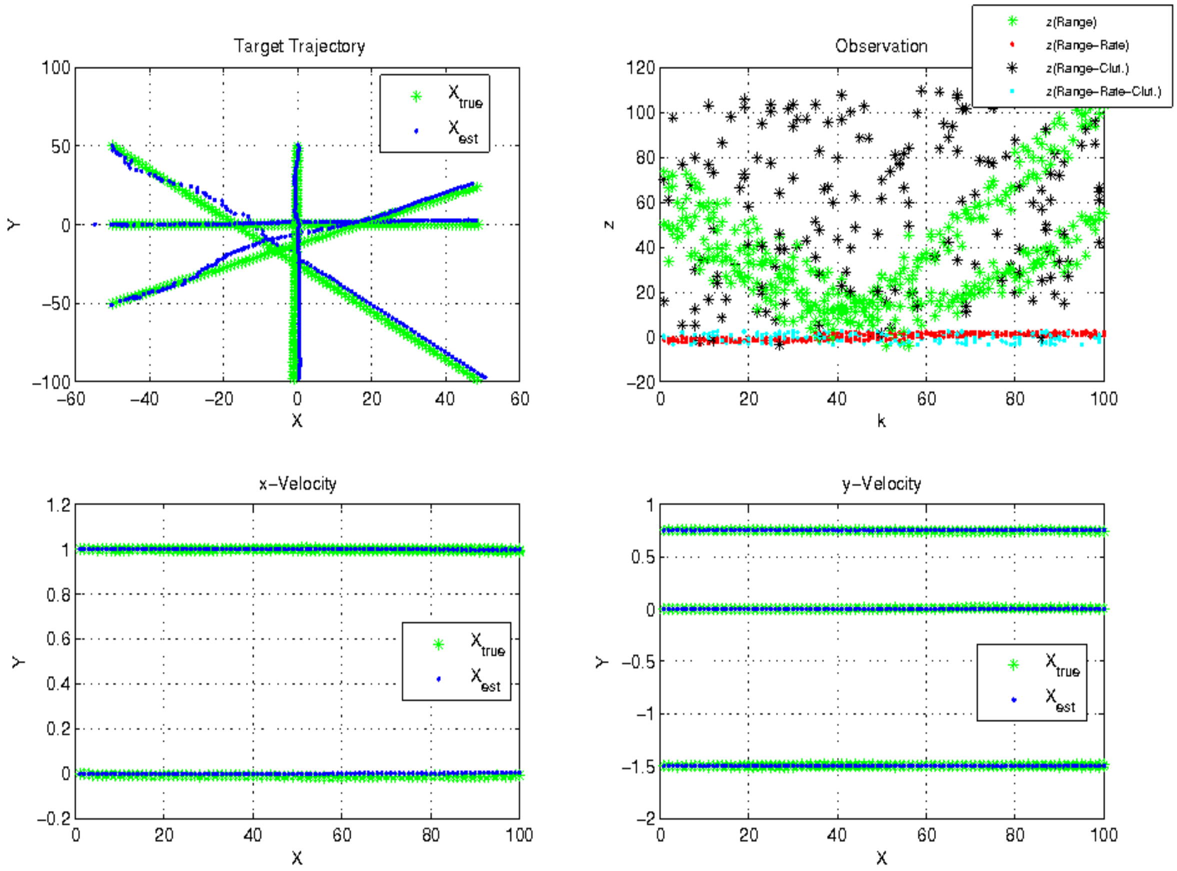

Figure 2.4: MCJPDA Filter Performance: True and Estimated Trajectories for Four Targets (Top Left); Target and Clutter Associated Measurements (Top Right, Green and Black Stars Represent Target and Clutter Associated Range Measurements, respectively, and Red and Cyan Dots Represent Target and Clutter Associated Range-Rate Measurements, respectively); Velocity in the y-direction (Bottom Right); and Velocity in the x-direction (Bottom Left).

Chapter 3

SINGLE TARGET SEQUENTIAL MONTE CARLO TRACK-BEFORE-DETECT FILTERING

3.1 Tracking Under Low Signal-to-Noise Ratio Conditions

Under low signal-to-noise ratio (SNR) conditions, it is possible to miss the detection of target associated measurements. In conventional radar systems, tracking low SNR moving targets using constant false alarm rate (CFAR) detectors [45, 46] can result in poor performance as thresholding can result in a loss of information. The probability of detection is low for targets with small radar cross section [45, 47], since, as the SNR decreases, the CFAR detection threshold needs to be increased; this requires additional measurements, resulting in increased number of false alarms.

The track-before-detect filter (TBDF) is a method proposed to improve tracking under low SNR conditions. TBDF algorithms based on the Hough transform, dynamic programming or maximum likelihood are generally computationally intensive [17]. However, with recent advancements in sequential Monte Carlo techniques, TBDF algorithms implemented using a particle filter (PF) are now computationally feasible [51, 52]. The PF based TBDF incorporates unthresholded data and a binary target existence variable into the target state estimation process. A recursive TBDF algorithm for a single target was proposed in [55] that uses PF based interacting multiple model (IMM) concept for a jump Markov nonlinear model [98]. For a single target, the modes correspond to a target entering the field of view (FOV) and to a target leaving the FOV. Following the IMM method, the target state estimates from both modes are integrated to derive the final state estimates.

3.2 Sequential Monte Carlo Track-before-detect Filtering

The PF based TBDF (PF-TBDF) proposed in [51] can work using a single scan of data like the PDA filter families, and it also supports nonlinear and non-Gaussian state space models.

3.2.1 State Space Model

We assume that we want to track a target moving in a 2-D plane with an unknown state vector $\mathbf{x}_k$ at time step k. As in Chapter 2, we consider the state model given by

$$\mathbf{x}_k = \mathbf{F}\,\mathbf{x}_{k-1} + \mathbf{v}_k \tag{3.1}$$

where $\mathbf{F}$ is the state transition matrix, assuming constant velocity motion and $\mathbf{v}_k$ is a modeling error random process with covariance matrix $\mathbf{Q}$. A target can be present or absent in the measurement space. This is modeled as a random process by introducing a random variable E_k which is modeled as a two state first order Markov chain. Specifically, $E_k \in \{0, 1\}$, where $E_k = 1$ represents the target existence in the FOV and $E_k = 0$ represents the target absence in the FOV. We consider two state transitional probabilities: the probability P_B of a target entering the FOV and the probability P_D of a target leaving the FOV. These probabilities are assumed known and are defined as $P_B \triangleq \Pr(E_k = 1 | E_{k-1} = 0)$, $P_D \triangleq \Pr(E_k = 0 | E_{k-1} = 1)$. Once a target is detected, the probability that the target remains in the FOV is $(1 - P_D)$. Similarly, once a target is detected to leave the FOV, the probability that target remains outside the FOV is given by $(1 - P_B)$. The corresponding transition matrix for the Markov process is

$$\boldsymbol{\Omega} = \begin{bmatrix} 1 - P_B & P_B \\ P_D & 1 - P_D \end{bmatrix}. \tag{3.2}$$

The initial target existence probability $\Pr(e_0 = 1)$ is also assumed to be known, where e_k is the event that represents the existence of a target.

We assume that each unthresholded measurement $z_k^{(a,b)}$, with center coordinate in the 2-D plane given by (a, b), is related to the target state vector according to

$$z_k^{(a,b)} = \begin{cases} h_k^{(a,b)}(\mathbf{x}_k) + w_k^{(a,b)}, & \text{for } E_k = 1 \\ \\ w_k^{(a,b)}, & \text{for } E_k = 0 \end{cases} \tag{3.3}$$

where $h_k^{(a,b)}(\mathbf{x}_k)$ is a possibly nonlinear function of $\mathbf{x}_k$ and the measurement noise $w_k^{(a,b)}$ is assumed to be independent and Gaussian distributed with variance r. The measurement vector $\mathbf{z}_k$ consists of multiple unthresholded measurements, as in Equation (3.3), and

$$\mathbf{Z}_k = \{\mathbf{z}_0, \mathbf{z}_1, \ldots, \mathbf{z}_k\}$$

where $\mathbf{Z}_k$ is the set of all measurement vectors up to time step k.

3.2.2 Bayesian Solution to Track-before-detect Filtering

Given the state and measurement models and the posterior probability density function (PDF) at time step $k-1$, $p(\mathbf{x}_{k-1}, E_{k-1}|\mathbf{Z}_{k-1})$, the task of PF-TBDF is to estimate the posterior PDF at time step k, $p(\mathbf{x}_k, E_k|\mathbf{Z}_k)$. This is a multiple-model problem in which the posterior PDF is dependent on the target existence condition or mode. For the single target case, there are two modes: target is present and target is absent. The posterior PDF needs to be estimated only when the target is present since the posterior PDF is undefined when the target is absent. Using the generic Bayesian solution for multiple switching dynamic models [17], the predicted PDF for the PF-TBDF is given by

$$p(\mathbf{x}_k, E_k = 1|\mathbf{Z}_{k-1}) = P_B \int p_b(\mathbf{x}_k)\, p(\mathbf{x}_{k-1}, E_{k-1} = 0|\mathbf{Z}_{k-1})\, d\mathbf{x}_{k-1} \ + $$
$$(1 - P_D) \int p(\mathbf{x}_k|\mathbf{x}_{k-1}, E_{k-1} = 1, E_k = 1)\, p(\mathbf{x}_{k-1}, E_{k-1} = 1|\mathbf{Z}_{k-1})\, d\mathbf{x}_{k-1} \quad (3.4)$$

where $p_b(\mathbf{x}_k)$ is an *a priori* known target distribution based on the assumption that the target is detected at time step k, and $p(\mathbf{x}_k|\mathbf{x}_{k-1}, E_{k-1} = 1, E_k = 1)$ is defined by the target state transition model. Given the predicted prior PDF and the likelihood function $p(\mathbf{Z}_k|\mathbf{x}_k, E_k = 1)$, the updated PDF can be written as

$$p(\mathbf{x}_k, E_k = 1|\mathbf{Z}_k) = \frac{p(\mathbf{Z}_k|\mathbf{x}_k, E_k = 1)\, p(\mathbf{x}_k, E_k = 1|\mathbf{Z}_{k-1})}{p(\mathbf{Z}_k|\mathbf{Z}_{k-1})}.$$

Since, the measurement noise is assumed to be independent between unthresholded measurements, the joint likelihood function can be written as

$$p(\mathbf{Z}_k|\mathbf{x}_k) = \begin{cases} \prod_a \prod_b \mathcal{N}(z_k^{(a,b)}; h_k^{(a,b)}(\mathbf{x}_k), r), & \text{for } E_k = 1 \\ \\ \prod_a \prod_b \mathcal{N}(z_k^{(a,b)}; 0, r), & \text{for } E_k = 0 \end{cases} \quad (3.5)$$

where $\mathcal{N}(z_k^{(a,b)}; h_k^{(a,b)}(\mathbf{x}_k), r)$ implies that $z_k^{(a,b)}$ is a Gaussian random variable with mean $h_k^{(a,b)}(\mathbf{x}_k)$ and variance r.

3.2.3 Particle Filter Implementation of Track-before-detect Filtering

The PF implementation of the aforementioned Bayesian recursive equations was originally performed in [51] by appending the state vector with the target existence variable E_k to form $\mathbf{y}_k = [\mathbf{x}_k^{\mathsf{T}}\ E_k]^{\mathsf{T}}$. The posterior PDF of the new state vector $\mathbf{y}_k$ is approximated using N particles $\mathbf{y}_k^{(n)}$ and their corresponding weights $w_k^{(n)}$, $n = 1, \ldots, N$; the resulting PF implementation steps are listed next.

- A set of particles for the target existence variable $E_k^{(n)}$ are generated using the past state $E_{k-1}^{(n)}$ and the state transition matrix $\mathbf{\Omega}$.

- The target states are predicted based on the target existence condition for each particle. Based on the current and past state of the target existence variable, there are two possible modes:
  - Mode 1: the target enters the FOV ($E_{k-1} = 0$ and $E_k = 1$):

    The target state particles are uniformly drawn at time step k based on some *a priori* information on the minimum and maximum possible values on the target state.
  - Mode 2: the target remains in the FOV ($E_{k-1} = 1$ and $E_k = 1$):

    The state transition model in Equation (3.1) is used to update the target state particles.

- The particle weights are computed by modifying the likelihood function in Equation (3.5) as

$$p(\mathbf{Z}_k|\mathbf{x}_k) \propto \begin{cases} \dfrac{\prod\limits_a \prod\limits_b \mathcal{N}(z_k^{(a,b)}; h_k^{(a,b)}, r)}{\prod\limits_a \prod\limits_b \mathcal{N}(z_k^{(a,b)}; 0, r)}, & \text{for } E_k = 1 \\ \\ 1, & \text{for } E_k = 0 \end{cases}$$

$$\propto \begin{cases} \prod\limits_a \prod\limits_b l(z_k^{(a,b)}|\mathbf{x}_k), & \text{for } E_k = 1 \\ \\ 1, & \text{for } E_k = 0 \end{cases} \tag{3.6}$$

  where $l(z_k^{(a,b)}|\mathbf{x}_k)$ is the measurement-dependent likelihood ratio.

- The computed weights are normalized and the particles are resampled.

- From the approximated posterior PDF of the appended state vector $\mathbf{y}_k$, the target existence probability $\Pr(e_k)$ is obtained as

$$\Pr(e_k) = \frac{1}{N} \sum_{n=1}^{N} E_k^{(n)} .$$

3.3 Efficient Particle Filter Based Track-before-detect Filtering

3.3.1 Algorithm Description

In the previous section, a PF based TBDF method was described in which the target existence variable is also included in the state vector. An efficient PF based method was proposed in [53] that does not include the target existence variable in the state vector. An analytical expression was also derived to estimate the target existence probability. Moreover, instead of using a single set of particles, the efficient PF-TBDF represents each mode (a target entering the FOV and a target remaining in the FOV) by a set of particles. This efficient approach integrates the PF implementation algorithm proposed for the IMM algorithm in [98] for a nonlinear jump Markov system. The two particle sets scheme enables one to efficiently assign different number of particles for the two modes, thereby avoiding particle degeneracy that typically happens during mode transition. Similar to the original PF-TBDF, this method also estimates the posterior PDF $p(\mathbf{x}_k, E_k = 1|\mathbf{Z}_k)$. The posterior PDF can be written as

$$p(\mathbf{x}_k, E_k = 1|\mathbf{Z}_k) = p(\mathbf{x}_k|E_k = 1, \mathbf{Z}_k) \Pr(E_k = 1|\mathbf{Z}_k). \tag{3.7}$$

In Equation (3.7), the target existence probability $\Pr(E_k = 1|\mathbf{Z}_k)$ is separated from the target's state parameters. The target state vector PDF conditioned on target existence can be written as

$$\begin{aligned} p(\mathbf{x}_k|E_k=1,\mathbf{Z}_k) =& \sum_{j=0}^{1} p(\mathbf{x}_k, E_{k-1}=j|E_k=1,\mathbf{Z}_k) \\ =& \; p(\mathbf{x}_k,|E_{k-1}=0,E_k=1,\mathbf{Z}_k)\Pr(E_{k-1}=0|E_k=1,\mathbf{Z}_k)+ \\ & \; p(\mathbf{x}_k,|E_{k-1}=1,E_k=1,\mathbf{Z}_k)\Pr(E_{k-1}=1|E_k=1,\mathbf{Z}_k). \end{aligned} \tag{3.8}$$

Thus, the target state vector PDF conditioned on target existence is a weighted mixture of two density functions. The density function $p(\mathbf{x}_k,|E_{k-1}=0,E_k=1,\mathbf{Z}_k)$ represents the target state vector PDF conditioned on a target entering the FOV. The density function $p(\mathbf{x}_k,|E_{k-1}=1,E_k=1,\mathbf{Z}_k)$ represents the target state vector PDF conditioned on a target remaining in the FOV. Using Bayes rule, the PDF corresponding to a target entering the FOV can be updated as

$$p(\mathbf{x}_k,|E_{k-1}=0,E_k=1,\mathbf{Z}_k) = l(z_k|\mathbf{x}_k,E_k=1)\,p(\mathbf{x}_k,|E_{k-1}=0,E_k=1)$$

where $p(\mathbf{x}_k,|E_{k-1}=0,E_k=1)=p_b(\mathbf{x}_k)$ is the *a priori* distribution described below Equation (3.4) and $l(z_k|\mathbf{x}_k,E_k=1)$ is the likelihood function in Equation (3.6). Similarly, the PDF corresponding to a target remaining in the FOV can be updated as

$$p(\mathbf{x}_k,|E_{k-1}=1,E_k=1,\mathbf{Z}_k) = l(z_k|\mathbf{x}_k,E_k=1)\,p(\mathbf{x}_k,|E_{k-1}=1,E_k=1,\mathbf{Z}_{k-1}).$$

The predicted density can be written as a function of the transition density and the posterior target state distribution at time step $k-1$,

$$\begin{aligned} p(\mathbf{x}_k|E_{k-1}=1,E_k=1,\mathbf{Z}_{k-1}) = \int & p(\mathbf{x}_k|\mathbf{x}_{k-1},E_{k-1}=1,E_k=1) \\ & p(\mathbf{x}_{k-1},|E_{k-1}=1,\mathbf{Z}_{k-1})\,d\mathbf{x}_{k-1}. \end{aligned}$$

Closed form expressions for the weights $\Pr(E_{k-1}=0|E_k=1,\mathbf{Z}_k)$ and $\Pr(E_{k-1}=1|E_k=1,\mathbf{Z}_k)$ in Equation (3.8) are derived in [53].

3.3.2 *Implementation of the Efficient PF-TBDF*

The implementation of the efficient PF-TBDF using a separate particle set for each mode is described next, following [53]. The posterior PDFs, $p(\mathbf{x}_k, | E_{k-1} = 1, E_k = 1, \mathbf{Z}_k)$ and $p(\mathbf{x}_k, | E_{k-1} = 0, E_k = 1, \mathbf{Z}_k)$ are approximated using the particle and weight sets $\mathbf{x}_{k-1}^{(n_1)}$ and $w_{k-1}^{(n_1)}$, $n_1 = 1, \ldots, N_1$ and $\mathbf{x}_{k-1}^{(n_2)}$ and $w_{k-1}^{(n_2)}$, $n_2 = 1, \ldots, N_2$ where N_1 and N_2 are the respective number of particles for each set. Given $p(\mathbf{x}_{k-1}, | E_{k-2} = 1, E_{k-1} = 1, \mathbf{Z}_{k-1})$ and the target existence probability $\Pr(e_{k-1})$ at time step $k-1$, the PF steps are listed next.

- At time step k, N_2 new particles are generated that are distributed according to the proposal density

  $$\mathbf{x}_k^{(n_2)} \approx q(\mathbf{x}_k | E_{k-1} = 0, E_k = 1, \mathbf{Z}_k).$$

  $n_2 = 1, 2, \ldots, N_2$ using the steps in Section 3.2.3.

- The corresponding weights are obtained using

  $$\tilde{w}_k^{(n_2)} = \frac{l(z_k | \mathbf{x}_k^{(n_2)}, E_k = 1)\, q(\mathbf{x}_k^{(n_2)} | E_{k-1} = 0, E_k = 1, \mathbf{Z}_k)}{N_2\, q(\mathbf{x}_k^{(n_2)} | E_{k-1} = 0, E_k = 1, \mathbf{Z}_k)}.$$

- The particle weights are normalized

  $$w_k^{(n_2)} = \frac{\tilde{w}_k^{(n_2)}}{\sum_{n_2=1}^{N_2} \tilde{w}_k^{(n_2)}}.$$

- N_1 new particles are generated that are distributed according to the proposal density

  $$\mathbf{x}_k^{(n_1)} \approx q(\mathbf{x}_k | E_{k-1} = 1, E_k = 1, \mathbf{Z}_k)$$

  $n_1 = 1, 2, \ldots, N_1$ using the target dynamic model in Equation (3.1).

- The particle weights are calculated using

$$\tilde{w}_k^{(n_1)} = \frac{l(z_k|\mathbf{x}_k^{(n_1)}, E_k = 1)}{N_1}.$$

- The particle weights are normalized

$$w_k^{(n_1)} = \frac{\tilde{w}_k^{(n_1)}}{\sum_{n_1=1}^{N_1} \tilde{w}_k^{(n_1)}}.$$

- The mixing probabilities are calculated as

$$\Pr{}^U(E_{k-1} = 1|E_k = 1, \mathbf{Z}_k) = [1 - P_D] \Pr(e_{k-1}) \sum_{n_1=1}^{N_1} \tilde{w}_k^{(n_1)},$$

$$\Pr{}^U(E_{k-1} = 0|E_k = 1, \mathbf{Z}_k) = P_B \, [1 - \Pr(e_{k-1})] \sum_{n_2=1}^{N_2} \tilde{w}_k^{(n_2)}.$$

  where $\Pr(e_{k-1})$ is the target existence probability at the previous time step, and P_B and P_D are the *a priori* probabilities of a target entering or leaving the FOV, respectively.

- The mixing probabilities are normalized

$$\Pr(E_{k-1} = 0|E_k = 1, \mathbf{Z}_k) = \frac{\Pr^U(E_{k-1} = 0|E_k = 1, \mathbf{Z}_k)}{\Pr^U(E_{k-1} = 0|E_k = 1, \mathbf{Z}_k) + \Pr^U(E_{k-1} = 1|E_k = 1, \mathbf{Z}_k)},$$

$$\Pr(E_{k-1} = 1|E_k = 1, \mathbf{Z}_k) = \frac{\Pr^U(E_{k-1} = 1|E_k = 1, \mathbf{Z}_k)}{\Pr^U(E_{k-1} = 0|E_k = 1, \mathbf{Z}_k) + \Pr^U(E_{k-1} = 1|E_k = 1, \mathbf{Z}_k)}.$$

- The probability of target existence is calculated using

$$\Pr(e_k) = \left[1 + \frac{(1 - P_b)\,(1 - \Pr(e_{k-1})) + P_D \Pr(e_{k-1})}{\Pr^U(E_{k-1} = 0|E_k = 1, \mathbf{Z}_k) + \Pr^U(E_{k-1} = 1|E_k = 1, \mathbf{Z}_k)}\right]^{-1}.$$

- The particle weights are scaled by the mixing probabilities as

$$w_k^{(n_1)} = \Pr(E_{k-1} = 1|E_k = 1, \mathbf{Z}_k) w_k^{(n_1)},$$

$$w_k^{(n_2)} = \Pr(E_{k-1} = 0|E_k = 1, \mathbf{Z}_k) w_k^{(n_2)}.$$

  The two set of particles are then combined to generate $N_2 + N_1$ particles.

- The particles are resampled and the number of particles are reduced from (N_2 + N_1) to N_1 to represent the posterior PDF of the target remaining in the FOV.

3.4 Target Tracking Example Using Image Measurements

3.4.1 Image Measurement Model

We consider tracking moving targets using image measurements from video cameras. Each measurement is considered to be a sequence of 2-D image frames with finite resolution, and each pixel in a frame is characterized by its grey-scale level. Each 2-D measurement frame is assumed to consists of $(N_x \times N_y)$ pixels with a pixel resolution $(\triangle_x \times \triangle_y)$. The center of the pixel $(a,\, b)$ is at the position $(a\triangle_x \times b\triangle_y)$. If a target is not present in a frame, the measurement contains only noise for all pixels. If a target is present in a frame, then the pixels in the vicinity of the target's current position contain signal plus noise. A point target and a sensor point spread function approximated by a 2-D Gaussian function is assumed in this measurement model. If a target is present in a measurement frame, it is characterized by its x and y coordinate position and its corresponding grey-scale level in that position. The grey-scale level is denoted as I_k. In addition to the target position and intensity, the component velocities also constitute the state vector. The targets state vector is then given by

$$\mathbf{x}_k = [x_k, \dot{x_k}, y_k, \dot{y_k}, I_k]^{\mathrm{T}}.$$

Assuming constant velocity target motion, the elements of the (5×5) state transition matrix $\mathbf{F}$ is given by

$$\mathbf{F} = \begin{bmatrix} 1 & \Delta T & 0 & 0 & 0 \\ 0 & 1 & 0 & 0 & 0 \\ 0 & 0 & 1 & \Delta T & 0 \\ 0 & 0 & 0 & 1 & 0 \\ 0 & 0 & 0 & 0 & 1 \end{bmatrix}$$

where ΔT is the time step interval and we assumed additive noise model for target intensity. The measurements from all pixels in Equation (3.3) are concatenated to generate the measurement vector

$$\mathbf{z}_k = \big[z_k^{(1,1)} \ z_k^{(1,2)} \ \ldots \ z_k^{(1,N_x)} \ z_k^{(2,1)} \ z_k^{(2,2)} \ \ldots \ z_k^{(2,N_y)} \ \ldots \ z_k^{(N_x,1)} \ \ldots \ z_k^{(N_x,N_y)}\big].$$

The likelihood function $l(z_k^{(a,b)}|\mathbf{x}_k)$ in Equation (3.6) can be simplified as

$$l(z_k^{(a,b)}|\mathbf{x}_k) \triangleq \exp\bigg\{ - \frac{h_k^{(a,b)}(\mathbf{x}_k)(h_k^{(a,b)}(\mathbf{x}_k) - 2z_k^{(a,b)})}{2r} \bigg\}, \tag{3.9}$$

where $h_k^{(a,b)}(\mathbf{x}_k)$ is the intensity contribution of a target present at the position (x_k, y_k) to the pixel (a, b). The imaging sensor measurement corresponding to a target is modeled using a Gaussian spread function with a point target assumption. The blurring introduced by the sensor is modeled by adjusting the spread factor σ, of the Gaussian spread function. For a target present at the position (x_k, y_k), this nonlinear spread function $h_k^{(a,b)}(\mathbf{x}_k)$ in the measurement model in Equation (3.3) can be modeled as

$$h_k^{(a,b)}(\mathbf{x}_k) = \tfrac{\triangle_x \triangle_y I_k}{2\pi\sigma^2} \exp\big\{ - \tfrac{(a\triangle_x - x_k)^2 + (b\triangle_y - y_k)^2}{2\sigma^2} \big\}. \tag{3.10}$$

3.4.2 Simulations

We have implemented the two PF-TBDF algorithms in MATLAB for tracking a single target in a 2-D plane under low SNR conditions, following the example used in

[17]. The covariance matrix $\mathbf{Q}$ for the noise $\mathbf{v}_k$ in Equation (3.1) is given by

$$\mathbf{Q} = \begin{bmatrix} \frac{q_1 \Delta T^4}{4} & \frac{q_1 \Delta T^3}{2} & 0 & 0 & 0 \\ \frac{q_1 \Delta T^3}{2} & q_1 \Delta T^2 & 0 & 0 & 0 \\ 0 & 0 & \frac{q_1 \Delta T^4}{4} & \frac{q_1 \Delta T^3}{2} & 0 \\ 0 & 0 & \frac{q_1 \Delta T^3}{2} & q_1 \Delta T^2 & 0 \\ 0 & 0 & 0 & 0 & q_2 \Delta T \end{bmatrix}$$

where q_1 and q_2 are the process noise parameters for the target motion and intensity,

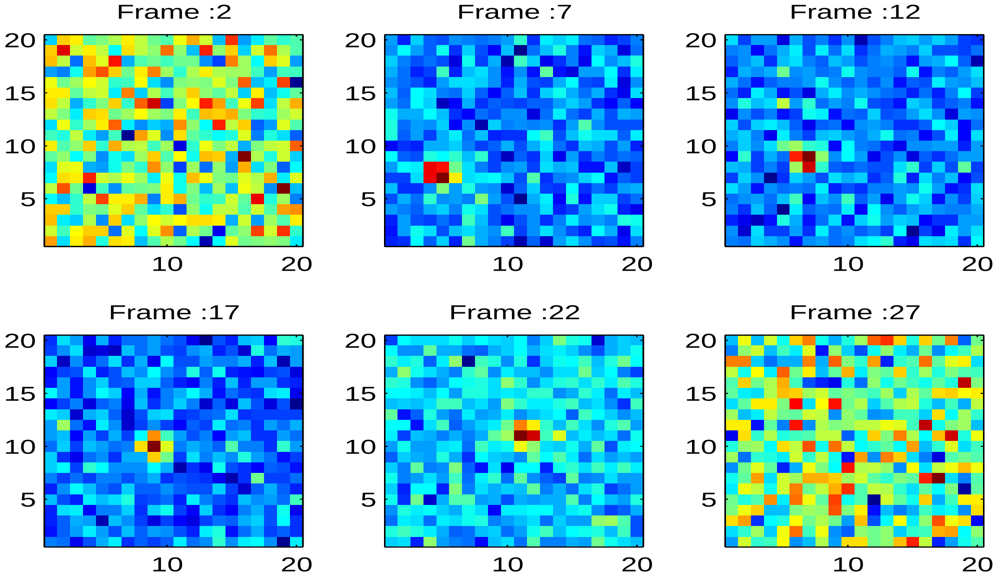

Figure 3.1: Measurement Frame at Different Time Steps at 20 dB Peak SNR. In all the Plots, the x and y Axes Correspond to the x and y Coordinates in the FOV, respectively.

respectively. Similar to the example in [17], 30 frames of measurements were generated with the following parameters, $\triangle_x = 1$, $\triangle_y = 1$, $N_x = 20$, $N_y = 20$, $\Delta T = 1$ s; the blurring parameter σ is set at 0.7. The algorithm performance is evaluated under different peak SNR conditions. The measurements were generated such that a target

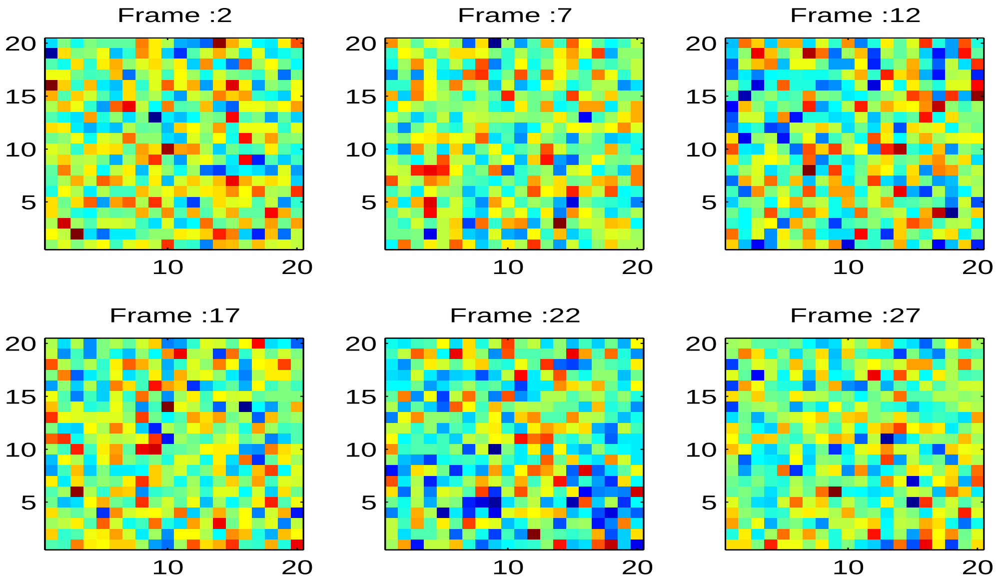

Figure 3.2: Measurement Frame at Different Time Steps at 6 dB Peak SNR.

enters the FOV at time step 7 and leaves the FOV at time step 23. The initial target position and velocity are set at (4.2,7.2) m, and (0.45 0.25) m/s respectively. Figure 3.1 shows the measurement frame at different time steps and 20 dB peak SNR. Since the peak SNR is high, the target position can be observed simply by the distinct pixels. Figure 3.2 shows the measurement frame at 6 dB peak SNR. In this case, it is not possible to detect the existence of the target by visual inspection. We thus aim to demonstrate the performance of the PF-TBDF under this low SNR condition. The noise parameters are set at $q_1 = 0.001$, $q_2 = 0.01$ and $r = 1$. The state transition probabilities are assumed to be $P_B = 0.05$, $P_D = 0.05$, $\Pr(e_0) = 0.05$. The parameters used in generating the particles when a target enters the FOV are $\nu_{\max} = 0.5$ and $\nu_{\min} = 0.2$. The target intensity range is set to $I_{\min} = 10$, $I_{\max} = 30$; this range reflects the expected 0 to 20 dB peak SNR. The number of particles are set to 15,000 particles for both N_1 and N_2.

Figure 3.3 shows the target existence probability at 6 dB peak SNR ($I_0 = 6.14$),

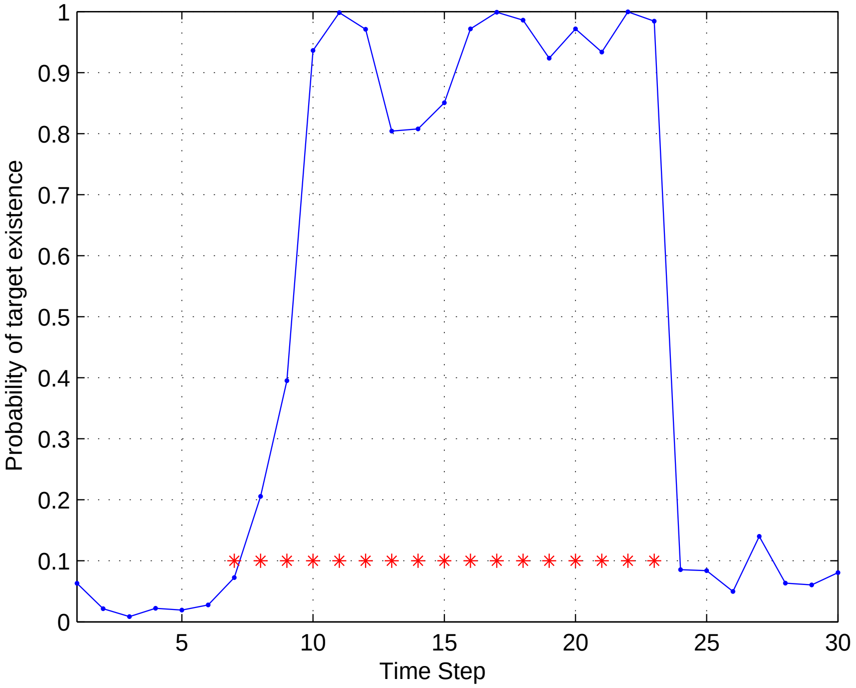

Figure 3.3: Target Existence Probability at 6 dB Peak SNR (Red Stars Represent the Time Steps at which the Target Truly Exist).

at different time steps using the efficient PF-TBDF method. As demonstrated in the figure, the target existence probability is accurately estimated. It takes about 3 frames for the probability to increase after the target enters the FOV, and the probability decreased quickly after the target left the FOV.

Figure 3.4 shows the particle distribution of the target position variables, and the histogram of the target intensity. The particle distribution is random before the appearance of a target. Once the target enters the FOV, the particle distribution is concentrated around the true target position. Similarly, the particles disperse after the target leaves the FOV. The same phenomenon is observed with the target intensity as more particles are concentrated around the true intensity value of 6.14. Figure 3.5 shows the tracking performance of the efficient PF-TBDF. The top plots

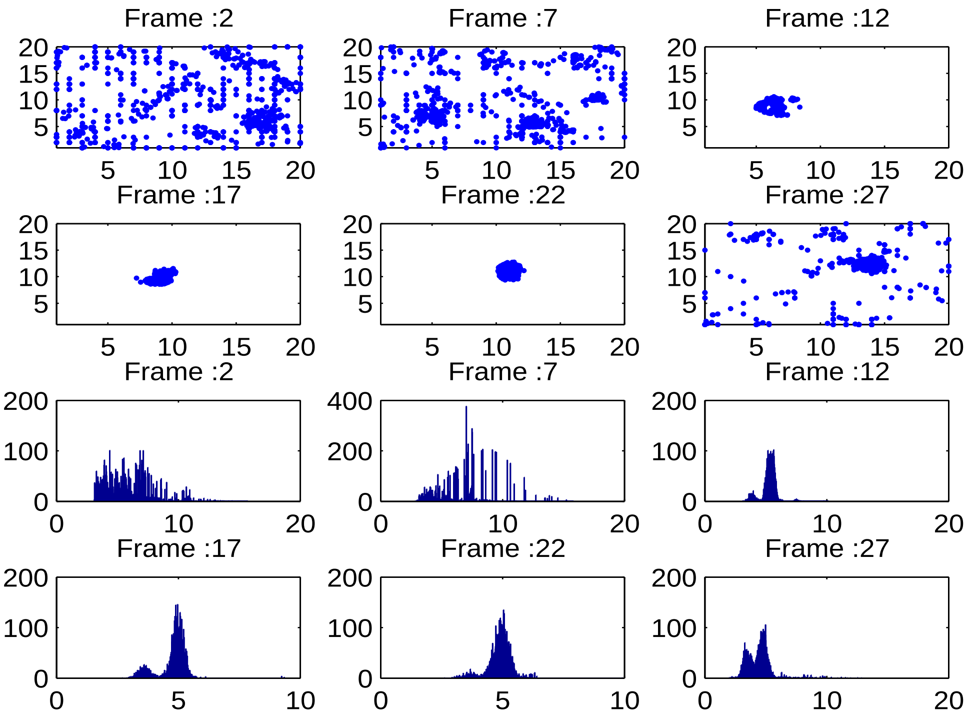

Figure 3.4: Particle Distribution for Target Position (Top 6 Plots, where the x and y Axes Represent the x and y Coordinates in the FOV, respectively); Histogram of Target Intensity Estimate at Different Frames (Bottom 6 Plots, where the x and y Axes Represent Intensity and Number of Particles with the Corresponding Intensity Value, respectively).

of the figure shows the true and estimated target position (shown separately for the x and y coordinates). From Figure 3.5, the estimates are very close to the true value after time step 10. The bottom plot shows the true and estimated target trajectory. As it can be seen, the PF-TBDF was able to closely track the target even under very low SNR conditions.

The performance of the efficient PF-TBDF is compared with the original PF-TBDF method using the same number of particles. Figure 3.6 shows the target

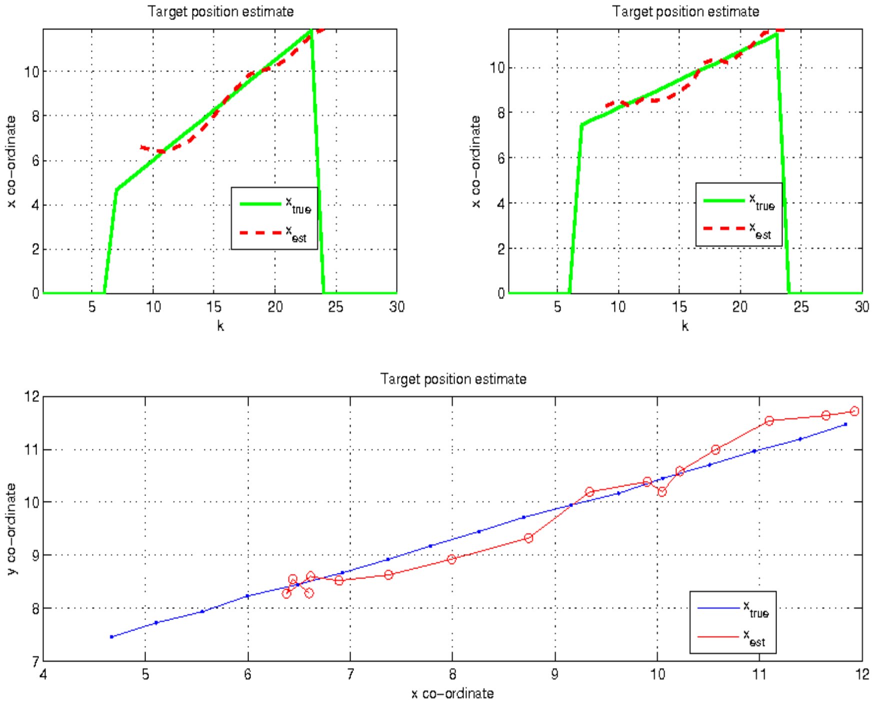

Figure 3.5: Target Position Estimates, x Coordinate (Top Left); and y Coordinate (Top Right). True and Estimated Target Trajectory at 6 dB Peak SNR (Bottom).

existence probability under three different peak SNR conditions (12 dB, 6 dB, 3 dB). The results were obtained by averaging 25 Monte Carlo simulations. The root mean-squared error (RMSE) between the estimated and true target position is calculated to compare the two algorithms and the RMSE is calculated using

$$\text{RMSE} = \sqrt{(x_{\text{true}} - x_{\text{est}})^2 + (y_{\text{true}} - y_{\text{est}})^2}.$$

Figure 3.7 shows the position RMSE for both methods and both algorithms appear to have similar detection performance. However, under lower SNR conditions, the position error using the efficient PF-TBDF is lower than the original PF-TBDF. In the simulations, it was also observed that the efficient PF-TBDF provides similar performance even when the number of particles is reduced. However, with the original

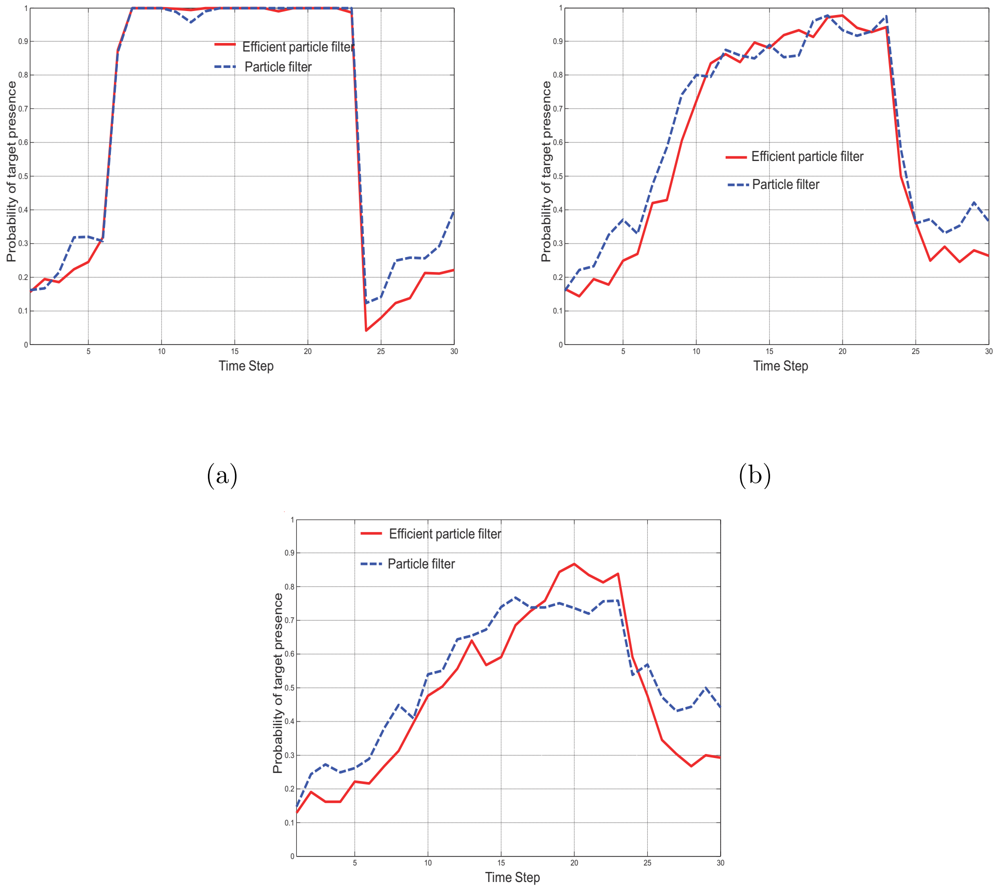

(a)

(b)

(c)

Figure 3.6: Target Existence Probability for the Original PF-TBDF and the Efficient PF-TBDF Methods (a) SNR = 12 dB; (b) SNR = 6 dB; and (c) SNR = 3 dB.

PF-TBDF, the performance deteriorates as the number of particles is reduced. In the original PF-TBDF method, the number of particles used for detecting a target entering the FOV and for tracking a target remaining in the FOV is unevenly split between the two target transition modes. This results in inaccurate detection of a target entering the FOV or inaccurate state estimation of a target remaining in the FOV. With the efficient PF-TBDF, a fixed number of particles is assigned for both modes, thus reducing the inaccuracy under each mode.

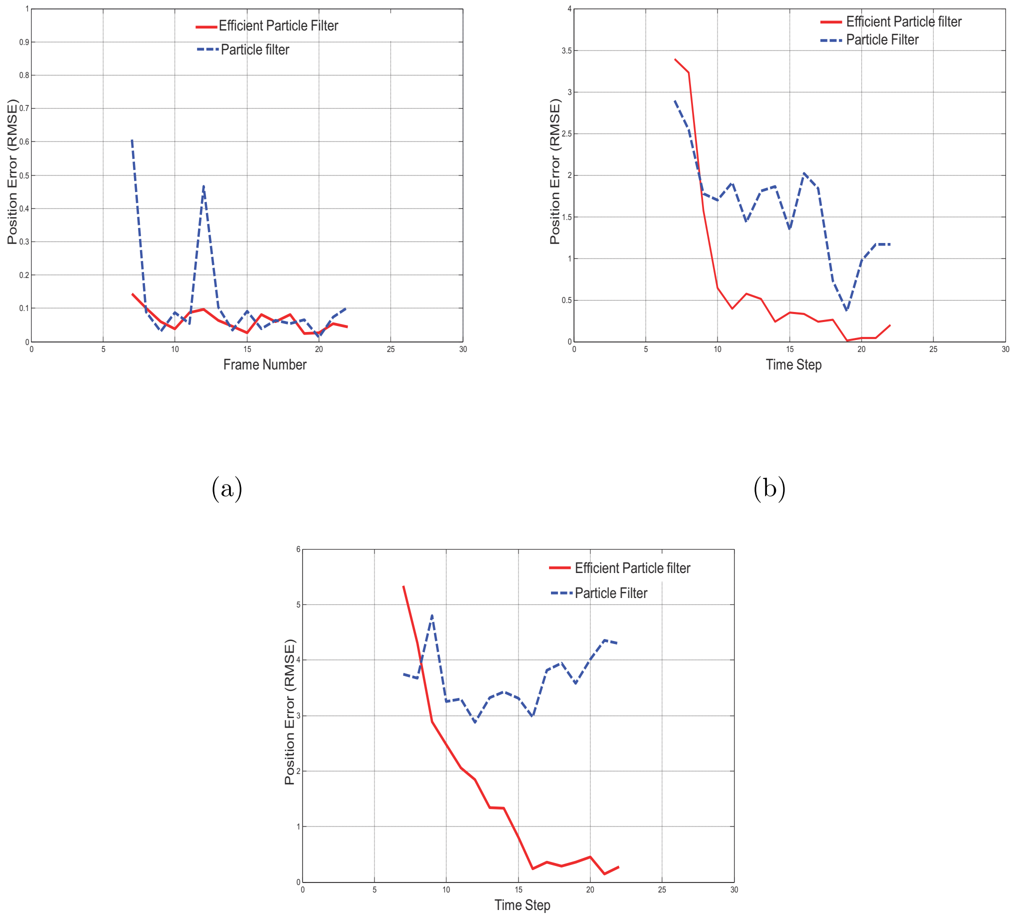

(a) (b)

(c)

Figure 3.7: Position RMSE for the Original PF-TBDF and the Efficient PF-TBDF Methods (a) SNR = 12 dB; (b) SNR = 6 dB; and (c) SNR = 3 dB.

3.5 Target Tracking Example Using Radar Measurements

3.5.1 Radar Measurement Model

In a general radar system, the sensor measurements are in the form of range and range-resolution bins, obtained by correlating the received data with the time-frequency shifted versions of the transmitted baseband signal [45]. The transmitter of a pulse Doppler radar system sends a series of N_p pulses with a pulse repetition interval time T_{PRI}. Each transmitted pulse $s[n]$ consists of N_s samples and has sampling frequency f_s. The radar receiver receives signals that are reflected by targets and interfering objects. The signals received over a period of N_p pulses is referred to as a dwell measurement. The range is estimated by keeping track of the round trip delay for the reflected pulse. The target range r_k and the delay τ_k at the kth transmission are related as

$$r_k = \frac{c\,\tau_k}{2}$$

where r_k is the range in meters at time step k, c is the velocity of propagation and τ_k is the corresponding round trip delay in seconds. If a target is moving, then the reflected signal undergoes frequency scaling due to the Doppler effect. Under the narrowband assumption, this frequency scaling is approximated as a frequency shift that depends on the speed of a moving target. Hence, one can estimate the speed of a moving target by estimating the Doppler frequency using the measurements from N_p pulses. The Doppler frequency ν_k and the range-rate $\dot{r}_k$ are related as

$$\nu_k = \frac{2\,\dot{r}_k}{c} f_c$$

where $\dot{r}_k$ is the range-rate in m/s at time step k, and f_c is the carrier frequency in Hz. The received complex baseband signal is first matched-filtered to improve the SNR. If all transmitted pulses have the same duration and also with the same pulse repetition interval, the matched filter output is the cross-ambiguity function between the received and transmitted signal at zero Doppler shift $(\mathrm{AF}(\tau, 0))$ [46]. Thus, each sample corresponds to the time lag index which in-turn corresponds to a particular target range bin. The slow-time samples are then generated by sampling the matched filtered output every $N_{\mathrm{PRI}} = f_s T_{\mathrm{PRI}}$ samples [45]. The target's range-rate is estimated by first estimating the Doppler frequency of the received signal using spectral analysis on the slow time samples. The resulting resolution bin dimension is given by $(\triangle_r \times \triangle_{\dot{r}})$, where $\triangle_r$ and $\triangle_{\dot{r}}$ correspond to range and range-rate resolution, respectively. The range resolution is determined by the bandwidth of the transmitted baseband signal and the range-range resolution is determined by the number of pulses used for spectral processing. The center of the bin (a, b) is at the position $(a\triangle_r \times b\triangle_{\dot{r}})$. Figure 3.8 shows how the 2-D measurement matrix that corresponds to the ambiguity function of the received signal is generated in a realistic pulse-Doppler radar system.

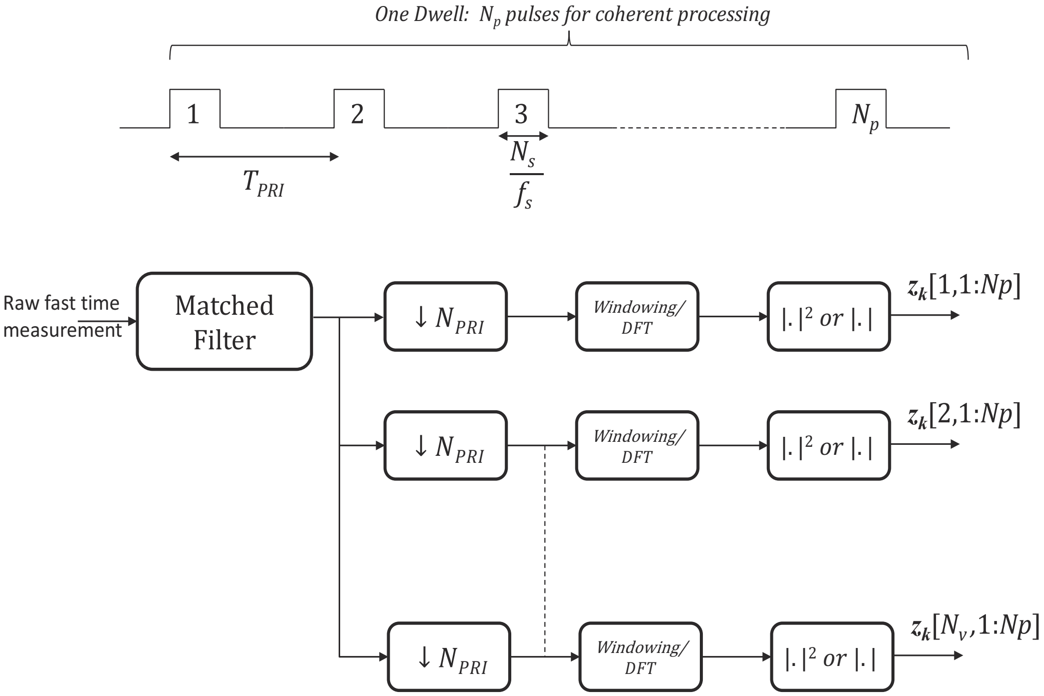

Figure 3.8: Range and Range-Rate Processing of a Pulse-Doppler Radar System.

The measurement matrix contains a peak corresponding to the target's range and range-rate. The auto ambiguity function of the modulating signal determines the degree of spreading in the vicinity of the peak corresponding to a true target or clutter. The function $h_k^{(a,b)}$ in the measurement Equation (3.3) is related to the range and range-rate of a particular target as

$$h_k^{(a,b)}(\mathbf{x}_k) = \left| I_k \frac{\sin(\pi N_p(\nu_b - \nu_k)T_{\mathrm{PRI}})}{\sin(\pi(\nu_b - \nu_k)T_{\mathrm{PRI}})} \sum_{n=0}^{N_s-1} s[n_a - n - n_k] e^{-j2\pi(\nu_b-\nu_k)nT_{\mathrm{PRI}}} \right| \tag{3.11}$$

where n_a is the lag index corresponding to a particular range and ν_b is the Doppler frequency corresponding to a particular range-rate in bin $(a,\, b)$, the relation between them is given by

$$n_a = \mathrm{round}\left\{ \frac{2\, a \triangle_r}{c} f_s \right\}, \qquad \nu_b = \frac{2\, b \triangle_{\dot{r}}}{c} f_c$$

n_k and ν_k are the lag index and the Doppler frequency corresponding to a target with a certain range and range-rate, respectively at time step k. The range and the range-rate are in-turn nonlinearly related to the target state vector $\mathbf{x}_k = [x_k\ \dot{x}_k\ y_k\ \dot{y}_k]^{\mathrm{T}}$ where (x_k, y_k) and $(\dot{x}_k, \dot{y}_k)$ are the 2-D coordinates of the target's position and velocity respectively and their relations are given in Equations (2.15) and (2.16).

3.5.2 Simulations Using Rayleigh Measurement Noise

In the image measurement example, the additive measurement noise was assumed to be Gaussian and this is not always a realistic assumption in radar applications. If the complex raw measurement is assumed to be Gaussian, then the magnitude spectrum of the matched filter output is either Rayleigh or Rician distributed depending on the existence of a target in a range bin. Thus, the likelihood function in Equation (3.9) is modified for different measurement noise distributions. The likelihood ratio with the Rayleigh noise assumption is derived as [53],

$$l(z_k^{(a,b)}|\mathbf{x}_k) \triangleq \exp\left\{ -\frac{[h_k^{(a,b)}(\mathbf{x}_k)]^2}{2r} \right\} I_o\left(-\frac{h_k^{(a,b)}(\mathbf{x}_k) z_k^{(a,b)}}{2r} \right) \tag{3.12}$$

where $I_0(\cdot)$ is the zeroth order modified Bessel function of the first kind and r is the variance of the in-phase and quadrature components of additive complex Gaussian noise.

In addition to range and range-rate measurements, a radar system can also provide measurements from the azimuthal and elevation look directions to track a moving target in a 3-D space. For tracking a target in 2-D space, only the azimuthal look directions measurement is necessary. In our simulations, we have considered 2-D space by generating measurements from only one azimuthal direction and the target positions were restricted to be always present in this direction. We have implemented a simple pulse-Doppler radar system with the parameters shown in Table 3.1. The measurements from this simulated radar system is used to track a single moving target in Rayleigh noise.

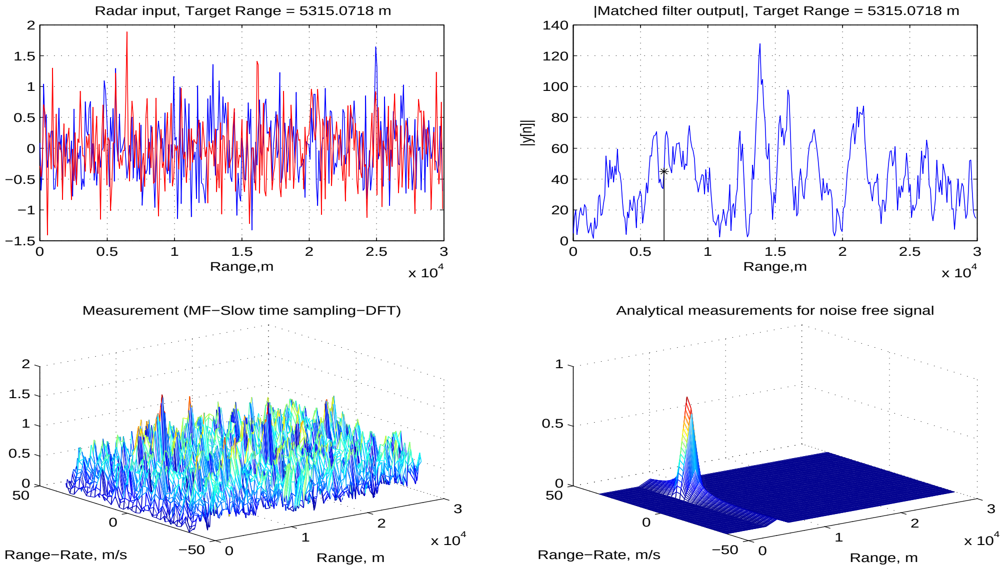

Figure 3.9: Signal Condition at Various Points in the Radar System at 15 dB Peak SNR: Raw Received Signal (Top Left); Matched Filter Output (Top Right); Noise-Free Range and Range-Rate Measurement (Bottom Right); and Noisy Range and Range-Rate Measurement (Bottom Left).

Figure 3.9 shows the complex radar input signal, the matched filter output, noisy measurement at 15 dB peak SNR and the noise-free measurement. For the chosen

Table 3.1: Simulated Pulse-Doppler Radar System Parameters

Radar Parameter	**Value**
Azimuthal Look Direction	45^o
Beamwidth	30^o
Carrier Frequency	10.0 GHz
Baseband Signal	pulse
Range Gate	[1500, 30000] m
Maximum Velocity	37.5 m/s (135 km/hr)
Maximum Doppler Shift	2.5 kHz
Pulse Width	10 μs
Pulse Interval, T_{PRI}	200 μs
Duty Cycle	0.05
Number of Pulses, N_p	32
Fast Time Sampling, f_s	1.6 MHz
Range Resolution	1500 m
Range-Rate Resolution	2.34 m/s
Measurement Sampling Interval	20 s
State Model	Constant velocity
Measurement Model	Nonlinear with Rayleigh noise
Tracker	PF-TBDF
Number of Particles	4,000 + 4,000 = 8,000

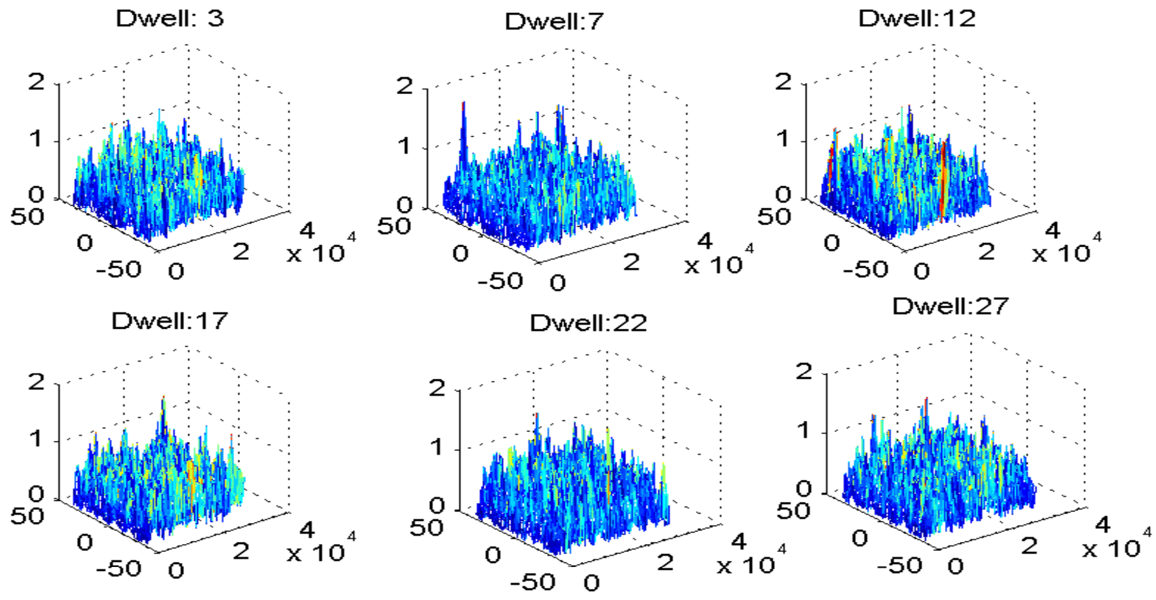
Dwell: 3

Dwell:7

Dwell:12

Dwell:17

Dwell:22

Dwell:27

Figure 3.10: Measurement Frame with Rayleigh Noise at Different Time Steps at 15 dB Peak SNR. In all the Plots, the x, y and z Axes Correspond to Range in m, Range-Rate in m/s, and Intensity, respectively.

radar parameters, 15 dB peak SNR at the matched filter output corresponds to -33 dB SNR for the unthresholded radar measurement. Figure 3.10 shows the measurement matrix at different time steps. The target enters and leaves te FOV at time steps 5 and 23, respectively. For a given SNR, the measurement with Rayleigh noise has more higher amplitude spikes than a Gaussian distributed noise and the intensity of these spikes are comparable to the peak corresponding to the target. Thus, it is even more difficult to track a target in Rayleigh noise. Figure 3.11 shows the particle distribution of the target position and the intensity for the efficient PF-TBDF algorithm. The particles for the intensity are distributed around 1.2 and the true intensity at 15 dB peak SNR is 1.41. When the target is not present, the particles in the position plane are distributed at 45^o with approximately 30^o tolerance. This is consistent with the original radar parameters in Table 3.1. Figure 3.12 shows the estimated and true target position and the PF-TBDF method is able to accurately track a target in Rayleigh noise.

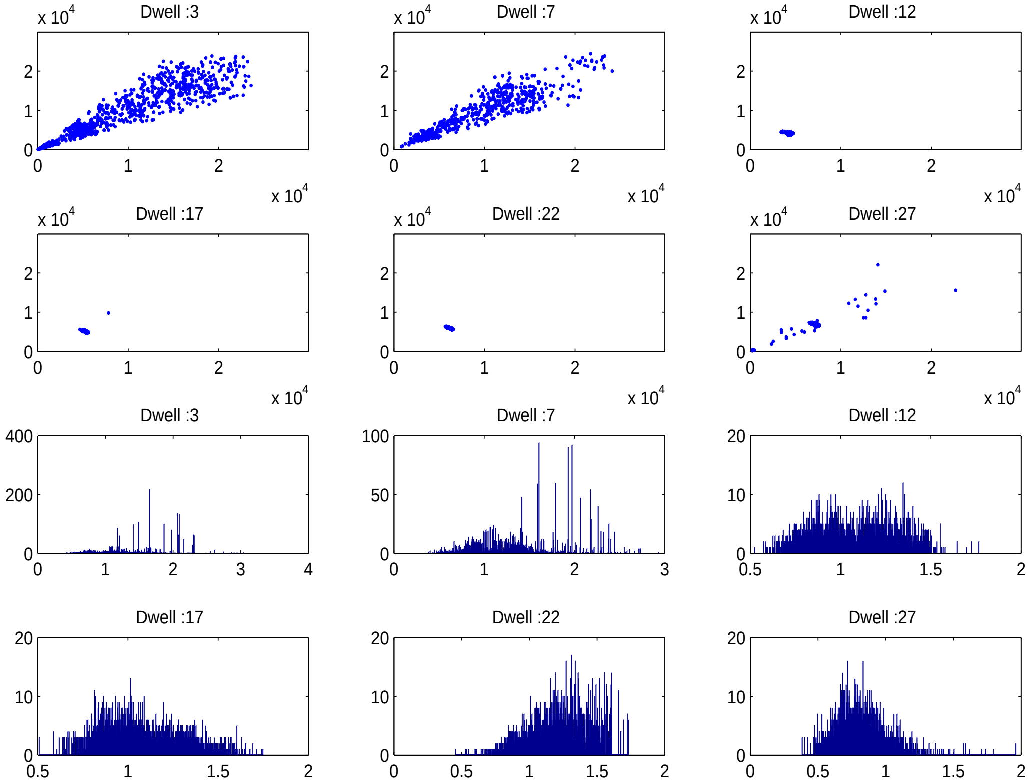

Figure 3.11: Particle Distribution for Target Position at 15 dB Peak SNR (Top 6 Plots, where the x and y Axes Represent the x and y Coordinates in the FOV, respectively); and Histogram of Target Intensity Estimate at Different Frames (Bottom 6 Plots, where the x and y Axes Represent Intensity and Number of Particles with the Corresponding Intensity Value, respectively).

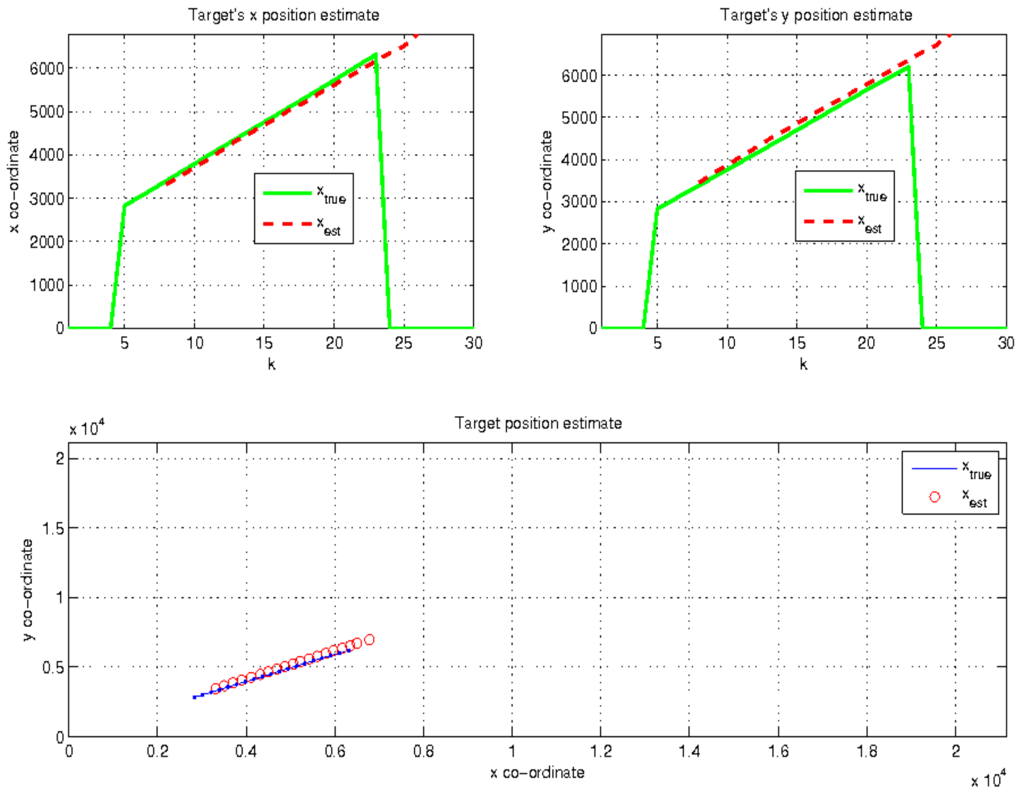

Figure 3.12: Target Position Estimates, x Coordinate (Top Left); y Coordinate (Top Right). True and Estimated Target Trajectory at 15 dB Peak SNR (Bottom).

3.5.3 Simulations with Measurements in Clutter

We investigate the PF-TBDF performance for tracking a target in the presence of clutter. Although the measurement model does not explicitly include clutter, we can still consider the clutter as a target. If we assume that there is no consistent trajectory for the clutter, then the PF-TBDF should inherently ignore the clutter as a consistent moving target thereby rejecting the clutter as noise. The amplitude of the clutter can be modeled by various distributions [99]. The type of distribution to use depends greatly on the specific radar application scenario. For example, sea clutter from a low grazing angle radar is modeled using heavy tailed distributions such as K-distribution and Weibull distribution. A compound Gaussian model was also proposed to accurately model sea clutter [100]. In our simulations, we used the Weibull distribution to model clutter amplitude and the average number of clutter is assumed to be Poisson distributed. Figure 3.13 shows the target existence probability under two test cases: 18 dB peak SNR and average number of clutter associated measurement is 10 measurements per dwell; 15 dB peak SNR, average number of clutter associated measurement is 5 measurements per dwell. As shown in the figure, the PF-TBDF algorithm was able to detect the existence of a target at low SNR and high clutter density. The target onset detection is slower at lower SNR. Figure 3.14 shows the target trajectory estimate for both test cases, where the PF-TBDF algorithm is able to track the moving target with high degree of accuracy.

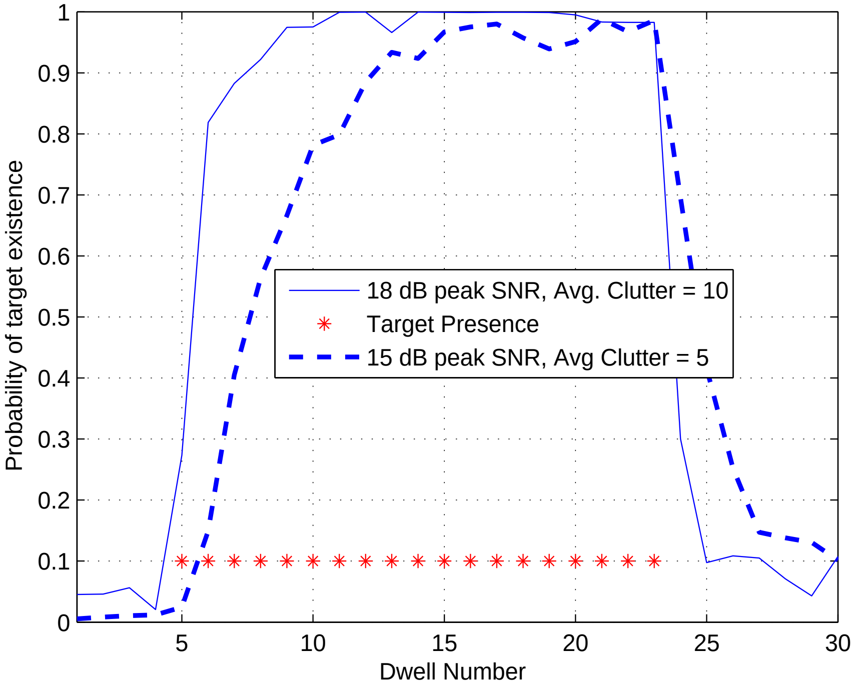

Figure 3.13: Target Existence Probability for Different Peak SNR Values and Clutter Densities.

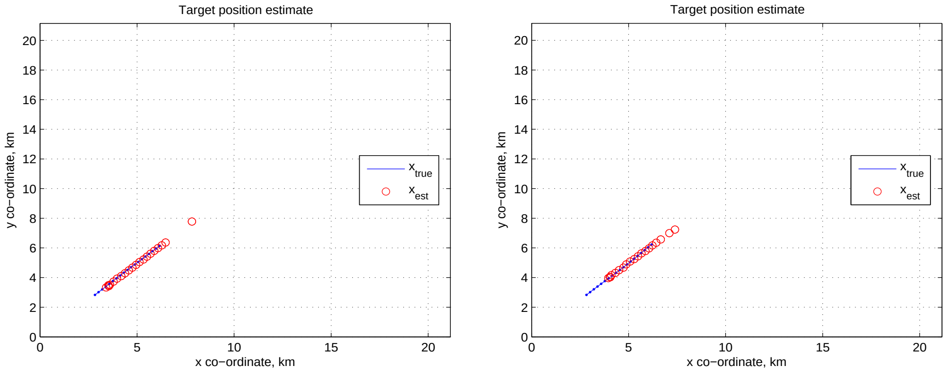

(a) (b)

Figure 3.14: True and Estimated Target Trajectory: (a) SNR = 18 dB, 10 Clutter Measurements Per Dwell; and (b) SNR = 15 dB, 5 Clutter Measurements Per Dwell.

Chapter 4

MULTIPLE TARGET TRACK-BEFORE-DETECT FILTERING

4.1 Tracking Multiple Targets Under Low Signal-to-Noise Ratio Conditions

The track-before-detect filter (TBDF) algorithm discussed in Chapter 3 was extended to track multiple targets [101], as mentioned in Chapter 1. However, this method was only shown to work well for a small number of targets. The state vector dimension in this method does not account for a varying number of targets, and it does not completely address the uncertainty in the actual number of existing targets. Recently, an RFS-based approach, the labeled multiple Bernoulli filter has been used to track multiple targets under low signal-to-noise ratio (SNR) conditions [74].

In this chapter, given a known maximum possible number of targets, we provide an alternate algorithm that generalizes the recursive TBDF in [53] to track a varying number of targets in low SNR and high clutter [76, 77] without any need for an explicit track management step. Since the number of targets that are present in the field of view (FOV) is not known *a priori*, we estimate the joint posterior probability density function (PDF) under all possible target existence combinations [76]. These joint PDFs are derived under the recursive Bayesian framework, and the state vectors corresponding to all the targets in the different modes are then appropriately mixed to derive the overall target state estimates. This is an interacting multiple model (IMM) algorithm in which the different target motion models in the regular IMM structure are replaced by all possible target existence combinations or modes. Hence, we refer to our algorithm as multiple mode multiple target TBDF (MM-MT-TBDF) to differentiate from the regular IMM algorithm [102]. The probability corresponding to each mode is also calculated, and the existence probability of each target is calculated from this mode probability. We avoid an explicit track management step by estimating an exhaustive set of multi-target posterior PDFs such that the target-to-track association is implicitly achieved through the unique definition of target combinations. The target states are validated using the estimated target existence probability. We also propose a particle filter (PF) implementation of the MM-MT-TBDF method that can also support nonlinear and non-Gaussian models. Although the PHDF approach is an encompassing framework, it is still not possible to practically estimate the joint PDF of the multi-target state vector for a time-varying number of targets. Recent advances in agile radar processing [103] require the posterior PDF of the state vector to dynamically select waveform parameters. For example, a single target TBDF based waveform design technique was considered in [104] that uses the posterior PDF estimate to minimize the tracking error. Using this approach, the set of estimated joint PDFs at time step k can be used to predict the tracking error at time step $k+1$ and the waveform parameters at time step $k+1$ that minimizes the predicted tracking error can be optimally selected [103].

4.2 Multiple Mode Multiple Target Tracking Model

4.2.1 State Model for Dynamically-varying Number of Targets

We consider the radar problem of tracking a maximum number of $\mathscr{L}$ targets. We define the state vector corresponding to the ℓth target, $\ell=1,\ldots,\mathscr{L}$ at time step k as

$$\mathbf{x}_{k,\ell} = [x_{k,\ell}\ \dot{x}_{k,\ell}\ y_{k,\ell}\ \dot{y}_{k,\ell}\ I_{k,\ell}]^{\mathtt{T}}$$

where $(x_{k,\ell},\ y_{k,\ell})$, $(\dot{x}_{k,\ell},\ \dot{y}_{k,\ell})$, and $I_{k,\ell}$ are the ℓth target's two-dimensional (2-D) Cartesian coordinates for position and velocity, and radar cross section (RCS) intensity level, respectively, and $\mathtt{T}$ denotes vector transpose. This definition of state vector is appropriate for an air-to-ground or ground-to-ground radar systems in which targets are localized on the ground. Possible applications may include tracking moving cars on a rural road or tracking small boats on the sea surface. Note that the state vector could be easily extended to 3-D space to include target tracking radar system applications such as ground-to-air or air-to-air. The multi-target state model we propose accounts for the fact that not all targets are present at each time step. In particular, at any time step, targets can enter, leave or remain in the FOV. The total number of possible target existence combinations or modes is $M = 2^{\mathscr{L}}$. This number includes the case of no targets present, all $\mathscr{L}$ targets present, and all possible combinations of $\mathscr{L} - 1, \mathscr{L} - 2, \ldots, 1$ targets present. Mode $i = 1$ assumes that no targets are present and mode $i = M$ assumes that all $\mathscr{L}$ targets are present. Note that we assume that the order in which the targets appear in the FOV is not important. We introduce a binary target presence indicator variable $C^i_\ell \in \{0, 1\}$, $i = 1, \ldots, M$, with 1 (or 0) if the ℓth target is present (or is not present) in the ith mode. A simple example with $M = 4$ modes for $\mathscr{L} = 2$ targets is demonstrated in Table 4.1. In our proposed method, we keep track of all possible target combinations and estimate the joint posterior PDF of the state vector corresponding to all target combinations. The

Table 4.1: Target Presence Indicator Values for $\mathscr{L} = 2$ Targets ($M = 4$ Modes).

Mode	Target presence indicator values			
i	C^i_2	C^i_1	Target 2	Target 1
1	0	0	not present	not present
2	0	1	not present	present
3	1	0	present	not present
4	1	1	present	present

state vector dimension is determined by the number of possible targets $\mathscr{L}_i$ in the ith mode. The target state vector in each mode at time step k is expressed as $\mathbf{x}_k^{[i]}$, $i = 2, \ldots, M$ to take into consideration the varying number of targets and the resulting changes in the multi-target state vector dimension. For example, the multi-target state vector for the Mth mode is $\mathbf{x}_k^{[M]} = [\mathbf{x}_{k,1}^{\mathtt{T}} \;\; \mathbf{x}_{k,2}^{\mathtt{T}} \ldots \mathbf{x}_{k,\mathscr{L}}^{\mathtt{T}}]^{\mathtt{T}}$ since all $\mathscr{L}$ targets are present in this mode. The state vector for all other modes can be defined from $\mathbf{x}_k^{[M]}$ as $\mathbf{x}_k^{[i]} = \mathbf{P}_{M\to i}\mathbf{x}_k^{[M]}$, where the projection matrix of size $(5\mathscr{L}_i \times 5\mathscr{L})$ is defined as

$$\mathbf{P}_{M\to i} = \begin{bmatrix} \mathbf{e}_{J^{[i]}(1)} & \ldots & \ldots \mathbf{e}_{J^{[i]}(\mathscr{L}_i)} \end{bmatrix}^{\mathtt{T}} \otimes \mathbf{I}_5 \tag{4.1}$$

where $J^{[i]}$ is the set (arranged in increasing order) of all targets that are assumed present in mode i, $\mathbf{e}_n$ is the $(\mathscr{L} \times 1)$ binary vector whose elements are zero except the nth element set to one, $\mathbf{I}_5$ is the (5×5) identity matrix, and $\otimes$ is the Kronecker product. For example, with $M = 4$ modes for $\mathscr{L} = 2$ targets, the projection matrix $\mathbf{P}_{4\to 2}$ to obtain the state vector for the mode that contains only Target 1 ($i = 2$ in Table 4.1) can be written as

$$\mathbf{P}_{4\to 2} = \begin{bmatrix} 1 & 0 \end{bmatrix} \otimes \mathbf{I}_5 = \begin{bmatrix} 1 & 0 & 0 & 0 & 0 & 0 & 0 & 0 & 0 & 0 \\ 0 & 1 & 0 & 0 & 0 & 0 & 0 & 0 & 0 & 0 \\ 0 & 0 & 1 & 0 & 0 & 0 & 0 & 0 & 0 & 0 \\ 0 & 0 & 0 & 1 & 0 & 0 & 0 & 0 & 0 & 0 \\ 0 & 0 & 0 & 0 & 1 & 0 & 0 & 0 & 0 & 0 \end{bmatrix}.$$

The state vector for mode $i = 2$ is obtained as

$$\mathbf{x}_k^{[2]} = \mathbf{P}_{4\to 2}\mathbf{x}_k^{[4]} = \begin{bmatrix} 1 & 0 & 0 & 0 & 0 & 0 & 0 & 0 & 0 & 0 \\ 0 & 1 & 0 & 0 & 0 & 0 & 0 & 0 & 0 & 0 \\ 0 & 0 & 1 & 0 & 0 & 0 & 0 & 0 & 0 & 0 \\ 0 & 0 & 0 & 1 & 0 & 0 & 0 & 0 & 0 & 0 \\ 0 & 0 & 0 & 0 & 1 & 0 & 0 & 0 & 0 & 0 \end{bmatrix} \begin{bmatrix} \mathbf{x}_{k,1} \\ \mathbf{x}_{k,2} \end{bmatrix}.$$

The dynamic multi-target state model for each mode can then be written as

$$\mathbf{x}_k^{[i]} = \mathbf{F}^{[i]}\,\mathbf{x}_{k-1}^{[i]} + \mathbf{v}_k^{[i]} \tag{4.2}$$

where $\mathbf{v}_k^{[i]} = \mathbf{P}_{M\to i}[\mathbf{v}_{k,1}^{\mathsf{T}}\ \mathbf{v}_{k,2}^{\mathsf{T}} \ldots \mathbf{v}_{k,\mathscr{L}}^{\mathsf{T}}]^{\mathsf{T}}$ and $\mathbf{v}_{k,\ell}$ is a modeling error random process with covariance matrix $\mathbf{Q}_\ell$. If the same target motion model is assumed for all targets, then $\mathbf{F}^{[i]} = \mathbf{F} \otimes \mathrm{I}_{\mathscr{L}_i}$. The state transition matrix for a constant velocity target motion is given by

$$\mathbf{F} = \begin{bmatrix} 1 & \Delta T & 0 & 0 & 0 \\ 0 & 1 & 0 & 0 & 0 \\ 0 & 0 & 1 & \Delta T & 0 \\ 0 & 0 & 0 & 1 & 0 \\ 0 & 0 & 0 & 0 & 1 \end{bmatrix}.$$

where ΔT is the time step interval and the state transition for the intensity variable of the state vector is modeled using the random walk model as

$$I_{k+1,\ell} = I_{k,\ell} + \mathbf{v}_{k,\ell}(5)$$

where $\mathbf{v}_{k,\ell}(5)$ is the fifth element of the vector $\mathbf{v}_{k,\ell}$.

4.2.2 Mode Transition Matrix

The uncertainty of a target being present or absent in the measurement space is modeled as a random process with a two state first order Markov chain [17]. The transitional probabilities, the probability of the ℓth target entering the FOV, $P_{B,\ell}$, and the probability of the ℓth target leaving the FOV, $P_{D,\ell}$, are assumed to be known. Once the ℓth target appears in the FOV, the probability that it remains present in the FOV is $(1 - P_{D,\ell})$. Similarly, the probability that it does not enter the FOV is given by $(1 - P_{B,\ell})$. The transition matrix for the Markov process corresponding to the ℓth target can then be written as

$$\mathbf{T}_\ell = \begin{bmatrix} 1-P_{B,\ell} & P_{B,\ell} \\ P_{D,\ell} & 1-P_{D,\ell} \end{bmatrix}.$$

In addition to estimating the joint posterior PDF of each mode, we also estimate the probability of mode m_k at time step k. This variable is modeled as a discrete random process following an M-state first order Markov chain. Specifically, the probability that the mode changes from mode j at time $k-1$ to mode i at time k is given by $\mathbf{\Omega}_{j,i} = \Pr(m_k = i | m_{k-1} = j)$, $i, j = 1, \ldots, M$. Assuming that the individual target transitions are independent of each other, we construct the $(M \times M)$ transition probability matrix $\mathbf{\Omega}$ using the *a priori* transition matrix of each individual target $\mathbf{T}_\ell$. Specifically, for a given number of targets $\mathscr{L}$, we generalize the mode transition matrix as

$$\mathbf{\Omega} = \mathbf{T_1} \otimes \mathbf{T_2} \ldots \otimes \mathbf{T}_{\mathscr{L}}. \tag{4.3}$$

Note that the sum of the mode transition probabilities along any row of $\mathbf{\Omega}$ is unity and $0 \leq \mathbf{\Omega}_{j,i} \leq 1$. The target presence indicator value $C_\ell^i = q$, $q \in \{0,1\}$, $i = 1, \ldots, M$, is defined as $q = 1$ (or $q = 0$) if the ℓth target is present (or is not present) in the ith mode. For the simple example with $M = 4$ modes for $\mathscr{L} = 2$ targets in Table 4.1, the corresponding (4×4) mode transition matrix assuming that both targets have the same transition matrix $T_1 = T_2$ and $P_{B_1} = P_{B_2} = P_B$ and $P_{D_1} = P_{D_2} = P_D$, is given by

$$\mathbf{\Omega} = \begin{bmatrix} (1-P_B)^2 & P_B(1-P_B) & (1-P_B)P_B & P_B^2 \\ P_D(1-P_B) & (1-P_D)(1-P_B) & P_D P_B & (1-P_D)P_B \\ (1-P_B)P_D & P_B P_D & (1-P_D)(1-P_B) & P_B(1-P_D) \\ P_D^2 & (1-P_D)P_D & P_D(1-P_D) & (1-P_D)^2 \end{bmatrix} \tag{4.4}$$

In practice, it may be difficult to obtain *a priori* information on transition probabilities of individual targets entering or leaving a scene. Hence, we can assume that these event probabilities are identical for all targets, i.e., $P_{B,\ell} = P_B$ and $P_{D,\ell} = P_D$ for $\ell = 1, \ldots, \mathscr{L}$.

4.2.3 Measurement Model Using Image Data

Each measurement frame is assumed to consists of $(N_x \times N_y)$ pixels. The pixel resolution cell dimension is given by $(\triangle_x \times \triangle_y)$. The center of the pixel $(a,\, b)$ is at the position $(a\triangle_x \times b\triangle_y)$. If no targets are present in a frame, then the measurement contains only noise for all pixels. If a target is present in a frame, then the pixels in the vicinity of the target's current position contain both signal and noise. We consider point targets and a sensor point spread function approximated by a 2-D Gaussian density. Unlike the single target TBDF, when there is at least one target, the measurement function varies depending on the mode at time step k. The measurement model for multiple targets is given by

$$z_k^{(a,b)} = \begin{cases} \displaystyle\sum_{\ell=0}^{\mathscr{L}_i} C_\ell^i \, h_k^{(a,b)}(\mathbf{x}_{k,\ell}^{[i]}) + w_k^{(a,b)}, & \text{for } i = 2, \ldots, M \\ \\ w_k^{(a,b)}, & \text{for } i = 1 \end{cases} , \tag{4.5}$$

$$h_k^{(a,b)}(\mathbf{x}_{k,\ell}^{[i]}) = \tfrac{\triangle_x \triangle_y I_{k,\ell}}{2\pi\Sigma^2} \exp\big\{ - \tfrac{(a\triangle_x - x_{k,\ell})^2 + (b\triangle_y - y_{k,\ell})^2}{2\Sigma^2} \big\}, \tag{4.6}$$

where Σ is a known parameter that controls the blurring introduced by the sensor and $\mathbf{x}_{k,\ell}^{[i]}$ is the ℓth target's state vector in mode i. The measurement noise $w_k^{(a,b)}$ in each pixel is assumed to be independent and Gaussian distributed with variance r. Similar to the single target case, the measurement vector is given by

$$\mathbf{z}_k = \big[z_k^{(1,1)} \; z_k^{(1,2)} \; \ldots \; z_k^{(1,b)} \; z_k^{(2,1)} \; z_k^{(2,2)} \; \ldots \; z_k^{(2,b)} \; \ldots \; z_k^{(a,1)} \; \ldots \; z_k^{(a,b)} \big]^{\mathtt{T}}$$

and

$$\mathbf{Z}_k = [\mathbf{z}_1^{\mathtt{T}}\ \mathbf{z}_2^{\mathtt{T}}\ \ldots\ \mathbf{z}_k^{\mathtt{T}}]^{\mathtt{T}}$$

where $\mathbf{Z}_k$ is the vector of all the measurements up to time k.

4.2.4 Measurement Model Using Radar Data

As we are using the TBDF for multiple targets, the measurement model uses unthresholded measurements, similar to the single target case in Chapter 3. We assume that the measurement frame consists of pre-processed data from a radar system for different range $r_{k,\ell}$, range-rate $\dot{r}_{k,\ell}$ and azimuthal angle $\theta_{k,\ell}$ bins for the ℓth target. One example of a measurement frame could be the cross-ambiguity function between the transmitted and radar received signal. Measurements from independent multiple sensors are integrated in the problem formulation. The range, range-rate and azimuthal angle are related to the state vector as

$$\begin{aligned}
r_{k,\ell} &= \sqrt{(x_{k,\ell} - x_s)^2 + (y_{k,\ell} - y_s)^2} \\
\dot{r}_{k,\ell} &= \frac{\dot{x}_{k,\ell}(x_{k,\ell} - x_s) + \dot{y}_{k,\ell}(y_{k,\ell} - y_s)}{\sqrt{(x_{k,\ell} - x_s)^2 + (y_{k,\ell} - y_s)^2}} \\
\theta_{k,\ell} &= \arctan\left(\frac{y_{k,\ell} - y_s}{x_{k,\ell} - x_s}\right)
\end{aligned}$$

and the sensor is located at (x_s, y_s).

Each measurement frame is assumed to consist of $(N_r \times N_{\dot{r}} \times N_\theta)$ bins. The range, range-rate and azimuthal angle bin resolutions are denoted by $\Delta_r, \Delta_{\dot{r}}, \Delta_\theta$, respectively. The (a, b, c)th cell for $a = 1, 2, \ldots, N_r$, $b = 1, 2, \ldots, N_{\dot{r}}$, $c = 1, 2, \ldots, N_\theta$, is then centered around $(a\,\Delta_r \times b\,\Delta_{\dot{r}} \times c\,\Delta_\theta)$. The measurements in all the bins simply consists of noise if no targets are present. If a target is present, then the measurements in the bins that are in the vicinity of the target's current position consist of both signal and noise. We assume a point target model and a sensor point spread function that can be approximated by a 3-D Gaussian function. Based on this assumption, the measurement equation is given by

$$z_k^{(a,b,c)} = \begin{cases} \displaystyle\sum_{\ell=1}^{\mathscr{L}_i} C_\ell^i \; h_k^{(a,b,c)}(\mathbf{x}_{k,\ell}^{[i]}) + v_k^{(a,b,c)}, & i = 2 \ldots M \\ \\ v_k^{(a,b,c)}, & i = 1 \end{cases} \tag{4.7}$$

where C_ℓ^i is the target presence indicator value in Equation (4.3) of the ℓth target in the ith mode, and

$$h_k^{(a,b,c)}(\mathbf{x}_{k,\ell}^{[i]}) = A_k \, \exp\left(- \left(\frac{a\,\Delta_r - r_{k,\ell}}{2\sigma_r}\right)^2 - \left(\frac{b\,\Delta_{\dot{r}} - \dot{r}_{k,\ell}}{2\sigma_{\dot{r}}}\right)^2 - \left(\frac{c\,\Delta_\theta - \theta_{k,\ell}}{2\sigma_\theta}\right)^2 \right). \tag{4.8}$$

where $A_k = \frac{\Delta_r \Delta_{\dot{r}} \Delta_\theta I_{k,\ell}}{(2\pi)^{3/2} \sigma_r, \sigma_{\dot{r}}, \sigma_\theta}$ is the normalized amplitude, $I_{k,\ell}$ is the intensity of the received signal from the ℓth target and $\sigma_r, \sigma_{\dot{r}}, \sigma_\theta$ are known parameters that control the spreading introduced by the radar system. Note that, these parameters can normally be derived from the ambiguity function of the radar transmitted signal [45]. The independent and identically distributed measurement noise samples $v_k^{(a,b,c)}$ in Equation (4.7) are assumed to be Gaussian with zero-mean and variance ν_k. The overall measurement vector is given by

$$\mathbf{z}_{k,s} = [z_{k,s}^{(1,1,1)} \; \ldots \; z_{k,s}^{(1,1,N_\theta)} \; \ldots \; z_{k,s}^{(1,N_{\dot{r}},N_\theta)} \; \ldots \; z_{k,s}^{(N_r,N_{\dot{r}},N_\theta)}]^{\mathsf{T}}$$

and the sequence $\mathbf{z}_k = [\mathbf{z}_{k,1}^{\mathsf{T}} \; \mathbf{z}_{k,2}^{\mathsf{T}} \; \ldots \; \mathbf{z}_{k,S}^{\mathsf{T}}]^{\mathsf{T}}$ is the set of all measurements from all S independent and homogeneous sensors and $\mathbf{Z}_k = [\mathbf{z}_1^{\mathsf{T}} \; \mathbf{z}_2^{\mathsf{T}} \; \ldots \; \mathbf{z}_k^{\mathsf{T}}]^{\mathsf{T}}$ represents all the measurements up to time k.

4.3 Multiple Mode Multiple Target Track-before-detect Filtering

4.3.1 Posterior Density for Multiple Mode Multiple Targets

In a multi-target tracking problem with a varying number of targets, the number of existing targets is not known *a priori*. Hence, we provide a set of joint distributions of multi-target state vectors conditioned on all possible target existence combinations and the corresponding probability of different target combinations. In a broader sense, this is similar to a multiple hypothesis tracking algorithm in which each mode is equivalent to a hypothesis. Unlike the single target recursive TBDF in [53], we estimate two different sets of conditional PDFs. The first set of PDFs corresponds to the posterior joint PDFs conditioned on the mode state at time steps $(k-1)$ and k, and the second set of PDFs belongs to the posterior joint PDF conditioned on the mode state at time step k only. The second set of PDFs are obtained as a weighted mixture of a subset of the first set of joint PDFs that have the same state vector dimension. These subset of PDFs are the PDFs that transitioned to a particular mode from all possible modes. Once we have a set of mode-conditioned PDFs, we can derive the PDFs of individual target states as a weighted linear combination of marginalized PDFs that are conditioned on all relevant modes in which the targets are assumed present. Thus, our approach uses a discrete PDF to characterize all possible target combinations and the corresponding joint PDFs of the target states are characterized by continuous distributions. This is similar to the random finite set approach in which the target states of a random set is modeled by a continuous distribution and the cardinality of the random set is modeled by a discrete distribution [37]. Specifically, given the state and measurement models and the posterior PDF $p(\mathbf{x}_{k-1}^{[i]}|\mathbf{Z}_{k-1})$, $\forall\, i$, at time $k-1$, the MM-MT-TBDF estimates the posterior PDF $p(\mathbf{x}_{k,\ell}|\mathbf{Z}_k)$ at time k and the corresponding target existence probability $\Pr(e_{k,\ell}|\mathbf{Z}_k)$, where $e_{k,\ell}$ is the event corresponding to the ℓth target's presence. We assume that the initial mode probability, $\Pr(m_0 = i|\mathbf{Z}_0), i = 1, \ldots, M$, is known *a priori*. If this value is not known, then we can assume that no targets are initially present, i.e., we can assume that $\Pr(m_0 = i|\mathbf{Z}_0) = 0$, for $i = 2, \ldots, M$, and $\Pr(m_0 = 1|\mathbf{Z}_0) = 1$.

The tracking of multiple targets, assuming a varying number of targets, is a multiple mode problem in which the posterior PDF, including the dimension of the state vector, is dependent on the target mode. As the different modes are mutually exclusive, $\Pr(m_k = i, m_k = j|\mathbf{Z}_k) = 0$, $\forall\, i \neq j$, the posterior PDF can be written as

$$p(\mathbf{x}_{k,\ell}|\mathbf{Z}_k) = \sum_{i=1}^{M} C_\ell^i \, p(\mathbf{x}_{k,l}^{[i]}, m_k = i\,|\mathbf{Z}_k) \tag{4.9}$$

where $\mathbf{x}_{k,l}^{[i]}$ is the state vector corresponding to the ℓth target present in mode i. Here, even though the superscript $[i]$ and the mode condition event $m_k = i$ seems redundant, we explicitly denote the state vector as $\mathbf{x}_{k,l}^{[i]}$ to emphasize the fact that the dimension of the state vector in mode i varies with the number of assumed targets in mode i. The marginal PDF is obtained by marginalizing the joint PDF which can be written as

$$p(\mathbf{x}_k^{[i]}, m_k = i\,|\mathbf{Z}_k) = p(\mathbf{x}_k^{[i]}|m_k = i, \mathbf{Z}_k)\Pr(m_k = i\,|\mathbf{Z}_k)$$

for $i = 2, \ldots, M$ and $P_{k,i} \triangleq \Pr(m_k = i\,|\mathbf{Z}_k)$ is the posterior mode probability. Note that we do not include $i = 1$ in this range as we do not need to estimate the posterior PDF when no targets are present. Using the Bayesian solution for multiple switching models [17], the target state PDF conditioned on a particular mode can be obtained as the weighted mixture of M density functions

$$\begin{aligned} p\big(\mathbf{x}_k^{[i]}|m_k = i, \mathbf{Z}_k\big) &= \sum_{j=1}^{M} p(\mathbf{x}_k^{[i]}|m_{k-1} = j, m_k = i, \mathbf{Z}_k)\Pr(m_{k-1} = j|m_k = i, \mathbf{Z}_k) \\ &= \sum_{j=1}^{M} p_{j,i}(\mathbf{x}_k^{[i]}|\mathbf{Z}_k)\Pr(m_{k-1} = j|m_k = i, \mathbf{Z}_k) \end{aligned} \tag{4.10}$$

for $i = 2, \ldots, M$. The target state PDF $p(\mathbf{x}_k^{[i]}|m_{k-1} = j, m_k = i, \mathbf{Z}_k)$ conditioned on transitioning from mode j at time $k-1$ to mode i at time k is denoted by $p_{j,i}(\mathbf{x}_k^{[i]}|\mathbf{Z}_k)$. Given the mode state at time step k, the mixing weights $\Pr(m_{k-1} = j|m_k = i, \mathbf{Z}_k)$ provide the probability that the current state is transitioned from mode j at time step k-1. Using Bayes rule, the above mentioned mode conditioned state PDF can be expanded as

$$p_{j,i}(\mathbf{x}_k^{[i]}|\mathbf{Z}_k) = \frac{p(\mathbf{z}_k|m_{k-1}=j, m_k=i, \mathbf{x}_k^{[i]})\, p(\mathbf{x}_k^{[i]}|m_{k-1}=j, m_k=i, \mathbf{Z}_{k-1})}{p(\mathbf{z}_k|m_{k-1}=j, m_k=i, \mathbf{Z}_{k-1})}$$

$$= \frac{p_{j,i}(\mathbf{z}_k|\mathbf{x}_k^{[i]})\, p_{j,i}(\mathbf{x}_k^{[i]}|\mathbf{Z}_{k-1})}{p_{j,i}(\mathbf{z}_k|\mathbf{Z}_{k-1})} \tag{4.11}$$

where we denote $p(\mathbf{z}_k|m_{k-1}=j, m_k=i, \mathbf{x}_k^{[i]})$, $p(\mathbf{x}_k^{[i]}|m_{k-1}=j, m_k=i, \mathbf{Z}_{k-1})$, and $p(\mathbf{z}_k|m_{k-1}=j, m_k=i, \mathbf{Z}_{k-1})$ by $p_{j,i}(\mathbf{z}_k|\mathbf{x}_k^{[i]})$, $p_{j,i}(\mathbf{x}_k^{[i]}|\mathbf{Z}_{k-1})$, and $p_{j,i}(\mathbf{z}_k|\mathbf{Z}_{k-1})$, respectively. If we divide both numerator and denominator by $p(\mathbf{z}_k|m_k=0)$, which assumes that no targets are present [51], we can express the posterior PDF as a function of the likelihood ratios,

$$L_{j,i}(\mathbf{z}_k|\mathbf{x}_k^{[i]}) = \frac{p_{j,i}(\mathbf{z}_k|\mathbf{x}_k^{[i]})}{p(\mathbf{z}_k|m_k=0)},$$

$$L_{j,i}(\mathbf{z}_k|\mathbf{Z}_{k-1}) = \frac{p_{j,i}(\mathbf{z}_k|\mathbf{Z}_{k-1})}{p(\mathbf{z}_k|m_k=0)},$$

as

$$p_{j,i}\left(\mathbf{x}_k^{[i]}|\mathbf{Z}_k\right) = \frac{L_{j,i}\left(\mathbf{z}_k|\mathbf{x}_k^{[i]}\right)\; p_{j,i}\left(\mathbf{x}_k^{[i]}|\mathbf{Z}_{k-1}\right)}{L_{j,i}(\mathbf{z}_k|\mathbf{Z}_{k-1})} \tag{4.12}$$

where the denominator is the normalization term

$$L_{j,i}(\mathbf{z}_k|\mathbf{Z}_{k-1}) = \int L_{j,i}\left(\mathbf{z}_k|\mathbf{x}_k^{[i]}\right)\; p_{j,i}\left(\mathbf{x}_k^{[i]}|\mathbf{Z}_{k-1}\right) d\mathbf{x}_k^{[i]} \tag{4.13}$$

and $L_{j,i}(\mathbf{z}_k|\mathbf{x}_k^{[i]})$ is the joint likelihood function conditioned on the previous and current modes. Note that, when no targets are present, the likelihood function does not depend on the target state or the mode condition at previous time step.

4.3.2 Likelihood Function for Image Measurements

Since the measurement noise is assumed to be independent between pixels, the joint likelihood function in Equation (4.11) can be written as

$$p_{j,i}(\mathbf{z}_k|\mathbf{x}_k^{[i]}) = \begin{cases} \displaystyle\prod_{a=1}^{N_x}\prod_{b=1}^{N_y}\mathcal{N}(\mathbf{z}_k^{(a,b)};\Upsilon_k^{(a,b)}(\mathbf{x}_k^{[i]}),\nu_k), & m_{k-1}=1\ldots M,\ m_k=2\ldots M \\ \displaystyle\prod_{a=1}^{N_x}\prod_{b=1}^{N_y}\mathcal{N}(\mathbf{z}_k^{(a,b)};0,\nu_k), & m_k=1 \end{cases}$$

where $\mathcal{N}(\mathbf{z}_k^{(a,b)};\Upsilon_k^{(a,b)}(\mathbf{x}_k^{[i]}),\nu_k)$ implies that $\mathbf{z}_k^{(a,b)}$ has a Gaussian distribution with mean $\Upsilon_k^{(a,b)}(\mathbf{x}_k^{[i]})$ and variance ν_k, $\Upsilon_k^{(a,b)}(\mathbf{x}_k^{[i]})=\sum_{\ell=1}^{\mathscr{L}} C_\ell^i\, h_k^{(a,b)}(\mathbf{x}_{k,\ell}^{[i]})$ is the cumulative contribution to pixel (a,b) from all the targets in mode i and $h_k^{(a,b)}(\mathbf{x}_{k,\ell}^{[i]})$ is defined in Equation (4.6) in Section 4.2.3. The likelihood ratio in Equation (4.13) can be written as

$$L_{j,i}(\mathbf{z}_k|\mathbf{x}_k^{[i]}) = \begin{cases} \dfrac{\displaystyle\prod_{a=1}^{N_x}\prod_{b=1}^{N_y}\mathcal{N}(\mathbf{z}_k^{(a,b)};\Upsilon_k^{(a,b)}(\mathbf{x}_k^{[i]}),\nu_k)}{\displaystyle\prod_{a=1}^{N_x}\prod_{b=1}^{N_y}\mathcal{N}(\mathbf{z}_k^{(a,b)};0,\nu_k)}, & m_{k-1}=1\ldots M,\ m_k=2\ldots M \\ 1, & m_k=1 \end{cases}$$

$$= \begin{cases} \displaystyle\prod_{a\epsilon\beta_x(\mathbf{x}_k^{[i]})}\ \prod_{b\epsilon\beta_y(\mathbf{x}_k^{[i]})} l(z_k^{(a,b)}|\mathbf{x}_k^{[i]}), & m_{k-1}=1\ldots M,\ m_k=2\ldots M \\ 1, & m_k=1 \end{cases} \tag{4.14}$$

where $\beta_x(\mathbf{x}_k^{[i]})$ and $\beta_y(\mathbf{x}_k^{[i]})$ are the set of pixels in the neighbourhood of the pixels corresponding to those in which the targets in mode i are present and the likelihood ratio in Equation (4.14) can be derived as

$$l(z_k^{(a,b)}|\mathbf{x}_k^{[i]}) \triangleq \exp\left\{-\frac{\Upsilon_k^{(a,b)}(\mathbf{x}_k^{[i]})(\Upsilon_k^{(a,b)}(\mathbf{x}_k^{[i]})-2z_k^{(a,b)})}{2\nu_k}\right\}.$$

4.3.3 Likelihood Function for Radar Measurements

Since the measurement noise is assumed independent between bins, the joint likelihood function in Equation (4.11), when the measurement consists of range and range-rate in Equation (4.7), can be written as

$$p_{j,i}(\mathbf{z}_k|\mathbf{x}_k^{[i]})=\begin{cases}\displaystyle\prod_{a=1}^{N_r}\prod_{b=1}^{N_{\dot{r}}}\prod_{c=1}^{N_\theta}\mathcal{N}(z_k^{(a,b,c)};\Upsilon_k^{(a,b,c)}(\mathbf{x}_k^{[i]}),\nu_k), & m_{k-1}=1\ldots M,\ m_k=2\ldots M\\ \displaystyle\prod_{a=1}^{N_r}\prod_{b=1}^{N_{\dot{r}}}\prod_{c=1}^{N_\theta}\mathcal{N}(z_k^{(a,b,c)};0,\nu_k), & m_k=1\end{cases}$$

where $\Upsilon_k^{(a,b,c)}(\mathbf{x}_k^{[i]})=\sum_{\ell=1}^{\mathscr{L}}C_\ell^i\,h_k^{(a,b,c)}(\mathbf{x}_{k,\ell}^{[i]})$ is the cumulative contribution to bin (a,b,c) from all the targets in mode i and $h_k^{(a,b,c)}(\mathbf{x}_{k,\ell}^{[i]})$ is defined in Equation (4.8) in Section 4.2.4. In order to reduce the computational load, only the bins in the neighbourhood of existing targets are used. The likelihood function in Equation (4.12) can be written as

$$L_{j,i}(\mathbf{z}_k|\mathbf{x}_k^{[i]})=\begin{cases}\displaystyle\prod_{a\epsilon\beta_r(\mathbf{x}_k^{[i]})}\ \prod_{b\epsilon\beta_{\dot{r}}(\mathbf{x}_k^{[i]})}\ \prod_{c\epsilon\beta_\theta(\mathbf{x}_k^{[i]})}\lambda(z_k^{(a,b,c)}|\mathbf{x}_k^{[i]}), & m_{k-1}=\forall\ M,\ m_k=2\ldots M\\ 1, & m_k=1\end{cases}\tag{4.15}$$

where $\beta_r(\mathbf{x}_k^{[i]})$, $\beta_{\dot{r}}(\mathbf{x}_k^{[i]})$ and $\beta_\theta(\mathbf{x}_k^{[i]})$ are the set of all range, range-rate and azimuthal angle bin numbers, respectively, that are in the neighborhood of the bin numbers corresponding to those in which the targets in mode i are present and

$$\lambda(z_k^{(a,b,c)}|\mathbf{x}_k^{[i]})\triangleq\exp\left\{-\frac{\Upsilon_k^{(a,b,c)}(\mathbf{x}_k^{[i]})(\Upsilon_k^{(a,b,c)}(\mathbf{x}_k^{[i]})-2z_k^{(a,b,c)})}{2\nu_k}\right\}.$$

4.3.4 Prediction Step of MM-MT-TBDF

In the recursive Bayesian framework, given the posterior mode conditioned PDF, $p(\mathbf{x}_{k-1}^{[i]}|m_{k-1}=j,m_k=i,\mathbf{Z}_{k-1})$, at time step $k-1$, we need to first predict the PDF of the state vector at time step k conditioned on the modes $m_{k-1}=j$ and $m_k=i$.

Note that, as the state vector at time step $k-1$ does not depend on the mode condition at time step k, the prediction is done based on the mode conditioned PDF $p(\mathbf{x}_{k-1}^{[i]}|m_{k-1}=j, \mathbf{Z}_{k-1})$. Since the state vector dimension of the jth mode at time $k-1$ is not always equal to the state vector dimension of the ith mode, the prediction step is performed only after transforming the state vector of the jth mode. Similar to Equation (4.1), we define a projection matrix $\mathbf{P}_{j\to i} : \mathbb{R}^{D_j} \to \mathbb{R}^{D_i}$ to transform the state vector from the jth mode to the ith mode. Specifically, the projection matrix causes the following transformation

$$\mathbf{y}_{k-1}^{[i]} = \mathbf{P}_{j\to i}\mathbf{x}_{k-1}^{[j]} \tag{4.16}$$

where the dimension of $\mathbf{P}_{j\to i}$ is $(D_i \times D_j)$, where $D_i = 5\mathscr{L}_i$ is the dimension of the ith mode. Similar to (4.1), the projection matrix $\mathbf{P}_{j\to i}$ is separately defined based on the target combination differences between the two modes. Specifically,

$$\mathbf{P}_{j\to i} = \begin{bmatrix} \varepsilon_{O_j(J^{[i]}(1)))} & \dots & \dots \varepsilon_{O_j(J^{[i]}(\mathscr{L}_i))} \end{bmatrix}^{\mathtt{T}} \otimes \mathbf{I}_5$$

where $J^{[i]}$ is defined below Equation (4.1) in Section 4.2.1, $O_j(J^{[i]}(q))$ is the arrangement order number in the target combination of mode j for the target corresponding to the qth element of the set $J^{[i]}$, ε_n is the $(\mathscr{L}_j \times 1)$ binary vector whose elements are all zeros except the nth element is set to one. If a target in the ith mode is not present in the jth mode, then $O_j(J^{[i]}(\cdot))$ is set to zero and the corresponding binary vector is replaced with a zero vector. This condition corresponds to a new target that can enter the FOV and the elements corresponding to the newly entered targets are randomly updated from an *a priori* PDF for a new target. For example, if the jth mode assumes that only Target 2 is present, and the ith mode assumes that Target 1 and Target 2 are present, then $J^{[4]} = \{1,2\}$, $O_3(J^{[4]}(1)) = 0$, $O_3(J^{[4]}(2)) = 1$, $\mathbf{P}_{3\to 4} = [\mathbf{0}_5; \mathbf{I}_5]$ where 4 and 3 correspond to the mode numbers defined in Table 4.1, and $\mathbf{0}_5$ is a (5×5) matrix of all zeros. The predicted state PDF conditioned on the previous and current modes is then given by

$$p_{j,i}(\mathbf{x}_k^{[i]}|\mathbf{Z}_{k-1}) \; = \int p_{j,i}(\mathbf{x}_k^{[i]}|\mathbf{y}_{k-1}^{[i]}, \mathbf{Z}_{k-1})\, p(\mathbf{y}_{k-1}^{[i]}|m_{k-1} = j, \mathbf{Z}_{k-1})\, d\mathbf{y}_{k-1}^{[i]}. \tag{4.17}$$

The state dynamic model in (4.2) is used to update the PDF $p_{j,i}(\mathbf{x}_k^{[i]}|\mathbf{y}_{k-1}^{[i]}, \mathbf{Z}_{k-1})$, and the predicted PDF is used in Equation (4.12) to update the posterior PDF.

4.3.5 Joint PDF Mixture Weights Calculation in MM-MT-TBDF

The weights in Equation (4.10) can be expanded using Bayes rule as

$$\begin{aligned}\Pr(m_{k-1} = j|m_k = i, \mathbf{Z}_k) &= \frac{p_{j,i}(\mathbf{z}_k|\mathbf{Z}_{k-1})\Pr(m_{k-1} = j|m_k = i, \mathbf{Z}_{k-1})}{p(\mathbf{z}_k|m_k = i, \mathbf{Z}_{k-1})} \\ &= \frac{p_{j,i}(\mathbf{z}_k|\mathbf{Z}_{k-1})\, \boldsymbol{\Omega}_{j,i}\, P_{k-1,j}}{p(\mathbf{z}_k|m_k = i, \mathbf{Z}_{k-1})\Pr(m_k = i|\mathbf{Z}_{k-1})}.\end{aligned}$$

Here, $P_{k-1,j} \triangleq \Pr(m_{k-1} = j|\mathbf{Z}_{k-1})$ is the posterior mode probability at time $k-1$. The term $\Pr(m_k = i|m_{k-1} = j, \mathbf{Z}_{k-1})$ is set to the mode transition probability $\boldsymbol{\Omega}_{j,i}$ since the event $m_k = i$ at time k conditioned on the event $m_{k-1} = j$ at time $k-1$ does not depend on the measurement at time $k-1$. The weights can thus be expressed as a function of the likelihood ratio as

$$\Pr(m_{k-1} = j|m_k = i, \mathbf{Z}_k) = \frac{L_{j,i}(\mathbf{z}_k|\mathbf{Z}_{k-1})\, \boldsymbol{\Omega}_{j,i}\, P_{k-1,j}}{L(\mathbf{z}_k|m_k = i, \mathbf{Z}_{k-1})\Pr(m_k = i|\mathbf{Z}_{k-1})}$$

where $L_{j,i}(\mathbf{z}_k|\mathbf{Z}_{k-1})$ is computed using Equation (4.13), and the denominator is a normalization term. The weights are calculated as

$$\Pr(m_{k-1} = j|m_k = i, \mathbf{Z}_k) = \frac{L_{j,i}(\mathbf{z}_k|\mathbf{Z}_{k-1})\, \boldsymbol{\Omega}_{j,i}\, P_{k-1,j}}{\sum_{j'=1}^{M} L_{j',i}(\mathbf{z}_k|\mathbf{Z}_{k-1})\, \boldsymbol{\Omega}_{j',i}\, P_{k-1,j})}\,. \tag{4.18}$$

4.3.6 Mode Probability Calculation for the MM-MT-TBDF

The posterior mode probability $P_{k,i}$ can be computed as

$$P_{k,i} = \sum_{j=1}^{M} \Pr(m_k = i | m_{k-1} = j, \mathbf{Z}_k) \Pr(m_{k-1} = j | \mathbf{Z}_k) \tag{4.19}$$

The first term in Equation (4.19) can be expanded using Bayes rule as

$$\Pr(m_k = i | m_{k-1} = j, \mathbf{Z}_k) = \frac{p_{j,i}(\mathbf{z}_k | \mathbf{Z}_{k-1}) \, \boldsymbol{\Omega}_{j,i} \, P_{k-1,j}}{p(\mathbf{z}_k | \mathbf{Z}_{k-1}) \Pr(m_{k-1} = j | \mathbf{Z}_k)}.$$

When substituted back in Equation (4.19), we can obtain

$$P_{k,i} = \frac{\displaystyle\sum_{j=1}^{M} \Lambda_{j,i} \, \boldsymbol{\Omega}_{j,i} \, P_{k-1,j}}{\displaystyle\sum_{j=1}^{M} \left[\boldsymbol{\Omega}_{j,i} \, P_{k-1,j} + \sum_{i'=2}^{M} \Lambda_{j,i'} \, \boldsymbol{\Omega}_{j,i'} \, P_{k-1,j} \right]} \tag{4.20}$$

where $\Lambda_{j,i} \triangleq L_{j,i}(\mathbf{z}_k | \mathbf{Z}_{k-1})$ and $P_{k-1,j}$ is the posterior mode probability at time $k-1$. When no targets are present, $\Lambda_{j,1} = 1$, $\forall j$ at time step k. The salient functional steps of the algorithm are listed in Algorithm 1 and the block diagram of the algorithm is shown in Figure 4.1. The single target recursive TBDF in [53] is a special case of the MM-MT-TBDF algorithm with $\mathscr{L} = 1$.

Algorithm 1 Algorithmic Steps of MM-MT-TBDF

```
Initialize distribution function $p(\mathbf{x}_0^{[i]} | m_0 = i, \mathbf{Z}_0)$ and mode probability $P_{0,i}$ for $i = 2, \ldots, M$.
for $k = 1$ to $K$ do
    Step 1: Predict the state distribution function $p_{j,i}(\mathbf{x}_k^{[i]} | \mathbf{Z}_{k-1})$, conditioned on mode $j$ at time step $k-1$ and mode $i$ at time step $k$, using Equation (4.17) for $j = 1, \ldots M$ and $i = 2, \ldots, M$.
    Step 2: Compute the likelihood function, conditioned on modes $j$ and $i$, using Equations (4.14) or (4.15).
    Step 3: Update the posterior state density function $p_{j,i}(\mathbf{x}_k^{[i]} | \mathbf{Z}_k)$, conditioned on mode $j$ at time step $k-1$ and mode $i$ at time step $k$, using Equation (4.12).
    Step 4: Compute the mixing probabilities $\Pr(m_{k-1} = j | m_k = i, \mathbf{Z}_k)$, using Equation (4.12).
    Step 5: Compute the posterior mode probabilities $P_{k,i}$ using Equation (4.20).
    Step 6: Compute the target state posterior density conditioned on a mode, $p(\mathbf{x}_k^{[i]} | m_k = i, \mathbf{Z}_k)$, using Equation (4.10).
    Step 7: Marginalize the target state posterior density in Step 6 to obtain the posterior density of individual targets in mode $i$.
    Step 8: Combine the marginal density functions from all modes using Equation (4.9) to obtain the marginal density function of the $\ell$th target.
end for
```

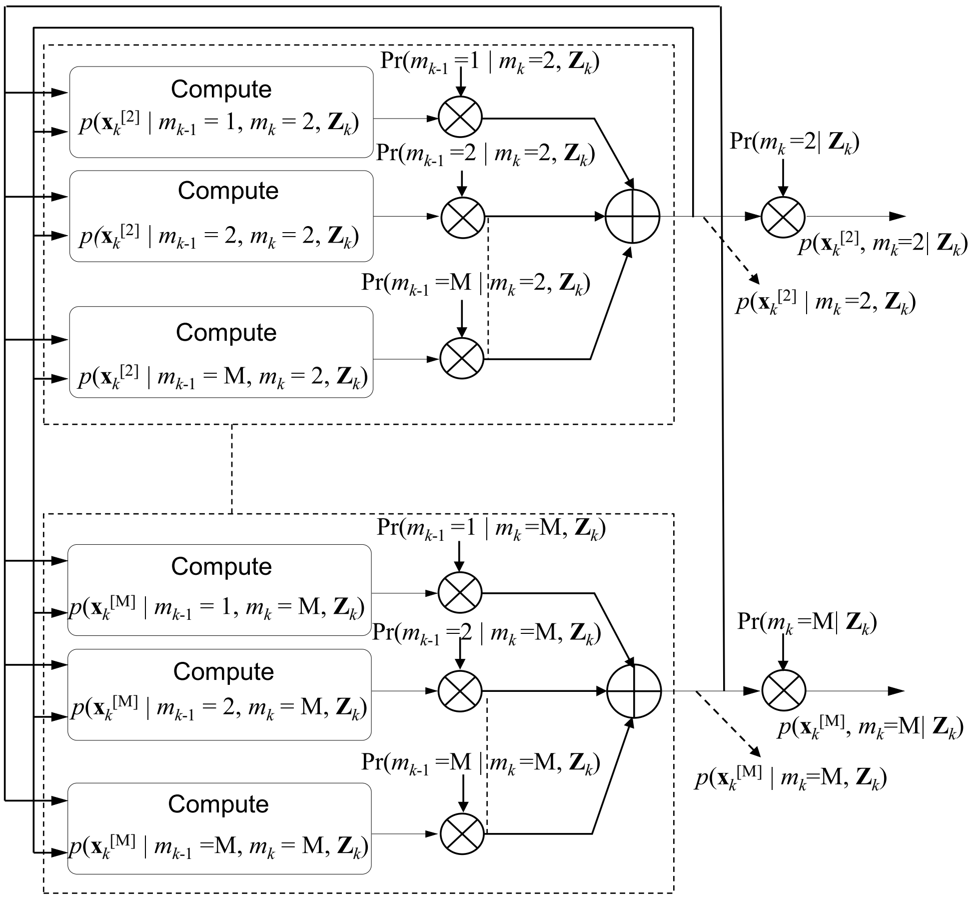

Figure 4.1: MM-MT-TBDF Algorithm Block Diagram for Multiple Target Tracking.

Thus, the detection of a new target is tracked by observing the mode probabilities and a newly detected target and its corresponding trajectory is implicitly labelled through the corresponding mode definition. Figure 4.2 illustrates our method with an example scenario in which $\mathscr{L} = 2$ targets enter and leave the FOV at different time steps. The figure shows only the dominant probabilities corresponding to the different mode transitions and the PDFs corresponding to these dominant probabilities.

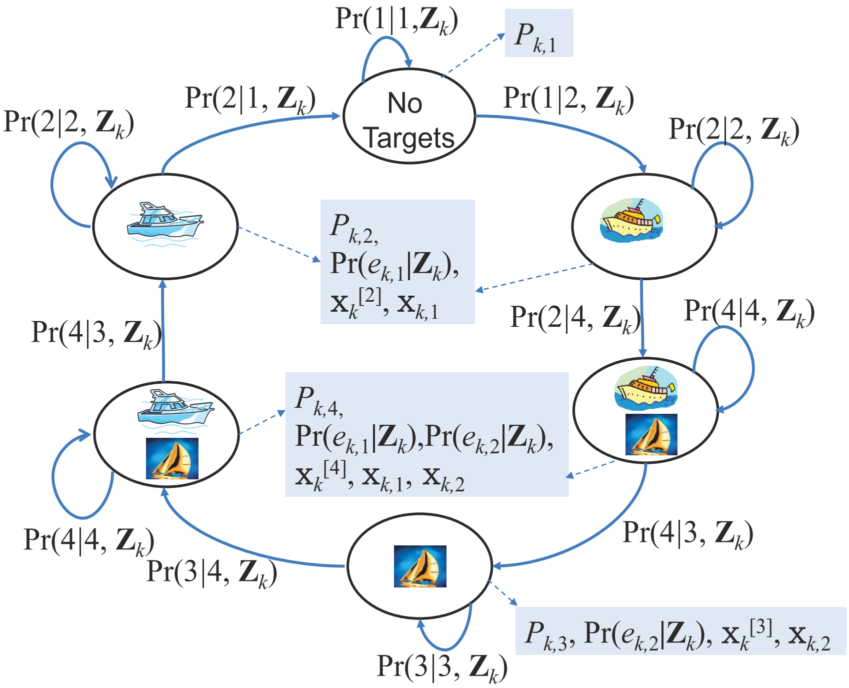

Figure 4.2: Illustration of MM-MT-TBDF Algorithm for $\mathscr{L} = 2$ Targets Showing the Dominant Probabilities and the Relevant Posterior PDFs for Different Mode Transitions.

4.4 Particle Filter Implementation of Multiple Mode Multiple Target TBDF

In the previous section, we derived the Bayesian solution of the MM-MT-TBDF algorithm. When the state and measurement models are nonlinear and non-Gaussian, then the TBDF needs to be solved using sequential Monte Carlo (SMC) techniques such as particle filtering. Unlike the multiple model TBDF in [101], we employ two layers of IMM structure to derive the posterior PDF. The first layer of IMM structure is used to estimate the mode conditioned PDF and the second layer is used to estimate the PDF of the target state vector. The particle filter (PF) based implementation (MM-MT-TBDF-PF) is also proposed to implement the MM-MT-TBDF algorithm.

The proposed algorithm employs three layers of particle filters. The first layer of PFs approximate the posterior PDF of target states $\mathbf{x}_k^{[i]}$, conditioned on mode i at time step k and mode j at time step $k-1$. This approximation is given by

$$p(\mathbf{x}_k^{[i]}|m_{k-1}=j, m_k=i, \mathbf{Z}_k) \approx \sum_{n=1}^{N_{j,i}} \phi_k^{(j,i,n)}\ \delta(\mathbf{x}_k^{[i]} - \mathbf{x}_k^{(j,i,n)})\,. \tag{4.21}$$

The next layer of PFs approximating the mode conditioned posterior PDFs are given by

$$p(\mathbf{x}_k^{[i]}|m_k=i, \mathbf{Z}_k) \approx \sum_{n=1}^{N_i} \chi_k^{(i,n)}\ \delta(\mathbf{x}_k^{[i]} - \mathbf{x}_k^{(i,n)})\,. \tag{4.22}$$

The final layer of PFs approximates the posterior PDF of individual targets as

$$p(\mathbf{x}_{k,\ell}|\mathbf{Z}_k) \approx \sum_{n=1}^{N_\ell} w_{k,\ell}^{(n)} \delta(\mathbf{x}_{k,\ell} - \mathbf{x}_{k,\ell}^{(n)}). \tag{4.23}$$

4.4.1 MM-MT-TBDF Using Sampling Importance Resampling Particle Filter

We begin this algorithm by initializing the particles $\mathbf{x}_0^{(i,n)}$ and weights $\chi_0^{(i,n)}$, $i=2,\ldots,M$ for all modes. At time step k, $N_{j,i}$ new particles are generated to approximate $p(\mathbf{x}_k^{[i]}|m_{k-1}=j, m_k=i, \mathbf{Z}_k)$, for all i and j. The samples are generated depending on whether or not a particular target is present in the previous mode. There are three possible target transitions.

- *Target enters the FOV:*

  If a target in mode i was not present in mode j, then this target is considered as a target that entered the FOV at time step k and the particles are generated based on a known *a priori* distribution for a new target. If no *a priori* information about a new target is available, a uniform distribution can be assumed. Specifically, the target position particles can be drawn uniformly from the FOV, and the target state velocity particles can be drawn from a uniform distribution whose range values are the expected minimum and maximum target velocities. The target intensity particles can also be drawn from a uniform distribution whose range values are selected based on the expected peak SNR in the measurement. Since the proposed algorithm is for tracking multiple targets, the position vector cannot be simply sampled from the FOV in order to avoid drawing samples in the vicinity of the already detected target position. To avoid this problem, samples in the neighbourhood of the already detected target are not selected. One optimal way is to compute the Mahalanobis distance between the generated particles and the mean position of the already detected targets. The Mahalanobis distance is calculated as

$$D(\hat{\mathbf{x}}_{k-1,d}, \mathbf{x}_{k,\ell}) = (\hat{\mathbf{x}}_{k,\ell}^{(n)} - \mu_{k-1}^{d})^{\mathtt{T}}\, S_{k-1}^{d}\, (\hat{\mathbf{x}}_{k,\ell}^{(n)} - \mu_{k-1}^{d})$$

where d is the already detected target with sample mean position estimate vector μ_{k-1}^{d} and corresponding sample position covariance estimate matrix S_{k-1}^{d} at time step $k-1$, $\hat{\mathbf{x}}_{k,\ell}^{(n)}$ is the position vector of the generated particles for target ℓ. It was shown in [54] that a lower number of particles are needed if the samples are generated directly from the measurement. However, we observed that selecting a subset of measurements by thresholding does not work well under low SNR conditions. For best performance, we propose a balanced approach in which a large number (N_{nb}) of uniformly distributed new target particles are used. The likelihood function for this large set of particles is computed first and the $N_{j,i}$ highest likelihood particles are selected from this large set. Following this procedure helps to localize the computation only during the new target particle generation rather than propagating a large set of particles through the remaining steps described below. Even though the likelihood function computation monotonically involves the measurements, choosing a higher amplitude measurement bin may not necessarily result in a higher likelihood function value since the likelihood function is also a function of the neighbourhood bins. From our simulations, we noted that choosing state vectors corresponding to higher amplitude measurement bins resulted in poor performance at lower SNR conditions (less than 0 dB SNR) since most of the chosen higher amplitude bins corresponded to noise spikes. If *a priori* information is available as in [75], then a reduced number of initial particles are needed.

- *Target leaves FOV:*

  A target has left the FOV if it is present in mode j but not in mode i. The particles corresponding to this target at time step k in mode i are ignored.

- *Target remains in FOV:*

  If a target is already present in the FOV during mode j and remains in the FOV during mode i, then the particles for $p_{j,i}(\mathbf{x}_k^{[i]}|\mathbf{Z}_k)$ are updated using Equation (4.2).

Finally, the states of all the targets that are present in mode i are then concatenated to approximate $p_{j,i}(\mathbf{x}_k^{[i]}|\mathbf{Z}_{k-1})$.

The weights for the $N_{j,i}$ particles are computed using the mode conditioned joint likelihood function in Equation (4.15) as

$$\tilde{\phi}_k^{(j,i,n)} \propto L(\mathbf{z}_k|\mathbf{x}_k^{(j,i,n)}, m_{k-1}=j, m_k=i)\,\frac{p(\mathbf{x}_k^{(j,i,n)}|\mathbf{y}_{k-1}^{(i,n)}, \mathbf{Z}_k)}{q(\mathbf{x}_k^{(j,i,n)}|\mathbf{y}_{k-1}^{(i,n)}, \mathbf{Z}_k)}$$

where $\mathbf{y}_{k-1}^{(i,n)}$ is the set of particles corresponding to mode i at time step $k-1$ derived by collating particles corresponding to mode j at time step $k-1$. If the targets are assumed to move independently, the above weight calculation can be written as

$$\tilde{\phi}_k^{(j,i,n)} \propto L(\mathbf{z}_k|\mathbf{x}_k^{(j,i,n)}, m_{k-1}=j, m_k=i)\prod_{\ell=1}^{\mathscr{L}_i}\frac{p(\mathbf{x}_{k,\ell}^{(j,i,n)}|\mathbf{y}_{k-1,\ell}^{(i,n)}, \mathbf{Z}_k)}{q(\mathbf{x}_{k,\ell}^{(j,i,n)}|\mathbf{y}_{k-1,\ell}^{(i,n)}, \mathbf{Z}_k)} \qquad (4.24)$$

where $\mathscr{L}_i$ is the number of targets in mode i. The weights are normalized by

$$\Lambda'_{j,i} = \sum_{n=1}^{N_{j,i}} \tilde{\phi}_k^{(j,i,n)} \tag{4.25}$$

to obtain $\phi_k^{(j,i,n)} = \tilde{\phi}_k^{(j,i,n)} / \Lambda'_{j,i}$ and $\Lambda'_{j,i}$ is the particle approximation of $\Lambda_{j,i}$ in Equations (4.13) and (4.20). Given the initial mode probability $P_{0,i}$, for all i, the mixing probabilities in Equation (4.18) are then calculated as

$$\Pr(m_{k-1} = j | m_k = i, \mathbf{Z}_k) = \frac{\Lambda'_{j,i} \; \boldsymbol{\Omega}_{j,i} \; P_{k-1,j}}{\displaystyle\sum_{j'=1}^{M} \Lambda'_{j',i} \; \boldsymbol{\Omega}_{j',i} \; P_{k-1,j'}} \; . \tag{4.26}$$

The mode conditioned PDF in Equation (4.25) can be approximated as

$$p(\mathbf{x}_k^{[i]} | m_k = i, \mathbf{Z}_k) \approx \sum_{j=0}^{M-1} \sum_{n=1}^{N_{j,i}} \Pr(j,i) \phi_k^{(j,i,n)} \; \delta(\mathbf{x}_k^{[i]} - \mathbf{x}_k^{(j,i,n)}) \; . \tag{4.27}$$

The number of particles representing $p(\mathbf{x}_k^{[i]} | m_k = i, \mathbf{Z}_k)$ is equal to the sum of the particles representing each mode transition. In order to reduce the computational complexity, the weights of the above particles are sorted and the N_i highest weights with their corresponding particles are selected. The sorted weights are then normalized and resampled to obtain $\chi_k^{(i,n)}$. The mode conditioned probability can then be approximated as in Equation (4.25). Note that the particles $\mathbf{x}_k^{(i,n)}$ are resampled to avoid sample degeneracy [15]. The marginal mode conditioned posterior PDF of the ℓth target $p(\mathbf{x}_{k,\ell} | \mathbf{Z}_k)$ is obtained by selecting particles corresponding to that particular target i.e.,

$$p(\mathbf{x}_{k,\ell}^{[i]} | m_k = i, \mathbf{Z}_k) \approx \sum_{n=1}^{N_i} \chi_k^{(i,n)} \; \delta(\mathbf{x}_{k,\ell}^{[i]} - \mathbf{x}_{k,\ell}^{(i,n)}) \; .$$

The mode probabilities are computed using Equation (4.20) by substituting $\Lambda'_{j,i}$ for $\Lambda_{j,i}$. The mode probability corresponding to no targets being present is obtained by subtracting the sum of the probabilities of other modes from 1, i.e.,

$$P_{k,0} = 1 - \sum_{i=2}^{M} P_{k,i}.$$

Finally, the particles corresponding to all the modes that include the ℓth target are combined and weighted accordingly, based on the mode probability. Specifically,

$$p(\mathbf{x}_{k,\ell}|\mathbf{Z}_k) \approx \sum_{i=2}^{M} \sum_{n=1}^{N_i} C_\ell^i P_{k,i} \chi_k^{(i,n)} \ \delta(\mathbf{x}_{k,\ell}^{[i]} - \mathbf{x}_{k,\ell}^{(i,n)}) \ . \tag{4.28}$$

As mentioned above, during the mixing process, the number of particles representing $p(\mathbf{x}_{k,\ell}|\mathbf{Z}_k)$ is equal to the sum of the particles representing each mode. The weights of the above particles are sorted and the N_ℓ highest weights with their corresponding particles are selected. The sorted weights are then normalized and resampled to get $w_{k,\ell}^{(n)}$ which will be used in approximating $p(\mathbf{x}_{k,\ell}|\mathbf{Z}_k)$ as in Equation (4.23). The target existence probability of the ℓth target is obtained by summing up the relevant mode probabilities as

$$\Pr(e_{k,\ell}|\mathbf{Z}_k) = \sum_{i=2}^{M} C_\ell^i P_{k,i} \ . \tag{4.29}$$

The PF implementation steps of the MM-MT-TBDF algorithm are summarized in Algorithm 2.

Algorithm 2 Algorithmic Steps of MM-MT-TBDF-PF

```
Initialize the particle distribution of $p(\mathbf{x}_0^{[i]}|m_0 = i, \mathbf{Z}_0)$ and mode probability $P_{0,i}$ for $i = 2, \ldots, M$

for $k = 1$ to $K$ do
    Step 1: Predict the particle distribution for $p_{j,i}(\mathbf{x}_k^{[i]}|\mathbf{Z}_{k-1})$, conditioned on mode $j$ at time step $k-1$ and mode $i$ at time step $k$ for $j = 1, \ldots M$ and $i = 2, \ldots, M$
        • Particles for new targets entering the FOV:
            $\mathbf{x}_{k,nb}^{(n)} \sim q(\mathbf{x}_{k,\ell}^{(j,i,n)})$, $n = 1, \ldots, N_{nb}$, $N_{nb} \gg N_{j,i}$ , $\ell = 1, \ldots \mathscr{L}_i$
            Compute the likelihood function $L(Z_k|\mathbf{x}_{k,nb}^{(n)})$
            Pick $N_{j,i}$ highest likelihood particles and set them to $\mathbf{x}_{k,\ell}^{(j,i,n)}$
        • Particles for targets remaining in the FOV:
            $\mathbf{x}_{k,\ell}^{(j,i,n)} \sim p(\mathbf{x}_{k,\ell}^{(j,i,n)}|\mathbf{y}_{k-1,\ell}^{(i,n)})$ $n = 1, \ldots, N_{j,i}$, $\ell = 1, \ldots \mathscr{L}_i$,
        • Concatenate the new particles to get $\mathbf{x}_k^{(j,i,n)}$
    Step 2: Compute the joint likelihood function, conditioned on modes $j$ and $i$, using Equation (4.15)
    Step 3: Compute the weights $\{\tilde{\phi}_k^{(j,i,n)}\}_{n=1}^{N_{i,j}}$ as in Equation (4.24) as a function of the proposal density function
    Step 4: Compute the cumulative weights $\Lambda'_{j,i}$ using Equation (4.25)
    Step 5: Normalize the weights $\{\phi_k^{(j,i,n)}\}_{n=1}^{N_{i,j}}$
    Step 6: Compute the mixing probabilities $\Pr(m_{k-1} = j|m_k = i, \mathbf{Z}_k)$ using Equation (4.26)
    Step 7: Update the mode conditioned posterior PDF, $p(\mathbf{x}_k^{[i]}|m_k = i, \mathbf{Z}_k)$, using Equation (4.27)
    Step 8: Pick $N_i$ highest weights and normalize the weights to get $\{\chi_k^{(i,n)}\}_{n=1}^{N_i}$
    Step 9: Resample the normalized weights to get $\mathbf{x}_k^{(i,n)}$
    Step 10: Marginalize the posterior PDF to get $\mathbf{x}_{k,\ell}^{(i,n)}$, $\ell = 1, \ldots, \mathscr{L}_i$
    Step 11: Compute the posterior mode probabilities $P_{k,i}$ using Equation (4.20)
    Step 12: Compute the individual target state posterior PDF $p(\mathbf{x}_{k,\ell}|\mathbf{Z}_k)$, using Equation (4.28)
    Step 13: Pick $N_\ell$ highest weights and normalize the weights to get $\{w_{k,\ell}^{(n)}\}_{n=1}^{N_\ell}$
    Step 14: Resample the normalized weights to get $\mathbf{x}_{k,\ell}^{(n)}$, $\ell = 1, \ldots, \mathscr{L}$
    Step 15: Compute the target existence probability using Equation (4.29)
end for
```

4.5 Simulations

In all our simulations involving multiple targets, the optimal sub-pattern assignment (OSPA) metric [105] is used to compare the tracking performances of various methods. We have used the OSPA metric over the standard root mean-squared error (RMSE) metric to properly quantify the overall algorithm performance in terms of target cardinality error and localization error. The cardinality error quantifies the number of times the algorithm missed detecting an existing target or falsely detecting a non-existent target. The localization error quantifies how well the tracker follows the true target location.

4.5.1 Tracking Three Targets Using Image Measurements

In this section, we demonstrate the performance of the proposed MM-MT-TBDF algorithm for a 2-D image measurement to track three targets using the same set of measurement parameters used by the authors in [67]. The measurement is generated using a constant velocity target motion model and additive Gaussian process noise. The covariance matrix $\mathbf{Q}$ for the noise $\mathbf{v}_k$ for a discrete-time equivalent of a continuous-time model of constant velocity target motion [93] is given by

$$\mathbf{Q} = \begin{bmatrix} \frac{q_1 \Delta T^3}{3} & \frac{q_1 \Delta T^2}{2} & 0 & 0 & 0 \\ \frac{q_1 \Delta T^2}{2} & q_1 \Delta T & 0 & 0 & 0 \\ 0 & 0 & \frac{q_1 \Delta T^3}{3} & \frac{q_1 \Delta T^2}{2} & 0 \\ 0 & 0 & \frac{q_1 \Delta T^2}{2} & q_1 \Delta T & 0 \\ 0 & 0 & 0 & 0 & q_2 \Delta T \end{bmatrix} \tag{4.30}$$

where q_1 and q_2 are the process noise parameters for the target motion and intensity respectively and $\Delta T = 1$ s. The process noise parameters were selected as $q_1 = 0.0001$, $q_2 = 0.01$ and the measurement noise variance was $r = 1$. The measurement frames were generated at different SNR conditions: 19.8, 16.3, 13.8 and 10.2 dB with the corresponding intensity value of $I_{0,\ell} = 30, 20, 15, 10$, respectively for all ℓ. Twenty five frames of measurements were generated with the following parameters, $\triangle_x = 1$, $\triangle_y = 1$, $N_x = 20$, $N_y = 20$, blurring parameter $\Sigma = 0.7$. The measurements are generated such that the first target appeared in the first frame and left in the 21st frame. The second and third targets appeared in the 5th and 11th frames, respectively, and stayed in the FOV during the remainder of the measurement frames. The initial kinematic state vectors were [14.2 -0.1 7.2 0.1], [6.2 0.0 4.0 0.1] and [0.0 0.1 10.2 0.12] for Targets 1, Target 2, and Target 3, respectively. Figures 4.3(a) and 4.3(b) show the measurements from frame 15 at 19.8 dB and 10.2 dB peak SNR, respectively. Note that the targets are barely visible at 10.2 dB peak SNR. The parameters used in the generation of new target particles are $\nu_{\max} = -1$ and $\nu_{\min} = 1$, $I_{\min} = I_{0,\ell} - 5$, $I_{\max} = I_{0,\ell} + 5$. The probabilities in Equation (4.4) are $P_B = 0.01$ and $P_D = 0.02$. The number of neighborhood pixels used for the calculation of the likelihood function in Equation (4.14) is set 3. The number of the particles in this simulation is set to 10,000 for all layers of particles filters, that is $N_{j,i}$, N_i and N_ℓ for all i, j and ℓ. The number of particles for new targets, N_{nb} is also set at 10,000.

Figure 4.4(a) shows the corresponding probability of target existence for all three targets indicating the latency involved in detecting the target mode transitions. In general, for all targets, as the SNR decreases, the detection latency increases. Figure 4.4(b) shows the OSPA tracking error with the OSPA parameter set to $c = 40$ and $p = 2$ at 19.8 dB, 16.3 dB, 13.8 dB and 10.2 dB peak SNR. The cardinality and the localization error is very small at 19.8 dB and 16.3 dB. Note that when the cardinality error is very small, it is shown that the algorithm correctly tracks the number of existing targets without any false detection. The cardinality error at 13.8 dB SNR is slightly high indicating that there is a one frame delay in detecting when

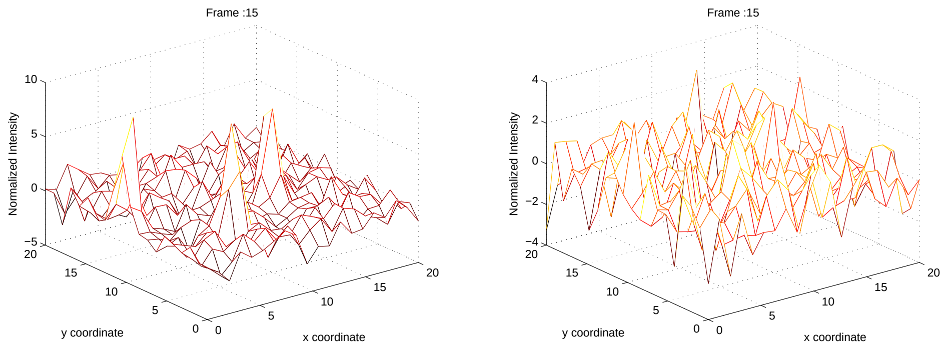

(a) (b)

Figure 4.3: Measurement Frames: (a) Time Step 15, 19.8 dB Peak SNR. (b) Time Step 15, 10.2 dB Peak SNR

Target 2 enters the FOV around the 5th frame. Similarly at 10.2 dB SNR, there was a two-frame delay in detecting when the third target entered the FOV around the 11th frame. This latency trend is also evident from the probability of target detection in Figure 4.4(a). Despite the delay in detecting a target, the localization error at lower SNR is still good, confirming the excellent performance of our proposed algorithm under lower SNR measurement conditions.

4.5.2 Tracking Three Targets Using Radar Measurements

For the radar simulations, we used the OSPA parameters $p = 2$ and $c = 16$. The value of the cut-off parameter $c = 16$ provides a good balance between the localization and the cardinality error. Moreover, the FOV in our simulations is in the same order of magnitude as the cut-off parameter. In this measurement model, we assume constant velocity and Gaussian noise models with the covariance matrix of the state transition matrix defined in Equation (4.30). The process noise variance parameters are $q_1 =$ 0.01 and $q_2 = 0.001$. The tracking FOV is [0 16.97] m in both the x and y direction. Measurements from two sensors located at (0, 0) and (0, 16.97) m are

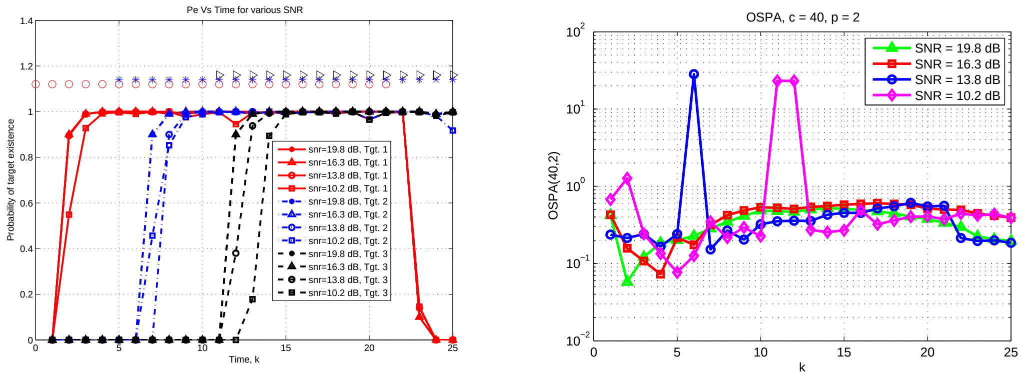

(a) (b)

Figure 4.4: Image Measurement Case: (a) Target Existence Probability (Red Circles, Blue Stars and Black Triangles Indicate the Frames at which Target 1, Target 2 and Target 3 Truly Exist, respectively); and (b) Tracking Error at Different SNR Conditions, OSPA(40,2).

used in our simulations. A single measurement frame consists of (48 × 48 × 48) bins resulting in the following measurement bin resolutions, range $\Delta_r = 0.509$ m, range-rate $\Delta_{\dot{r}} = 0.0766$ m/s, and azimuthal angle $\Delta_\theta = 0.0334$ radians. The corresponding measurement ranges are: range [0 24) m, range-rate [-1.8 1.8) m/s and azimuthal angel $[0\ \pi/2)$ radians for sensor 1 and $(-\pi/2\ 0]$ radians for sensor 2. The spread factors used in the measurement models are: $\sigma_r = 1.1$ m , $\sigma_{\dot{r}} = 0.35$ m/s, $\sigma_\theta = 0.06$ radians. The measurement noise variance ν_k is set to 1. Therefore, the peak SNR corresponding to the ℓth target is calculated as

$$\mathrm{SNR}_{\mathrm{peak}} = \frac{[\Delta_r \Delta_{\dot{r}} \Delta_\theta I_{k,\ell}]^2}{((2\pi)^{3/2} \sigma_r \sigma_{\dot{r}} \sigma_\theta)^2 \nu_k} \,. \tag{4.31}$$

The expected target component velocity range is set to [-1 1] m/s, and the expected peak SNR range is set to [-3 6] dB. We used low SNR conditions for all our simulations to demonstrate that the proposed algorithm can work under difficult environmental conditions. It is important to note that the proposed algorithm can also be used

Table 4.2: True Target Combination at Different Time Steps

Time Step, k	**1-4**	**5-12**	**13-20**	**21-25**	**26-33**	**34-41**	**41-46**
Target Combination	None	1	1,2	1,2,3	2,3	3	None
Mode, i	1	2	5	8	7	4	1

at higher SNR conditions. The measurements were generated with the intensity corresponding to 3 dB peak SNR, and the instantaneous peak SNR is sometimes lower than the pre-determined peak SNR due to the discretization of the measurement into grids. The probabilities of a target entering (P_B) and leaving (P_D) the FOV are both 0.02. In our first simulation, the measurements were generated at 0 dB peak SNR such that the first target enters and leaves the FOV at frame 5 and frame 25, respectively; the second target enters at frame 13 and leaves during frame 33; and the third target enters during frame 21 and leaves during frame 41. Table 4.2 shows the true target combinations at different time steps along with the corresponding mode number. The initial positions and velocities for each of the targets are (4.2, 1.2) m and (0.35, 0.70) m/s, (16.2, 2.2) m and (-0.70, 0.15) m/s, and (1.2, 16.2) m and (0.65, -0.45) m/s, respectively. The number of the particles in this simulation is set to 500 for all layers of particles filters, $N_{j,i}$, N_i and N_ℓ for all i, j and ℓ. Unless otherwise mentioned, for new targets, the number of initial particles, N_{nb}, is always set at 10 times the actual number of particles used in that mode, i.e. $N_{nb} = 10N_{j,i}$. Note that the number of new target particles is eventually reduced to $N_{j,i}$ after picking only $N_{j,i}$ particles from a larger set. Figure 4.5 shows the estimated averaged mode probability over 30 Monte Carlo simulations corresponding to all possible modes in Table 4.2. It is obvious from the plots that the proposed algorithm closely follows the true mode transition. Figure 4.6(a) shows the true and estimated target trajectories for all three

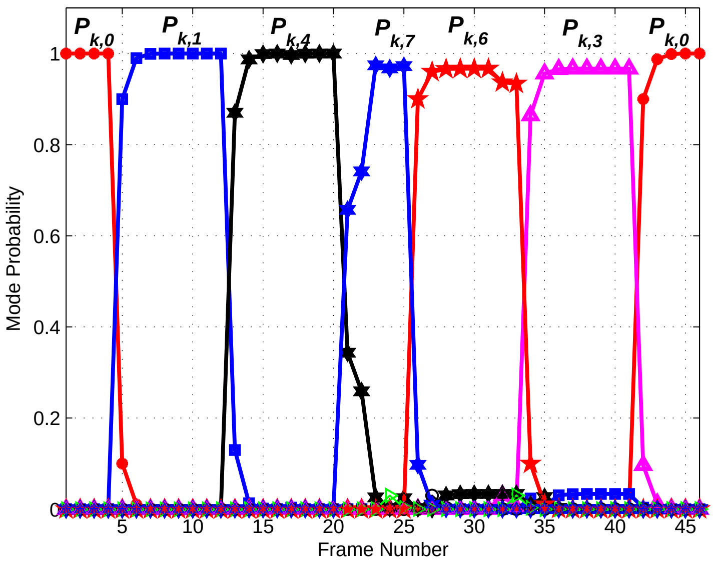

Figure 4.5: Mode Probability for Three Targets at 3 dB Peak SNR.

targets in all Monte Carlo simulations. Initially the estimated target location deviates from the true location, however, the estimated target location converged to the true location as more measurements were received. Figure 4.6(b) shows the corresponding OSPA averaged over 30 Monte Carlo simulations. The cardinality error dominates the OSPA during the true mode transitions at frames 13, 21, 26, 33 that correspond to the target events: appearance of Target 2, appearance of Target 3, disappearance of Target 1 and disappearance of Target 3, respectively. The localization error is in general very small, around 0.3 m.

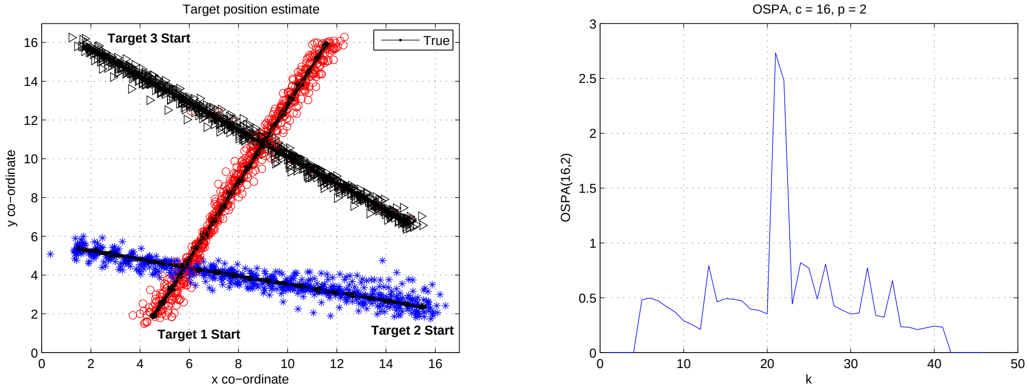

(a) (b)

Figure 4.6: Radar Measurement Tracking of Three Targets at 3 dB Peak SNR: (a) True and Estimated Target Trajectories (Solid Lines Represent the True Target Trajectory and Red Circles, Blue Stars and Black Triangles Represent the Estimated Trajectory of Target 1, Target 2 and Target 3 respectively; and (b) Tracking Error, OSPA(16,2).

Chapter 5

EFFICIENT IMPLEMENTATION OF MULTIPLE TARGET TRACK-BEFORE-DETECT FILTERING

5.1 Computational Issues of the Multiple Mode Multiple Target Track-before-detect Filter

In Chapter 4, we proposed the multiple mode multiple target track-before-detect filter (MM-MT-TBDF), and we discussed its particle filter (PF) implementation (MM-MT-TBDF-PF). The proposed algorithm suffers from the curse of dimensionality when the maximum number of targets increases. In this chapter, we propose a partitioning based method to mitigate the curse of dimensionality problem thereby improving the tracking performance for a given number of particles. This method partitions the multi-target space into a single target space to generate proposal particles and then uses the measurement to select only highly likelihood particles from a set of particles generated from the single target space partition. The proposal particles generated this way result in greatly improving the tracking performance. The Markov chain Monte Carlo (MCMC) step using the Metropolis-Hastings method [17] is also integrated into the proposal particle generation step to reduce sample impoverishment. The number of target combinations can grow exponentially as the maximum number of targets increases. To mitigate the effects of curse of dimensionality, we propose a heuristical decision-directed based approach to keep the computational complexity of the algorithm as a linear function of the maximum number of targets.

5.2 Proposal Function Using PF Partition Method

The performance of the PF based algorithm can suffer if the same number of particles is assigned for all possible modes in the MM-MT-TBDF-PF. For example, a mode with three targets uses the same number of particles as a mode with only one target even though the number of parameters to be estimated in the first case is three times higher than the latter case. Assigning the same number of particles to all the modes can become a problem when the dimensionality of the multi-target state vector increases. This problem can be avoided by assigning different number of particles to different modes. However, the total number of particles can grow significantly as the number of targets that are assumed present in a mode increases. Moreover, the amount of computations necessary to run different PFs for all the modes increases drastically since the combinatorial complexity increases exponentially as a function of the total number of targets. In this chapter, we propose a method that is based on state space partitioning to reduce the number of particles in order to reduce the overall computational complexity. Since the number of modes can grow exponentially as a function of the maximum number of targets, even a small decrease in the number of particles can have an overall impact on the computational performance.

In [106], a method was proposed to estimate the joint multi-target probability density function (PDF) to track an unknown number of targets; the method introduced different proposal functions by partitioning the single target state space and illustrated that a fewer number of particles (orders of magnitude smaller) were required. The computational complexity was reduced by incorporating information from measurements into the proposal function. Our proposed MM-MT-TBDF partitioning (MM-MT-TBDF-IP) also uses measurement information during the particle generation step for the posterior PDF conditioned on mode i at time k and mode j

at time $k-1$. We use the simplified form of the sequential partitioning algorithm by exploiting the fact that the number of assumed targets in a mode is known. In most cases, the number of partitions needed is then equal to the number of targets. In [106], three different partitioning methods were proposed: independent, coupled and adaptive partitioning. Our proposed algorithm can incorporate all three methods. Without loss of generality, in what follows, we only describe the independent partitioning (IP) method. The coupled and adaptive partitioning methods can be used if the targets are moving close to each other.

The sequential partitioning algorithm [106, 107] has five major steps: partition sampling, partition weight computation, resampling of partition weights, particle weights computation and resampling of particles. In Chapter 4, Section 4.4.1, the predicted density function conditioned on the current and previous mode $p_{j,i}(\mathbf{x}_k^i|\mathbf{Z}_{k-1})$ was approximated using the particles for targets entering the field of view (FOV) and remaining in the FOV. Using the IP method, the likelihood function corresponding to the predicted particles for each target in a mode is computed. The likelihood function for each target is termed the partition weights $\alpha_{k,l}^{(j,i,n)}$ in [106], and i, j are the mode numbers at time steps k and $(k-1)$, respectively and n is the corresponding particle number of the partition weight. The partition weights are normalized and resampled to generate a new set of predicted particles. The new particles closely approximate the true underlying density function since the density also incorporates the measurement information. If we assume that the targets are moving independently, the joint proposal function can be written as

$$q(\mathbf{x}_k^{(j,i,n)}|\mathbf{y}_{k-1}^{(j,i,n)}, \mathbf{Z}_k) = \prod_{\ell=1}^{\mathscr{L}_i} q(\mathbf{x}_{k,\ell}^{(j,i,n)}|\mathbf{y}_{k-1,\ell}^{(j,i,n)}, \mathbf{Z}_k) \tag{5.1}$$

where $\mathscr{L}_i$ is the number of targets in mode i. Since the proposal function is now also a function of the measurement likelihood, the proposal density function for each target that will be used in Equation (4.24) can be written as [107]

$$q(\mathbf{x}_{k,\ell}^{(j,i,n)}|\mathbf{y}_{k-1,\ell}^{(j,i,n)},\mathbf{Z}_k) = \begin{cases} \alpha_{k,l}^{(j,i,n)} q(\tilde{\mathbf{x}}_{k,\ell}^{(j,i,n)}), & \text{target entering FOV} \\ \\ \alpha_{k,l}^{(j,i,n)} p(\tilde{\mathbf{x}}_{k,\ell}^{(j,i,n)}|\mathbf{y}_{k-1,\ell}^{(i,n)}), & \text{target remaining in FOV} \end{cases}$$

where $p(\tilde{\mathbf{x}}_{k,\ell}^{(j,i,n)}|\mathbf{y}_{k-1,\ell}^{(i,n)})$ is the posterior PDF conditioned on modes at time steps k and $(k-1)$ and it is represented by a PF in Equation (4.21), whose weights are obtained using Equation (4.24), $\mathbf{y}_{k-1,\ell}^{(i,n)}$ is the ℓth target's state vector corresponding to mode j at time step $(k-1)$ that is transformed to mode i using Equation (4.16) and $\tilde{\mathbf{x}}_{k,\ell}^{(i,n)}$ is the particle corresponding to the ℓth target's partition for the corresponding modes i and j at time steps k and $(k-1)$, respectively. The implementation steps of the IP method that replace Step 1 and Step 3 of Algorithm 2, respectively, are shown in Algorithm 3.

Algorithm 3 PF Proposal Steps Using Independent Partitioning Method

```
Step 1: Predict the particle distribution for $p_{j,i}(\mathbf{x}_k^{[i]}|\mathbf{Z}_{k-1})$, conditioned on mode $j$ at time $k-1$ and mode $i$ at time $k$ for $j = 0, 1, \ldots M-1$ and $i = 1, \ldots, M-1$.

    • Particles for new targets entering the FOV:
        $\hat{\mathbf{x}}_{k,nb}^{(j,i,n)} \sim q(\tilde{\mathbf{x}}_{k,\ell}^{(j,i,n)})$, $n = 1, \ldots, N_{nb}$, $N_{nb} \gg N_{j,i}$, $\ell = 1, \ldots, \mathscr{L}_i$

    • Particles for targets remaining in the FOV:
        $\tilde{\mathbf{x}}_{k,\ell}^{(j,i,n)} \sim p(\tilde{\mathbf{x}}_{k,\ell}^{(j,i,n)}|\mathbf{y}_{k-1,\ell}^{(i,n)})$ $n = 1, \ldots, N_{j,i}$, $\ell = 1, \ldots, \mathscr{L}_i$

    • Compute partition weights:
        Particles for new targets entering the FOV:   $\tilde{\alpha}_{k,l}^{(j,i,n)} \propto p(\mathbf{Z}_k|\hat{\mathbf{x}}_{k,nb}^{(j,i,n)})$
        Pick only $N_{j,i}$ highest likelihood particles and set them to $\tilde{\mathbf{x}}_{k,\ell}^{(j,i,n)}$
        Particles for targets remaining in the FOV:   $\tilde{\alpha}_{k,l}^{(j,i,n)} \propto p(\mathbf{Z}_k|\tilde{\mathbf{x}}_{k,\ell}^{(j,i,n)})$

    • Normalize partition weights:
        $\tilde{\alpha}_{k,l}^{(j,i,n)} = \frac{\tilde{\alpha}_{k,l}^{(j,i,n)}}{\sum_{n=1}^{N_{j,i}} \tilde{\alpha}_{k,l}^{(j,i,n)}}$

    • Resample the normalized particles to obtain $\mathbf{x}_{k,\ell}^{(j,i,n)}$ and $\alpha_{k,l}^{(j,i,n)}$

    • Concatenate the new particles from all partitions to obtain $\mathbf{x}_k^{(j,i,n)}$

Step 3: Compute the particle weights using the proposal function in Equation (5.1),

    • $\tilde{\phi}_k^{(j,i,n)} = \frac{L(\mathbf{z}_k|\mathbf{x}_k^{(j,i,n)}, m_{k-1} = j, m_k = i)}{N_{j,i} \prod_{\ell=1}^{\mathscr{L}_i} \alpha_{k,l}^{(j,i,n)}}$
```

5.3 MM-MT-TBDF-IP with Markov Chain Monte Carlo

Sample impoverishment is a common problem with particle filters, especially when the process model noise variance is small [16]. This is the result of lack of sample diversity during the generation of predicted particles. There exist many methods to mitigate the problem of sample impoverishment [17], [16]. We used the Markov Chain Monte Carlo (MCMC) approach to increase sample diversity without affecting the estimated posterior density function. Specifically, we used the Metropolis-Hastings [17] algorithm to perform the resample-move operation (MM-MT-TBDF-IP-MCMC). As shown in the previous section, the particles approximating the posterior density function conditioned on the current and previous mode are resampled to obtain $\mathbf{x}_k^{(j,i,n)}$. The covariance of this distribution can be estimated from the current particle distribution. In order to improve the sample diversity, a perturbation is added to the existing particles by adding new samples that are drawn from a Gaussian distribution with zero mean and the covariance equal to the one estimated from the particle distribution. The conditional sample move operation is then performed based on the likelihood ratio of the particles before and after the addition of the perturbation. The Metropolis-Hastings sample move step is performed only for surviving targets. With out the Metropolis-Hastings step, the remaining MCMC steps simply constitute the regularized particle filter [17]. This MCMC step is performed after Step 5 in Algorithm 2 as a new Step 5a. The MCMC steps used in our algorithm are summarized in Algorithm 4.

Algorithm 4 Metropolis-Hasting Steps for MM-MT-TBDF-IP-MCMC

Step 5a:

- For a target that survives from previous time step, compute the posterior covariance matrix S_ℓ from the predicted particle distribution $\mathbf{x}_{k,\ell}^{(j,i,n)}$. For a new target entering the FOV, set the covariance matrix to some pre-defined value, $S_\ell = S_{nb}$.

- Obtain samples from the Gaussian random process, $\epsilon \sim \mathcal{N}(0, S_\ell)$. Use the random process ϵ to add a perturbation to the resample particles.

- Add some jitter to the already resampled particles $\dot{\mathbf{x}}_{k,\ell}^{(j,i,n)} = \mathbf{x}_{k,\ell}^{(j,i,n)} + h_{opt} S_\ell^{1/2} \epsilon$ where $h_{opt} = 0.9397(\frac{1}{N_{j,i}})^{1/9}$, the various constants are described in [16, 17].

- Compute the Metropolis-Hastings acceptance probability,

$$\beta = \min \left\{ 1, \frac{p(\mathbf{Z}_k | \dot{\mathbf{x}}_{k,\ell}^{(j,i,n)}) p(\dot{\mathbf{x}}_{k,\ell}^{(j,i,n)} | \mathbf{y}_{k-1,\ell}^{(i,n)})}{p(\mathbf{Z}_k | \mathbf{x}_{k,\ell}^{(j,i,n)}) p(\mathbf{x}_{k,\ell}^{(j,i,n)} | \mathbf{y}_{k-1,\ell}^{(i,n)})} \right\}.$$

- for $n = 1{:}N_{j,i}$

  Draw a number $u \sim \mathcal{U}$ [0 1]

  A resampled particle $\mathbf{x}_{k,\ell}^{(j,i,n)}$ is moved to a new location $\dot{\mathbf{x}}_{k,\ell}^{(j,i,n)}$ only if $u \leq \beta$

  end

5.4.1 *Tracking Three Targets Using Radar Measurements*

In the first simulation, we analyze the tracking result of the MM-MT-TBDF-IP-MCMC method for the simulation used in Section 4.5.2. Figure 5.1 shows the estimated averaged mode probability at different frames over 30 Monte Carlo simulations. The mode probability values are more accurate when compared to the mode probability obtained using the MM-MT-TBDF-PF method in Figure 4.5. For example, the mode probability value when Targets 2 and 3 are present is higher with the partitioning method, and it takes longer for the other method to detect the presence of all three targets. Figure 5.2 shows the true and estimated target trajectories for all three targets in all Monte Carlo simulations. The variance of the target position estimate is much smaller when compared to the MM-MT-TBDF-PF method in Figure

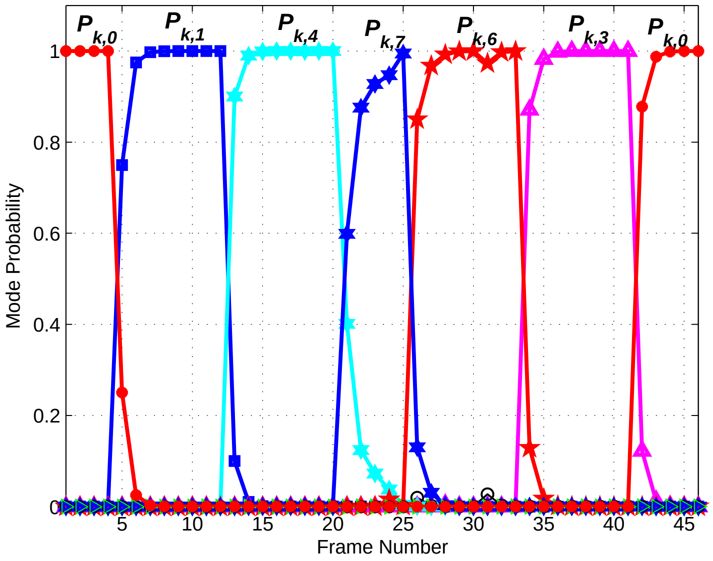

Figure 5.1: Mode Probability for Three Targets at 3 dB Peak SNR (MM-MT-TBDF-IP-MCMC).

4.6(a). The faster convergence rate of the target position estimate with the partitioning method is evident from the target position estimate in the vicinity of its initial position. Figure 5.3 shows the corresponding OSPA averaged over 30 Monte Carlo simulations with 500 particles. The cardinality error dominates the OSPA when the first target appears at frame 5, second target appears at frame 13 and also when the third target appears at frame 21, implying that once in a while, there is a one frame latency in detecting a new target that enters the FOV. The OSPA also shows that the algorithm is able to quickly detect a target leaving the FOV since the OSPA value is low at frames 25, 33 and 41. The localization error is around 0.1 m. The figure also shows the OSPA with different number of particles along with the one from the MM-MT-TBDF-PF method. For the same number of particles, the localization error

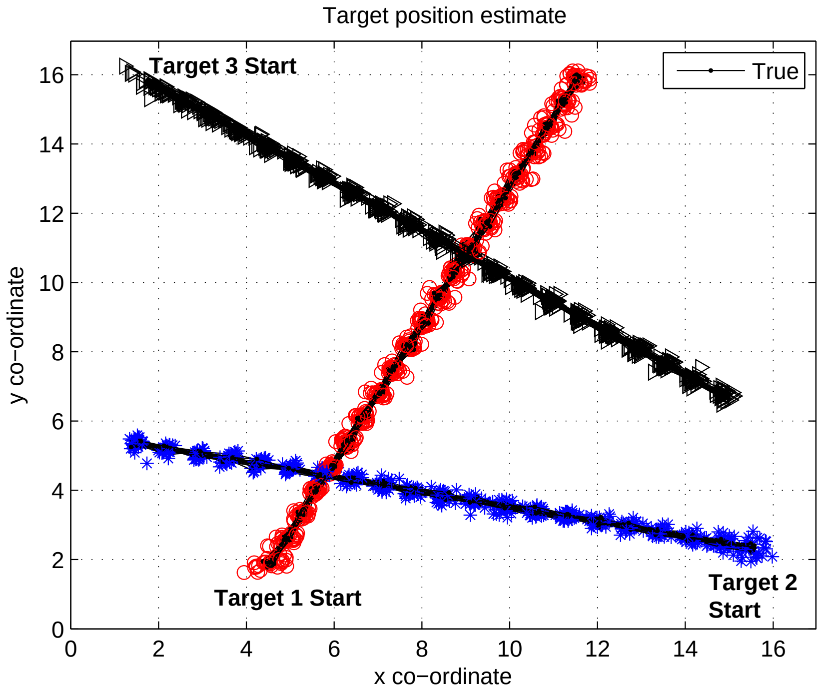

Figure 5.2: True and Estimated Target Trajectories for Three Targets at 3 dB Peak SNR.

using the partition method is three times smaller than the other method. In other words, the MM-MT-TBDF-IP-MCMC method needs a smaller number of particles to achieve similar tracking performance as the MM-MT-TBDF-PF method. This is evident with the OSPA for 100 and 50 particles in Figure 5.3 where the tracking error is in the same order as for the MM-MT-TBDF-PF method. This result agrees with the findings in [106] that the regular PF method needs an order of magnitude higher number of particles than the IP method to achieve similar tracking error. The averaged OSPA with the IP method is higher at a lower process model variance. Therefore, partitioning the target state space helps us to achieve better tracking performance while reducing the required number of particles.

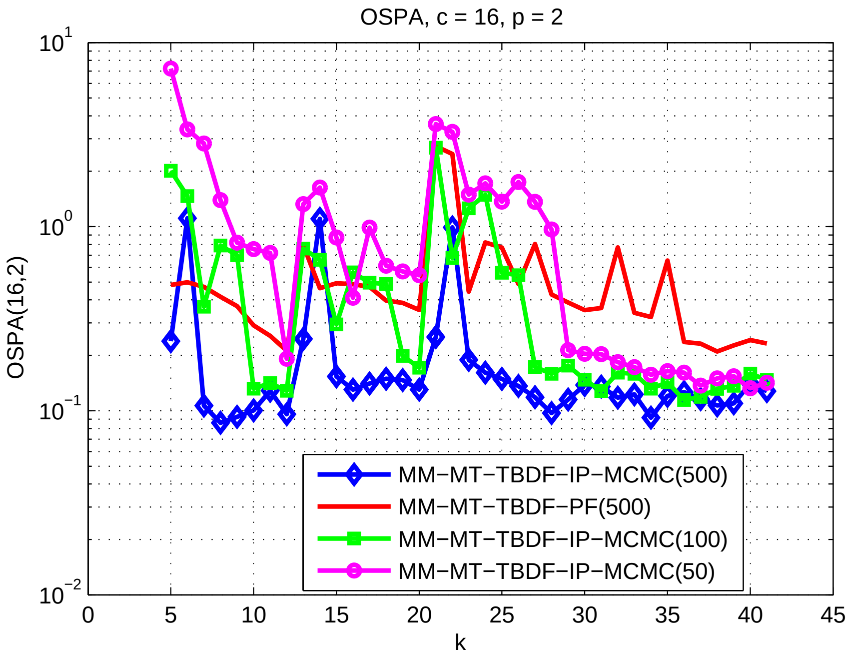

Figure 5.3: OSPA(40,2) for Three Targets at 3 dB Peak SNR.

5.4.2 Comparison of Different PF Schemes

In our second simulation, we have compared the performances of the MM-MT-TBDF-PF, MM-MT-TBDF-IP and MM-MT-TBDF-IP-MCMC methods at various process model noise variance q_1 in Equation (4.30). As before, three targets were considered in the same simulation set up; 500 particles were used for all three methods, and 30 Monte Carlo simulations were run to obtain the averaged OSPA for each variance. The averaged OSPA was again averaged across time to obtain a single OSPA value for a given q_1. Figure 5.4 compares the averaged OSPA for different values of q_1. The averaged OSPA for the MM-MT-TBDF-PF method is much higher than for the other two methods. The error introduced by the sample impoverishment is improved using the MCMC steps. In general, the OSPA with the MCMC step is the lowest among the three proposed methods at every process model variance value. As expected, the tracking error for all methods increases drastically when the process model variance is increased. This shows that the performance of the MM-MT-TBDF is in general limited by the process model variance. Thus, for the rest of the simulations, we use the MM-MT-TBDF-IP with the MCMC step.

5.4.3 Effects of Intensity Modeling Error Variance

In our TBDF application, the target intensity, which is a measure of target radar cross section (RCS), is estimated as one of the parameters of the state vector. In the state model, we assumed that the target intensity follows a random walk model. The uncertainty in the target RCS can be included by increasing the variance of the modeling error. In this simulation, we compare the performance for different values of the variance parameter q_2 in Equation (4.30) at 3 dB peak SNR. Figure 5.5(a) shows the instantaneous peak SNR corresponding to the first target at all time steps from

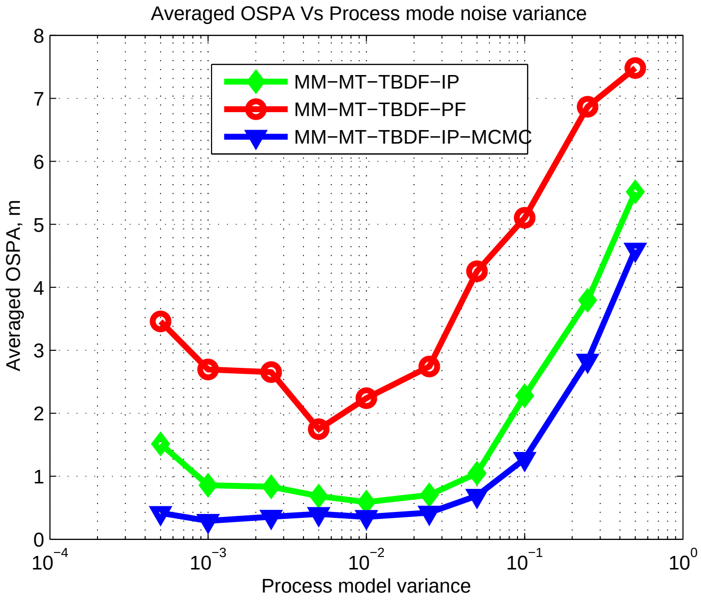

Figure 5.4: OSPA Vs Process Model Variance.

one Monte Carlo simulation. The instantaneous peak SNR at lower values varies by only a small amount from the average peak SNR whereas for higher q_2 values the instantaneous value deviates by a large amount. Figure 5.5(b) shows the tracking error for $q_2 = 0.001, 0.01, 0.1, 1$ with the initial target kinematic parameters set to be the same as in Figure 5.2. As expected, the tracking error increases as the variance increases. The tracking error at higher variances is dominated by the cardinality error, implying that the probability of first establishing a target trajectory is lower at higher variances. In realistic scenarios, more sophisticated statistical models such as the fluctuating target amplitude model [55] can be incorporated into our method by modifying the measurement model and the likelihood function.

5.4.4 Effects of Spreading Factors

In actual radar systems, the spreading factor along the range direction (σ_r) could be a function of the cross-correlation properties of the transmitted baseband signal

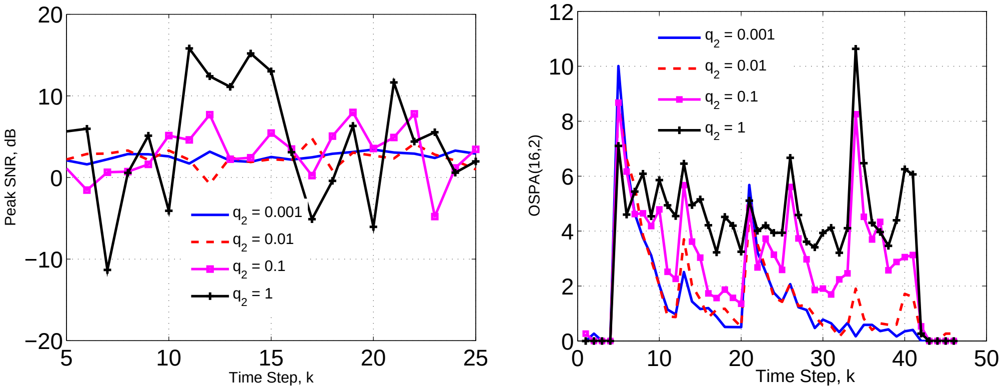

(a) (b)

Figure 5.5: Effects of Intensity Modeling Error Variance: (a) Instantaneous Peak SNR for Target 1; and (b) OSPA Versus Time for Various Values of q_2.

whereas the spreading factor in the range-rate direction ($\sigma_{\dot{r}}$) could be related to the number of pulses used for coherent processing [45]. The spreading factor in the azimuthal direction (σ_θ) is controlled by the antenna beamwidth [47]. In this simulation, we evaluate the performance of our algorithm for different values of spreading factors in order to investigate the degree of difficulty in tracking a low observable targets by radars with different system parameters. We compare the tracking performance under four different cases (i) $\sigma_r = 0.509$ m, $\sigma_{\dot{r}} = 0.077$ m/s, and $\sigma_\theta = 0.033$ rad, (ii) $\sigma_r = 0.636$ m, $\sigma_{\dot{r}} = 0.096$ m/s, and $\sigma_\theta = 0.041$ rad, (iii) $\sigma_r = 0.764$ m, $\sigma_{\dot{r}} = 0.116$ m/s, and $\sigma_\theta = 0.049$ rad, (iv) $\sigma_r = 0.891$ m, $\sigma_{\dot{r}} = 0.135$ m/s, and $\sigma_\theta = 0.058$ rad. The "one sigma" measure for all four cases corresponds to 1, 1.25, 1.5, 1.75, respectively, times the bin resolution in each measurement axis. In this section and the following sections, we refer to these four cases as 1σ, 1.25σ, 1.5σ, and 1.75σ, respectively. Figure 5.6(a) and 5.6(b) show the tracking error and the target existence probability respectively, for all four cases at 3 dB peak SNR averaged over 60 Monte Carlo simulations.

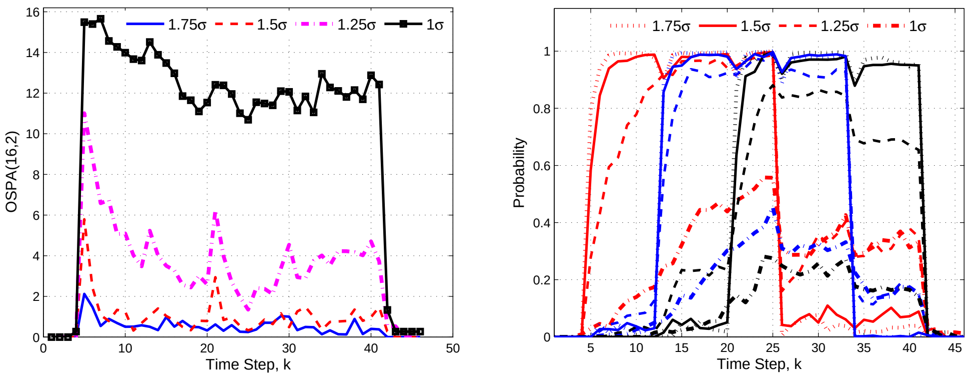

(a)

(b)

Figure 5.6: Effects of Spreading Factors: (a) OSPA Versus Time for Various Spreading Factors; and (b) Probability of Target Existence Computed Using Equation (4.29), Red: Target 1, Blue: Target 2, Black: Target 3.

The tracking error is very small for the 1.75σ case and for 1.5σ case, the tracking error is still small except during mode transitions. The increased error at these times is due to the increased cardinality error. When the spreading factor is at 1.25σ, it takes a long time to detect new targets that entered the FOV. This is seen from the slow rise of the target existence probability. The localization error is reduced as more measurements are processed. The tracking performance is severely affected for the 1σ case. This is due to that fact that as the number of bins occupied by the target associated measurement is reduced, the discrimination between noise and target is minimal. Despite the poor multi-target tracking performance, the algorithm is still able to reasonably detect the presence of all three targets as seen from Figure 5.6(b). The target existence probability for Target 1 from time steps 25 to 41 is high since, Targets 2 and/or 3 are not being detected before Target 1 leaves the FOV. Hence, Targets 2 or 3 are detected as Target 1 after correctly detecting the disappearance of the original Target 1. Therefore, the OSPA is dominated by the cardinality error due to this higher probability of missed targets. The mode probabilities estimated using Equation (4.19) and averaged over all Monte Carlo runs are shown in Figure 5.7 for the test cases (i) and (iii). The figure shows the probabilities corresponding to all possible modes in Table 4.2. The proposed algorithm closely follows the true mode transition and the mode probabilities decrease as the spreading factor is decreased.

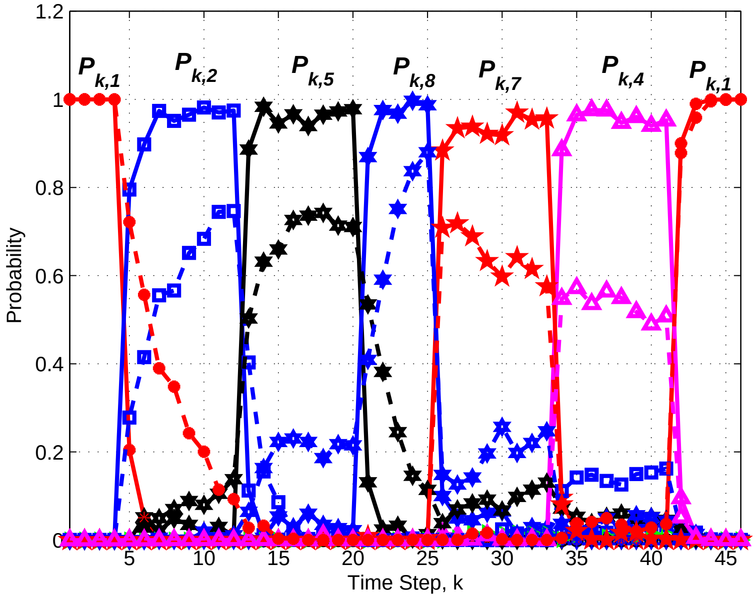

Figure 5.7: Mode Probability Computed Using Equation (4.19) For Three Targets Case, Solid: $\sigma_r = 0.509, \sigma_{\dot{r}} = 0.077, \sigma_\theta = 0.033$ (1σ), Dashed: $\sigma_r = 0.764, \sigma_{\dot{r}} = 0.116, \sigma_\theta = 0.049$ (1.5σ).

5.4.5 Peak SNR Analysis

Figure 5.8 compares the averaged OSPA ($c = 16$, $p = 2$, averaged across all time steps from 30 Monte Carlo runs) for varying peak SNRs at four spreading factor cases. When the spreading factors are at 1.75σ and 1.5σ, the error is also reasonable at lower

SNR values. The tracking performance at 1.25σ degrades for SNR less than 3 dB and for 1σ case, the algorithm provides useful results only when the SNR is above 5 dB. As we increase the SNR, the tracking error for all four cases converges to a lower value. Since the tracking performance is sensitive to the spreading factors, one can employ SNR dependent waveform agile signal processing to dynamically adjust the transmitted waveform parameters to provide a trade-off between tracking error and range/range-rate resolution [103], [104].

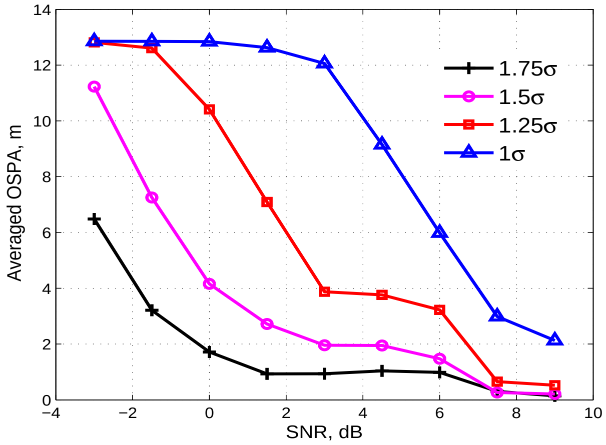

Figure 5.8: Averaged OSPA Vs. Peak SNRs.

5.4.6 *Closely Moving Targets Tracking Analysis*

The tracking accuracy for three closely-moving targets is demonstrated next to investigate the ability to resolve closely-moving targets. Two cases are considered: (i) targets moving in the opposite direction and (ii) targets moving closely in the same direction. In the first case, we investigate the ability to continually track targets that come close to each other and proceed in the opposite direction. In the latter case, we consider the case of resolving two closely-moving targets. The initial target states in the first case are set to (2.2, 0.2) m and (0.3, 0.50) m/s, (12.2, 13.2) m and (-0.40,

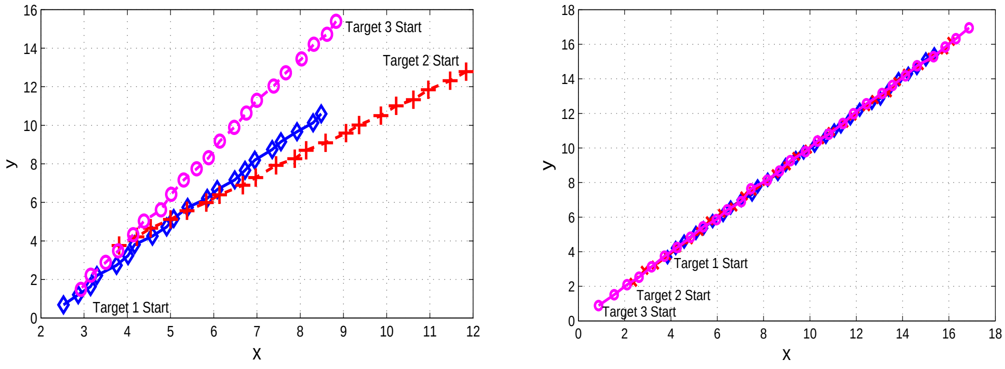

(a) (b)

Figure 5.9: Closely-Moving Targets Case: (a) Trajectory of Targets Moving in Opposite Direction; and (b) Trajectory of Targets Moving in Same Direction.

-0.45) m/s, and (9.2, 16.2) m and (-0.30, -0.70) m/s for Target 1, Target 2, and Target 3, respectively, and the targets enter and leave the FOV at time steps 5, 13, 21 and 25, 33, 41, respectively. In the second case, the initial kinematic states for Targets 1–3 are (3.4, 3.4) m and (0.4, 0.4) m/s, (1.9, 1.9) m and (0.475, 0.475) m/s, and (0.4, 0.4) m and (0.55, 0.55) m/s, respectively and the targets enter and leave the FOV at time steps 4, 7, 10 and 33, 36, 39, respectively. Figure 5.10(a) shows the Euclidean distance between target pairs for both test cases. Targets are within 1 m of each other at time step 25 and 32 for case (i) and (ii), respectively. In the second case, the Euclidean distance between targets in range-rate is around 0.1-0.2 m/s ($\approx$ 1.5–3 times the bin resolution) and the Euclidean distance between targets in the look direction is around 0.01 degrees (less than one bin resolution). Figure 5.9(a) and Figure 5.9(b) show the target trajectories for both test cases. Figure 5.10(b) shows the tracking error averaged over 60 Monte Carlo runs at 3 dB peak SNR with the spreading factor set to 1.5σ. The cardinality error is generally high around mode transitions than the well separated targets case. The tracking error for case (ii) is high from time steps

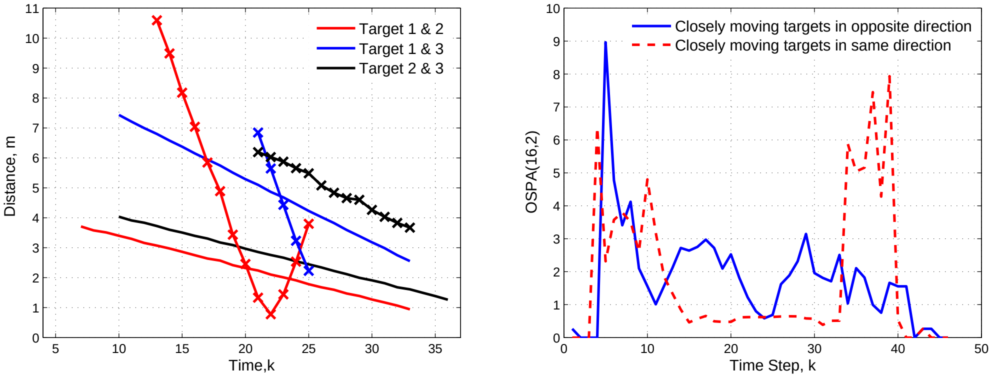

(a) (b)

Figure 5.10: Closely-Moving Targets Case: (a) Euclidean Distance Between 3 Closely-Moving Targets (Crosses Represent Targets Moving in Opposite Directions); and (b) Tracking Error, OSPA(16, 2).

33–39 since the targets come close to each other before one of them leaves from the FOV and the algorithm continues to track the non-existent target. This is because the predicted measurement likelihood corresponding to this target is high due to the presence of other targets in the neighbourhood of the predicted target state. For a target that leaves the FOV with similar kinematic state estimates as another existing target, the predicted state vector obtained using the state transition matrix is also estimated in the vicinity of the already existing target. Hence, it takes longer to detect the disappearance of closely-moving targets.

5.4.7 Six Targets Tracking Analysis

The algorithm performance for $\mathscr{L} = 5$ to track six closely-spaced targets at 3 dB peak SNR with the spreading factor set at 1.5σ is demonstrated in Figures 5.11 and 5.12. The initial positions and velocities for Targets 1–6 are (2.2, 2.2) m and (0.32, 0.32) m/s, (2.2, 0.2) m and (0.33,0.32) m/s, and (13.2, 15.2) m and (-0.14,

-0.32) m/s, and (13.2, 16.2) m and (-0.16, -0.34) m/s, and (10.1, 2.1) m and (-0.09, 0.09) m/s, and (11.1, 1.2) m and (-0.29, 0.14) m/s, respectively. Targets 1–6 enter and leave the FOV at time steps 5 and 45, 11 and 51, 17 and 57, 23 and 63, and 29 and 69, and 50 and 65, respectively. The initial target states are selected such

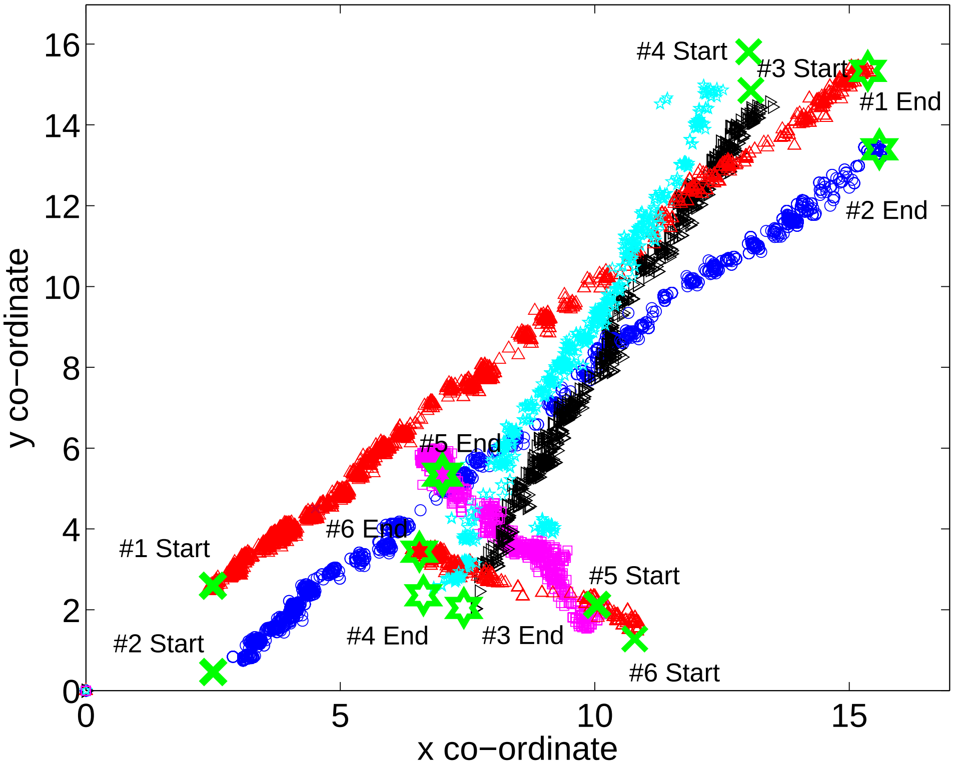

Figure 5.11: Particle Distribution for Tracking Six Targets Case with $\mathscr{L} = 5$ Targets.

that there are two sets of closely-spaced targets with each set of targets moving in opposite direction and the target pairs {1,3}, {1,4}, {2,3}, {3,5}, {4,5} and {4,6} cross each other at time steps 30, 34, 36, 50, 56 and 61, respectively. Figure 5.11 shows the higher likelihood particles corresponding to the marginal distribution of each detected target. The starting and ending position of targets are indicated by cross and star shaped markers, respectively. Target 6 entered the FOV after the first target has disappeared, and it is detected and tracked with a track identity as Target 1. This is indicated by the red color particles for Target 1 and Target 6. Figure 5.12 shows the estimated target trajectories and the algorithm is able to track the targets closely with the exception of Target 4 for which there is a latency in detecting that target.

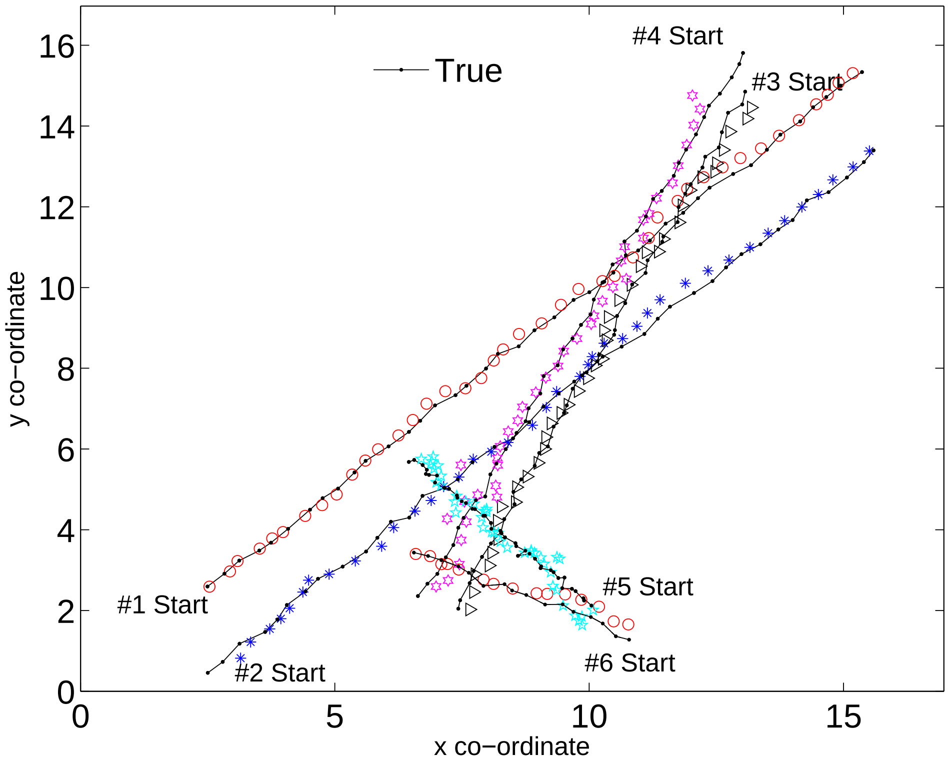

Figure 5.12: True and Estimated Trajectories for Tracking Six Targets Case with $\mathscr{L} = 5$ Targets.

5.4.8 Performance Comparison Between PHDF-TBDF and MM-MT-TBDF-IP-MCMC

In this section, we show the performance of the partitioning method for the 2-D image measurement discussed in Section 4.5.1 to track three targets using the same set of measurement parameters used by the authors in [67] and in Section 4.5.1. In [67], the performance of PHDF-TBDF was compared using a single sensor and multiple sensors and it was showed that the PHDF-TBDF needs measurements from at least 5 sensors for better tracking performance. In our simulation, we showed that we can obtain better results even with a single sensor measurement with our proposed algorithm. Figure 5.13 shows the tracking error (OSPA) with $c = 40$ and $p = 2$ at 19.8 dB, 16.3 dB, 13.8 dB peak SNR after averaging the OSPA from 100 Monte Carlo simulations (same number of Monte Carlo simulations used in [67]).

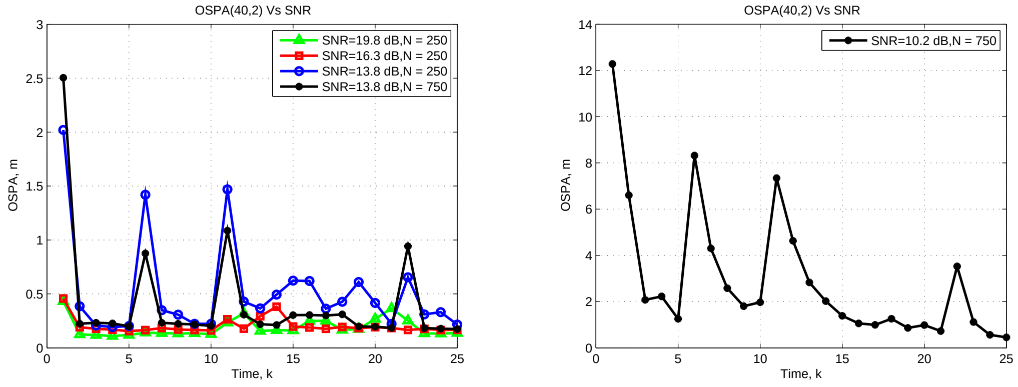

(a) (b)

Figure 5.13: Image Measurement Case: (a) OSPA at Different Peak SNR (19.8 dB, 16.3 dB, 13.8 dB); and (b) OSPA at 10.2 dB Peak SNR.

The tracking error is small at 19.8 dB and 16.3 dB even when using a smaller number of particles. The cardinality error is very small, indicating that the algorithm correctly tracks the number of existing targets without any false detection. The cardinality error at 13.8 dB SNR is slightly high especially around the time when a new target entered the FOV at frames 1, 5 and 11 and when the third target leaves the FOV at frame 21. The localization error from frame 12 to 16 using 250 particles is higher when compared to higher SNR. The localization error decreases when 750 particles are used. Figure 5.13(b) shows the OSPA at 10.2 dB SNR. The tracking error in this case is much higher than the other SNR conditions. It takes more time for the algorithm to detect a target that enters the FOV and a disappearing target. Figure 5.14 shows the corresponding probability of target existence for all three targets indicating the latency involved in detecting the target mode transitions. When the OSPA using our proposed algorithm is compared against the results showed in [67], our algorithm vastly out performs the PHDF-TBDF algorithm using a single sensor. In fact, even with 5 sensors, the PHDF-TBDF filter does not perform as well as our algorithm.

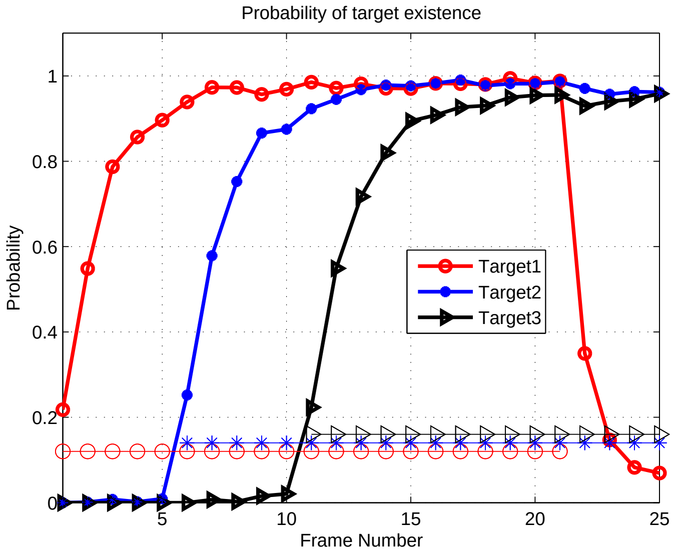

Figure 5.14: Probability of Target Existence.

5.5 Computational Complexity Analysis

5.5.1 Heuristic Decision-directed Approaches

One of the drawbacks of our proposed method is that the number of modes increases exponentially as a function of the maximum number of targets. The IP step greatly reduces the required number of particles. However, some of the computational gains achieved by the IP is offset by the increase in computations required by the MCMC. We thus demonstrate how to greatly reduce the combinatorial complexity of the proposed algorithm using two decision-directed practices based on the estimated mode and target existence probabilities.

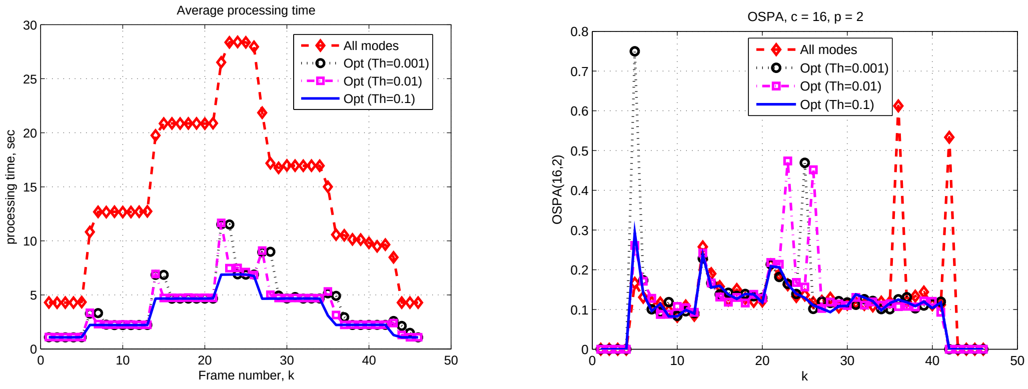

(a) (b)

Figure 5.15: Computational Analysis: (a) Processing Time Difference Between all Modes and Mode Probability Selected Modes; and (b) OSPA Difference Between all Modes and Mode Probability Selected Modes.

For the first practice, if the estimated number of existing targets is less than the assumed maximum number of targets, then there is no need to propagate particles corresponding to all the modes. For example, if at time step k, there is only one target in the FOV, then the computations to propagate the PF to modes that transition from three targets present are not necessary. In order to determine which PF mode propagations are needed, we can compare the mode probability at the previous time step $k-1$ to a threshold. Specifically, if the probability corresponding to mode j at time $k-1$ is very small, then at time k, the PF steps corresponding to $p(\mathbf{x}_k^{[i]}|m_{k-1}=j, m_k=i, \mathbf{Z}_k)$ for all i at time k are not computed. Similarly, if the mode probability for mode i at time k is small, then the PF corresponding to $p(\mathbf{x}_k^{[i]}|m_k=i, \mathbf{Z}_k)$ is not executed at time k. When this practice is followed, the number of particles needed to approximate the posterior PDF of the ℓth target in Equation (4.28) and the mode conditioned joint PDF in Equation (4.27) is much smaller as the particles corresponding to low probability modes are ignored. For the second practice, if the target existence probability at time $k-1$ is very small, then it is not necessary to propagate the continuing particles. As a result, during the implementation of the first layer of PFs, we propagate the continuing particles and corresponding partitions only if the target existence probability estimate at the previous time step is greater than some threshold. As the number of selected modes is dependent on the probability threshold, the processing time also varies as a function of the threshold. In our simulations, we compare the processing time using 0.1%, 1%, and 10% thresholds. Figure 5.15(a) shows the time required to process one time step of data in MATLAB using a 2.5 GHz Intel i5 core processor with and without the two aforementioned practices; the simulation is for tracking $\mathscr{L}=3$ targets at 3 dB peak SNR using 1,000 particles. The initial target parameters used to generate Figure 5.15(a) is used for this analysis. The peak processing time (PPT) is reached when all targets are present. Our simulations showed that when all modes are selected, the PPT is 28 s; 7 s are needed when only the high probability modes are selected. The PPT increases only slightly when the thresholds are reduced. The number of modes with significant mode probability is usually higher during mode transitions. Hence,

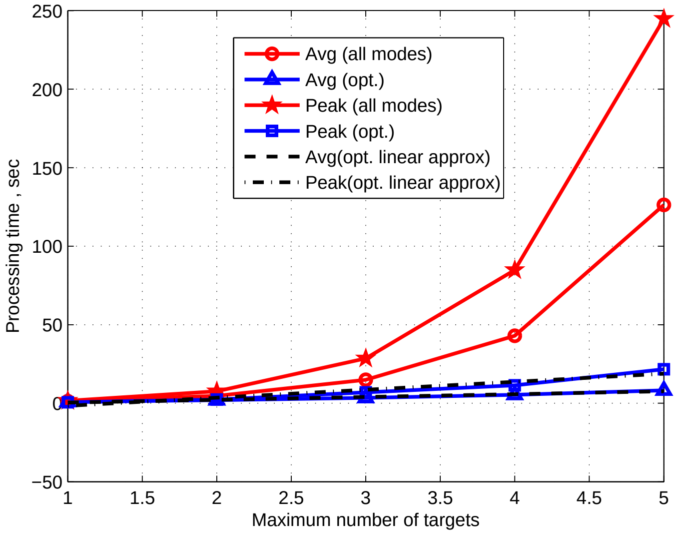

Figure 5.16: Average and Peak Processing Time for Different Maximum Number of Targets.

the processing time is higher around the mode transitions at lower thresholds. Figure 5.15(b) shows the OSPA comparing the different test cases. Although the tracking error is similar for all test cases, the best tracking performance was obtained with a 10% threshold. The increased tracking error for the other cases resulted from the increased cardinality error during mode transitions. This could be due to the noisy measurements preventing occasional false detections of target existence when a higher threshold is used. Overall, the computational cost is reduced with no significant loss in tracking performance when the low probability modes are ignored. Figure 5.16 shows the average and PPT per time step for different maximum number of targets $\mathscr{L}$. As shown, the average and PPT increase almost linearly instead of exponentially as a function of the maximum number of targets, when the practices are applied. Using linear regression, the average and PPT for 1,000 particles with a 10% threshold can be linearly approximated by $(1.803\mathscr{L} - 1.447)$ s and $(5.11\mathscr{L} - 6.765)$ s, respectively.

5.5.2 Effects of Particle Filter Size

Figure 5.17 shows the performance improvement that can be achieved by increasing the number of particles ($N_{j,i}$, N_i and N_ℓ) at 3 dB and -3 dB peak SNR for the three targets case in Figure 5.17(a). The averaged OSPA reaches a steady state error for the 3 dB case at 1,000 particles, and for the -3 dB case, it reaches the steady state error at around 2,500 particles. It requires more number of particles at -3 dB SNR to achieve a similar tracking error as in the 3 dB case. Figure 5.17(b) shows the corresponding average and PPT per time step for different number of particles and the processing time is similar under both SNR conditions.

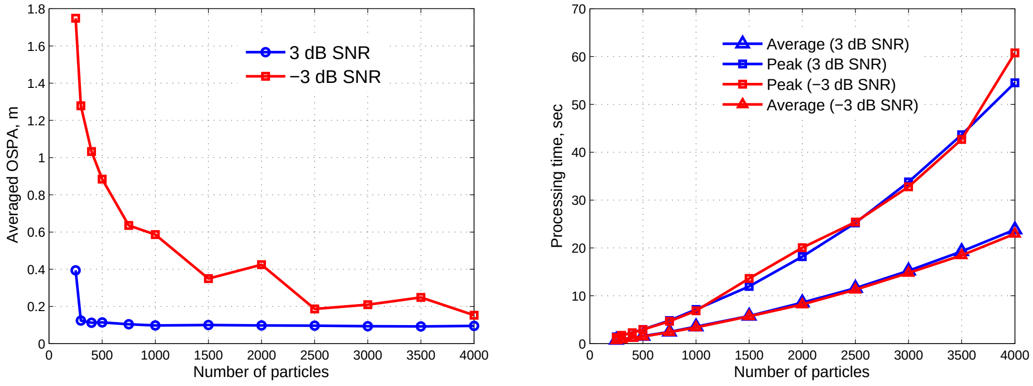

(a)

(b)

Figure 5.17: Effects of Partilce Filter Size for $\mathscr{L} = 3$ Targets: (a) Tracking Error; and (b) Average and Peak Processing Time.

Chapter 6

TRACK-BEFORE-DETECT FILTERING OF MULTIPLE TARGETS IN SEA CLUTTER

6.1 Target Tracking in Sea Clutter

Target detection and tracking in clutter is a challenging problem, especially when the reflected signal characteristics from clutter are similar to target associated signals. In moving target indicator applications, clutter effects can be mitigated using coherent processing by separating the moving target from stationary clutter objects using simple filtering steps in the frequency domain [45]. However, in sea based radars, the radial velocity of clutter is usually high due to the presence of moving waves on the sea surface. The radial velocity of these waves can be significant depending on the sea state that is influenced by various weather and wind conditions [89]. The spiky nature of sea clutter further complicates the target detection and tracking problem. These target like outliers can increase false target detections which in turn affects the computational complexity of conventional detect-before-track algorithms due to combinatorial processing. Hence, accurate modeling of the sea clutter random process is critical for improved tracking performance. The compound Gaussian model [89] is a well established statistical model to characterize the reflected signal associated with sea clutter. The tracking problem becomes more complicated when the radar cross section (RCS) of the target to be tracked is very small. For example, in maritime surveillance applications, it is of critical importance to detect and track a small enemy boat [108]. It was shown in [109] that the signal-to-clutter ratio (SCR) can be improved using real sea clutter by performing principal component analysis (PCA) on the received data and selecting only the principal components that correspond to a few of the lowest singular values. The main assumption in this method is that the clutter level is usually much higher than the target associated signal and that by selecting only the minor components, the target associated components are separated from the clutter. Using this approach, a subspace based sea clutter suppression method was proposed in [110] that improves the detection performance. Despite using accurate statistical models and various signal enhancement techniques, conventional detect-before-track methods still suffer from heavy clutter and low RCS. The tracking problem becomes even more difficult if there is a need to track multiple low observable sea targets. The SMC based track-before-detect filter (TBDF) algorithm for tracking low observable targets can be an attractive alternative as it can be combined with particle filtering (PF) methods [17].

Estimating the clutter statistics from raw measurement is one way to improve the detection and tracking of targets in clutter environments. Since the clutter associated returns evolve over time, the clutter information must be estimated directly from the measurements [111]. Most of the methods rely on estimating the clutter statistics from the neighbourhood bins of a range-Doppler bin under consideration. Three well-known clutter estimation methods relating to a constant false alarm rate (CFAR) were compared in [112]: cell averaging, cell averaging greatest of, and order statistics. It was shown that the OS method is more susceptible to the effects of spiky sea clutter whereas the CA method is the most robust among the three methods. In [113], the clutter point spatial density in non-homogeneous clutter background was estimated using maximum likelihood (ML) and approximated Bayesian methods. The intensity function of this non-homogeneous Poisson point process was approximated by a Gaussian mixture model and then integrated into the probability hypothesis density filter (PHDF). Moreover, the clutter spatial density was estimated over the entire field of view (FOV) and the tracker output was used to enhance the estimate of clutter spatial density. A PF based ML method was used to estimate the clutter parameters [114, 115]. In [116, 117], any non-homogeneous clutter spatial density was modeled as a Gaussian mixture. The approximated Bayesian estimate of the intensity function was updated iteratively using the normal-Wishart mixture PHDF. This clutter intensity function estimate was integrated with joint integrated probabilistic data association or multiple hypothesis testing algorithms to track multiple targets. In this method, the clutter spatial density estimation problem was converted into a clutter generator estimation problem solved using the PHDF. The likelihood function of the clutter generator was assumed to be Gaussian with unknown mean and covariance, and the clutter generator PHDF was derived using a mixture of normal-Wishart probability density function (PDF). A closed form expression for the clutter generator PHDF was also derived.

A recursive TBDF was proposed in [118] for estimating clutter statistics as a part of the likelihood evaluation step. Specifically, the clutter level was estimated by averaging over a set of nearby bins not affected by a target. Guard bins around the target state were used to estimate the clutter variance, and a grid based numerical evaluation was used to compute the likelihood ratio for Rayleigh distributed clutter. A multi-scale adaptive single target TBDF method using the beamlet transform was proposed in [119] for maritime environments. In this method, the longest chained beamlet path whose length was greater than a threshold was detected as a potential target. In [120], a Viterbi-like multi scan TBDF algorithm was proposed in complex Gaussian clutter using space-time processing and the algorithm's detection performance was analyzed.

Very few multiple target TBDF methods in spiky sea clutter environments have been considered thus far in the literature. In this chapter, we extend our proposed multiple mode multiple target TBDF (MM-MT-TBDF) algorithm [76, 81] for complex Gaussian (low resolution radar) and compound Gaussian (high resolution, low grazing radar) sea clutter using pulse Doppler radar measurements. The likelihood functions needed for the TBDF approach can be computed using classical techniques, thereby exploiting some of the optimal methods that have already been derived through rigorous mathematical steps. For the compound Gaussian model, the texture component is assumed to follow a known distribution function [121, 122]. In this case, the optimal generalized likelihood function is not mathematically tractable. Hence, various sub-optimal but asymptotic detectors have been proposed in the literature [85, 123, 124]. In [110], instead of a known *a priori* distribution assumption, the texture component is assumed to be deterministic. Based on this assumption, we derive an optimal likelihood function and the ML estimation of the texture component and the speckle covariance matrix which can be implemented using a fixed point algorithm [83, 84]. We also investigate the relationship between this optimal and the sub-optimal likelihood function in [85].

6.2 Measurement from Pulse Doppler Radar with Clutter

A pulse Doppler radar transmits a series of pulses with a pulse repetition interval T_{PRI}. To increase the radar range resolution, these pulses are modulated by higher bandwidth (f_s) signals such as frequency modulated chirps [45]. The modulated baseband signal is further modulated by the carrier frequency f_c before emitting from the transmitting antenna. The transmitted signal is reflected by many scatterers that are present in the FOV of the radar. The received complex baseband signal after carrier demodulation is typically sampled at the frequency equal to the bandwidth (f_s) of the baseband modulating signal and these samples are referred as fast time samples. The Doppler processing is performed through spectral analysis of the samples obtained by sampling the received signal at the rate of $1/T_{\text{PRI}}$. The samples used for the spectral analysis are referred as slow time samples. The period during which the measurements from a set of pulses used for Doppler analysis is referred as dwell.

We consider measurements from a pulse Doppler radar that is operating at a pulse repetition interval T_{PRI} and transmitting N_p pulses per dwell in the presence of fast-varying clutter. Each dwell is assumed to transmit the same pulse $s[n] = s[n/f_s]$, $n = 0, 1, \ldots N_s - 1$ where N_s is the number of samples and f_s is the sampling frequency. The received signal consists of reflections from multiple targets from all the dwell pulses, in addition to clutter due to multiple undesirable reflections from scatterers. It is assumed that the number of scatterers and their Doppler frequency remain the same during the transmission of all N_p pulses in the same dwell. Assuming that measurements are received from a preset direction of arrival (DOA), an $(N_v \times N_p)$ measurement matrix corresponding to the received signal from all N_p pulses at the kth dwell can be written as

$$\mathbf{Y}_k = \mathbf{S}(\mathbf{T}_k + \mathbf{A}_k) + \mathbf{W}_k \tag{6.1}$$

where $\mathbf{W}_k$ is the $(N_v \times N_p)$ uncorrelated measurement noise matrix, and $N_v = \zeta_{N_v} - \zeta_1 + 1$ is the number of range bins in the validation gate (i.e., the region of measurement selection for track updates) where ζ_i is the ith range bin in the validation gate. In this linear model, the overall clutter scatterer contribution at the kth dwell is generalized by the $(N_r \times N_p)$ reflectivity matrix $\mathbf{A}_k$ as

$$\mathbf{A}_k = \begin{bmatrix} a_k[\zeta_1, 0] & a_k[\zeta_1, 1] & \ldots & a_k[\zeta_1, N_p - 1] \\ a_k[\zeta_2, 0] & a_k[\zeta_2, 1] & \ldots & a_k[\zeta_2, N_p - 1] \\ \vdots & \vdots & \vdots & \vdots \\ a_k[\zeta_{N_r}, 0] & a_k[\zeta_{N_r}, 1] & \ldots & a_k[\zeta_{N_r}, N_p - 1] \end{bmatrix} \tag{6.2}$$

where $N_r = N_v + N_s - 1$, and the matrix elements $a_k[\zeta_i, p]$, containing both reflectivity and Doppler shift are defined as

$$a_k[\zeta_i, p] = \xi_k[\zeta_i, p] e^{j2\pi\nu_{\zeta_i} p T_{\mathrm{PRI}}}. \tag{6.3}$$

where $\xi_k[\zeta_i, p]$ is the clutter reflectivity, ν_{ζ_i} is the Doppler shift at range bin ζ_i, and $p = 0, 1, \ldots N_p - 1$. Similarly, the reflectivity matrix $\mathbf{T}_k$ for multiple targets can be written as a sparse matrix with non-zero complex reflectivity value in those range bins where a point target is present at the kth dwell. The range bin number corresponding to the range of the ℓth target at the kth dwell is represented as $\zeta_{k,\ell}$, where we also include the dwell index k to indicate that the range bin corresponding to the ℓth target varies with time. The range of the ℓth target and the corresponding range bin $\zeta_{k,\ell}$ are related as [45, 47]

$$\zeta_{k,\ell} = \mathrm{round}\left(\frac{2r_{k,\ell}}{c} f_s\right) \tag{6.4}$$

where c is the velocity of propagation, and $r_{k,\ell}$ is the range of the ℓth target. The target reflectivity and the Doppler shift for the ℓth target is represented as $I_{k,\ell}$ and $\nu_{k,\ell}$, respectively, where we assume that the target reflectivity is constant across all N_p pulses. As in Equation (7.2), the range-rate information of a target is absorbed in the complex reflectivity. The reflected signal from a target is modulated across N_p pulses by a slowly varying signal with the Doppler frequency $\nu_{k,\ell}$. Under narrowband conditions, the Doppler frequency and the target range-rate $\dot{r}_{k,\ell}$ are related as [45, 47],

$$\nu_{k,\ell} = \frac{2\dot{r}_{k,\ell}}{c} f_c \tag{6.5}$$

where f_c Hz is the carrier frequency. A circulant $(N_v \times N_r)$ signal matrix $\mathbf{S}$ is constructed from the transmitted signal $s[n]$ as

$$\mathbf{S} = \begin{bmatrix} s[N_s-1] & 0 & \dots & s[0] & 0 & \dots & 0 & 0 \\ 0 & s[N_s-1] & \dots & s[1] & s[0] & 0 & \dots & 0 \\ \vdots & \vdots & \vdots & \vdots & \vdots & \vdots & \vdots & \vdots \\ 0 & 0 & \dots & 0 & s[N_s-1] & \dots & s[1] & s[0] \end{bmatrix}. \tag{6.6}$$

Here we assume that the same baseband signal $s[n]$ is used to transmit at all dwell instances. The measurements at the kth dwell are vectorized to form the $(N_v N_p \times 1)$ vector

$$\mathbf{z}_k = \mathrm{vec}(\mathbf{Y}_k)$$

where $\mathrm{vec}(\mathbf{Y}_k)$ forms the $(N_v N_p \times 1)$ vector formed by concatenating the columns of $\mathbf{Y}_k$ and $\mathbf{Z}_k = \{\mathbf{z}_1, \mathbf{z}_2, \dots, \mathbf{z}_k\}$ represents all the measurements up to dwell k.

In order to consider the contribution of the ℓth target present in the range bin $\zeta_{k,\ell}$, the measurement vector extracted from the $\zeta_{k,\ell}$th row vector of $\mathbf{Y}_k$ in Equation (6.1) can be written as

$$\mathbf{z}_k[\zeta_{k,\ell}] = \sum_{j=1}^{\mathscr{L}_i} b_{j,\ell} \mathbf{s}[\nu_{k,j}] + \mathbf{c}_k^{\mathtt{T}}[\zeta_{k,\ell}] \tag{6.7}$$

where $\mathbf{c}_k[\zeta_{k,\ell}]$ is the clutter measurement vector corresponding to the $\zeta_{k,\ell}$th row of matrix $\mathbf{SA}_k$ in Equation (6.1). In order to jointly detect the existence of closely spaced multiple targets, the reflectivity contribution from all targets to the range bin $\zeta_{k,\ell}$ should be considered. Here we assume that $\mathscr{L}_i$ targets are present in the preset DOA. The summation term in the model in Equation (6.7) represents the signal level contribution to the range bin $\zeta_{k,\ell}$ from all targets that are present in the neighbouring range bins, and it is the vector corresponding to the $\zeta_{k,\ell}$th row of matrix

$\mathbf{ST}_k$ in Equation (6.1). The scale factor $b_{j,\ell}$ is the reflectivity contribution of the jth target to the range bin $\zeta_{k,\ell}$, $j=1,\ldots\mathscr{L}_i$. The reflectivity contribution $b_{j,\ell}$ from the jth target is a function of its reflectivity $I_{k,j}$, and it depends on the correlation properties of the signal $s[n]$. Specifically, the contribution from the ℓth target to the range bin $\zeta_{k,\ell}$ is $b_{\ell,\ell} = I_{k,\ell}$, and if the jth target is far away from the ℓth target, then $b_{j,\ell} = 0$. The Doppler frequency corresponding to all targets are denoted as $\nu_{k,j}$ and

$$\mathbf{s}[\nu_{k,j}] = [1 \; e^{-j2\pi\nu_{k,j}T_{\mathrm{PRI}}} \ldots e^{-j2\pi\nu_{k,j}(N_p-1)T_{\mathrm{PRI}}}]^{\mathtt{T}}.$$

Equation (6.7) can be written in matrix form as

$$\mathbf{z}_k[\zeta_{k,\ell}] \; = \tilde{\mathbf{S}}_\ell \mathbf{b}_\ell + \mathbf{c}_{k,l}[\zeta_{k,\ell}], \tag{6.8}$$

where $\tilde{\mathbf{S}}_\ell$ is the $(N_p \times \mathscr{L}_i)$ matrix

$$\tilde{\mathbf{S}}_\ell = \begin{bmatrix} \mathbf{s}[\nu_{k,1}] & \ldots & \mathbf{s}[\nu_{k,\mathscr{L}_i}] \end{bmatrix}$$

and the $(\mathscr{L}_i \times 1)$ vector $\mathbf{b}_\ell$ is given by

$$\mathbf{b}_\ell = \begin{bmatrix} b_{1,\ell} & \ldots & b_{\mathscr{L}_i,\ell} \end{bmatrix}^{\mathtt{T}}.$$

6.3 Compound Gaussian Clutter Model

6.3.1 Factors Affecting Statistical Sea Clutter Modeling

Different statistical models for clutter have been considered based on analyzing data from real-life radar measurements. For example, in a typical data association based target tracking application, the number of clutters that are being detected inside the validation gate are usually assumed to be Poisson distributed [20]. The clutter density is often assumed to be known *a priori*. If no *a priori* information is available regarding the spatial density of the clutter, then it is commonly assumed to be uniformly distributed in the FOV. In target detection problems, the clutter model parameters of a selected probability density function [99], [125–128] are implicitly estimated from measurements [129] and then used in the generalized likelihood ratio test (GLRT) [46]. Based on this GLRT, a CFAR detector can be designed [45, 47, 130]. The detector performance is usually very sensitive to the type of statistical clutter model selected for a particular application and therefore new techniques are being developed to examine the validity of the chosen model using real-life clutter measurements [131].

The backscatter signal level in a radar application can vary substantially based on the grazing angle, thus directly affecting the underlying statistical model for the received backscatter. For example, the backscatter level from sea clutter at higher grazing angles is very high when compared to the level at lower grazing angles. The clutter level difference between high and low grazing angles can vary by many tens of dB. The backscattering in a low grazing angle radar is influenced by multiple path reflections around the crests of sea waves. The multiple path reflections together with the shadowing of wave trough can result in constructive and destructive cancellation [47]. Different long tailed distributions have been suggested [89, 126–128, 132, 133] to model this random phenomenon for a low grazing angle radar. Subsequent experimental studies have found real data to be consistent with many of these distributions [100, 134–138].

Another factor that affects the clutter statistics is the radar resolution. In a low resolution radar, the cross sectional area corresponding to a single range bin is high. The backscattered signal is a result of multiple reflections from many physical objects that are present in this large area. The reflected signal from a large number of such independent and randomly located scatterers is usually modeled as complex Gaussian. The corresponding distributions in magnitude and magnitude squared form are Rayleigh and exponential distributions, respectively. For low-resolution radars, complex Gaussian is an appropriate approximations since the combined reflections from many independent clutters in a low resolution range bin can be approximated by the complex Gaussian distribution following the central limit theorem [92]. In high resolution radars, the cross section area of a range bin under illumination is small, therefore, the backscatter signals will exhibit spiky structures which can no longer be approximated by complex Gaussian. This behaviour is more prominent in sea clutters in which reflections from gravity waves and sea swells [89] can give rise to spiky reflected signals that can be modeled using long tailed distributions. In [139] many of the long tailed distributions were shown to provide a good fit to real data from a high resolution radar in the Ka-band and in a sea clutter environment.

In this section, we use the complex Gaussian clutter model for a low resolution radar and the compound Gaussian sea clutter model for a high resolution, low grazing angle radar. These clutter models are incorporated into our MM-MT-TBDF algorithm and the tracking performance under different SCR values is analyzed.

6.3.2 Speckle and Texture Sea Clutter Components

Clutter from a high resolution, low grazing angle radar has been characterized by various long tailed probabilistic models such as compound Gaussian [140], K-distribution [89, 128, 133], compound K-distribution [141], log-normal [126], Weibull [127, 142], non central gamma distribution [143], chi-square [130], and generalized compound [144] distributions. Recently, the Pareto distribution has also been proposed for a high resolution radar with both high [145], [146] and low grazing angles [147]. In our work, we adopted the compound Gaussian distribution to model sea clutter, and using some simple and reasonable assumptions, we present a framework for MM-MT-TBDF in sea clutter.

In the compound Gaussian model, clutter from sea surface is characterized by two components, namely speckle and texture. The speckle component is due to rapidly fluctuating, small scale structures with smaller decorrelation time, and it is modeled using a complex Gaussian distribution. The speckle component is due to the presence of multiple scatterers and it decorrelates through the relative motion of the small structures. Recently, the validity of the complex Gaussian assumption for the speckle component was corroborated using real radar data from the Ka-band, even for range resolution in the order of few centimeters [139]. The texture component is a slowly varying large scale structure that modulates the speckle component. The texture component has a longer correlation time, and it is associated with the long sea waves and swell structure. The texture component is usually modeled using either the gamma distribution [89] or inverse gamma distribution [121]. Using these two components, clutter at the kth dwell can be modeled using the compound Gaussian model as

$$c_k[\zeta_i, p] = \sqrt{\tau_k[\zeta_i, p]_k}\, u_k[\zeta_i, p]$$

where $\tau_k[\zeta_i, p] \geq 0$ represents the texture component that modulates the speckle component $u[\zeta_i, p]$ corresponding to the pth pulse at range bin ζ_i. When the texture is modeled as a gamma distribution, then the compound Gaussian model is the well known K-distribution. The clutter from all pulses in the kth dwell is represented as

$$\boldsymbol{c}_k[\zeta_i] = \left[\sqrt{\tau_k[\zeta_i, 0]} u_k[\zeta_i, 0], \ldots \quad \ldots \quad \sqrt{\tau_k[\zeta_i, N_p - 1]} u_k[\zeta_i, N_p - 1]\right]^{\mathtt{T}}.$$

In general, the texture component within a dwell is also assumed to be randomly distributed. However, if we choose the dwell duration to be very small, we could assume that the texture component is the same for all pulses in a dwell [110]. This is a reasonable assumption due to the slow varying nature of the texture component.

During this very short dwell duration, the delays corresponding to the scatterers and their Doppler shifts in the signal model in Equation (6.1) are assumed constant. The clutter vector can now be written as

$$\boldsymbol{c}_k[\zeta_i] = \sqrt{\tau_k[\zeta_i]} \;\; [u_k[\zeta_i, 0] \;\; u_k[\zeta_i, 1] \;\; \ldots \;\; u_k[\zeta_i, N_p - 1]]^{\mathsf{T}} . \tag{6.9}$$

The speckle component is assumed to vary from pulse to pulse since minor perturbations in the same scale sea structures can change the overall effect of multiple path reflections. The clutter covariance matrix is given by $\tau_k[\zeta_i]\boldsymbol{\Sigma}$, where $\boldsymbol{\Sigma}$ is the $(N_p \times N_p)$ complex covariance matrix of the speckle component that is assumed to be the same for all range bins. Since the dwell duration is assumed small, the speckle decorrelation time is greater than the pulse interval duration and therefore, the speckle covariance matrix is assumed to be a non-identity matrix.

6.3.3 Doppler Model for Sea Clutter

The sea surface consists of many complex but significant structures. The small ripples on the sea surface are generated by blowing winds and these transfer the energy to longer waves. When the wind is blowing at a constant speed, then these sea waves reach an equilibrium condition [89] and are modulated by sea swells from neighborhood regions that are stimulated by turbulent weather conditions. Clutter from local wind driven ripples is usually modeled as Bragg's scattering [47]. The radial velocity of these ripple waves is usually low. The radial velocity associated with the modulating sea swells is usually higher than that of the Bragg's scattering. Many empirical studies have shown that the averaged Doppler spectrum of sea clutter can be modeled by a combination of fast non-Bragg scattering associated with the sea swells and a slow Bragg's scattering that is associated with the smaller capillary waves [138, 148, 149]. The relation between the mean value of the backscatter signal and the mean Doppler shift were investigated in [88, 150]. A linear approximation model that relates the texture component and the Doppler frequency was used in [87] to model the Doppler spectra. We used this model to generate complex clutter measurements with Doppler information as follows.

- We randomly generate a Doppler frequency corresponding to Bragg's scattering that is assumed to have a Gaussian distribution whose mean μ_{Bragg} corresponds to a lower frequency and its variance σ^2_{Bragg} is set to a fixed pre-determined value.

- We generate the Doppler frequency corresponding to sea swell by randomly sampling from a Gaussian distribution whose mean frequency $\mu_k^{swell}[\zeta_i] = A_{swell} + B_{swell}\tau_k[\zeta_i]$ is linearly related to the texture component value, where A_{swell} and B_{swell} are model parameters. The variance of the Gaussian distribution σ^2_{swell} is selected from another Gaussian distribution with preset mean and variance [87, 88].

- The Doppler frequency corresponding to a dwell in Equation (7.2) is randomly selected between a Bragg's scattering frequency or a swell frequency such that the averaged Doppler spectra over a large number of dwells consists of two main Doppler components similar to the one fitted from real data in [138, 148, 149].

6.4 Likelihood Function in Complex Gaussian Clutter

In most radars operating in a heavily cluttered environment, the clutter strength is much higher than that of the measurement noise. Thus, for simplicity, we use the likelihood function derived assuming that only clutter is present. A similar derivation can be extended to include noise following the principles mentioned in [125, 151]. The target presence condition in a range bin can be formulated as a binary hypothesis problem. From Equation (6.8), we consider the measurement $\mathbf{z}_k[\zeta_{k,\ell}]$ corresponding to range bin $\zeta_{k,\ell}$ from all N_p pulses in dwell k. Using this measurement, the two hypothesis are given by

$$\begin{aligned} H_0 : \quad & \mathbf{z}_k[\zeta_{k,\ell}] = \mathbf{c}_k^{\mathtt{T}}[\zeta_{k,\ell}] \\ H_1 : \quad & \mathbf{z}_k[\zeta_{k,\ell}] = \tilde{\mathbf{S}}_\ell \mathbf{b}_\ell + \mathbf{c}_k^{\mathtt{T}}[\zeta_{k,\ell}] \end{aligned} \, . \tag{6.10}$$

Without loss of generality, we replace the measurement vector $\mathbf{z}_k[\zeta_{k,\ell}]$ with $\mathbf{z}_{k,\ell}$ to simplify notation. In this section, we explain only about the likelihood function in mode i and recall $\mathscr{L}_i$ is the number of targets in mode i. Based on the binary hypothesis model in Equation (6.10) and the complex Gaussian assumption, we can write the generalized likelihood ratio for a range bin corresponding to the state vector $\mathbf{x}_{k,\ell}^{[i]}$ in mode i as [152]

$$L(\mathbf{z}_k | \mathbf{x}_{k,\ell}^{[i]}) = \mathbf{L}_0 / \mathbf{L}_1, \tag{6.11}$$

where

$$\mathbf{L}_0 = N_T + \mathbf{z}_{k,\ell}^{\mathtt{H}} \hat{\boldsymbol{\Sigma}}^{-1} \mathbf{z}_{k,\ell} \, ,$$

$$\mathbf{L}_1 = N_T + (\mathbf{z}_{k,\ell} - \tilde{\mathbf{S}}_\ell \mathbf{b}_\ell)^{\mathtt{H}} \hat{\boldsymbol{\Sigma}}^{-1} (\mathbf{z}_{k,\ell} - \tilde{\mathbf{S}}_\ell \mathbf{b}_\ell) \, .$$

Here, $\mathtt{H}$ represents conjugate transpose, $\hat{\boldsymbol{\Sigma}}$ is the ML sample covariance estimate of the complex covariance matrix of the clutter statistics that is obtained using $N_T > N_p$ secondary range bins [152]. Specifically, the sample covariance matrix estimate is given by

$$\hat{\boldsymbol{\Sigma}} = \frac{1}{N_T} \sum_{n=1}^{N_T} \mathbf{z}_k[n] \mathbf{z}_k[n]^{\mathtt{H}}. \tag{6.12}$$

where $\mathbf{z}_k[1], \ldots, \mathbf{z}_k[N_T]$ are the secondary range bins in the vicinity of the range bin under testing. The likelihood ratio in (6.11) depends on the reflectivity of multiple targets. The explicit estimation of the target reflectivity can be avoided by substituting the analytical solution of $\mathbf{b}_\ell$ that maximizes the likelihood function in (6.11). The likelihood function is maximized when the quadratic quantity in $\mathbf{L}_1$ is minimized. For a positive definite matrix $\hat{\Sigma}$, the weighted least squares solution of $\mathbf{b}_\ell$ that minimizes the quadratic term is given by

$$\mathbf{b}_\ell^{(LS)} = (\tilde{\mathbf{S}}_\ell^{\mathtt{H}} \hat{\boldsymbol{\Sigma}}^{-1} \tilde{\mathbf{S}}_\ell)^{-1} (\tilde{\mathbf{S}}_\ell^{\mathtt{H}} \hat{\boldsymbol{\Sigma}}^{-1} \mathbf{z}_{k,\ell}).$$

Substituting $\mathbf{b}_\ell^{(LS)}$ in $\mathbf{L}_1$ we obtain

$$\mathbf{L}_1 = N_T + \mathbf{z}_{k,\ell}^{\mathtt{H}} \hat{\boldsymbol{\Sigma}}^{-1} \mathbf{z}_{k,\ell} - (\mathbf{z}_{k,\ell}^{\mathtt{H}} \hat{\boldsymbol{\Sigma}}^{-1} \tilde{\mathbf{S}}_\ell) \mathbf{b}_\ell^{(LS)}.$$

Upon further simplification, the generalized likelihood function can now be derived as

$$L(\mathbf{z}_k | \mathbf{x}_{k,\ell}^{[i]}) = \frac{1}{1 - \eta_{\mathrm{G}}(\mathbf{z}_k | \mathbf{x}_{k,\ell}^{[i]})} \,,$$

where

$$\eta_{\mathrm{G}}(\mathbf{z}_k | \mathbf{x}_{k,\ell}^{[i]}) = \frac{(\mathbf{z}_{k,\ell} \hat{\boldsymbol{\Sigma}}^{-1} \tilde{\mathbf{S}}_\ell^{\mathtt{H}})(\tilde{\mathbf{S}}_\ell^{\mathtt{H}} \hat{\boldsymbol{\Sigma}}^{-1} \tilde{\mathbf{S}}_\ell)^{-1} (\tilde{\mathbf{S}}_\ell^{\mathtt{H}} \hat{\boldsymbol{\Sigma}}^{-1} \mathbf{z}_{k,\ell})}{(N_T + \mathbf{z}_{k,\ell}^{\mathtt{H}} \hat{\boldsymbol{\Sigma}}^{-1} \mathbf{z}_{k,\ell})}. \tag{6.13}$$

Thus, the contribution of targets present in the neighbourhood range bins are also considered in the generalized likelihood function derivation. The likelihood value tends to infinity if a target exists in the selected range bin; otherwise it tends to zero [152]. Since we use the generalized likelihood function, there is no need to estimate the signal intensities $I_{k,\ell}$. The dimension of the matrix $\tilde{\mathbf{S}}_\ell$ in mode i depends on the number of assumed targets in that mode, and the predicted Doppler frequencies of the corresponding targets are used to construct the columns of this matrix. If the targets are moving farther apart such that the reflected signals from other targets do not contribute to the range bin corresponding to the ℓth target, i.e., $\tilde{\mathbf{S}}_\ell = \mathbf{s}[\nu_{k,\ell}]$, then the test statistic can be further simplified as

$$\eta_{\mathrm{G}}(\mathbf{z}_k | \mathbf{x}_{k,\ell}^{[i]}) = \frac{\left| \mathbf{s}[\nu_{k,\ell}]^{\mathtt{H}} \hat{\boldsymbol{\Sigma}}^{-1} \mathbf{z}_{k,\ell} \right|^2}{\mathbf{s}[\nu_{k,\ell}]^{\mathtt{H}} \ \hat{\boldsymbol{\Sigma}}^{-1} \ \mathbf{s}[\nu_{k,\ell}] \ \left[N_T + \mathbf{z}_{k,\ell}^{\mathtt{H}} \ \hat{\boldsymbol{\Sigma}}^{-1} \ \mathbf{z}_{k,\ell} \right]} \,. \tag{6.14}$$

This simplified likelihood function is the same expression derived in [152] for detecting a single target.

6.5 Likelihood Function in Compound Gaussian Clutter

In the compound Gaussian case, the binary hypothesis problem in Equation (6.10) is still valid. The additive clutter is assumed to be complex compound Gaussian distributed, and the derivation of the generalized likelihood function is more involved than that of the complex Gaussian case, leading to different detector forms [121, 123, 124, 153–155]. As the clutter covariance matrix is a critical parameter in a GLRT detector, the covariance matrix of compound Gaussian clutter is a research topic under investigation [122, 156–159].

6.5.1 Asymptotic Generalized Likelihood Function

An asymptotically optimum GLRT detector that is independent of the texture PDF was proposed in [124]. The test statistics using this detector for well separated targets can be written as

$$\eta_{\mathrm{LQ}}(\mathbf{z}_k|\mathbf{x}_{k,\ell}^{[i]}) = \frac{\left|\mathbf{s}[\nu_{k,\ell}]^{\mathrm{H}}\mathbf{M}^{-1}\mathbf{z}_{k,\ell}\right|^2}{\left(\mathbf{s}[\nu_{k,\ell}]^{\mathrm{H}}\mathbf{M}^{-1}\mathbf{s}[\nu_{k,\ell}]\right)\left(\mathbf{z}_{k,\ell}^{\mathrm{H}}\mathbf{M}^{-1}\mathbf{z}_{k,\ell}\right)} \tag{6.15}$$

where $\mathbf{M}$ is the clutter covariance matrix in the range bin under test. Note that, in the compound Gaussian model, the clutter power between range bins is not assumed the same, hence the clutter covariance matrix is different between different range bins. This detector is derived based on the linear-quadratic (LQ) detector originally derived for a compound Gaussian clutter with the assumption that the covariance matrix $\mathbf{M}$ is known [85, 86]. This detector is referred to as normalized matched filter (NMF). When we assume that the texture component is constant across the entire dwell, then the test statistic only depends on the structure of the speckle covariance matrix and can then be written as

$$\eta_{\mathrm{LQ}}(\mathbf{z}_k|\mathbf{x}_{k,\ell}^{[i]}) = \frac{\left|\mathbf{s}[\nu_{k,\ell}]^{\mathtt{H}}\boldsymbol{\Sigma}^{-1}\mathbf{z}_{k,\ell}\right|^2}{\left(\mathbf{s}[\nu_{k,\ell}]^{\mathtt{H}}\boldsymbol{\Sigma}^{-1}\mathbf{s}[\nu_{k,\ell}]\right)\left(\mathbf{z}_{k,\ell}^{\mathtt{H}}\boldsymbol{\Sigma}^{-1}\mathbf{z}_{k,\ell}\right)} \tag{6.16}$$

Recall that we assume that the speckle covariance matrix structure is the same for all range bins. When the covariance matrix Σ is substituted by its estimate, the detector is called M-adaptive NMF (M-ANMF) or Σ-adaptive NMF (Σ-ANMF) depending on the covariance matrix estimation method [123, 156]. The M-ANMF sample covariance estimate is given by

$$\hat{\boldsymbol{\Sigma}}_M = \frac{1}{N_T}\sum_{n=1}^{N_T}\mathbf{z}_k[n]\mathbf{z}_k[n]^{\mathtt{H}} \tag{6.17}$$

and the Σ-ANMF sample covariance estimate based on the normalized secondary range bins is given by

$$\hat{\boldsymbol{\Sigma}}_\Sigma = \frac{1}{N_T}\sum_{n=1}^{N_T}\frac{\mathbf{z}_k[n]\mathbf{z}_k[n]^{\mathtt{H}}}{\frac{1}{N_p}\mathbf{z}_k[n]^{\mathtt{H}}\mathbf{z}_k[n]} \tag{6.18}$$

where N_T is the number of secondary range bins. A different estimator for $\boldsymbol{\Sigma}$ was proposed in [156] under the assumption that the clutter power spectral density is symmetric about the zero Doppler frequency. However, this assumption does not generally hold for the averaged Doppler spectrum of real sea clutter as it exhibits an asymmetric pattern around the peak Doppler frequency [89, 138]. In [123], the detector in Equation (6.15) was reformulated by replacing the covariance matrix with its eigen decomposition. The covariance matrix is assumed to be circulant so that the basis function of the discrete Fourier transform (DFT) can be used as the eigenvectors [160]. The normalized sample mean of the DFT coefficients of the measurement vectors from the primary and secondary range bins are approximated as the eigenvalues. In computer simulations, this detector has been shown to perform better than the M-ANMF and Σ-ANMF detectors. However, the circulant matrix assumption is reasonable only when a large number of pulses are used for coherent processing.

6.5.2 Adaptive Generalized Likelihood Function Based on Kelly's Method

In this section, we derive a multiple target generalized likelihood function for compound Gaussian clutter by following Kelly's approach [152]. For the binary hypothesis problem in Equation (6.10), we assume that $\mathbf{z}_{k,\ell}$ represents the measurement for the range bin corresponding to the state vector $\mathbf{x}_{k,\ell}^{[i]}$ in mode i, and we denote $\tau_{k,\ell} \triangleq \tau_k[\zeta_\ell]$ as the texture component in the corresponding range bin where $\mathbf{z}_{k,n}$, $\tau_{k,n}$, $n = 1 \ldots N_T$ are the dwell measurement and texture components, respectively, for N_T neighbourhood range bins. These training measurements are referred to as secondary measurement vectors. The clutter distribution from all these $N_T + 1$ bins are assumed independent and follows a zero mean circularly symmetric complex Gaussian distribution with varying power levels. The total power of the speckle component can be included into the texture component such that the trace of the speckle covariance matrix is N_p. Using the above assumptions, the joint PDF under H_0 hypothesis is given by

$$p(\mathbf{z}_{k,\ell}, \mathbf{z}_{k,1}, \ldots \mathbf{z}_{k,N_T} \big| H_0, \tau_{k,\ell}, \tau_{k,1} \ldots \tau_{k,N_T}) = \mathcal{N}(\mathbf{z}_{k,\ell}; \mathbf{0}, \tau_{k,\ell}\boldsymbol{\Sigma}) \prod_{n=1}^{N_T} \mathcal{N}(\mathbf{z}_{k,n}; \mathbf{0}, \tau_{k,n}\boldsymbol{\Sigma})$$

where $\mathcal{N}(\mathbf{z}_{k,\ell}; \mathbf{0}, \tau_{k,\ell}\boldsymbol{\Sigma})$ implies that $\mathbf{z}_{k,\ell}$ is a Gaussian vector with mean $\mathbf{0}$ and covariance matrix $\tau_{k,\ell}\boldsymbol{\Sigma}$, and $\mathbf{0}$ is a $(N_p \times 1)$ column vector with all elements set to zero. The joint PDF under H_1 hypothesis is given by

$$p(\mathbf{z}_{k,\ell}, \mathbf{z}_{k,1}, \ldots \mathbf{z}_{k,N_T} \big| H_1, \tau_{k,\ell}, \tau_{k,1} \ldots \tau_{k,N_T}) = \mathcal{N}(\mathbf{z}_{k,\ell}; \tilde{\mathbf{S}}_\ell \mathbf{b}_\ell, \tau_{k,\ell}\boldsymbol{\Sigma}) \prod_{n=1}^{N_T} \mathcal{N}(\mathbf{z}_{k,n}; \mathbf{0}, \tau_{k,n}\boldsymbol{\Sigma})$$

where $\tilde{\mathbf{S}}_\ell \mathbf{b}_\ell$ is the target associated reflected signal in Equation (6.10). If the texture component is modeled as a random parameter, it is very difficult to jointly maximize the PDF $p(\mathbf{z}_{k,\ell}, \mathbf{z}_{k,1}, \ldots \mathbf{z}_{k,N_T} \big| H_1)$ under H_1 hypothesis, using Kelly's approach.

Hence, a closed-form solution in this case does not exist [85, 86]. We consider instead the texture component as a time varying deterministic variable as in [110]. Unlike other sub-optimal detectors mentioned in the literature, we can follow Kelly's approach to derive the closed form optimal likelihood function when the compound Gaussian model parameters are known. If the model parameters are unknown, then the ML estimate of the model parameters can also derived that results in a generalized likelihood function. The deterministic texture component assumption can be shown to hold using real data since the texture component varies slowly. We also estimate the time varying texture components for every dwell using the iterative fixed point algorithm which provides the exact maximum likelihood estimate for deterministic $\tau_{k,n}$ [84]. The joint PDFs under both hypothesis can now be written as

$$p(\mathbf{z}_{k,\ell}, \mathbf{z}_{k,1}, \ldots \mathbf{z}_{k,N_T} \big| H_0) = \mathcal{N}(\mathbf{z}_{k,\ell}; \mathbf{0}, \tau_{k,\ell}\boldsymbol{\Sigma}) \prod_{n=1}^{N_T} \mathcal{N}(\mathbf{z}_{k,n}; \mathbf{0}, \tau_{k,n}\boldsymbol{\Sigma}).$$

$$p(\mathbf{z}_{k,\ell}, \mathbf{z}_{k,1}, \ldots \mathbf{z}_{k,N_T} \big| H_1) = \mathcal{N}(\mathbf{z}_{k,\ell}; \tilde{\mathbf{S}}_\ell \mathbf{b}_\ell, \tau_{k,\ell}\boldsymbol{\Sigma}) \prod_{n=1}^{N_T} \mathcal{N}(\mathbf{z}_{k,n}; \mathbf{0}, \tau_{k,n}\boldsymbol{\Sigma})$$

where $\tau_{k,\ell}$ and $\tau_{k,n}$ are deterministic parameters. The PDF under hypothesis H_0 can be expanded as

$$\begin{aligned} p(\mathbf{z}_{k,\ell}, \mathbf{z}_{k,1}, \ldots \mathbf{z}_{k,N_T} \big| H_0) &= \frac{(\pi^{N_p}|\boldsymbol{\Sigma}|)^{-(N_T+1)}}{\tau_{k,\ell}^{N_p} \prod_{n=1}^{N_T} \tau_{k,n}^{N_p}} \exp\left[- \frac{\mathbf{z}_{k,\ell}^{\mathtt{H}} \boldsymbol{\Sigma}^{-1} \mathbf{z}_{k,\ell}}{\tau_{k,\ell}} \right] \\ & \prod_{n=1}^{N_T} \exp\left[- \frac{\mathbf{z}_{k,n}^{\mathtt{H}} \boldsymbol{\Sigma}^{-1} \mathbf{z}_{k,n}}{\tau_{k,n}} \right] \end{aligned}$$

where $|\mathbf{\Sigma}|$ is the determinant of the matrix $\mathbf{\Sigma}$. Using matrix properties, we can simplify the above form as

$$\begin{aligned} p(\mathbf{z}_{k,\ell}, \mathbf{z}_{k,1}, \ldots \mathbf{z}_{k,N_T}\big|H_0) &= \frac{(\pi^{N_p}|\mathbf{\Sigma}|)^{-(N_T+1)}}{\tau_{k,\ell}^{N_p}\prod_{n=1}^{N_T}\tau_{k,n}^{N_p}} \exp\left[-\operatorname{tr}\biggl(\frac{\mathbf{\Sigma}^{-1}\mathbf{z}_{k,\ell}\mathbf{z}_{k,\ell}^{\mathtt{H}}}{\tau_{k,\ell}}\biggr)\right] \\ &\quad \prod_{n=1}^{N_T}\exp\left[-\operatorname{tr}\biggl(\frac{\mathbf{\Sigma}^{-1}\mathbf{z}_{k,n}\mathbf{z}_{k,n}^{\mathtt{H}}}{\tau_{k,n}}\biggr)\right] \\ &= \frac{(\pi^{N_p}|\mathbf{\Sigma}|)^{-(N_T+1)}}{\tau_{k,\ell}^{N_p}\prod_{n=1}^{N_T}\tau_{k,n}^{N_p}} \exp\left[-\operatorname{tr}\biggl(\mathbf{\Sigma}^{-1}\left[\frac{\mathbf{z}_{k,\ell}\mathbf{z}_{k,\ell}^{\mathtt{H}}}{\tau_{k,\ell}} + \frac{\mathbf{z}_{k,1}\mathbf{z}_{k,1}^{\mathtt{H}}}{\tau_{k,1}} \ldots + \frac{\mathbf{z}_{k,N_T}\mathbf{z}_{k,N_T}^{\mathtt{H}}}{\tau_{k,N_T}}\right]\biggr)\right] \end{aligned}$$

where $\operatorname{tr}(\cdot)$ is the trace of a matrix. The above form can be further simplified as

$$p(\mathbf{z}_{k,\ell}, \mathbf{z}_{k,1}, \ldots \mathbf{z}_{k,N_T}\big|H_0) = \left[\frac{(\pi^{N_p}|\mathbf{\Sigma}|)^{-1}}{[\tau_{k,\ell}^{N_p}\prod_{n=1}^{N_T}\tau_{k,n}^{N_p}]^{\frac{1}{(N_T+1)}}} \exp\left[-\operatorname{tr}\bigl(\mathbf{\Sigma}^{-1}\mathbf{T}_0\bigr)\right]\right]^{N_T+1} \tag{6.19}$$

where

$$\mathbf{T}_0 = \frac{1}{N_T+1}\left[\frac{\mathbf{z}_{k,\ell}\mathbf{z}_{k,\ell}^{\mathtt{H}}}{\tau_{k,\ell}} + \sum_{n=1}^{N_T}\frac{\mathbf{z}_{k,n}\mathbf{z}_{k,n}^{\mathtt{H}}}{\tau_{k,n}}\right].$$

Similarly, the joint PDF under the H_1 hypothesis can be written as

$$p(\mathbf{z}_{k,\ell}, \mathbf{z}_{k,1}, \ldots \mathbf{z}_{k,N_T}\big|H_1) = \left[\frac{(\pi^{N_p}|\mathbf{\Sigma}|)^{-1}}{\Bigl(\tau_{k,\ell}^{N_p}\prod_{n=1}^{N_T}\tau_{k,n}^{N_p}\Bigr)^{\left(\frac{1}{N_T+1}\right)}} \exp\left[-\operatorname{tr}\bigl(\mathbf{\Sigma}^{-1}\mathbf{T}_1\bigr)\right]\right]^{N_T+1} \tag{6.20}$$

where

$$\mathbf{T}_1 = \frac{1}{N_T+1}\biggl(\frac{(\mathbf{z}_{k,\ell}-\tilde{\mathbf{S}}_\ell\mathbf{b}_\ell)(\mathbf{z}_{k,\ell}-\tilde{\mathbf{S}}_\ell\mathbf{b}_\ell)^{\mathtt{H}}}{\tau_{k,\ell}} + \sum_{n=1}^{N_T}\frac{\mathbf{z}_{k,n}\mathbf{z}_{k,n}^{\mathtt{H}}}{\tau_{k,n}}\biggr).$$

6.5.3 Maximum Likelihood Estimation of Clutter Statistics

In order to obtain the likelihood function, we first need to estimate the clutter statistics $\mathbf{\Sigma}$ and $\tau_{k,n}$ in Equations (6.19) and (6.20). The ML estimates of these parameters can be obtained by maximizing the joint PDF over these parameters,

$$\hat{\Theta} = \arg\max_{\Theta} p(\mathbf{z}_{k,\ell}, \mathbf{z}_{k,1}, \dots \mathbf{z}_{k,N_T} \big| H_j)$$

where $j = 0$, 1, and $\Theta = \{\mathbf{\Sigma}, \tau_{k,\ell}, \tau_{k,1}, \dots \tau_{k,N_T}\}$.

In order to estimate the speckle covariance matrix, we first assume that the texture components are known and obtain the speckle covariance matrix estimate by maximizing the logarithm of the PDF. By using the following matrix properties

$$\frac{\partial}{\partial \mathbf{\Sigma}} \log(|\mathbf{\Sigma}|) = \mathbf{\Sigma}^{-1},$$

$$\frac{\partial}{\partial \mathbf{\Sigma}} \mathrm{tr}(\mathbf{\Sigma}^{-1}\mathbf{T}_j) = \mathbf{T}_j \mathbf{\Sigma}^{-2},$$

and equating

$$\frac{\partial}{\partial \mathbf{\Sigma}} \log(p(\mathbf{z}_{k,\ell}, \mathbf{z}_{k,1}, \dots \mathbf{z}_{k,N_T} \big| H_j)) = 0$$

, we obtain

$$-\frac{\partial}{\partial \mathbf{\Sigma}} \log(|\mathbf{\Sigma}|) + \frac{\partial}{\partial \mathbf{\Sigma}} \mathrm{tr}(\mathbf{\Sigma}^{-1}\mathbf{T}_j) = 0$$

$$\hat{\mathbf{\Sigma}} = \mathbf{T}_j$$

Under the H_1 hypothesis, the target reflectivity information is not available; we can instead use only the secondary range bins to estimate the covariance matrix

$$\hat{\mathbf{\Sigma}} = \frac{1}{N_T} \sum_{n=1}^{N_T} \frac{\mathbf{z}_{k,n}\mathbf{z}_{k,n}^{\mathtt{H}}}{\tau_{k,n}}. \tag{6.21}$$

If the clutter covariance matrix is known, then the ML estimate of the texture components can be obtained by equating $\partial \log\{p(\mathbf{z}_{k,1}, \dots \mathbf{z}_{k,N_T} \big| H_0)\}/\partial \tau_{k,n} = 0$. The ML estimate for $n = 1, \dots N_T$ is then given by

$$\frac{\partial}{\partial \tau[i]} \log\left(p(\mathbf{z}_{k,1}, \dots \mathbf{z}_{k,N_T} \big| H_0)\right) = -\frac{N_p}{\tau_{k,n}} + \frac{\mathrm{tr}(\mathbf{\Sigma}^{-1}\mathbf{z}_{k,n}^{\mathtt{H}}\mathbf{z}_{k,n})}{\tau_{k,n}^2} = 0$$

$$\hat{\tau}_{k,n} = \frac{\mathrm{tr}(\boldsymbol{\Sigma}^{-1}\mathbf{z}_{k,n}\mathbf{z}_{k,n}^{\mathtt{H}})}{N_p} \tag{6.22}$$

The texture for the range bin under test $\hat{\tau}_{k,\ell}$ cannot be estimated without knowing the target reflectivity. Instead, we can use the estimated texture from one of the past frames as it changes slowly.

6.5.4 Calculation of Generalized Likelihood Ratio

Using Equations (6.19) and (6.20) and substituting the ML estimate of the speckle covariance matrix in Equation (6.21) for $\boldsymbol{\Sigma}$, the $(N_T + 1)$th root generalized likelihood ratio as a function of the unknown multiple targets reflectivity and texture component can now be written as

$$L(\tau_{k,\ell}, \tau_{k,n}, \mathbf{b}_\ell) = \frac{|\mathbf{T}_0|}{|\mathbf{T}_1|}.$$

Since the generalized likelihood ratio is still dependent on the unknown multiple targets reflectivity, this ratio can be further modified by minimizing the denominator as a function of $\mathbf{b}_\ell$. We first define a new matrix $\boldsymbol{\Psi}$ as

$$\boldsymbol{\Psi} = \sum_{n=1}^{N_T} \frac{\mathbf{z}_{k,n}\mathbf{z}_{k,n}^{\mathtt{H}}}{\tau_{k,n}}. \tag{6.23}$$

Using the determinant lemma, we can write,

$$|\mathbf{T}_0| = \frac{|\boldsymbol{\Psi}|}{(N_T + 1)^{N_p}} \left(1 + \frac{\mathbf{z}_{k,\ell}^{\mathtt{H}}\boldsymbol{\Psi}^{-1}\mathbf{z}_{k,\ell}}{\tau_{k,\ell}}\right),$$

$$|\mathbf{T}_1| = \frac{|\boldsymbol{\Psi}|}{(N_T + 1)^{N_p}} \left(1 + \frac{(\mathbf{z}_{k,\ell} - \tilde{\mathbf{S}}_\ell\mathbf{b}_\ell)^{\mathtt{H}}\boldsymbol{\Psi}^{-1}(\mathbf{z}_{k,\ell} - \tilde{\mathbf{S}}_\ell\mathbf{b}_\ell)}{\tau_{k,\ell}}\right).$$

Substituting the above two equations in the likelihood function, we obtain

$$L(\tau_{k,\ell}, \mathbf{b}_\ell) = \frac{\tau_{k,\ell} + \mathbf{z}_{k,\ell}^{\mathtt{H}}\boldsymbol{\Psi}^{-1}\mathbf{z}_{k,\ell}}{\tau_{k,\ell} + (\mathbf{z}_{k,\ell} - \tilde{\mathbf{S}}_\ell\mathbf{b}_\ell)^{\mathtt{H}}\boldsymbol{\Psi}^{-1}(\mathbf{z}_{k,\ell} - \tilde{\mathbf{S}}_\ell\mathbf{b}_\ell)}. \tag{6.24}$$

The above likelihood function is maximized when the denominator is minimized. The denominator is minimized when the quadratic term is minimized. The value of $\mathbf{b}_\ell$ that minimizes the quadratic term is the solution to the weighted least squares problem,

$$\tilde{\mathbf{S}}_\ell \mathbf{b}_\ell = \mathbf{z}_{k,\ell},$$

and the error vector is weighted by the positive definite weighting matrix $\mathbf{\Psi}^{-1}$. The weighted least squares solution is given by

$$\mathbf{b}_\ell^{(LS)} = (\tilde{\mathbf{S}}_\ell^{\mathtt{H}} \mathbf{\Psi}^{-1} \tilde{\mathbf{S}}_\ell)^{-1} (\tilde{\mathbf{S}}_\ell^{\mathtt{H}} \mathbf{\Psi}^{-1} \mathbf{z}_{k,\ell})$$

The minimum quadratic term than maximizes the likelihood function can be derived as

$$(\mathbf{z}_{k,\ell} - \tilde{\mathbf{S}}_\ell \mathbf{b}_\ell)^{\mathtt{H}} \mathbf{\Psi}^{-1} (\mathbf{z}_{k,\ell} - \tilde{\mathbf{S}}_\ell \mathbf{b}_\ell) = \mathbf{z}_{k,\ell}^{\mathtt{H}} \mathbf{\Psi}^{-1} \mathbf{z}_{k,\ell} - (\mathbf{z}_{k,\ell}^{\mathtt{H}} \mathbf{\Psi}^{-1} \tilde{\mathbf{S}}_\ell)(\tilde{\mathbf{S}}_\ell^{\mathtt{H}} \mathbf{\Psi}^{-1} \tilde{\mathbf{S}}_\ell)^{-1} (\tilde{\mathbf{S}}_\ell^{\mathtt{H}} \mathbf{\Psi}^{-1} \mathbf{z}_{k,\ell}).$$

Substituting the above term in Equation (6.24), we obtain

$$L(\tau_{k,\ell}) = \frac{1}{1 - \dfrac{(\mathbf{z}_{k,\ell}^{\mathtt{H}} \mathbf{\Psi}^{-1} \tilde{\mathbf{S}}_\ell)(\tilde{\mathbf{S}}_\ell^{\mathtt{H}} \mathbf{\Psi}^{-1} \tilde{\mathbf{S}}_\ell)^{-1} (\tilde{\mathbf{S}}_\ell^{\mathtt{H}} \mathbf{\Psi}^{-1} \mathbf{z}_{k,\ell})}{\tau_{k,\ell} + \mathbf{z}_{k,\ell}^{\mathtt{H}} \mathbf{\Psi}^{-1} \mathbf{z}_{k,\ell}}}. \tag{6.25}$$

If we set,

$$\eta_{\text{CG-K}}(\mathbf{z}_k | \mathbf{x}_{k,\ell}^{[i]}, \tau_{k,\ell}) = \frac{(\mathbf{z}_{k,\ell}^{\mathtt{H}} \mathbf{\Psi}^{-1} \tilde{\mathbf{S}}_\ell)(\tilde{\mathbf{S}}_\ell^{\mathtt{H}} \mathbf{\Psi}^{-1} \tilde{\mathbf{S}}_\ell)^{-1} (\tilde{\mathbf{S}}_\ell^{\mathtt{H}} \mathbf{\Psi}^{-1} \mathbf{z}_{k,\ell})}{\tau_{k,\ell} + \mathbf{z}_{k,\ell}^{\mathtt{H}} \mathbf{\Psi}^{-1} \mathbf{z}_{k,\ell}} \tag{6.26}$$

then

$$L(\tau_{k,\ell}) = \frac{1}{1 - \eta_{\text{CG-K}}(\mathbf{z}_k | \mathbf{x}_{k,\ell}^{[i]}, \tau_{k,\ell})}.$$

Finally, substituting the ML estimate of the speckle covariance matrix in $\mathbf{\Psi}$ and using the ML estimate of the texture component, we obtain

$$\eta_{\text{CG-K}}(\mathbf{z}_k | \mathbf{x}_{k,\ell}^{[i]}, \hat{\tau}_{k,\ell}) = \frac{(\mathbf{z}_{k,\ell}^{\mathtt{H}} \hat{\mathbf{\Sigma}}^{-1} \tilde{\mathbf{S}}_\ell)(\tilde{\mathbf{S}}_\ell^{\mathtt{H}} \hat{\mathbf{\Sigma}}^{-1} \tilde{\mathbf{S}}_\ell)^{-1} (\tilde{\mathbf{S}}_\ell^{\mathtt{H}} \hat{\mathbf{\Sigma}}^{-1} \mathbf{z}_{k,\ell})}{N_T \hat{\tau}_{k,\ell} + \mathbf{z}_{k,\ell}^{\mathtt{H}} \hat{\mathbf{\Sigma}}^{-1} \mathbf{z}_{k,\ell}}. \tag{6.27}$$

If the targets are moving further apart from each other, then the above test statistic simplifies to

$$\eta_{\text{CG-K}}(\mathbf{z}_k|\mathbf{x}_{k,\ell}^{[i]}, \hat{\tau}_{k,\ell}) = \frac{\left|\mathbf{s}[\nu_{k,\ell}]^{\mathtt{H}}\hat{\boldsymbol{\Sigma}}^{-1}\mathbf{z}_{k,\ell}\right|^2}{\mathbf{s}[\nu_{k,\ell}]^{\mathtt{H}}\ \hat{\boldsymbol{\Sigma}}^{-1}\ \mathbf{s}[\nu_{k,\ell}]\ \left[N_T\hat{\tau}_{k,\ell} + \mathbf{z}_{k,\ell}^{\mathtt{H}}\ \hat{\boldsymbol{\Sigma}}^{-1}\ \mathbf{z}_{k,\ell}\right]} . \tag{6.28}$$

6.5.5 Fixed Point Algorithm for ML Estimation of Clutter Statistics

When both the clutter statistics are not known, then it is not easy to solve Equations (6.21) and (6.22). The equations must be considered as two transcendental equations and simultaneously solved. An iterative procedure called approximate maximum likelihood function (AML) was proposed in [83] to estimate the clutter parameters for the texture component by assuming texture to be either random or deterministic. For the assumed deterministic texture component, this algorithm results in the ML estimate of the speckle covariance matrix [84] whereas, for the assumed random texture component, it results in an approximate ML estimate. This algorithm was analyzed in [84] and a fixed point estimate solution was formulated due to the implicit algebraic structure of the two transcendental equations. This algorithm was also shown to converge to the true solution irrespective of the initialization. The algorithmic steps of this method are provided in Algorithm 5, where N_{AML} refers to the number of iterations. The covariance matrix is initialized with the normalized sample covariance matrix estimate in Equation (6.19).

Algorithm 5 Algorithmic Steps of AML Estimates for Deterministic Texture

```
Initialize the speckle covariance matrix as
    $\hat{\mathbf{\Sigma}}^{(0)} = \frac{1}{N_T} \sum_{n=1}^{N_T} \frac{\mathbf{z}_{k,n}\mathbf{z}_{k,n}^{\mathtt{H}}}{\frac{1}{N_p}\mathbf{z}_{k,n}^{\mathtt{H}}\mathbf{z}_{k,n}}$
for $j = 1$ to $N_{\mathrm{AML}}$ do
    Step 1: Estimate the texture component of the secondary range bins surrounding the range bin under test
        $\hat{\tau}_{k,n}^{(j)} = \frac{\mathrm{tr}(\hat{\mathbf{\Sigma}}^{(j-1)}\mathbf{z}_{k,n}\mathbf{z}_{k,n}^{\mathtt{H}})}{N_p}$
    Step 2: Update the speckle covariance matrix
        $\hat{\mathbf{\Sigma}}^{(j)} = \frac{1}{N_T} \sum_{n=1}^{N_T} \frac{\mathbf{z}_{k,n}\mathbf{z}_{k,n}^{\mathtt{H}}}{\hat{\tau}_{k,n}^{(j)}}$
    Step 3: Normalize the covariance matrix such that the trace of the matrix is $N_p$
        $\hat{\mathbf{\Sigma}}^{(j)} = \frac{N_p\hat{\mathbf{\Sigma}}^{(j)}}{\mathrm{tr}(\hat{\mathbf{\Sigma}}^{(j)})}$
end for
```

6.5.6 Relation Between Test Statistics

The CG-K statistic ($\eta_{\text{CG-K}}$) derived in Section 6.5.4 for well separated targets is related to the asymptotic linear quadratic test statistic η_{LQ} in Equation (6.16) as

$$\eta_{\text{CG-K}} = \eta_{\text{LQ}} \left[\frac{\mathbf{z}_{k,\ell}^{\mathtt{H}} \mathbf{\Sigma}^{-1} \mathbf{z}_{k,\ell}}{\mathbf{z}_{k,\ell}^{\mathtt{H}} \mathbf{\Sigma}^{-1} \mathbf{z}_{k,\ell} + \tau_{k,\ell} N_T} \right].$$

This suggests that, for a positive definite matrix $\mathbf{\Sigma}$ and the positive texture component $\tau_{k,\ell}$, $\eta_{\text{CG-K}}$ is always smaller than η_{LQ}. Under H_0,

$$\eta_{\text{CG-K},H_0} = \eta_{\text{LQ},H_0} \left[\frac{\mathbf{y}_{k,\ell}^{\mathtt{H}} \mathbf{y}_{k,\ell}}{\mathbf{y}_{k,\ell}^{\mathtt{H}} \mathbf{y}_{k,\ell} + N_T} \right]$$

where

$$\mathbf{y}_{k,\ell} = \mathbf{\Sigma}^{-1/2} \mathbf{u}_{k,\ell}$$

is the whitened version of the speckle component $\mathbf{u}_{k,\ell}$ in Equation (6.9) and $\eta_{\text{CG-K}}$ is invariant to texture under H_0. Under H_1,

$$\eta_{\text{CG-K},H_1} = \eta_{\text{LQ},H_1} \left[\frac{\mathbf{y}_{k,\ell}^{\mathtt{H}} \mathbf{y}_{k,\ell}}{\mathbf{y}_{k,\ell}^{\mathtt{H}} \mathbf{y}_{k,\ell} + N_T} \right] \left[\frac{1 + \varrho / (\mathbf{y}_{k,\ell}^{\mathtt{H}} \mathbf{y}_{k,\ell})}{1 + \varrho / (\mathbf{y}_{k,\ell}^{\mathtt{H}} \mathbf{y}_{k,\ell} + N_T)} \right]$$

where

$$\varrho = \left| I_{k,\ell} \sqrt{\frac{\mathbf{r}^{\mathtt{H}} \mathbf{r}}{\tau_{k,\ell}}} + \frac{\mathbf{y}_{k,\ell}^{\mathtt{H}} \mathbf{r}}{\sqrt{\mathbf{r}^{\mathtt{H}} \mathbf{r}}} \right|^2 - \frac{|\mathbf{y}_{k,\ell}^{\mathtt{H}} \mathbf{r}|^2}{\mathbf{r}^{\mathtt{H}} \mathbf{r}}$$

and $\mathbf{r} = \mathbf{\Sigma}^{-1/2} \, \mathbf{s}[\nu_\ell]$. For a positive definite matrix $\mathbf{\Sigma}$, the scale factor under H_1 is greater than the one under H_0 when $\varrho > 0$. This condition is satisfied when one of the following two conditions are met: (i) $I_{k,\ell}$ is real and positive, and (ii) $|I_{k,\ell}|^2 \mathbf{r}^{\mathtt{H}} \mathbf{r} > -2\sqrt{\tau_{k,\ell}} \text{Re}\{I_{k,\ell} \mathbf{y}_{k,\ell}^{\mathtt{H}} \mathbf{r}\}$. The second condition can be satisfied for moderately high SCR. Thus, the variance of $\eta_{\text{CG-K},H_0}$ is smaller than the variance of η_{LQ,H_0}. Under H_1, $\eta_{\text{CG-K},H_1}$ is a scaled version of η_{LQ,H_1}, even though the scaling value is smaller than that under H_0. Therefore, the probability of false alarm with CG-K is smaller than with the LQ; the probability of detection is similar for both methods. Hence, the proposed likelihood function is expected to perform better than the sub-optimal method when one of the two conditions is satisfied.

6.6 Track-before-detect Filtering Framework in Clutter

The different generalized likelihood ratios discussed in the previous sections were originally derived for a CFAR detector. In the our TBDF framework, we use the generalized likelihood ratio in the state update step of our TBDF tracker in Equation (4.12). For a given target state vector in mode i at the kth dwell, the range and Doppler information are computed using Equations (6.4) and (6.5). The generalized likelihood function corresponding to a target in mode i is computed using the derived range and Doppler information. The range bin is used to identify the measurement vector $\mathbf{z}_{k,\ell}$ and the Doppler information is used to construct the known signal vector $\mathbf{s}[\nu_\ell]$ and $\mathbf{s}[\nu_{\ell_i}]$ in Equation (6.7). The likelihood function for the ℓth target can be written as

$$L(\mathbf{z}_k|\mathbf{x}_{k,\ell}^{[i]}) = \frac{1}{1-\eta(\mathbf{z}_k|\mathbf{x}_{k,\ell}^{[i]})}. \tag{6.29}$$

The generalized likelihood function in Equation (6.1) is always greater than one since under hypothesis H_0, the target intensity $I_{k,\ell}$ is zero, the ratio in Equation (6.25) becomes one, and the test statistic η lies between zero and one. In order to increase the dynamic range of the generalized likelihood ratio, we create a new likelihood function that varies from zero to infinity as

$$L(\mathbf{z}_k|\mathbf{x}_{k,\ell}^{[i]}) = \frac{\eta(\mathbf{z}_k|\mathbf{x}_{k,\ell}^{[i]})}{1-\eta(\mathbf{z}_k|\mathbf{x}_{k,\ell}^{[i]})}.$$

When implementing the multi-target TBDF using particle filters, it is advantageous to use the likelihood function with this dynamic range since the joint multi-target

PDF is approximated by the product of likelihood functions. If one of the target does not exist, then the weights tend to zero and when all the targets are present, then the weights tend to have very high values. Finally, the joint generalized likelihood ratio corresponding to all targets in mode i is computed. If the clutter in each range bin is assumed to be independent of each other, then the generalized joint likelihood function conditioned on modes at time steps k and $(k-1)$, $m_{k-1}=1,\dots,M$ and $m_k=2,\dots,M$ in Equation (4.12) is given by

$$L_{j,i}(\mathbf{z}_k|\mathbf{x}_k^{[i]}) = \prod_{\ell=0}^{\mathscr{L}} \Big(L(\mathbf{z}_k|\mathbf{x}_{k,\ell}^{[i]})\Big)^{C_\ell^i} \ ,$$

and $L_{j,i}(\mathbf{z}_k|\mathbf{x}_k^{[i]})=1$ for $m_k=1$, where m_k and m_{k-1} are the mode condition at time steps k and $(k-1)$. Since we are interested only in tracking, it is not necessary to explicitly estimate the intensity of the target associated return signal $I_{k,\ell}$. However, target intensity information is implicitly used through its ML estimate [152] that is included in the generalized likelihood function. Therefore, unlike the CFAR detector in which the generalized likelihood ratio was compared with a threshold, we use the generalized likelihood ratio to update the particles corresponding to either a new target, a surviving target or a disappearing target. The test statistics corresponding to all three methods considered in this chapter are summarized in Table 6.1 for well separated targets.

6.7 Simulations

6.7.1 Low Resolution Radar and Complex Gaussian Clutter

In the first simulation scenario, we investigated the tracking performance of our algorithm using pulse Doppler measurements from a low resolution radar in the presence of clutter. A pulse Doppler radar operating with the parameters shown in Table 6.2 with complex Gaussian clutter is used to generate the measurement using the

Table 6.1: Test Statistics for Complex Gaussian and Compound Gaussian Clutter with Random and Deterministic Texture Component

Method	**Test Statistic**
Gaussian (Kelly)	Equation (6.14) $$\eta_{\mathrm{G}}(\mathbf{z}_k \vert \mathbf{x}_{k,\ell}^{[i]}) = \frac{\left\vert \mathbf{s}[\nu_{k,\ell}]^{\mathtt{H}} \hat{\boldsymbol{\Sigma}}^{-1} \mathbf{z}_{k,\ell} \right\vert^2}{\mathbf{s}[\nu_{k,\ell}]^{\mathtt{H}} \ \hat{\boldsymbol{\Sigma}}^{-1} \ \mathbf{s}[\nu_{k,\ell}] \ \left[N_T + \mathbf{z}_{k,\ell}^{\mathtt{H}} \hat{\boldsymbol{\Sigma}}^{-1} \mathbf{z}_{k,\ell} \right]}$$
Compound Gaussian (Asymptotic linear quadratic)	Equation (6.16) $$\eta_{\mathrm{LQ}}(\mathbf{z}_k \vert \mathbf{x}_{k,\ell}^{[i]}) = \frac{\left\vert \mathbf{s}[\nu_{k,\ell}]^{\mathtt{H}} \hat{\boldsymbol{\Sigma}}^{-1} \mathbf{z}_{k,\ell} \right\vert^2}{\left(\mathbf{s}[\nu_{k,\ell}]^{\mathtt{H}} \hat{\boldsymbol{\Sigma}}^{-1} \mathbf{s}[\nu_{k,\ell}] \right) \left(\mathbf{z}_{k,\ell}^{\mathtt{H}} \hat{\boldsymbol{\Sigma}}^{-1} \mathbf{z}_{k,\ell} \right)}$$
Compound Gaussian (Deterministic texture; Kelly)	Equation (6.28) $$\eta_{\mathrm{CG\text{-}K}}(\mathbf{z}_k \vert \mathbf{x}_{k,\ell}^{[i]}) = \frac{\left\vert \mathbf{s}[\nu_{k,\ell}]^{\mathtt{H}} \hat{\boldsymbol{\Sigma}}^{-1} \mathbf{z}_{k,\ell} \right\vert^2}{\mathbf{s}[\nu_{k,\ell}]^{\mathtt{H}} \ \hat{\boldsymbol{\Sigma}}^{-1} \ \mathbf{s}[\nu_{k,\ell}] \ \left[N_T \hat{\tau}_{k,\ell} + \mathbf{z}_{k,\ell}^{\mathtt{H}} \ \hat{\boldsymbol{\Sigma}}^{-1} \ \mathbf{z}_{k,\ell} \right]}$$

signal model described in Equations (6.1). For illustration purposes, measurements from DOA equal to 45^o are considered thereby restricting the motion of targets in one particular direction

Table 6.2: Simulated Low Resolution Radar System Parameters

Radar Parameter	**Value**
Carrier frequency, f_c	10 GHz
Baseband signal	Linear FM pulse
Baseband bandwidth	2 MHz
Fast time sampling, f_s	2 MHz
Pulse Width, N_s	8 samples
Pulse interval time, T_{PRI}	500 μs
Validation range gate	15 km to 26.175 km
Number of valid range bins, N_r	200
Range resolution	75 m
Maximum radial velocity	30 m/s (108 km/hr)
DOA	45^o
Beamwidth	0.703^o
Cross-range resolution range	184 m to 321 m
Beam scan rate	20 rotations per minute
Dwell interval	3 s
Number of pulses per dwell, N_p	20
Motion model	Constant velocity

The initial positions and velocities for three targets are (14,140, 14,140) m and (-4.2, -4.1) m/s, (14,494, 14,494) m and (-7.7, -7.8) m/s, and (13,574, 13,574) m and (-7.95, -7.9) m/s, respectively. The time steps for the three targets entering and leaving the FOV are given by 5 and 25, 13 and 33, and 21 and 41, respectively. Figure 6.1(a) and Figure 6.1(b) show the x and y coordinates of the targets at different time steps. Figure 6.2(a) shows the absolute value of the measurement dwells described in Equation (6.1) at 0 dB SCR. As it can be seen, the three targets entering and leaving at different time steps are barely visible at 0 dB SCR. In this simulation, we consider the tracking performance of our proposed algorithm at -6, -9, and -12 dB SCRs. The number of particles in this simulation is set to 500 for all particle filters, N_T is set to 70 range bins, $q_1 = q_2 = 0.1$, and the maximum and minimum velocity is set at 8.5 m/s and -8.5 m/s, respectively. All the remaining relevant parameters of the algorithm are the same as in the previous simulations. Figure 6.2(b) shows the tracking error averaged over 100 Monte Carlo simulations and the cut-off parameter is set to the same order as the FOV ($c = 4,000$). Since the FOV is much larger in this simulation scenario, the OSPA parameter c_g is set to 4,000.

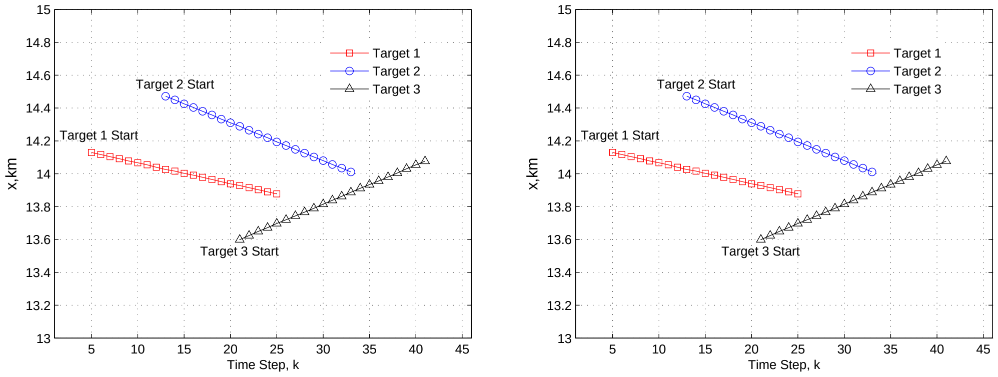

(a)

(b)

Figure 6.1: (A) Target Trajectory in the x Coordinate; and (b) Target Trajectory in the y Coordinate.

The tracking error is very small at -6 dB with slightly higher cardinality error around the time when the targets are entering the FOV. The cardinality error is higher at -9 dB, and the tracking error is very high at time steps 20–25 when all the targets are present. This increased error is dominated mostly due to the delayed detection of the third target, as the proximity of the first target is closer to the third target's initial position. Once a target is detected, the localization error is eventually reduced as seen around the vicinity of time steps 6–10 and 25–30. The localization error is generally low and the OSPA is limited by the range resolution. At -12 dB SCR, the tracking performance of the algorithm degrades drastically and the joint detection of all three targets becomes very difficult. Nevertheless, the algorithm is able to detect at least one target, as evident by the relatively reduced tracking error around time steps 8–12 and 33–40.

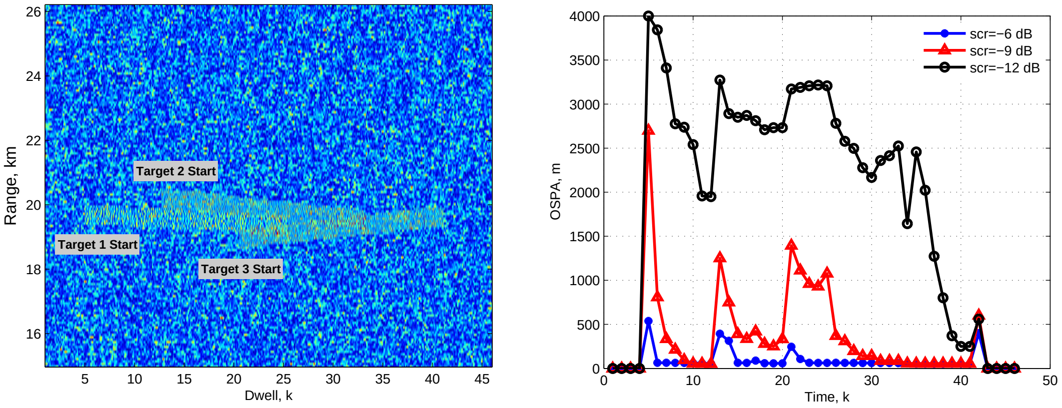

(a) (b)

Figure 6.2: (A) Absolute Value of Measurement Dwells at 0 dB SCR. (b) Tracking Error, OSPA(4000,2).

6.7.2 High Resolution Radar and Compound Gaussian Clutter

In this section, we discuss the simulation results for a simulated high resolution radar in compound Gaussian modeled clutter. The simulated radar parameters are given in Table 6.3. Specifically, we compared the performance of our proposed method with the two likelihood functions (LQ and CG-K) discussed in Section 6.4. The speckle components were randomly generated from a complex Gaussian random process whose correlation properties were estimated in [110] using real radar measurements collected with the Osborne Head Gunnery Range (OHGR) IPIX radar [161]. The texture was generated from a correlated gamma distributed random process with scale b_g and shape c_g parameters [89]. We also used the texture correlation estimated in [110]. The Doppler model parameters discussed in Section 6.3.3 are set to $\mu_{\text{Bragg}} = -15$ Hz, $\sigma_{\text{Bragg}} = 7.07$ Hz, $A_{\text{swell}} = 50$ Hz, $B_{\text{swell}} = 5.95$ Hz. The standard deviation σ_{swell} is randomly sampled from a Gaussian distribution with mean and standard deviation equal to 60 Hz. The degree of spikiness of the texture component is controlled by the shape parameter c_g; decreasing c_g results in more spiky clutter. The averaged Doppler clutter spectrum for different values of c_g is shown in Figure 6.3. For higher c_g values, the averaged Doppler spectrum is centered around the assumed Bragg's model parameters, whereas for lower values, the frequency centers around the swell model parameters. Figure 6.4 shows the absolute value of the pulse Doppler measurements for different values of c_g. The targets are visible in Figure 6.4(a) for $c_g = 10$ at 3 dB SCR, however they are not clearly distinguishable as the c_g value is decreased. For $c_g = 0.2$, a lot of target like clutter components can be observed. In this case, for a given SCR over the entire FOV, the instantaneous SCR appears much lower in some range bins for $c_g = 0.2$ when compared to $c_g = 10$. This phenomenon is typical for high resolution radars because the reflected clutter power from a range bin

Table 6.3: Simulated High Resolution Radar System Parameters

Radar Parameter	**Value**
Carrier frequency, f_c	10 GHz
Baseband signal	Linear FM pulse
Baseband bandwidth	25 MHz
Fast time sampling, f_s	25 MHz
Pulse Width, N_s	10 samples
Pulse interval time, T_{PRI}	500 μs
Validation range gate	15.25 km to 16.75 km
Number of valid range bins, N_r	249
Range resolution	6 m
Maximum radial velocity	30 m/s (108 km/hr)
DOA	45^o
Beamwidth	0.703^o
Cross-range resolution range	93.59 m
Beam scan rate	240 rotations per minute
Dwell interval	0.25 s
Number of pulses per dwell, N_p	20
Motion model	Constant velocity

is smaller than that of a low resolution radar because of fewer number of scatterers in the physical area corresponding to a range bin.

We compared the performance of the algorithm for tracking three targets moving at constant velocity. The targets are assumed to leave and enter the FOV at different time instants (5 and 25 dwells, 13 and 33 dwells, 21 and 41 dwells for Targets 1, 2

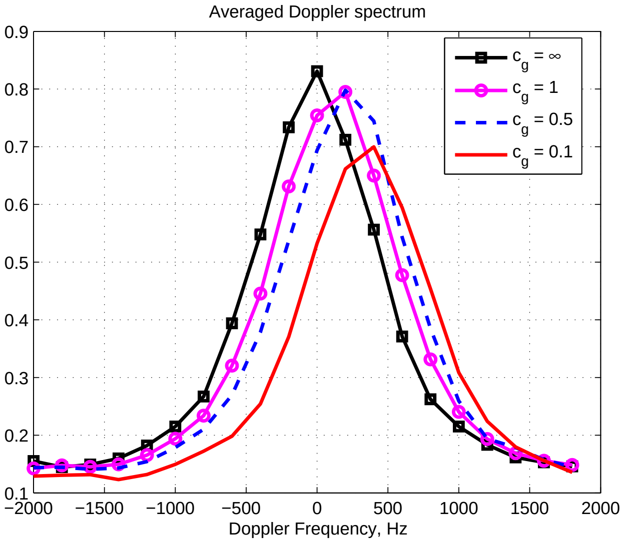

Figure 6.3: Averaged Doppler Spectrum for Different Values of c_g.

and 3, respectively). The corresponding initial positions and velocities were (11,312, 11,312) m and (-5.19, -5.18) m/s, (10,959, 10,959) m and (-6.62, -6.63) m/s, (11,666, 11,666) m and (-5.27, -5.26) m/s. The number of particles is set to 500 for all p article filters, N_T is set to 50 range bins, $q_1 = 1$, $q_2 = 0.1$, and the minimum and maximum velocity is set at 8 m/s and 8 m/s, respectively. We compared the performance of the proposed MM-MT-TBDF using the asymptotic detector (LQ) and Kelly's (CG-K) generalized likelihood functions. The effect of using the texture component from past frames is also analyzed by comparing the tracking performance with the true and estimated texture components. The LQ method is analyzed using two different covariance estimates: $\hat{\boldsymbol{\Sigma}}$ in (6.17) and the MLE assuming the texture component is known.

The tracking error was measured using the OSPA metric with cut-off parameter $c = 500$ and $p = 2$. The SCR was varied between -6, -3, and 0 dB, the values of c_g was varied between 0.2, 0.5, 1 and 10, and we averaged the OSPA values over 200 Monte Carlo simulations. Figure 6.5 shows the tracking error for all four cases for varying c_g.

The CG-K performs the best for all values of c_g. The CG-K has a similar performance with the estimated and true texture for moderately spiky clutter, and the tracking error averages around 30 m. The LQ performs poorly when the clutter is spiky for all covariance matrix estimations. For $c_g = 0.2$, the CG-K tracking performance degraded when using the past frame's texture component, as compared to the true texture component. However, the CG-K with estimated texture components still performed better than LQ. Similarly, Figure 6.6 shows the tracking error for all four cases for varying SCR. At -6 dB SCR, the LQ method performed better than the other two methods but had more false alarms between dwells 41-46. The performance of the two CG-K based methods was generally better than the two LQ methods at higher SCR. The OSPA metric was higher during target mode transition periods (cardinality error) that happened at dwells 5, 13, 20, 25, 33, and it indicated some delay in detecting a target entering or leaving the FOV.

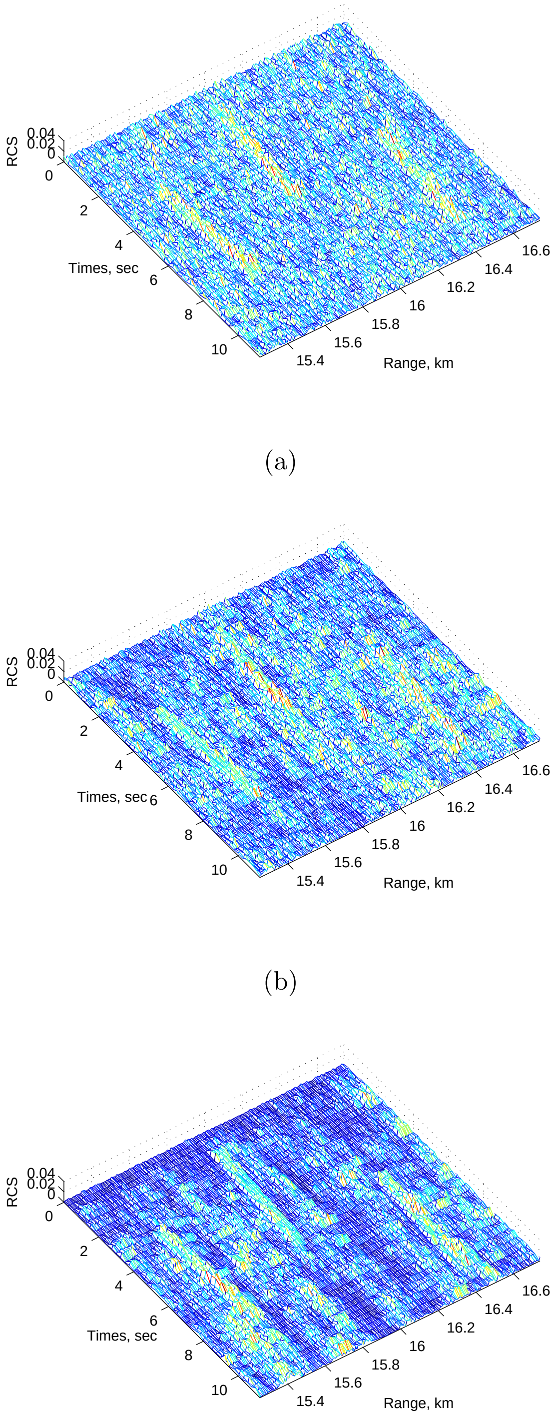

(a)

(b)

(c)

Figure 6.4: Fast Time Measurement, SCR=3 dB: (a) c_g=10;(b) c_g=0.5; (c) c_g=0.2.

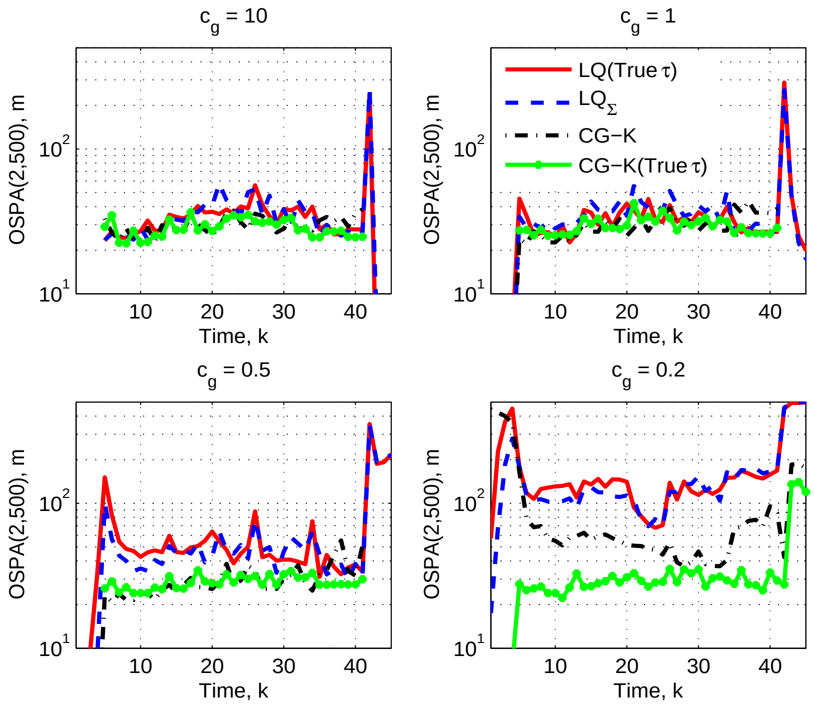

Figure 6.5: Tracking Error for Different Values of c_g and SCR = 3 dB.

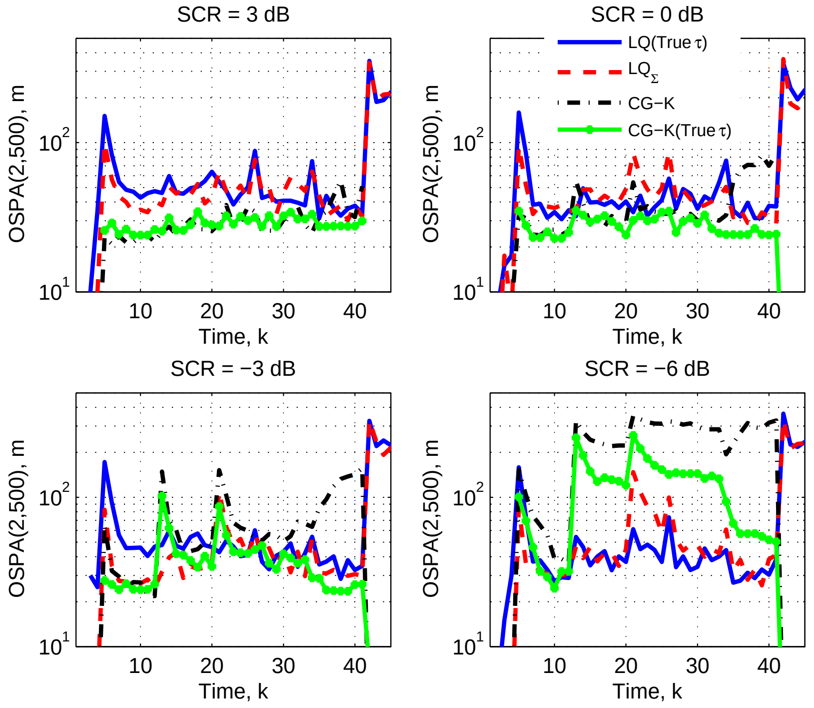

Figure 6.6: Tracking Error for Different Values of SCR and $c_g = 0.5$.

Chapter 7

ESTIMATION OF RAPIDLY-VARYING SEA CLUTTER USING NEAREST KRONECKER PRODUCT APPROXIMATION

7.1 Rapidly-varying Sea Clutter Characterization

The detection and tracking of a target with low radar cross-section (RCS) in maritime environments is an extremely challenging problem. The target's kinematic state estimation problem is complicated by reflections from fast moving sea waves, causing target-like interference with substantial Doppler shifts. As a result, moving target indicator methods, such as Doppler filtering [45], may not provide effective ways to track a slow moving target in such environments. Various statistical modeling based sea clutter characterization methods were used in combination with target detection algorithms [126, 127, 162]. A principal component analysis based clutter rejection technique was used in [109, 110] to improve target detection performance. Experimental results indicated that sea clutter amplitude follows a long-tailed, non-Gaussian distribution [100, 134, 135, 138]. The compound Gaussian (CG) distribution is a well-established statistical model for characterizing the spiky nature of sea clutter [89]. Using the CG model, the small scale structures on the sea surface are modeled as speckle, following a complex Gaussian distribution with a short decorrelation time. This speckle component is modulated by a slow varying texture component that is associated with long sea waves and swell structures. Many adaptive detection approaches applied the CG model with pulse integration, assuming knowledge of the slow-time temporal covariance matrix of the range bin under testing [82, 85, 121, 123]. The sample covariance matrix estimate was derived by assuming statistical independence between neighboring range bins [83, 84, 156]. However, using real data, reflections from sea surface were found to be correlated over a distance of 100 m [89]. Therefore, detection of targets using the space-time correlation properties of sea clutter must be considered for optimal detection and tracking performance. Note that space-time correlation properties include both temporal information (or measurement from slow-time samples) as well as spatial information (or measurement from fast-time samples) corresponding to the physical range location in the field-of-view (FOV) of a radar from which the reflected signal has originated from.

A dynamic sea clutter model and a sea clutter space-time covariance matrix estimation method were proposed in [163–165]. The dynamic state space model approach to estimate sea clutter statistics is important in tracking the heterogeneity of the underlying sea clutter. The validity of this state space model was also investigated with real sea clutter. However, the practical feasibility of this algorithm in real-life applications is not possible since it estimates all the elements of the covariance matrix. The number of elements of the covariance matrix exponentially increases with the number of range bins and the number of pulses used for coherent processing. In addition to computational issues, the positive definiteness of the estimated matrix cannot be ensured since the matrix elements are estimated by a set of independent multiple particle filters. Moreover, the measurement model assumes the knowledge of a noisy covariance matrix which was estimated by averaging a large number of measurements.

In this chapter, we propose a modified clutter estimation algorithm to avoid the aforementioned drawbacks by imposing a Kronecker product (KP) assumption on the space-time covariance matrix [90, 91]. In the literature, many methods have been proposed to estimate the covariance matrix when its structure is in the KP form [166–168]. For example, the nearest KP approximation [169] was used in [170] to approximate the space-time covariance matrix for wind speed data. In our proposed method, we use the aforementioned sea clutter model and space-time covariance matrix state model but we reformulate it such that the number of elements to be estimated is drastically reduced due to KP assumption. A particle filter (PF) [17] based implementation method is also proposed to estimate the matrix elements. In addition, our proposed model does not require a large number of measurements as the likelihood function used to update the particle weights requires a significantly fewer number of pulse Doppler measurements. Finally, the proposed method is guaranteed to always provide a positive definite matrix solution. We provide an application of our proposed method by extending the track-before-detect filter (TBDF) in [53] to our measurement model by making use of the estimated space-time covariance matrix and show improved tracking performance by comparing with the TBDF using the compound Gaussian assumption.

7.2 Rapidly-varying Sea Clutter Model

7.2.1 Measurement Model

We consider the same pulse Doppler radar measurement model discussed in Section 6.2. We assume that the same transmit signal is used within each dwell. At the receiver, we assume that the region of measurement selection for track updates or validation gate at the kth dwell consists of $N_v = \zeta_{N_v} - \zeta_1 + 1$ range bins. Assuming no target is present, the noisy observation signal $y(n/f_s, p)$ from the pth pulse at the kth dwell is sampled at f_s Hz to obtain

$$y_k[n,p] = \sum_{m=n-N_s+1}^{n} a_k[m,p]s[n-m] + w_k[n,p]\,, \tag{7.1}$$

where $n = \zeta_1, \ldots, \zeta_{N_v} + N_s - 1$, $p = 0, \ldots, N_p - 1$, $w_k[n,p]$ is assumed to be zero-mean, white Gaussian observation noise at the kth dwell and pth pulse, the clutter reflectivity $a_k[m, p]$ is defined as

$$a_k[m, p] = \xi_k[m, p] e^{j2\pi\nu_m p T_{\mathrm{PRI}}}. \tag{7.2}$$

where $\xi_k[m, p]$ is the clutter reflectivity, and ν_m is the Doppler shift corresponding to the clutter at the mth range bin. At the kth dwell, considering all N_p pulses and $N_v + 2N_s - 1$ range bins, the overall scatterer contribution is represented by the $((N_v + 2N_s - 1) \times N_p)$ reflectivity matrix $\mathbf{A}_k$ defined in Equation (6.2) whose (m, p)th element is $a_k[m, p]$. In Section 6.2, a dwell measurement matrix consists of an $(N_v \times N_p)$ matrix and this matrix correspond to reflectivity contribution from N_r range bins, where $N_r = N_v + N_s - 1$. In this chapter, tracking is performed using the measurement obtained by matched filtering the raw dwell measurement and therefore, we require an $(N_r \times N_p)$ dwell measurement matrix that results from $(N_v + 2N_s - 1)$ range bins. Hence, we use more number of range bins in the reflectivity matrix $\mathbf{A}_k$.

If a target is present, the signal in Equation (7.1) includes both the target and clutter. If β_k is the target reflectivity at range bin ζ_k, which is assumed unknown [152], with Doppler shift ν_k, then the received measurement is

$$y_k[n, p] = \beta_{k,p} s[n - \zeta_k] + \sum_{m=n-N_s+1}^{n} a_k[m, p] s[n - m] + w_k[n, p].$$

where $\beta_{k,p} = \beta_k \exp(j2\pi\nu_k p T_{\mathrm{PRI}})$. Note that the range r_k and range rate $\dot{r}_k$ of the target at the kth dwell are given by $r_k = \zeta_k c/(2f_s)$ and $\dot{r}_k = \nu_k c/(2f_c)$, where c is the velocity of propagation and f_c Hz is the carrier frequency. In [163, 164], the $(N_r^2 N_p^2 \times N_r^2 N_p^2)$ space-time clutter covariance matrix was obtained by estimating the covariance matrix of the vectorized reflectivity matrix $\mathbf{A}_k$. Note, however, that estimating the covariance of the reflectivity matrix results in an increased number of parameters to be estimated since N_r range bins are needed to obtain the measurements for N_v range bins. We reduced this complexity by directly estimating the covariance of the matched filter output as this only requires N_v range bins. The output of the matched filter is given by

$$z_k[n,p] = \sum_{m=n}^{n+N_s-1} y_k[m,p]\, s^*[m-n] \tag{7.3}$$

for $n = \zeta_1, \ldots, \zeta_{N_v}$, $p = 0, \ldots, N_p - 1$. Here, we use $y_k[n,p]$ as defined in Equation (7.1) and assume that only clutter is present. The overall clutter measurements at the kth dwell after matched filtering can be represented by the $(N_v \times N_p)$ matrix $\mathbf{Z}_k$. The matrix operation can be written in matrix form as

$$\mathbf{Z}_k = \mathbf{M}\mathbf{Y}_k \tag{7.4}$$

where the $(N_v \times N_r)$ matrix M is given by

$$\mathbf{M} = \begin{bmatrix} s^*[0] & s^*[1] & \ldots & s^*[N_s-1] & 0 & \ldots & 0 & 0 \\ 0 & s^*[0] & s^*[1] & \ldots & s^*[N_s-1] & 0 & \ldots & 0 \\ \vdots & \vdots & \vdots & \vdots & \vdots & \vdots & \vdots & \vdots \\ 0 & 0 & \ldots & 0 & s^*[0] & s^*[1] & \ldots & s^*[N_s-1] \end{bmatrix}$$

and the $(N_r \times N_p)$ raw pulse Doppler measurement matrix $\mathbf{Y}_k$ at the kth dwell is given by

$$\mathbf{Y}_k = \begin{bmatrix} y_k[\zeta_1,0] & y_k[\zeta_1,1] & \ldots & y_k[\zeta_1,N_p-1] \\ y_k[\zeta_2,0] & y_k[\zeta_2,1] & \ldots & y_k[\zeta_2,N_p-1] \\ \vdots & \vdots & \vdots & \vdots \\ y_k[\zeta_{N_r},0] & y_k[\zeta_{N_r},1] & \ldots & y_k[\zeta_{N_r},N_p-1] \end{bmatrix}. \tag{7.5}$$

7.2.2 Measurement State Space Model

As sea clutter is dynamically varying, its state transitions between adjacent range bins depending on the relative velocity of sea waves with respect to the radar. A dynamic model was proposed in [164] in which the spectral component of the received signal is allowed to transition from one range bin to its adjacent bins depending on the Doppler shift. Based on this model, the scattering matrix corresponding to the $(N_v \times N_p)$ measured signal $\mathbf{Z}_k$ in Equation (7.4) is obtained as

$$\mathbf{B}_k = \mathbf{Z}_k \mathbf{D} \tag{7.6}$$

where $\mathbf{D}$ is an $(N_p \times N_p)$ discrete Fourier transform matrix. The elements of $\mathbf{D}$ are such that the first $(N_p-1)/2$ columns list the negative Doppler shifts, the middle column is the zero Doppler shift, and the remaining columns list the positive Doppler shifts. In this model, most of the sea clutter components can be shown to concentrate around the middle column under calm sea state conditions but move away from the middle column under turbulent conditions.

We represent the clutter state transition in vector form by stacking the columns of $\mathbf{B}_k$ from left to right to form the $(N_v\, N_p \times 1)$ vector, $\mathbf{b}_k = \text{vec}(\mathbf{B}_k)$. The operator $\text{vec}(\cdot)$, vectorizes a matrix by stacking all the columns of the matrix. For example, if $\mathbf{B}_k = [\mathbf{b}_1\, \mathbf{b}_2\, \ldots\, \mathbf{b}_{N_p}]$, where $\mathbf{b}_i$ is the ith $(N_v \times 1)$ column of matrix $\mathbf{B}_k$, then $\text{vec}(\mathbf{B}_k) = [\mathbf{b}_1^{\mathtt{T}}\ \mathbf{b}_2^{\mathtt{T}}\ \ldots\ \mathbf{b}_{N_p}^{\mathtt{T}}]^{\mathtt{T}}$. We similarly represent the matched filter output at the kth dwell as the $(N_v N_p \times 1)$ vector $\mathbf{z}_k = \text{vec}(\mathbf{Z}_k)$. Using the KP property A.2 in Appendix A [171], and Equation (7.6), the relation between the two vectors $\mathbf{b}_k$ and $\mathbf{z}_k$ can be written as

$$\mathbf{b}_k = (\mathbf{D}^{\mathtt{H}} \otimes \mathbf{I}_{N_v})\, \mathbf{z}_k$$

where $\mathtt{H}$ denotes Hermitian transpose and $\mathbf{I}_{N_v}$ is the $(N_v \times N_v)$ identity matrix. The KP operator $\otimes$ computes the KP on the $(N_p \times N_p)$ matrix $\mathbf{D}^{\mathtt{H}}$ and the $(N_v \times N_v)$ matrix $\mathbf{I}_{N_v}$ to form an $(N_v\, N_p \times N_v\, N_p)$ block matrix. The measurement vector can be obtained from the spectral vector as

$$\mathbf{z}_k = (\mathbf{D}^{-\mathtt{H}} \otimes \mathbf{I}_{N_v})\, \mathbf{b}_k. \tag{7.7}$$

The clutter state transition is modeled using the state equation as

$$\mathbf{b}_{k+1} = \mathbb{F}\mathbf{b}_k + \mathbf{v}_{k+1} \tag{7.8}$$

where $\mathbf{v}_{k+1}$ is the modeling random error process assumed to be a zero-mean complex Gaussian process with covariance $\mathbf{V}_{k+1}$. The $(N_v\, N_p \times N_v\, N_p)$ state transition matrix $\mathbb{F}$ (defined in Equation (9) in [164]) represents the scattering movement between dwells and populates the range-Doppler bins moving into the validation gate. It represents the transition of a fast moving clutter between range bins n and $n+l$ if the reflector is moving away from the radar and between range bins n and $n-l$ if the reflector is moving towards the radar; the value of l is determined by the Doppler shift. Specifically, the state transition matrix $\mathbb{F}$ is an $(N_v\, N_p \times N_v\, N_p)$ block diagonal matrix constructed from $(N_v \times N_v)$ submatrices $\mathbb{F}_q$. For negative Doppler shifts, $q = -(N_p-1)/2, \ldots, -1$, [163–165]

$$\mathbb{F}_q = \begin{bmatrix} 2^{|q|-1}e^{-|q|\gamma} & 2^{|q|-1}e^{-(|q|+1)\gamma} & \ldots & (2^{|q|-1}-1)e^{-(N_v+1)\gamma} & \ldots & (2^{|q|-1}-|q|+1)e^{-(N_v+|q|-1)\gamma} \\ \vdots & \vdots & \vdots & \vdots & \vdots & \vdots \\ 2e^{-2\gamma} & 2e^{-3\gamma} & \ldots & \ldots & \ldots & e^{-(N_v+1)\gamma} \\ e^{-\gamma} & e^{-2\gamma} & \ldots & \ldots & \ldots & e^{-N_v\gamma} \\ 1 & 0 & \ldots & \ldots & \ldots & 0 \\ \vdots & \vdots & \vdots & \vdots & \vdots & \vdots \\ 0 & \ldots & \ldots & 1 & \ldots & 0 \end{bmatrix}$$

and for positive Doppler shifts, $q = 1, \ldots, (N_p - 1)/2$

$$\mathbb{F}_q = \begin{bmatrix} 0 & \ldots & \ldots & 1 & \ldots & 0 \\ \vdots & \vdots & \vdots & \vdots & \vdots & \vdots \\ 0 & 0 & \ldots & \ldots & 1 & 0 \\ 0 & 0 & \ldots & \ldots & 0 & 1 \\ e^{-N_v \gamma} & \ldots & \ldots & \ldots & \ldots & e^{-\gamma} \\ e^{-(N_v+1)\gamma} & \ldots & \ldots & \ldots & 2e^{-3\gamma} & 2e^{-2\gamma} \\ \vdots & \vdots & \vdots & & & \\ (2^{|q|-1} - |q| + 1)e^{-(N_v+|q|-1)\gamma} & \ldots & (2^{|q|-1} - 1)e^{-(N_v+1)\gamma} & \ldots & 2^{|q|-1}e^{-(|q|+1)\gamma} & 2^{|q|-1}e^{-|q|\gamma} \end{bmatrix}.$$

For $q = 0$, $\mathbb{F}_0$ is the $(N_v \times N_v)$ identity matrix since the clutter with zero Doppler shifts does not transfer to adjacent range bins from dwell to dwell. The exponential averaging parameter γ controls the contribution from neighboring range bins. Figure 7.1 shows the structure of the spectral matrix and indicates the transition of clutter reflectivity between dwells. This state transition model was validated with real sea clutter in [165].

7.2.3 Clutter Covariance Matrix State Space Model

In order to estimate the clutter measurement covariance matrix $\mathbf{\Sigma}_{\mathbf{z}_k}$, we use the relation between $\mathbf{z}_k$ and $\mathbf{b}_k$ to relate their corresponding covariance matrices $\mathbf{\Sigma}_{\mathbf{z}_k}$ and $\mathbf{\Sigma}_{\mathbf{b}_k}$. From Equation (7.8), the covariance matrix of $\mathbf{b}_{k+1}$ can be written as

$$\mathbf{\Sigma}_{\mathbf{b}_{k+1}} = \mathbb{F}^{\mathrm{H}} \, \mathbf{\Sigma}_{\mathbf{b}_k} \, \mathbb{F} + \mathbf{G}_{k+1} \tag{7.9}$$

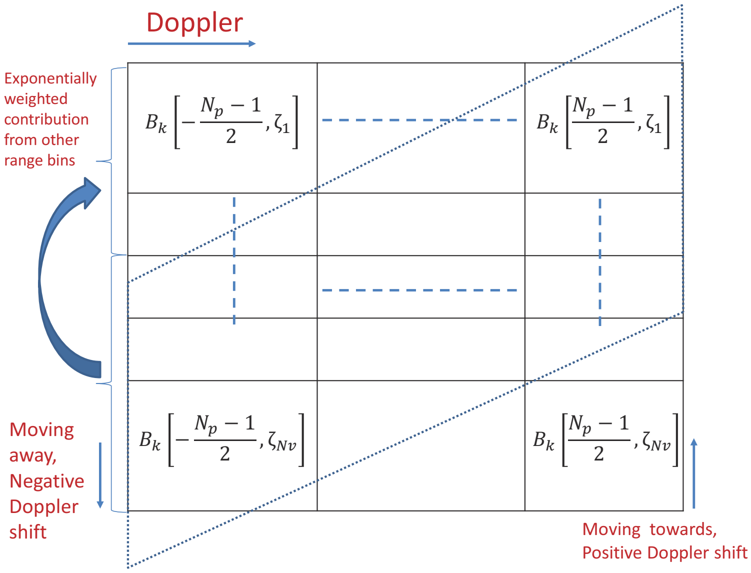

Figure 7.1: Sea Clutter Covariance Transition Model for the Matrix in Equation (7.6).

where $\mathbf{G}_{k+1}$ is assumed Wishart distributed with parameters $\mathbf{V}_{k+1}$ and $N_v\,N_p$ degrees of freedom, and

$$\boldsymbol{\Sigma}_{\mathbf{b}_k} = (\mathbf{D}^{\mathtt{H}} \otimes \mathbf{I}_{N_v})\boldsymbol{\Sigma}_{\mathbf{z}_k}(\mathbf{D} \otimes \mathbf{I}_{N_v}). \tag{7.10}$$

Replacing Equation (7.10) in Equation (7.9), we obtain

$$\boldsymbol{\Sigma}_{\mathbf{b}_{k+1}} = \mathbb{F}^{\mathtt{H}}\,(\mathbf{D}^{\mathtt{H}} \otimes \mathbf{I}_{N_v})\,\boldsymbol{\Sigma}_{\mathbf{z}_k}(\mathbf{D} \otimes \mathbf{I}_{N_v})\,\mathbb{F} + \mathbf{G}_{k+1}. \tag{7.11}$$

The covariance matrix $\boldsymbol{\Sigma}_{\mathbf{z}_k+1}$ is obtained by using the relation in Equation (7.7),

$$\boldsymbol{\Sigma}_{\mathbf{z}_k+1} = (\mathbf{D}^{-\mathtt{H}} \otimes \mathbf{I}_{N_v})\boldsymbol{\Sigma}_{\mathbf{b}_k+1}(\mathbf{D}^{-1} \otimes \mathbf{I}_{N_v}). \tag{7.12}$$

This covariance state space model is similar to the one in [164]. Thus, as the size of the covariance matrix grows exponentially with N_p and N_v, the estimation of the covariance in Equation (7.11) becomes very computationally intensive.

7.2.4 Covariance Nearest Kronecker Product Approximation

In the measurement model described in Section 7.2.1, the rows and columns of the raw fast time measurement can be modeled as a function of two random processes.

The rows of the measurement matrix can be treated as an $(N_p \times 1)$ random vector, $\mathbf{q}_k$, representing a temporal random process and the columns can be treated as an $((N_v + N_s - 1) \times 1)$ random vector, $\mathbf{c}_k$, representing the spatial random process. In particular, assuming that the temporal and spatial vectors have the same distribution for all range bins and pulses, respectively, then we can model the measurement matrix $\mathbf{Y}_k$ in Equation (7.5) as the KP on the two random vectors using

$$\mathbf{Y}_k = \mathbf{q}_k^{\mathtt{H}} \otimes \mathbf{c}_k \,. \tag{7.13}$$

The above measurement matrix can be written in vector form $\mathbf{y}_k = \text{vec}(\mathbf{Y}_k)$ as

$$\mathbf{y}_k = \mathbf{q}_k \otimes \mathbf{c}_k.$$

Using the KP property A.1 in Appendix A [171], the covariance of $\mathbf{y}_k$ can be written as

$$\begin{aligned} \boldsymbol{\Sigma}_{\mathbf{y}_k} &= E[(\mathbf{q}_k \otimes \mathbf{c}_k)(\mathbf{q}_k \otimes \mathbf{c}_k)^{\mathtt{H}}] = E[\mathbf{q}_k \mathbf{q}_k^{\mathtt{H}} \otimes \mathbf{c}_k \mathbf{c}_k^{\mathtt{H}}] \\ &= \boldsymbol{\Sigma}_{\mathbf{q}_k} \otimes \boldsymbol{\Sigma}_{\mathbf{c}_k}, \end{aligned}$$

where $E[.]$ is the expectation operator. Therefore, if we assume that the underlying physical process follows the KP form, then the covariance of the measurement is also in the KP form. Thus, even though the underlying random process from which the pulse Doppler measurement is obtained follows the KP form, we still need to ensure that the KP form is preserved after matched filtering. The matched filter output vector is shown to be related to the pulse Doppler measurement using Equation (7.4) as

$$\begin{aligned} \mathbf{z}_k &= (\mathbf{I}_{N_p} \otimes \mathbf{M}_{Nv \times (N_v + Ns)})\mathbf{y}_k \\ &= (\mathbf{I}_{N_p} \otimes \mathbf{M}_{Nv \times (N_v + Ns)})(\mathbf{q}_k \otimes \mathbf{c}_k) \\ &= (\mathbf{q}_k \otimes \mathbf{M}\mathbf{c}_k). \end{aligned}$$

The covariance of $\mathbf{z}_k$ can be simplified as

$$\begin{aligned}\mathbf{\Sigma}_{\mathbf{z}_k} &= E[(\mathbf{q}_k \otimes \mathbf{M}\mathbf{c}_k)(\mathbf{q}_k \otimes \mathbf{M}\mathbf{c}_k)^{\mathtt{H}}] \\ &= E[\mathbf{q}_k\mathbf{q}_k^{\mathtt{H}} \otimes \mathbf{M}\mathbf{c}_k\mathbf{c}_k^{\mathtt{H}}\mathbf{M}^{\mathtt{H}}] \\ &= \mathbf{\Sigma}_{\mathbf{q}_k} \otimes \mathbf{M}\mathbf{\Sigma}_{\mathbf{c}_k}\mathbf{M}^{\mathtt{H}} \\ &= \mathbf{\Sigma}_{\mathbf{q}_k} \otimes \mathbf{\Sigma}_{\mathbf{r}_k}\end{aligned} \tag{7.14}$$

where $\mathbf{\Sigma}_{\mathbf{r}_k} = \mathbf{M}\mathbf{\Sigma}_{\mathbf{c}_k}\mathbf{M}^{\mathtt{H}}$. Thus, the matched filtered measurement also follows the KP form when the raw pulse Doppler measurement is in KP form. The covariance matrix of $\mathbf{b}_k$ in Equation (7.10) can then be written in KP form as

$$\mathbf{\Sigma}_{\mathbf{b}_k} = (\mathbf{D}^{\mathtt{H}} \otimes \mathbf{I}_{N_v})(\mathbf{\Sigma}_{\mathbf{q}_k} \otimes \mathbf{\Sigma}_{\mathbf{r}_k})(\mathbf{D} \otimes \mathbf{I}_{N_v}) = \mathbf{\Sigma}_{\mathbf{t}_k} \otimes \mathbf{\Sigma}_{\mathbf{r}_k}$$

where $\mathbf{\Sigma}_{\mathbf{t}_k} = \mathbf{D}^{\mathtt{H}}\mathbf{\Sigma}_{\mathbf{q}_k}\mathbf{D}$. Substituting the above equation in Equation (7.9), the state space model can be simplified as

$$\mathbf{\Sigma}_{\mathbf{b}_{k+1}} = \mathbb{F}^{\mathtt{H}}\left(\mathbf{\Sigma}_{\mathbf{t}_k} \otimes \mathbf{\Sigma}_{\mathbf{r}_k}\right)\mathbb{F} + \mathbf{G}_{k+1}\,. \tag{7.15}$$

In the above KP model, even if the covariance matrix $\mathbf{\Sigma}_{\mathbf{b}_k}$ at dwell k is in KP form, the covariance matrix at dwell $k+1$ does not have to be in KP form due to the structure of the state transition matrix $\mathbb{F}$. Using Equation (7.12), the covariance of the matched filter output is given by

$$\begin{aligned}\tilde{\mathbf{\Sigma}}_{\mathbf{z}_k+1} = {} & (\mathbf{D}^{-\mathtt{H}} \otimes \mathbf{I}_{N_v})\mathbb{F}^{\mathtt{H}}\left(\mathbf{\Sigma}_{\mathbf{t}_k} \otimes \mathbf{\Sigma}_{\mathbf{r}_k}\right)\mathbb{F}(\mathbf{D}^{-1} \otimes \mathbf{I}_{N_v}) \;+ \\ & (\mathbf{D}^{-\mathtt{H}} \otimes \mathbf{I}_{N_v})\mathbf{G}_{k+1}(\mathbf{D}^{-1} \otimes \mathbf{I}_{N_v}).\end{aligned} \tag{7.16}$$

In order to maintain the KP form for the covariance matrix of the measurement at the $(k+1)$th dwell transition, we impose the following covariance constraint on Equation (7.18),

$$\mathbf{\Sigma}_{\mathbf{z}_{k+1}} = \mathbf{\Sigma}_{\mathbf{q}_{k+1}} \otimes \mathbf{\Sigma}_{\mathbf{r}_{k+1}} = \arg\min_{\mathbf{\Sigma}_{\mathbf{q}_{k+1}},\mathbf{\Sigma}_{\mathbf{r}_{k+1}}} \parallel \tilde{\mathbf{\Sigma}}_{\mathbf{z}_{k+1}} - \mathbf{\Sigma}_{\mathbf{q}_{k+1}} \otimes \mathbf{\Sigma}_{\mathbf{r}_{k+1}} \parallel_{\mathcal{F}} \tag{7.17}$$

where $\| \cdot \|_{\mathcal{F}}$ is the Frobenius matrix norm [172]. The minimization problem in Equation (7.17) corresponds to a nearest KP approximation (NKPA) problem [169]; the solution is the cross product of the singular vector corresponding to the maximum singular value of the permuted version of $\tilde{\mathbf{\Sigma}}_{\mathbf{z}_{k+1}}$. Specifically, the covariance matrix $\tilde{\mathbf{\Sigma}}_{\mathbf{z}_{k+1}}$ can be written as a block matrix using a set of $(N_v \times N_v)$ sized sub-matrices $\tilde{\mathbf{\Sigma}}^{(i,j)}_{\mathbf{z}_{k+1}}$, representing the covariance matrix between the ith and jth columns of the measurement matrix $\mathbf{Z}_{k+1}$. Specifically, the covariance matrix can be written as

$$\tilde{\mathbf{\Sigma}}_{\mathbf{z}_{k+1}} = \begin{bmatrix} \tilde{\mathbf{\Sigma}}^{(1,1)}_{\mathbf{z}_{k+1}} & \tilde{\mathbf{\Sigma}}^{(1,2)}_{\mathbf{z}_{k+1}} & \dots & \tilde{\mathbf{\Sigma}}^{(1,N_p)}_{\mathbf{z}_{k+1}} \\ \vdots & \vdots & \dots & \vdots \\ \tilde{\mathbf{\Sigma}}^{(N_p,1)}_{\mathbf{z}_{k+1}} & \tilde{\mathbf{\Sigma}}^{(N_p,2)}_{\mathbf{z}_{k+1}} & \dots & \tilde{\mathbf{\Sigma}}^{(N_p,N_p)}_{\mathbf{z}_{k+1}} \end{bmatrix}.$$

The $(N_p^2 \times N_p^2)$ permuted version of the block matrix is written as

$$\tilde{\mathbf{\Sigma}}^{(p)}_{\mathbf{z}_{k+1}} = \begin{bmatrix} \operatorname{vec}(\tilde{\mathbf{\Sigma}}^{(1,1)}_{\mathbf{z}_{k+1}})^{\mathtt{H}} \\ \vdots \\ \operatorname{vec}(\tilde{\mathbf{\Sigma}}^{(N_p,1)}_{\mathbf{z}_{k+1}})^{\mathtt{H}} \\ \operatorname{vec}(\tilde{\mathbf{\Sigma}}^{(1,2)}_{\mathbf{z}_{k+1}})^{\mathtt{H}} \\ \vdots \\ \operatorname{vec}(\tilde{\mathbf{\Sigma}}^{(N_p,2)}_{\mathbf{z}_{k+1}})^{\mathtt{H}} \\ \vdots \\ \operatorname{vec}(\tilde{\mathbf{\Sigma}}^{(N_p,N_p)}_{\mathbf{z}_{k+1}})^{\mathtt{H}} \end{bmatrix}.$$

According to the NKPA method, the original minimization problem in Equation (7.17) is recasted into a modified minimization problem using the permuted matrix as

$$\boldsymbol{\Sigma}_{\mathbf{z}_{k+1}} = \boldsymbol{\Sigma}_{\mathbf{q}_{k+1}} \otimes \boldsymbol{\Sigma}_{\mathbf{r}_{k+1}} = \arg \min_{\boldsymbol{\Sigma}_{\mathbf{q}_{k+1}}, \boldsymbol{\Sigma}_{\mathbf{r}_{k+1}}} \parallel \tilde{\boldsymbol{\Sigma}}^{(p)}_{\mathbf{z}_{k+1}} - \mathrm{vec}(\boldsymbol{\Sigma}_{\mathbf{q}_{k+1}})\mathrm{vec}(\boldsymbol{\Sigma}_{\mathbf{r}_{k+1}})^{\mathtt{H}} \parallel_{\mathcal{F}} \ .$$

The solution to the above minimization problem is a singular value decomposition problem in which the permuted matrix is approximated by a rank one matrix obtained by the cross product between the left and right singular vectors corresponding to the maximum singular value [172].

Thus, solving the minimization problem in Equation (7.17) using the NKPA results in a drastically reduced computational complexity in estimating the measurement covariance matrix. Specifically, the NKPA reduces the number of matrix elements to be estimated from $(N_p N_v (N_p N_v + 1)/2)$ to $[N_p(N_p + 1) + N_v(N_v + 1)]/2$. For example, if $N_p = 10$ pulses and $N_v = 10$ range bins, the element estimation reduction is from 5,050 to 110 elements.

7.3 Validation of KP Approximation Using Real Sea Clutter Measurement

We validated the KP form of the sea clutter covariance matrix using real clutter data from the DSTO INGARA radar sea clutter database [138]. The clutter data was obtained using the following radar parameter: 96 MHz signal bandwidth, 8 μs pulse width, 9.375 GHz carrier frequency, 500 Hz pulse repetition frequency, 1.5 m range resolution, and vertical-transmit, vertical-receive polarization. The wind speed was at 10-12 knots, resulting in a 2-3 sea state [138]. As the true covariance matrix was not available, the NKPA was validated using the sample covariance matrix, obtained by averaging across multiple dwells and calculated by constructing a measurement dwell with $N_p = 10$ pulses and $N_v = 10$ range bins. Figure 7.2(a) shows the singular values of the permuted sample covariance matrix computed by averaging over 4,000 dwells from 3 different data sets. The first singular value was the most dominant one

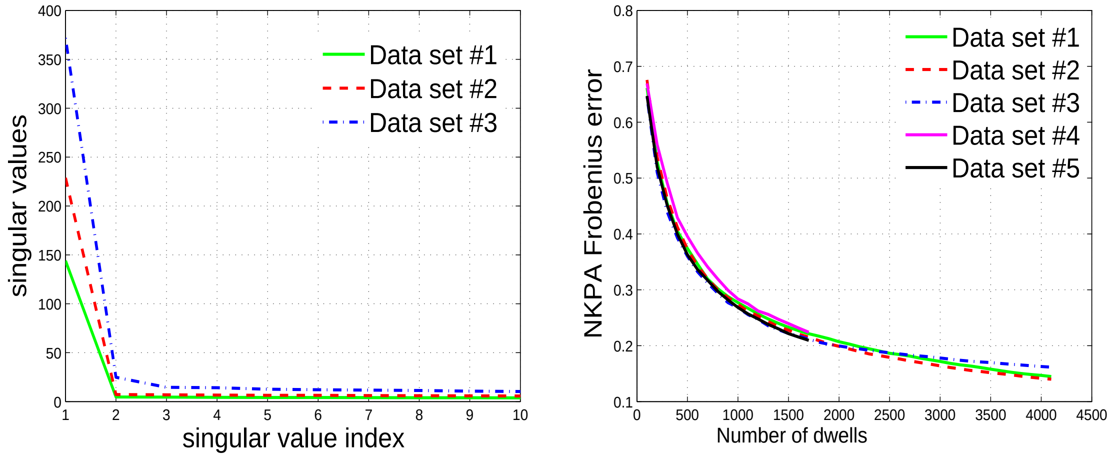

(a)

(b)

Figure 7.2: (a) Singular Value of the Permuted Covariance Matrix. (b) NKPA Error for Different Number of Dwells for Estimating the Sample Covariance Matrix.

for all 3 sets, thus most of the energy could be compacted by a single NKPA. The KP approximation quality is evaluated by calculating the normalized Frobenius error [172] as

$$e_{\mathcal{F}}(\tilde{\boldsymbol{\Sigma}}_{\mathbf{z}_k}, \boldsymbol{\Sigma}_{\mathbf{z}_k}) = \frac{\| \tilde{\boldsymbol{\Sigma}}_{\mathbf{z}_k} - \boldsymbol{\Sigma}_{\mathbf{z}_k} \|_{\mathcal{F}}}{\| \tilde{\boldsymbol{\Sigma}}_{\mathbf{z}_k} \|_{\mathcal{F}}} .$$

Figure 7.2(b) shows the normalized Frobenius norm error between the sample covariance and the NKPA as a function of sample size. As it can be seen, the error decreases as the number of samples increases implying that, as the sample covariance matrix asymptotically approaches the true covariance matrix, the approximation error is reduced. The approximation error is less than 0.2 for all data sets, indicating that the NKPA is a reasonable approximation to use.

7.4 Covariance Matrix Estimation Using Sequential Monte Carlo Technique

7.4.1 Estimation Approach

As the state model in Equation (7.15) is not linear, we use PF to estimate the covariance matrix elements [16]. The PF represents the spatial ($\boldsymbol{\Sigma}_{\mathbf{r}_k}$) and the temporal ($\boldsymbol{\Sigma}_{\mathbf{q}_k}$) covariance matrices by a set of particles $\boldsymbol{\Sigma}_{\mathbf{r}_k}^{(n)}$ and $\boldsymbol{\Sigma}_{\mathbf{q}_k}^{(n)}$, respectively, and corresponding weights $w^{(n)}$, $n = 1, \ldots, N$. Given the initial particle states, the predicted matrices at dwell $k+1$ are obtained using the state model in Equation (7.18). The predicted particles are updated using the clutter measurement likelihood function. Assuming that the clutter measurement vector in a dwell follows a circularly symmetric complex Gaussian distribution, and assuming that we have N_T independent and identically distributed dwells, the joint PDF of the measurement vector is given by

$$p(\mathbf{z}_k, \mathbf{z}_{k-1} \ldots \mathbf{z}_{k-N_T} | \boldsymbol{\Sigma}_{\mathbf{z}_k}) = \frac{1}{\pi^{N_p N_v N_T} |\boldsymbol{\Sigma}_{\mathbf{z}_k}|^{N_T}} \exp\left[\sum_{i=k-N_T}^{k-1} -\mathrm{tr}\left(\boldsymbol{\Sigma}_{\mathbf{z}_k}^{-1} \mathbf{z}_i \mathbf{z}_i^{\mathbf{H}} \right) \right]$$

where $\mathrm{tr}(\cdot)$ is the trace of a matrix. Here, we assume that the clutter statistics do not drastically change while the $(N_T + 1)$ measurements corresponding to past and current dwells are acquired. Since we assumed that the covariance matrix of the measurement is in KP form, i.e., $\boldsymbol{\Sigma}_{\mathbf{z}_k} = \boldsymbol{\Sigma}_{\mathbf{q}_k} \otimes \boldsymbol{\Sigma}_{\mathbf{r}_k}$, we obtain

$$\begin{aligned} p(\mathbf{z}_k, \mathbf{z}_{k-1} \ldots \mathbf{z}_{k-N_T} | \boldsymbol{\Sigma}_{\mathbf{z}_k}) &= \frac{|\boldsymbol{\Sigma}_{\mathbf{q}_k} \otimes \boldsymbol{\Sigma}_{\mathbf{r}_k}|^{-N_T}}{\pi^{N_p N_v N_T}} \exp\left[\sum_{i=k-N_T}^{k} -\mathrm{tr}\left((\boldsymbol{\Sigma}_{\mathbf{q}_k} \otimes \boldsymbol{\Sigma}_{\mathbf{r}_k})^{-1} \mathbf{z}_i \mathbf{z}_i^{\mathbf{H}} \right) \right] \\ &= \frac{|\boldsymbol{\Sigma}_{\mathbf{q}_k}|^{-N_T N_v} |\boldsymbol{\Sigma}_{\mathbf{r}_k}|^{-N_T N_p}}{\pi^{N_p N_v N_T}} \exp\left[-N_T \mathrm{tr}\left((\boldsymbol{\Sigma}_{\mathbf{q}_k}^{-1} \otimes \boldsymbol{\Sigma}_{\mathbf{r}_k}^{-1}) \hat{\boldsymbol{\Sigma}}_{z_k} \right) \right] \end{aligned}$$

where we used the KP properties A.4 and A.5 in Appendix A on any two square and invertible matrices. The sample covariance matrix in KP form is obtained from the measurement using the NKPA as

$$\hat{\boldsymbol{\Sigma}}_{z_k} = \arg \min_{\hat{\boldsymbol{\Sigma}}_{\mathbf{q}_k}, \hat{\boldsymbol{\Sigma}}_{\mathbf{r}_k}} \parallel \frac{1}{N_T} \sum_{i=k-N_T}^{k-1} \mathbf{z}_i \mathbf{z}_i^{\mathtt{H}} - \hat{\boldsymbol{\Sigma}}_{\mathbf{q}_k} \otimes \hat{\boldsymbol{\Sigma}}_{\mathbf{r}_k} \parallel_{\mathcal{F}}$$

Since the clutter can be fast varying, the number of samples used for the sample covariance estimate is usually much smaller than the vector dimension, i.e., $N_T \ll N_p\, N_v$. If we do not use the NKPA on the covariance matrix, the maximum likelihood estimate (MLE) is the sample covariance matrix, which is positive definite only if $N_T \geq N_p\, N_v$. However, by assuming the NKPA, the MLE in KP form is positive definite as long as $N_T \geq \max\left\{\frac{N_v}{N_p}, \frac{N_p}{N_v}\right\} + 1$ [173, 174].

Given the measurement vector, the particle weights are set proportional to the likelihood function

$$w^{(n)} \propto l\Big(\mathbf{z}_k |\ \boldsymbol{\Sigma}_{\mathbf{q}_k}^{(n)}, \boldsymbol{\Sigma}_{\mathbf{r}_k}^{(n)}\Big)\ .$$

The likelihood function given the measurement vector can now be derived as

$$\begin{aligned} l\Big(\mathbf{z}_k |\ \boldsymbol{\Sigma}_{\mathbf{q}_k}^{(n)}, \boldsymbol{\Sigma}_{\mathbf{r}_k}^{(n)}\Big) &= \frac{|\boldsymbol{\Sigma}_{\mathbf{q}_k}|^{-N_v} |\boldsymbol{\Sigma}_{\mathbf{r}_k}|^{-N_p}}{\pi^{N_p N_v}} \exp\left[-\operatorname{tr}\Big((\boldsymbol{\Sigma}_{\mathbf{q}_k}^{(n)})^{-1} \hat{\boldsymbol{\Sigma}}_{\mathbf{q}_k} \otimes (\boldsymbol{\Sigma}_{\mathbf{r}_k}^{(n)})^{-1} \hat{\boldsymbol{\Sigma}}_{\mathbf{r}_k} \Big) \right] \\ &= \frac{|\boldsymbol{\Sigma}_{\mathbf{q}_k}|^{-N_v} |\boldsymbol{\Sigma}_{\mathbf{r}_k}|^{-N_p}}{\pi^{N_p N_v}} \exp\left[-\operatorname{tr}\Big((\boldsymbol{\Sigma}_{\mathbf{q}_k}^{(n)})^{-1} \hat{\boldsymbol{\Sigma}}_{\mathbf{q}_k} \Big) \operatorname{tr}\Big((\boldsymbol{\Sigma}_{\mathbf{r}_k}^{(n)})^{-1} \hat{\boldsymbol{\Sigma}}_{\mathbf{r}_k} \Big) \right] \end{aligned}$$

where we have used the KP property A.3 in Appendix A. Here, the likelihood function computation is simplified since we compute the inverse and determinant of two matrices of low dimension instead of one matrix of higher dimension.

We demonstrate next that the positive definiteness of the covariance matrix estimate is preserved. Assuming that the initial covariance matrices $\boldsymbol{\Sigma}_{\mathbf{q}_k}$, $\boldsymbol{\Sigma}_{\mathbf{r}_k}$ and the modeling error matrix $\mathbf{G}_{k+1}$ are positive definite, then $\boldsymbol{\Sigma}_{\mathbf{b}_{k+1}}$ in Equation (7.15) is also positive definite. Using Equation (7.10), $\hat{\boldsymbol{\Sigma}}_{\mathbf{z}_{k+1}}$ in Equation (7.17) is also positive definite since, for a symmetric positive definite matrix, the solution to the NKPA also results in symmetric positive definite matrices [169]. Therefore, $\boldsymbol{\Sigma}_{\mathbf{q}_{k+1}}$ and $\boldsymbol{\Sigma}_{\mathbf{c}_{k+1}}$ in

Equation (7.17) are positive definite. Since all the particles correspond to positive definite matrices, the updated particles also correspond to positive definite matrices. This ensures that the proposed covariance matrix estimate is always positive definite.

7.4.2 Simulations

We demonstrated the PF implementation of the covariance estimation using an linear frequency modulated (LFM) signal with bandwidth $f_s = 15$ MHz, $f_c = 9.375$ GHz carrier frequency, $T_{\text{PRI}} = 2$ ms, $N_p = 11$ pulses per dwell, $N_s = 6$ samples, [8,000 8,300] m validation gate range, 10 m range resolution, 30 range bins and 60 rpm beam scan rate. The initial covariance matrix $\mathbf{\Sigma}_{z_0}$ was obtain assuming compound Gaussian distributed clutter whose speckle and texture correlation was based on real clutter from the Osborne Head Gunnery Range (OHGR) IPIX radar [110, 161]. The speckle samples were drawn from a circularly symmetric complex Gaussian distribution, and the texture components were distributed based on a gamma distribution. The sample covariance matrix was calculated from 3,300 independent dwell measurements. The fast time clutter measurement was obtained by drawing samples from a complex Gaussian distribution with the covariance matrix derived at each dwell using Equation (7.17). Figure 7.3 shows the transitioned covariance matrices at dwells 5 and 40. As can be seen from the figure, the covariance matrix structure at dwell 40 evolved differently from dwell 5 in accordance with the selected state transition matrix $\mathbb{F}$ in Equation (7.8).

We compared the mean-squared error (MSE) between the true and estimated temporal and spatial covariance matrices using a varying number of (50, 100, 250, and 500) particles in Figure 7.4, averaged over 25 Monte Carlo simulations. Also shown is the tracking MSE for the sample covariance matrix and its corresponding NKPA. The sample covariance matrix is obtained by averaging the measurement from

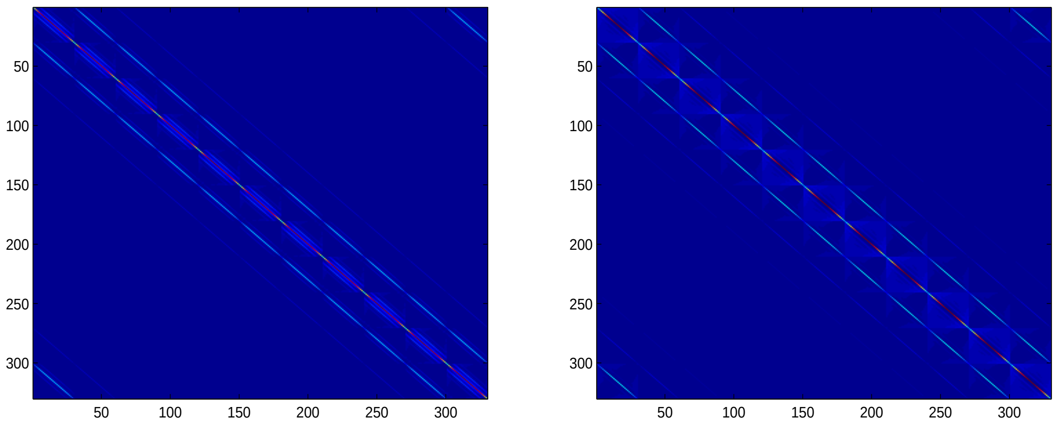

(a) (b)

Figure 7.3: Sea Clutter Covariance Matrix: (a) Dwell 5; and (b) Dwell 40.

five dwells. The tracking MSE for the sample covariance matrix is much higher; the MSE is somewhat reduced when the NKPA of the sample covariance matrix is used. The tracking MSE of our proposed estimation approach outperformed the other two methods. The improved performance of the covariance matrix estimation is due to exploiting the underlying physical model of the sea structure using the transition matrix $\mathbb{F}$ in Equation (7.8). Note that the tracking MSE can also be reduced by increasing the number of particles.

7.5 Track-before-detect Filtering in Sea Clutter

7.5.1 Track-before-detect Filtering Formulation with Clutter

In this section, we use the proposed NKPA-based covariance matrix estimation to track a low observable target in the presence of sea clutter. We consider a target moving in a two-dimensional (2-D) plane with state vector $\mathbf{x}_k = [x_k\, \dot{x}_k\, y_k\, \dot{y}_k]^{\mathtt{T}}$, where (x_k, y_k) and $(\dot{x}_k, \dot{y}_k)$ are the 2-D Cartesian coordinates of the target position and

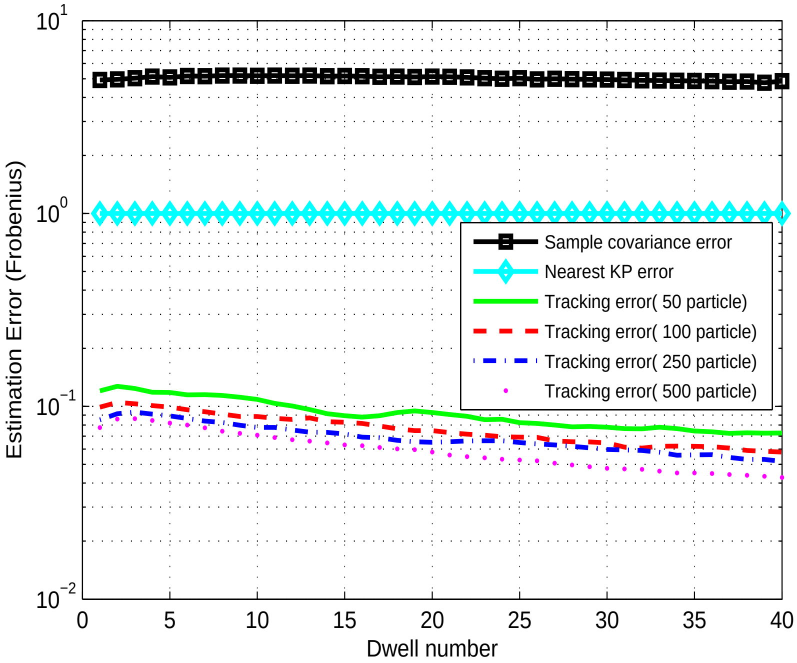

Figure 7.4: Covariance Matrix Estimation (Frobenius) Error

velocity, respectively, at the kth dwell. The target state is modeled as $\mathbf{x}_k = \mathbf{F}\mathbf{x}_{k-1} + \mathbf{w}_k$, where $\mathbf{F}$ is a state transition matrix for a constant velocity model described in Equation (2.6) and $\mathbf{w}_k$ is the modeling error.

The single target efficient PF based TBDF algorithm [53] described in Section 3.3 is modified for use with the measurement model. Using this algorithm, a target leaving the FOV and a target already in the FOV are represented by two sets of particles. The posterior probability density of the target is obtained as a weighted combination of the particles from both sets. The measurement component associated with the target is also present in the neighborhood of the range bin under testing (in which the target is present). This component is governed by the correlation properties of the transmitted signal [45]. Thus, detection and tracking must be performed using all the neighborhood range bins, including the range bin under testing. Specifically, for a target present at range bin ζ_k, the measurement data is extracted from the measurement matrix $\mathbf{Z}_k$ (that contains both the target and clutter) as

$$\mathbf{z}_{k,\zeta_k} = \mathrm{vec}\left(\begin{bmatrix} \mathbf{Z}_k[\zeta_k - N_h, 0] & \mathbf{Z}_k[\zeta_k - N_h, 1] & \ldots & \mathbf{Z}_k[\zeta_k - N_h, N_p - 1] \\ \vdots & \vdots & \vdots & \vdots \\ \mathbf{Z}_k[\zeta_k, 0] & \mathbf{Z}_k[\zeta_k, 1] & \ldots & \mathbf{Z}_k[\zeta_k, N_p - 1] \\ \vdots & \vdots & \vdots & \vdots \\ \mathbf{Z}_k[\zeta_k + N_h, 0] & \mathbf{Z}_k[\zeta_k + N_h, 1] & \ldots & \mathbf{Z}_k[\zeta_k + N_h, N_p - 1] \end{bmatrix}\right)$$

where N_h is the number of neighborhood bins. The covariance matrix $\mathbf{\Sigma}_{\mathbf{z}_{k,\zeta_k}}$ that corresponds to this vector is a principal sub-matrix of the full covariance matrix estimated in Section 7.2.4. This sub-matrix is also positive definite since any principal sub-matrix of a positive definite matrix is also positive definite [172]. Figure 7.5 illustrates the extraction of a submatrix from a complete covariance matrix for $N_v = 5, N_h = 1$ and $\zeta_k = 3$.

In an actual tracking application, estimating the clutter covariance matrix is a challenging problem as the measurements include the target component. In practice, the clutter is assumed homogeneous so that the clutter covariance can be estimated using range bins in the neighborhood of the range bin under testing. If the clutter is heterogeneous, then this assumption can lead to poor detection performance. Here, we exploit the state space clutter model to predict the clutter covariance matrix $\mathbf{\Sigma}_{\mathbf{z}_{k,\zeta_k}}$ from the previous clutter covariance matrix estimate $\mathbf{\Sigma}_{\mathbf{z}_{k-k_0,\zeta_k}}$. Specifically, we assume that the probability that the target is still present in range bin ζ_k at the $(k - k_0)$th dwell is very low. Thus, the sub-matrix $\mathbf{\Sigma}_{\mathbf{z}_{k,\zeta_k}}$ can be extracted from the

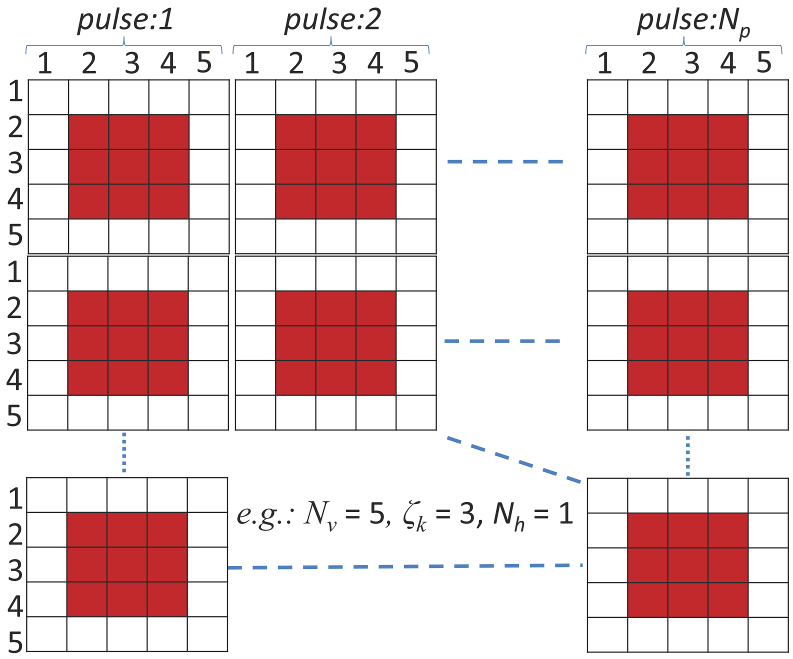

Figure 7.5: Illustration of Extracting a Principal Submatrix.

predicted covariance matrix $\mathcal{S}_{\mathbf{z}_k}$ that is obtained as

$$\begin{aligned}
\mathcal{S}_{\mathbf{z}_{k-k_0+1}} &= \mathrm{NKPA}[(\mathbf{D}^{-\mathtt{H}} \otimes \mathbf{I}_{N_v})\mathbb{F}^{\mathtt{H}}(\mathbf{D}^{\mathtt{H}}\boldsymbol{\Sigma}_{\mathbf{q}_{k-k_0}}\mathbf{D} \otimes \boldsymbol{\Sigma}_{\mathbf{r}_{k-k_0}})\mathbb{F}(\mathbf{D}^{-1} \otimes \mathbf{I}_{N_v})] \\
&\vdots \\
\mathcal{S}_{\mathbf{z}_k} &= \mathrm{NKPA}[(\mathbf{D}^{-\mathtt{H}} \otimes \mathbf{I}_{N_v})\mathbb{F}^{\mathtt{H}}(\mathbf{D}^{\mathtt{H}}\mathcal{S}_{\mathbf{q}_{k-1}}\mathbf{D} \otimes \mathcal{S}_{\mathbf{r}_{k-1}})\mathbb{F}(\mathbf{D}^{-1} \otimes \mathbf{I}_{N_v})]
\end{aligned}$$

where NKPA[$\mathbf{A}$] is the NKPA of a matrix $\mathbf{A}$. When a target is present in a range bin, the corresponding measurement vector is given by

$$\mathbf{z}_{k,\zeta_k} = \mathbf{a}_{k,\zeta_k}(\beta_k, \nu_k) + \mathbf{c}_{k,\zeta_k}$$

where β_k corresponds to the target reflectivity, ν_k is the target's Doppler shift and $\mathbf{c}_{k,\zeta_k}$ represents the clutter vector. If we define the cross-correlation of the transmitted signal as

$$a_s[n] = \sum_{m=0}^{N_s-1} s[m]s^*[m-n]\,,$$

then the signal vector $\mathbf{a}_{k,\zeta_k}$ is obtained by vectorizing the matrix formed by stacking the vectors $[a_s[m]\, a_s[m]e^{j2\pi\nu_k T_{\mathrm{PRI}}} \ldots a_s[m]e^{j2\pi\nu_k(N_p-1)T_{\mathrm{PRI}}}]^{\mathtt{T}}$, $m = -N_h, \ldots, N_h$ as

$$\mathbf{a}_{k,\zeta_k}(\beta_k, \nu_k) = \mathrm{vec}\left(\beta_k \begin{bmatrix} a_s[-N_h] & a_s[-N_h]e^{j2\pi\nu_k T_{\mathrm{PRI}}} & \ldots & a_s[-N_h]e^{j2\pi\nu_k(N_p-1)T_{\mathrm{PRI}}} \\ \vdots & \vdots & \vdots & \vdots \\ a_s[0] & a_s[0]e^{j2\pi\nu_k T_{\mathrm{PRI}}} & \ldots & a_s[0]e^{j2\pi\nu_k(N_p-1)T_{\mathrm{PRI}}} \\ \vdots & \vdots & \vdots & \vdots \\ a_s[N_h] & a_s[N_h]e^{j2\pi\nu_k T_{\mathrm{PRI}}} & \ldots & a_s[N_h]e^{j2\pi\nu_k(N_p-1)T_{\mathrm{PRI}}} \end{bmatrix}\right).$$

The detection and tracking is performed using the entirety of the selected vector $\mathbf{z}_{k,\zeta_k}$. Assuming that the clutter follows the circularly-symmetrix complex Gaussian distribution, the likelihood ratio given a target state vector is given by

$$\begin{aligned} l(\mathbf{z}_k|\mathbf{x}_k) &= \exp\left\{-\mathbf{z}_k^{\mathtt{H}}\mathcal{S}^{-1}_{z_k,\zeta_k}\mathbf{z}_k + (\mathbf{z}_k - \beta_k\mathbf{a}_k)^{\mathtt{H}}\mathcal{S}^{-1}_{z_k,\zeta_k}(\mathbf{z}_k - \beta_k\mathbf{a}_k)\right\} \\ &= \exp\left\{-|\beta_k|^2\mathbf{a}_k^{\mathtt{H}}\mathcal{S}^{-1}_{z_k,\zeta_k}\mathbf{a}_k + 2\Re\left(\beta_k^*\mathbf{a}_k^{\mathtt{H}}\mathcal{S}^{-1}_{z_k,\zeta_k}\mathbf{z}_k\right)\right\} \end{aligned}$$

where $\Re(.)$ denotes the real part of a complex number and for notational clarity, we dropped the suffix ζ_k in $\mathbf{z}_{k,\zeta_k}$ and $\mathbf{a}_{k,\zeta_k}$. The above likelihood ratio is a function of the target reflectivity also. The argument inside the exponential function in the likelihood ratio can be expanded as

$$-|\beta_k|^2\mathbf{a}_k^{\mathtt{H}}\mathcal{S}^{-1}_{k,\zeta_k}\mathbf{a}_k + 2\Re\left(\beta_k^*\mathbf{a}_k^{\mathtt{H}}\mathcal{S}^{-1}_{k,\zeta_k}\mathbf{z}_k\right) = -\mathbf{a}_k^{\mathtt{H}}\mathcal{S}^{-1}_{k,\zeta_k}\mathbf{a}_k\left|\beta_k - \frac{\mathbf{a}_k^{\mathtt{H}}\mathcal{S}^{-1}_{k,\zeta_k}\mathbf{z}_k}{\mathbf{a}_k^{\mathtt{H}}\mathcal{S}^{-1}_{k,\zeta_k}\mathbf{a}_k}\right|^2 + \frac{|\mathbf{a}_k^{\mathtt{H}}\mathcal{S}^{-1}_{k,\zeta_k}\mathbf{z}_k|^2}{\mathbf{a}_k^{\mathtt{H}}\mathcal{S}^{-1}_{k,\zeta_k}\mathbf{a}_k}\,.$$

Since $\mathcal{S}^{-1}_{k,\zeta_k}$ is a positive definite matrix, $\mathbf{a}_k^{\mathtt{H}}\mathcal{S}^{-1}_{k,\zeta_k}\mathbf{a}_k > 0$, and the exponential argument is maximized only when

$$\beta_k = \frac{\mathbf{a}_k^{\mathtt{H}}\mathcal{S}^{-1}_{k,\zeta_k}\mathbf{z}_k}{\mathbf{a}_k^{\mathtt{H}}\mathcal{S}^{-1}_{k,\zeta_k}\mathbf{a}_k}\,.$$

The generalized likelihood function is derived by substituting this value of β_k in the likelihood function,

$$l(\mathbf{z}_k|\mathbf{x}_k) \quad = \quad \exp\left\{\frac{|\mathbf{a}_k^{\mathtt{H}}\mathcal{S}_{k,\zeta_k}^{-1}\mathbf{z}_k|^2}{\mathbf{a}_k^{\mathtt{H}}\mathcal{S}_{k,\zeta_k}^{-1}\mathbf{a}_k}\right\}.$$

For real β_k, the likelihood ratio is maximized when,

$$\beta_k = \frac{\Re(\mathbf{a}_k^{\mathtt{H}}\mathcal{S}_{k,\zeta_k}^{-1}\mathbf{z}_k)}{\mathbf{a}_k^{\mathtt{H}}\mathcal{S}_{k,\zeta_k}^{-1}\mathbf{a}_k}$$

and the corresponding generalized likelihood ratio is written as

$$l(\mathbf{z}_k|\mathbf{x}_k) \quad = \quad \exp\left\{\frac{[\Re(\mathbf{a}_k^{\mathtt{H}}\mathcal{S}_{k,\zeta_k}^{-1}\mathbf{z}_k)]^2}{\mathbf{a}_k^{\mathtt{H}}\mathcal{S}_{k,\zeta_k}^{-1}\mathbf{a}_k}\right\}.$$

The above derived likelihood ratio is used in the particle update stage of the efficient PF based TBDF algorithm in Section 3.3.

7.5.2 Simulations

We applied the clutter estimation approach to a target tracking problem with similar parameters as in the previous simulation. We compared the performance of the algorithm to track a low observable target moving at constant velocity under varying SCR values. The target is assumed to leave and enter the FOV at dwells 5 and 30, respectively. The initial position and velocity for the target were set to (5,825.7, 5,825.7) m and (-5.4, -5.4) m/s, respectively. Figures 7.6(a), 7.6(b), and 7.6(c) show the measurement matrix for 9, 6, 3 dB SCRs, respectively. The target is hardly visible at 6 dB and 3 dB SCR values and the clutter distribution is spiky in nature with lots of target like components. Figure 7.7 shows the cross correlation of the baseband signal for different time lags. The cross-correlation is dominated by the correlation at zero time lag and it dominates even more when the bandwidth of the baseband signal is increased. Since the main objective of the TBDF method is

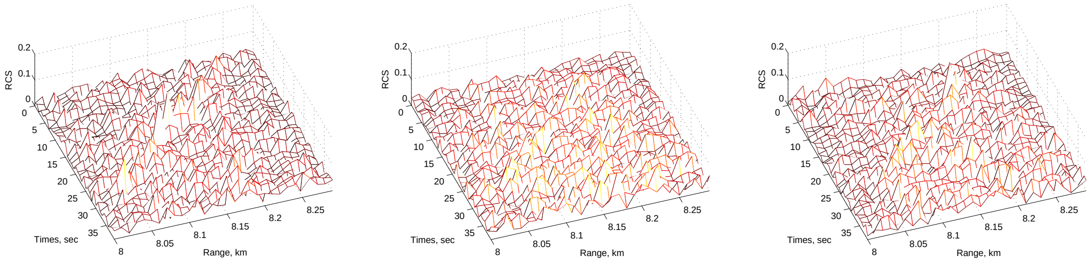

(a) (b) (c)

Figure 7.6: Pulse Doppler Radar Measurements: (a) SCR = 9dB; (b) SCR = 6 dB; and (c) SCR = 3 dB.

to track a target under low SCR conditions, the low energy cross-correlation values do not significantly contribute to the detection of a target in the presence of high clutter, we thus set $N_h = 3$.

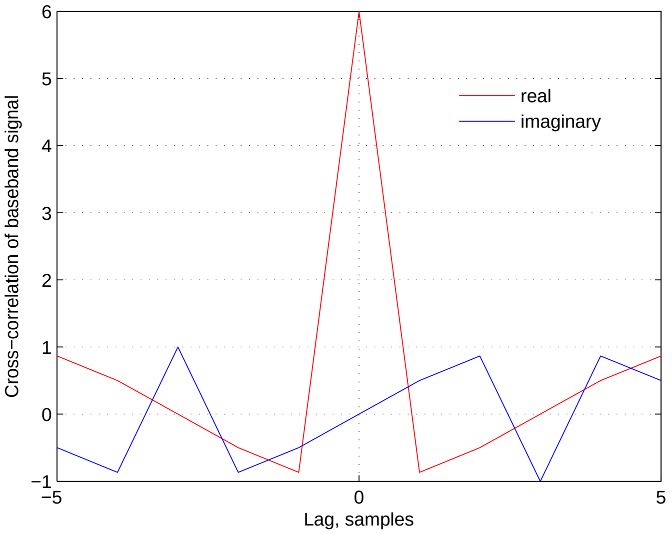

Figure 7.7: Cross-Correlation of the Baseband Signal.

The PF used 500 particles when the target survived and 2,500 particles when the target entered the FOV. The tracking error is quantified using the OSPA metric with parameters $c = 100$ and $p = 2$ [105], averaged over 25 Monte Carlo simulations. The tracking performance was analyzed under two conditions: (i) the measurement was generated as in Equation (7.10) and the covariance was estimated using Equations (7.15) and (7.17); (ii) both the measurement and the covariance followed the NKPA in Equations (7.15) and (7.17). Figures 7.11(a) and 7.11(c) show the probability of target existence and the tracking error for different SCRs. The latency in detecting a target increased as the SCR decreased. Similarly, there was delay in detecting a target leaving the FOV. The probability of detection was very low at 3 dB SCR and the tracking error was high. As the probability of detection was in general low, the probability of detecting a target leaving the FOV at 3 dB was also low, as evident by lower OSPA values during dwells 30-35. At 6 dB SCR, the probability of detection increased when the true model did not follow the NKPA; however, this did not result in improved tracking performance due to the higher OPSA values. In general, the tracking performance improved when the true and assumed models followed the NKPA. Nevertheless, the performance did not degrade significantly when the assumed (but not the true) model followed the NKPA. This result is relevant to real target tracking applications since, even if the actual covariance does not completely follow the KP structure, we can apply the NKPA without significantly affecting the tracking performance.

In the next simulation, we compare the tracking performance of the NKPA method with a TBDF method discussed in the previous chapter. Specifically, we used the asymptotic, linear quadratic (LQ) method discussed in Section 6.5.1 with the compound Gaussian assumption (CG-LQ). The covariance matrix for the likelihood function in Equation (6.16) is estimated using the normalized sample covariance method in Equation (6.19). The measurements are generated such that the KP property is not maintained. Figure 7.9 compares the tracking performance at 12, 9, 6 and 3 dB SCR conditions. The tracking performance of both the NKPA and CG-LQ methods

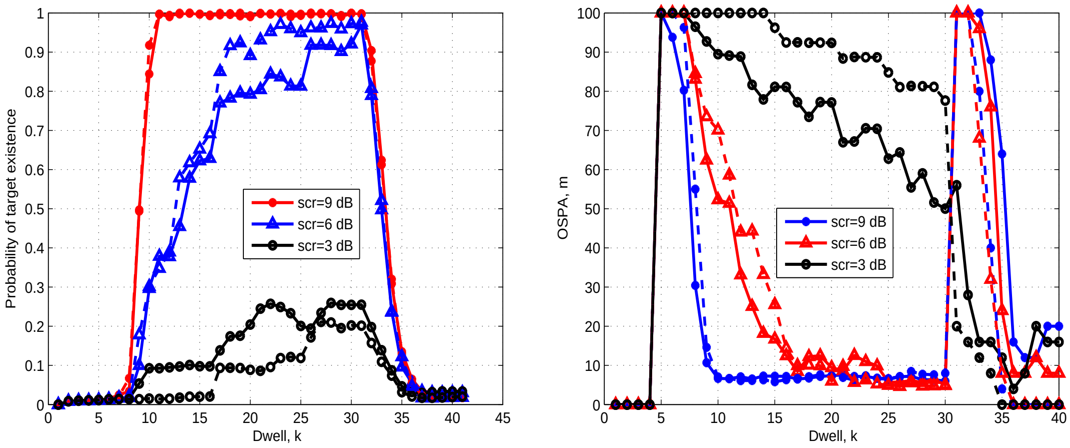

(a) (b)

Figure 7.8: (a) Probability of Target Existence; and (b) Tracking Error for Varying SCR: True and Assumed KP Models (Solid), and Assumed KP Model Only (Dash).

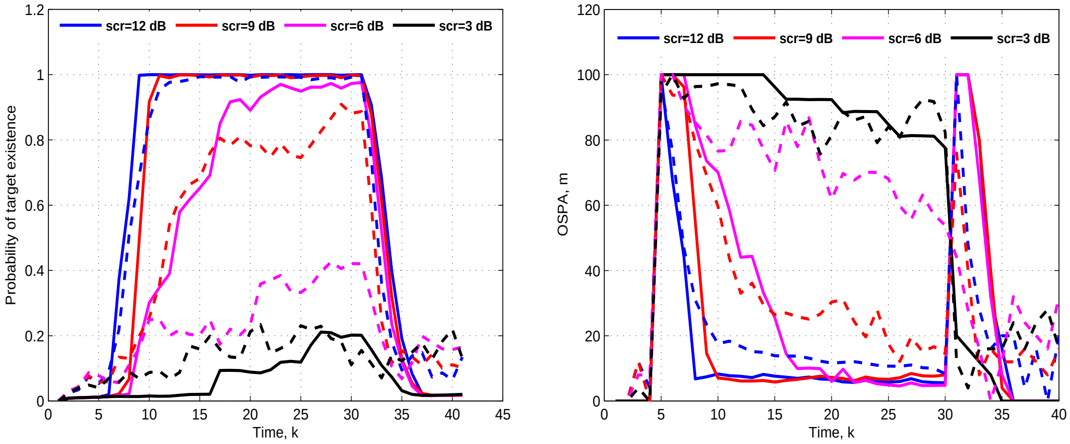

(a) (b)

Figure 7.9: (a) Probability of Target Existence; and (b) Tracking Error for Varying SCR: KP (Solid) and CG-LQ (Dash).

are comparable at 12 dB SCR. At lower SCR conditions, the target existence probability shown in Figure 7.9(a) is very different between the two methods. Specifically, the CG-LQ method with the independent range bin assumption results in very poor detection performance when the range bins in the measurement are correlated. On the other hand, the NKPA method processed with the space-time covariance matrix produces a much improved detection performance. The tracking performance shown in Figure 7.9(b) also follows a similar trend. Specifically, the tracking error using the NKPA method becomes significantly higher at 3 dB SCR, whereas with the CG-LQ method, the performance starts to deteriorate at 6 dB SCR. Therefore, by using the estimated space-time covariance matrix, we can expect to get improved detection and tracking performance.

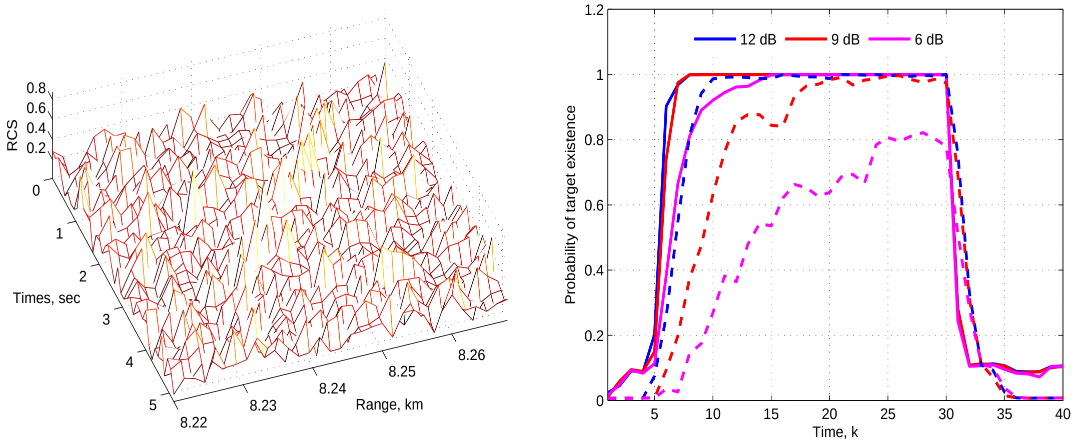

(a) (b)

Figure 7.10: (a) Real Sea Clutter Embedded with Synthetic Target at 12 dB SCR; and (b) Probability of Target Existence Probability Comparison with Real Sea Clutter: KP (Solid) and CG-LQ (Dash).

In the next simulation, we used the real sea clutter measurement from the IPIX radar described in Section 7.3 in which the pulse width of the radar is $N_s = 800$ samples. The measurement corresponding to the target is synthetically generated using the same parameters used in the IPIX radar. The FOV is set at [8,220 8,268.5] m resulting in 33 range bins at 1.5 m resolution and the number of pulses used for coherent processing is set at $N_p = 11$ and $N_h = 1$. The (33×11) clutter measurements are obtained using Equation (7.4) by matched filtering the raw measurements from 832 range bins that are extracted from the real recordings. The target associated measurement dwells are synthesized from the reflectivity matrix that contains 1632 range bins. The initial states for the target is set at (5,839.8 5,839.8) m and (-5.4 -5.4) m/s, and the target enters and leaves the FOV at time steps 5 and 30, respectively. Figure 7.10(a) shows the real sea clutter mixed with the synthetic target associated measurement at 12 dB SCR. The tracking performance of the NKPA and the CG-LQ methods is compared at 12, 9 and 6 dB SCR conditions at the matched filter output. The tracking performance was compared by setting the OSPA parameters to $c = 40$ and $p = 2$. Figure 7.10(b) shows the estimated target existence probability for both methods. As the clutter level is increased, it takes more time to detect the target with both methods. However, the detection rate of the CG-LQ method is significantly worse at 9 and 6 dB SCR. Figure 7.11 shows the corresponding tracking performance for both methods. When compared with the NKPA method, the CG-LQ method takes more time to detect a target when the SCR is reduced. Moreover, at 6 dB SCR, the localization error is also poor in addition to an increased cardinality error. Thus, for real sea clutter measurements, the NKPA method provides promising results when compared with the CG-LQ method in which the clutter statistics are computed from the neighbourhood range bins that are not independent of each other.

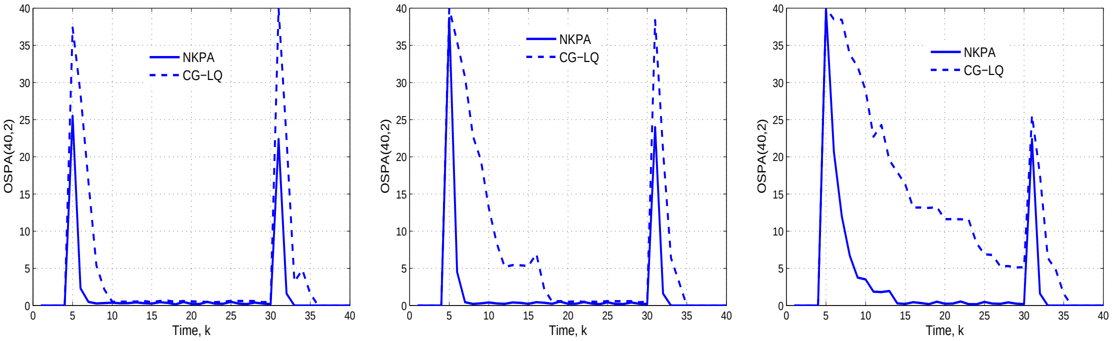

(a)

(b)

(c)

Figure 7.11: Tracking Error Comparison with Real Sea Clutter: (a) SCR=12 dB; (b) SCR = 9 dB; and (c) SCR = 6 dB.

Chapter 8

CONCLUSION AND FUTURE WORK

8.1 Conclusion

In this thesis, we derived a track-before-detect filter (TBDF) algorithm to track a varying number of targets under low signal-to-noise ratio (SNR) and low signal-to-clutter ratio (SCR) conditions that can be implemented using sequential Monte Carlo (SMC) techniques. The multiple target TBDF estimates the target states under all possible target existence combinations or modes using the derived multiple target joint posterior probability density function. The resulting multiple mode multiple target TBDF (MM-MT-TBDF) approach can keep track of targets entering or leaving a scene, and only the maximum number of targets over the duration of a track needs to be assumed known; the value of this number can be selected based on the application. As we demonstrated, the proposed MM-MT-TBDF algorithm resulted in adequate tracking performance, using the OSPA metric, when the SNR was as low as 0 dB. The algorithm was also shown to successfully track a much larger number of targets than other proposed methods in the literature. We also demonstrate that the MM-MT-TBDF performed better when compared to the probability hypothesis density TBDF for a simulation example using image measurements.

The MM-MT-TBDF is computationally expensive as most multiple target tracking algorithms due to the large number of combinatorial choices that need to be computed. In order to reduce the computational complexity without greatly affecting the tracking accuracy under severe tracking conditions, we introduced various techniques such as partition based proposal sampling. One of the inherent disadvantages with the proposed algorithm is that the number of modes can grow exponentially as a function of the maximum number of targets. We mitigated this problem by using a decision-directed approach in which the estimated mode transition and target presence probabilities are used to control whether to run a particle filter that corresponds to a particular mode transition. By using the decision-directed approach, the computational load becomes a linear function of the maximum number of targets. This problem can be further simplified by dynamically changing the maximum number of targets. Specifically, the maximum number of targets can be increased or decreased depending on the current estimate of the number of targets.

The computational load of the MM-MT-TBDF approach is also affected by the significant number of new particles required to accurately detect when a new target enters the field of view (FOV). This large number of particles is required as no *a priori* information is assumed on the new target. Techniques such as constrained particles filters [107] that assume that the kinematic state of a target that follows a pre-determined pattern can be easily integrated into our method. The *a priori* information used in knowledge aided radars [175] can also be exploited to reduce the number of new particles. The algorithm architecture of the MM-MT-TBDF also allows the implementation of the multiple particle filters (PFs) in a parallel computing system [176]. Since the mode conditioned particle filters are independent of each other, our proposed algorithm can run faster in a parallel computing system. Moreover, the algorithm architecture also provides flexibility in assigning different number of particles to approximate different mode-conditioned density functions.

In this thesis, we established a new paradigm for multiple target tracking based on target existence modes that is not restricted to low SNR conditions as originally designed for. Multiple target tracking with a dynamically varying number of targets is a difficult problem both for low and high SNRs. The MM-MT-TBDF can also be used under high SNR conditions, and we demonstrated that for a given number of particles, the tracking error reduces, as the SNR increases. We can therefore deduce that at higher SNR scenarios, we need a much smaller number of particles than when for tracking low observable targets. Thus, under high SNR conditions, the algorithm's computational complexity can be further reduced by adjusting the number of particles used in each PF.

When conventional detect before track methods are used to track targets in the presence of clutter, they assume certain average number of clutters per measurement, spatial distribution of clutter and probability of detection. Our proposed algorithm does not require knowledge of these model parameters as we can integrate it with methods to directly estimate clutter parameters from the measurements. We investigate the performance of the algorithm in both low and high resolution radars, and in particular, we concentrated on tracking scenes with high resolution radar in sea clutter environment. We used the sea clutter compound Gaussian model at different levels of sea spikes and clutter intensity levels. We also demonstrated the tracking capability of our algorithm for slow moving target scenarios, where a simple Doppler domain filtering cannot significantly improve tracking performance. The texture component of the compound Gaussian model is assumed deterministic and a generalized likelihood function is derived along with the maximum likelihood estimate of time varying deterministic texture. The improved tracking performance of this generalized likelihood function is then demonstrated by comparing with the tracking performance of the conventional sub-optimal likelihood function that assumes random texture component. One of the many challenges of target tracking in clutter is the estimation of clutter statistics. As most clutter parameter estimation methods use neighbourhood range and range rate bins, both target detector and tracker performance significantly degrade if the clutter is non-homogeneous in nature. We provided a state space model based approach to dynamically track the space-time covariance matrix of clutter and used the Kronecker product (KP) assumption to reduce the computational complexity of the covariance estimation algorithm.

8.2 Future Work

The KP approximation error for the space-time covariance matrix can be improved further by decomposing the space-time covariance matrix into a sum of many KP matrices [177]. Recent efforts in knowledge aided radars provide some promising results in accurately estimating the clutter covariance matrix [178, 179]. We thus plan to investigate some of these results in order to extend our KP approach to non-homogeneous clutter in a knowledge aided radar framework [180]. Although the compound Gaussian model has been proven to provide and adequate characterization of the sea clutter, we need to investigate more dynamic models [165] to track the fast varying nature of sea clutter. The proposed multiple target method can also be extended to support agile radar processing similar to the method described for single target TBDF in [104]. Finally, our proposed algorithm can be easily modified to include some of the methods already developed to support realistic radar applications. Specifically, the algorithm can be modified to support fluctuating target associated signal intensity [55], Rayleigh measurement noise [53], complex measurements [56] and dependent measurements [181].

REFERENCES

[1] R. E. Kalman, "A new approach to linear filtering and prediction problems," *Transactions of the ASME, Journal of Basic Engineering*, vol. 1, pp. 35–45, March 1960.

[2] V. Chandrasekar and B. Zafar, "Precipitation type determination from spaceborne radar observations," *IEEE Transactions on Geoscience and Remote Sensing*, vol. 42, pp. 2248–2253, October 2004.

[3] L. Mu, T. Xiangqian, S. Ming, and Y. Jun, "Research on key technologies for collision avoidance automotive radar," in *IEEE Symposium on Intelligent Vehicles*, pp. 233–236, June 2009.

[4] D. E. Sturim, M. S. Brandstein, and H. F. Silverman, "Tracking multiple talkers using microphone-array measurements," *IEEE International Conference on Acoustics, Speech, and Signal Processing*, vol. 1, pp. 371–374, April 1997.

[5] C. Wang and M. S. Brandstein, "Multi-source face tracking with audio and visual data," *Third IEEE Workshop on Multimedia Signal Processing*, pp. 169–174, 1999.

[6] H. G. Okuno, K. Nakadai, K. I. Hidai, H. Mizoguchi, and H. Kitano, "Human-robot interaction through real-time auditory and visual multiple-talker tracking," *IEEE International Conference on Intelligent Robotics and Systems*, vol. 3, pp. 1402–1409, 2001.

[7] S. Churchill, C. Randell, D. Power, and E. Gill, "Data fusion: Remote sensing for target detection and tracking," *IEEE International Proceedings on Geoscience and Remote Sensing Symposium*, vol. 1, pp. 609–612, September 2004.

[8] A. P. Goobic, M. E. Welser, S. T. Acton, and K. Ley, "Biomedical application of target tracking in clutter," *Thirty-Fifth Asilomar Conference on Signals, Systems and Computers*, vol. 1, pp. 88–92, 2001.

[9] Y. Bar-Shalom, X.-R. Li, and T. Kirubarajan, *Estimation with Applications to Tracking and Navigation.* Wiley-Interscience, 2001.

[10] H. W. Sorenson, *Kalman Filtering: Theory and Application.* IEEE Press, 1985.

[11] J. Sklansky, "Optimizing the dynamic parameter of a track-while-scan system," *RCA Review*, vol. 18, pp. 163–185, July 1957.

[12] T. R. Benedict and G. W. Bordner, "Synthesis of an optimal set of radar track-while-scan smoothing equations," *IRE Transaction on Automatic Control*, vol. AC-1, July 1962.

[13] P. R. Kalata, "α-β tracking systems: A survey," *American Control Conference*, pp. 832–836, June 1992.

[14] M. Athans, R. Wishner, and A. Bertolini, “Suboptimal state estimation for continuous-time nonlinear systems from discrete noisy measurements,” *IEEE Transactions on Automatic Control*, vol. 13, pp. 504–514, October 1968.

[15] S. Arulampalam, S. Maskell, N. Gordon, and T. Clapp, “A tutorial on particle filters for on-line non-linear/non-Gaussian Bayesian tracking,” *IEEE Transactions on Signal Processing*, vol. 50, pp. 174–188, 2001.

[16] A. Doucet, N. de Fretias, and N. Gordon, *Sequential Monte Carlo Methods In Practice.* Springer-Verlag, NY, 2001.

[17] B. Ristic, S. Arulampalam, and N. Gordon, *Beyond the Kalman Filter: Particle Filters for Tracking Applications.* Artech House Publishers, Boston, MA, 2004.

[18] S. Blackman and R. Popoli, *Design and Analysis of Modern Tracking System.* Artech House Publishers, New York, NY, 1999.

[19] Y. Bar-Shalom and X.-R. Li, *Multisensor Tracking: Principles and Techniques.* YBS Publishing, New York, NY, September 1995.

[20] Y. Bar-Shalom and T. E. Fortman, *Tracking and Data Association.* Orlando, FL: Academic, 1988.

[21] A. Farina and S. Pardini, “Track-while-scan algorithm in a clutter environment,” *IEEE Transactions on Aerospace and Electronic Systems*, vol. AES-14, pp. 769–779, September 1978.

[22] P. Smith and G. Buechler, “A branching algorithm for discriminating and tracking multiple objects,” *IEEE Transactions on Automatic Control*, vol. 20, pp. 101–104, February 1975.

[23] Y. Bar-Shalom and E. Tse, “Tracking in cluttered environment with probabilistic data association,” *Automatica*, vol. 11, pp. 451–460, 1975.

[24] T. Kirubarajan and Y. Bar-Shalom, “Probabilistic data association techniques for target tracking in clutter,” *Proceedings of IEEE*, vol. 92, no. 3, pp. 536–557, March 2004.

[25] Y. Bar-Shalom, F. Daum, and J. Huang, “The probabilistic data association filter,” *IEEE Controls System Magazine*, pp. 82–100, December 2009.

[26] N. Gordon, “A hybrid bootstrap filter for target tracking in clutter,” *IEEE Transactions on Aerospace and Electronic Systems*, vol. 33, pp. 353–358, 1997.

[27] G. W. Pulford, “Taxonomy of multiple target tracking methods,” *IEE Proceedings of Radar Sonar and Navigation*, vol. 152, no. 5, pp. 291–304, October 2005.

[28] D. Reid, “An algorithm for tracking multiple targets,” *IEEE Transactions on Automation and Control*, vol. 24,6, pp. 84–90, 1979.

[29] S. S. Blackman, "Multiple hypothesis tracking for multiple target tracking," *IEEE Aerospace and Electronics Systems Magazine*, vol. 19, no. 1, pp. 5–18, January 2004.

[30] T. E. Fortman, Y. Bar-Shalom, and M. Scheffe, "Sonar tracking of multiple targets using joint probabilistic data association," *IEEE Journal of Oceanic Engineering*, vol. 8, pp. 173–184, 1983.

[31] D. Sculz, W. Burgard, D. Fox, and A. B. Cremers, "Tracking multiple moving targets with a mobile robot using particle filters and statistical data association," *Proceeding of the IEEE International Conference on Robotics and Automation*, vol. 2, pp. 1665–1670, 2001.

[32] D. Sculz, W. Burgard, and D. Fox, "People tracking with mobile robots using sample-based joint probabilistic data association filters," *International Journal of Robotics Research 22*, vol. 2, pp. 99–116, 2003.

[33] S. Godsill, J. Vermaak, and P. Perez, "Monte Carlo filtering for multi-target and data association," *IEEE Transactions on Aerospace and Electronic Systems*, vol. 41, no. 1, pp. 309–332, January 2005.

[34] W. Ng, J. Li, S. Godsill, and J. Vermaak, "A review of recent results in multiple target tracking," *Proceedings of the 4th International Symposium on Image and Signal Processing and Analysis*, pp. 40–45, September 2005.

[35] R. P. S. Mahler, "Random set theory for target tracking and identification," in *Handbook of multisensor data fusion* (D. L. Hall and J. Llinas, eds.), pp. 1–33, Cambridge: CRC Press, 2001.

[36] R. P. S. Mahler, *Statistical Multisource-Multitarget Information Fusion.* Norwood, MA, USA: Artech House, Inc., 2007.

[37] B.-N. Vo, S. Singh, and A. Doucet, "Sequential Monte Carlo methods for multitarget filtering with random finite sets," *IEEE Transactions on Aerospace and Electronic Systems*, vol. 41, no. 4, pp. 1224–1245, 2005.

[38] R. Mahler, "Objective functions for Bayesian control-theoretic sensor management, 1: multitarget first-moment approximation," in *Proceedings of the IEEE Aerospace Conference*, vol. 4, pp. 1905–1923, 2003.

[39] R. P. S. Mahler, "Multitarget Bayes filtering via first-order multitarget moments," *IEEE Transactions on Aerospace and Electronic Systems*, vol. 39, no. 2, pp. 1152–1178, 2003.

[40] B.-T. Vo, B.-N. Vo, and A. Cantoni, "The cardinality balanced multi-target multi-Bernoulli filter and its implementations," *IEEE Transactions on Signal Processing,*, vol. 57, pp. 409–423, February 2009.

[41] B.-N. Vo and W.-K. Ma, "The Gaussian mixture probability hypothesis density filter," *IEEE Transactions on Signal Processing*, vol. 54, no. 11, pp. 4091–4104, 2006.

[42] B.-N. Vo, A. Pasha, and H. D. Tuan, "A Gaussian mixture PHD filter for nonlinear jump Markov models," in *Forty-Fifth IEEE Conference on Decision and Control*, pp. 3162–3167, 2006.

[43] S. Julier and J. Uhlmann, "Unscented filtering and nonlinear estimation," *Proceedings of IEEE*, vol. 92, no. 3, pp. 401–422, 2004.

[44] H. Sidenbladh, "Multi-target particle filtering for the probability hypothesis density," in *Proceedings of the Sixth International Conference of Information Fusion*, vol. 2, pp. 800–806, 2003.

[45] M. A. Richards, *Fundamentals of Radar Signal Processing.* New York: McGraw-Hill, 2005.

[46] S. M. Kay, *Fundamentals of Statistical Signal Processing, Volume 2: Detection Theory.* New Jersey: Prentice-Hall Inc, 1993.

[47] M. Skolnik, *Introduction to Radar Systems.* New York: McGraw-Hill, 3rd ed., 2001.

[48] G. Richards, "Application of the Hough transform as a track-before-detect method," in *Target Tracking and Data Fusion (Digest No: 1996/253), IEE Colloquium on*, pp. 1–3, November 1996.

[49] W. Yi, L. Kong, J. Yang, and X. Deng, "A tracking approach based on dynamic programming track-before-detect," in *IEEE Radar Conference*, pp. 1–4, May 2009.

[50] S. M. Tonissen and Y. Bar-Shalom, "Maximum likelihood track-before-detect with fluctuating target amplitude," *IEEE Transactions on Aerospace and Electronic Systems*, vol. 34, no. 3, pp. 796–809, July 1998.

[51] D. J. Salmond and H. Birch, "A particle filter for track-before-detect," *In Proceedings of the American Control Conference*, pp. 3755–3760, 2001.

[52] Y. Boers and H. Driessen, "Particle filter based detection for tracking," *In Proceedings of the American Control Conference*, pp. 4393–4397, Arlington, VA, USA, June 2001.

[53] M. G. Rutten, N. J. Gordon, and S. Maskell, "Efficient particle-based track-before-detect in Rayleigh noise," *International Conference on Information Fusion*, pp. 693–700, June 2004.

[54] M. G. Rutten, B. Ristic, and N. J. Gordon, "Comparison of particle filters for recursive track-before-detect," *International Conference on Information Fusion*, pp. 169–175, 2005.

[55] M. G. Rutten, N. J. Gordon, and S. Maskell, "Recursive track-before-detect with target amplitude fluctuations," *IEE Proceedings of Radar, Sonar and Navigation*, vol. 52, no. 5, pp. 345–352, October 2005.

[56] S. J. Davey, B. Cheung, and M. G. Rutten, "Track-before-detect for sensors with complex measurement," *Proceedings of the 12th International Conference on Information Fusion*, pp. 619–625, Seattle, WA, July 2009.

[57] Y. Boers and H. Driessen, "Multitarget particle filter track before detect application," *IEE Proceedings of Radar, Sonar and Navigation*, vol. 151, pp. 351–357, December 2004.

[58] M. Taj and A. Cavallaro, "Multi-camera track-before-detect," *IEEE International Conference on Distributed Smart Cameras, pp. 1–6*, September 2009.

[59] S. Buzzi, M. Lops, L. Venturino, and M. Ferri, "Track-before-detect procedures in a multi-target environment," *IEEE Transactions on Aerospace and Electronic Systems*, vol. 44, no. 3, pp. 1135–1150, 2008.

[60] M. Fallon and S. Godsill, "Multi target acoustic source tracking using track before detect," in *IEEE Workshop on Applications of Signal Processing to Audio and Acoustics*, pp. 102–105, 2007.

[61] P. Pertilä and M. S. Hämäläinen, "A track before detect approach for sequential Bayesian tracking of multiple speech sources," *IEEE International Conference on Acoustics, Speech and Signal Processing*, pp. 4974–4977, 2010.

[62] F. Lehmann, "Recursive Bayesian filtering for multitarget track-before-detect in passive radars," *IEEE Transactions on Aerospace and Electronic Systems*, vol. 48, no. 3, pp. 2458–2480, 2012.

[63] F. Papi, B.-T. Vo, M. Bocquel, and B.-N. Vo, "Multi-target track-before-detect using labeled random finite set," in *International Conference on Control, Automation and Information Sciences,*, pp. 116–121, November 2013.

[64] B. Ristic, D. Clark, and B.-N. Vo, "Improved SMC implementation of the PHD filter," in *Thirteenth Conference on Information Fusion*, pp. 1–8, 2010.

[65] K. Panta, B. Vo, and S. Singh, "Improved probability hypothesis density (PHD) filter for multitarget tracking," in *Third International Conference on Intelligent Sensing and Information Processing (ICISIP)*, pp. 213–218, 2005.

[66] K. Punithakumar, T. Kirubarajan, and A. Sinha, "A sequential Monte Carlo probability hypothesis density algorithm for multitarget track-before-detect," in *Proceedings SPIE: Signal and Data Processing of Small Targets*, vol. 5913, pp. 1–8, September 2005.

[67] R. Zhan and J. Zhang, "Improved multitarget track-before-detect for image measurements," in *Eleventh IEEE International Conference on Signal Processing*, vol. 3, pp. 2183–2187, 2012.

[68] B. K. Habtemariam, R. Tharmarasa, and T. Kirubarajan, "PHD filter based track-before-detect for MIMO radars," *Signal Processing*, vol. 92, pp. 667–678, Mar. 2012.

[69] H. Tong, H. Zhang, H. Meng, and X. Wang, “Multitarget tracking before detection via probability hypothesis density filter,” in *International Conference on Electrical and Control Engineering*, pp. 1332–1335, 2010.

[70] Y. Long, H. Xu, W. An, and L. Liu, “Track-before-detect for infrared maneuvering dim multi-target via MM-PHD,” *Chinese Journal of Aeronautics*, vol. 25, no. 2, pp. 252 – 261, 2012.

[71] K. Punithakumar, T. Kirubarajan, and A. Sinha, “Multiple-model probability hypothesis density filter for tracking maneuvering targets,” *IEEE Transactions on Aerospace and Electronic Systems*, vol. 44, no. 1, pp. 87–98, 2008.

[72] D. Clark, B. Ristic, B.-N. Vo, and B. T. Vo, “Bayesian multi-object filtering with amplitude feature likelihood for unknown object SNR,” *IEEE Transactions on Signal Processing*, vol. 58, pp. 26–37, January 2010.

[73] T. M. Wood, *Random Finitie Sets for Multitarget Tracking.* PhD thesis, University of Oxford, 2011.

[74] S. Reuter, B.-T. Vo, B.-N. Vo, and K. Dietmayer, “The labeled multi-Bernoulli filter,” *IEEE Transactions on Signal Processing*, vol. 62, pp. 3246–3260, June 2014.

[75] J. Wong, B. T. Vo, B. N. Vo, and R. Hoseinnezhad, “Multi-Bernoulli based track-before-detect with road constraints,” in *15th International Conference on Information Fusion*, pp. 840–846, July 2012.

[76] S. P. Ebenezer and A. Papandreou-Suppappola, “Multiple mode track-before-detect for multiple targets,” in *Proceedings of the International Waveform Design and Diversity Conference*, January 2012.

[77] S. P. Ebenezer and A. Papandreou-Suppappola, “Generalized recursive track-before-detect with proposal partitioning for tracking varying number of multiple targets in low SNR,” submitted to *IEEE Transactions on Signal Processing*, 2015.

[78] P. M. Djuric, T. Lu, and M. F. Bugallo, “Multiple particle filering,” *IEEE International Conference on Acoustics, Speech and Signal Processing*, pp. 1181–1184, 2007.

[79] L. Miao, J. J. Zhang, C. Chakrabarti, and A. Papandreou-Suppappola, “A new parallel implementation for particle filters and its application to adaptive waveform design,” *IEEE Workshop on Signal Processing Systems*, pp. 19–24, 2010.

[80] F. Daum and J. Huang, “Curse of dimensionality and particle filters,” in *Proceedings of IEEE Aerospace Conference*, vol. 4, pp. 1979–1993, March 2003.

[81] S. P. Ebenezer and A. Papandreou-Suppappola, “Multiple transition mode multiple target track-before-detect with partitioned sampling,” *IEEE International Conference on Acoustics, Speech and Signal Processing*, pp. 8008–8012, May 2014.

[82] S. P. Ebenezer and A. Papandreou-Suppappola, “Multiple target track-before-detect in compound Gaussian clutter,” *IEEE International Conference on Acoustics, Speech and Signal Processing*, April 2015.

[83] F. Gini and M. Greco, “Covariance matrix estimation for CFAR detection in correlated heavy tailed clutter,” *Signal Processing*, vol. 82, no. 12, pp. 1847–1859, 2002.

[84] F. Pascal, Y. Chitour, J. Ovarlez, P. Forster, and P. Larzabal, “Covariance structure maximum-likelihood estimates in compound Gaussian noise: Existence and algorithm analysis,” *IEEE Transactions on Signal Processing*, vol. 56, pp. 34–48, January 2008.

[85] F. Gini and M. Greco, “Suboptimum approach to adaptive coherent radar detection in compound-Gaussian clutter,” *IEEE Transactions on Aerospace and Electronic Systems*, vol. 35, pp. 1095–1104, July 1999.

[86] F. Gini, “Sub-optimum coherent radar detection in a mixture of K-distributed and Gaussian clutter,” *IEE Proceedings on Radar, Sonar and Navigation*, vol. 144, pp. 39–48, February 1997.

[87] S. Watts, “A new method for the simulation of coherent sea clutter,” in *IEEE Radar Conference*, pp. 52–57, May 2011.

[88] S. Watts, “Modeling and simulation of coherent sea clutter,” *IEEE Transactions on Aerospace and Electronic Systems*, vol. 48, pp. 3303–3317, October 2012.

[89] K. Ward, R. Tough, and S. Watts, *Sea Clutter: Scattering, the K Distribution and Radar Performance.* The Institute of Engineering and Technology, 2nd ed., 2013.

[90] S. P. Ebenezer and A. Papandreou-Suppappola, “Estimation of rapidly varying sea clutter using nearest Kronecker product approximation,” *IEEE International Conference on Acoustics, Speech and Signal Processing*, April 2015.

[91] S. P. Ebenezer and A. Papandreou-Suppappola, “Low RCS target tracking in estimated rapidly-varying sea clutter using a Kronecker product approximation algorithm,” submitted to *IEEE Journal of Selected Topics in Signal Processing, Special Issue on Advanced Signal Processing Techniques for Radar Applications*, 2015.

[92] A. Papoulis, *Probability, Random Variables, and Stochastic Process.* New York: McGraw-Hill, 1991.

[93] X. R. Li and V. P. Jilkov, "Survey of manuevering target tracking, Part I: Dynamic models," *IEEE Transactions on Aerospace and Electronic Systems*, vol. 39, pp. 1333–1364, October 2003.

[94] E. C. Anderson, "Monte Carlo methods and importance sampling." Lecture Notes for Statistics, October 1999.

[95] B. Y. Rubinstein, *Simulation and Monte Carlo Method.* New York:Wiley & Sons, 1981.

[96] S. Sarkka, A. Vehatri, and J. Lampinen, "Rao-Blackwellized Monte Carlo data association for multiple target tracking," *Proceedings of the Seventh International Conference on Information Fusion*, vol. I, pp. 583–590, 2004.

[97] A. Doucet, N. de Freitas, K. Murphy, and S. Russell, "Rao-Blackwellised particle filtering for dynamic Bayesian networks," in *Conference on Uncertainty in Artificial Intelligence*, pp. 176–183, 2000.

[98] H. Driessen and Y. Boers, "An efficient particle filter for nonlinear jump Markov systems," *IEE Seminar on Target Tracking: Algorithms and Applications*, Sussex, UK, March 2004.

[99] D. A. Shnidman, "Generalized radar clutter model," *IEEE Transactions on Aerospace and Electronic Systems*, vol. 35, no. 3, pp. 857–865, July 1999.

[100] K. D. Ward, C. Baker, and S. Watts, "Maritime surveillance radar, Part I: Radar scattering from the ocean surface," *IEE Proceedings of Communications, Radar and Signal Processing*, vol. 137, no. 2, pp. 51–62, 1990.

[101] Y. Boers and H. Driessen, "Multitarget particle filter track before detect application," *IEE Proceedings of Radar, Sonar and Navigation*, vol. 151, pp. 351–357, December 2004.

[102] E. Mazor, A. Averbuch, Y. Bar-Shalom, and J. Dayan, "Interacting multiple model methods in target tracking: a survey," *IEEE Transactions on Aerospace and Electronic Systems*, vol. 34, pp. 103–123, January 1998.

[103] S. Sira, A. Papandreou-Suppappola, D. Morrell, and D. Cochran, "Waveform-agile sensing for tracking multiple targets in clutter," in *Fortieth Annual Conference on Information Sciences and Systems*, pp. 1418–1423, 2006.

[104] R. Piwowarski, B. O'Donnell, J. J. Zhang, and A. Papandreou-Suppappola, "Waveform-agile track-before-detect for low observable targets," in *Proceedings of the International Waveform Design and Diversity Conference*, January 2012.

[105] D. Schuhmacher, B.-T. Vo, and B.-N. Vo, "A consistent metric for performance evaluation of multi-object filters," *IEEE Transactions on Signal Processing*, vol. 56, pp. 3447–3457, August 2008.

[106] C. Kreucher, K. Kastella, and A. O. Hero III, "Tracking multiple targets using a particle filter representation of the joint multitarget probability density," *Proceedings of SPIE International Symposium on Optical Science Technology*, vol. 5204, pp. 258–269, 2003.

[107] I. Kyriakides, D. Morrell, and A. Papandreou-Suppappola, "Sequential Monte Carlo methods for tracking multiple targets with deterministic and stochastic constraints," *IEEE Transactions on Signal Processing*, vol. 56, pp. 937–948, March 2008.

[108] E. Brekke, O. Hallingstad, and J. Glattetre, "Target tracking in heavy-tailed clutter using amplitude information," in *12th International Conference on Information Fusion*, pp. 2153–2160, July 2009.

[109] S. Suvorova, B. Moran, and M. Viola, "Adaptive modelling of sea clutter and detection of small targets in heavy clutter," in *Proceedings of the International Radar Conference*, pp. 614–618, September 2003.

[110] S. Sira, D. Cochran, A. Papandreou-Suppappola, D. Morrell, W. Moran, and S. Howard, "A subspace-based approach to sea clutter suppression for improved target detection," in *Fortieth Asilomar Conference on Signals, Systems and Computers*, pp. 752–756, October 2006.

[111] X. Li and N. Li, "Integrated real-time estimation of clutter density for tracking," *IEEE Transactions on Signal Processing*, vol. 48, pp. 2797–2805, October 2000.

[112] B. Armstrong and H. Griffiths, "CFAR detection of fluctuating targets in spatially correlated K-distributed clutter," *IEE Proceedings F (Radar and Signal Processing)*, vol. 138, pp. 139–152, April 1991.

[113] X. Chen, R. Tharmarasa, M. Pelletier, and T. Kirubarajan, "Integrated clutter estimation and target tracking using Poisson point processes," *IEEE Transactions on Aerospace and Electronic Systems*, vol. 48, pp. 1210–1235, April 2012.

[114] G. Poyiadjis, A. Doucet, and S. S. Singh, "Maximum likelihood parameter estimation in general state-space models using particle methods," in *Proceedings of the American Statistical Association*, 2005.

[115] A. Doucet and V. B. Tadić, "Parameter estimation in general state-space models using particle methods," *Annals of the Institute of Statistical Mathematics*, vol. 55, no. 2, pp. 409–422, 2003.

[116] X. Chen, R. Tharmarasa, T. Kirubarajan, and M. Pelletier, "Integrated clutter estimation and target tracking using JIPDA/MHT tracker," in *Proceedings of SPIE, Sensor Fusion and Target Recognition XIX*, vol. 7697, pp. 1–12, April 2010.

[117] X. Chen, R. Tharmarasa, M. Pelletier, and T. Kirubarajan, "Integrated Bayesian clutter estimation with JIPDA/MHT trackers," *IEEE Transactions on Aerospace and Electronic Systems*, vol. 49, pp. 395–414, January 2013.

[118] E. Brekke, T. Kirubarajan, and R. Tharmarasa, "Tracking dim targets using integrated clutter estimation," in *Optical Engineering and Applications*, pp. 669905–669905, International Society for Optics and Photonics, 2007.

[119] M. Farshchian and R. Raj, "A multi-scale and adaptive track-before-detect technique for maritime environments," in *IEEE International Conference on Radar*, pp. 818–823, May 2011.

[120] D. Orlando, L. Venturino, M. Lops, and G. Ricci, "Space-time adaptive algorithms for track-before-detect in clutter environments," in *IEEE International Conference on Radar*, pp. 1–6, October 2009.

[121] P. Stinco, M. Greco, and F. Gini, "Adaptive detection in compound-Gaussian clutter with inverse-gamma texture," in *IEEE International Conference on Radar*, vol. 1, pp. 434–437, October 2011.

[122] A. Balleri, A. Nehorai, and J. Wang, "Maximum likelihood estimation for compound-Gaussian clutter with inverse gamma texture," *IEEE Transactions on Aerospace and Electronic Systems*, vol. 43, pp. 775–779, April 2007.

[123] E. Conte, M. Lops, and G. Ricci, "Adaptive detection schemes in compound-Gaussian clutter," *IEEE Transactions on Aerospace and Electronic Systems*, vol. 34, pp. 1058–1069, October 1998.

[124] E. Conte, M. Lops, and G. Ricci, "Asymptotically optimum radar detection in compound-Gaussian clutter," *IEEE Transactions on Aerospace and Electronic Systems*, vol. 31, pp. 617–625, April 1995.

[125] S. Bocquet, "Calculation of radar probability of detection in K-distributed sea clutter and noise," Tech. Rep. DSTO-TN-1000, Joint Operations Divisions, Defense Science and Technology Organization, April 2001.

[126] A. Farina, A. Russo, and F. A. Studer, "Coherent radar detection in log-normal clutter," *IEE Proceedings F (Communications, Radar and Signal Processing)*, vol. 133, pp. 39–53, February 1986.

[127] A. Farina, A. Russo, F. Scannapieco, and S. Barbarossa, "Theory of radar detection in coherent Weibull clutter," *IEE Proceedings F (Communications, Radar and Signal Processing)*, vol. 134, pp. 174–190, April 1987.

[128] C. Baker, "K-distributed coherent sea clutter," *IEE Proceedings F (Radar and Signal Processing)*, vol. 138, pp. 89–92, April 1991.

[129] N. Redding, "Estimating the parameters of the K distribution in the intensity domain," Tech. Rep. DSTO-TR-0839, Surveillance Systems Division, Electronics and Surveillance Research Laboratory, Defense Science and Technology Organization, July 1999.

[130] D. Shnidman, "Radar detection probabilities and their calculation," *IEEE Transactions on Aerospace and Electronic Systems*, vol. 31, pp. 928–950, July 1995.

[131] M. A. Ritchie, A. Charlish, K. Woodbridge, and A. Stove, "Use of the Kullback-Leibler divergence in estimating clutter distributions," in *IEEE Radar Conference*, pp. 751–756, May 2011.

[132] H. Chan, "Radar sea-clutter at low grazing angles," *IEE Proceedings F (Radar and Signal Processing)*, vol. 137, pp. 102–112, April 1990.

[133] S. Watts, C. Baker, and K. D. Ward, "Maritime surveillance radar. Part II: Detection performance prediction in sea clutter," *IEE Proceedings F (Radar and Signal Processing)*, vol. 137, pp. 63–72, April 1990.

[134] T. Nohara and S. Haykin, "Canadian east coast radar trials and the K-distribution," *IEE Proceedings F (Radar and Signal Processing)*, vol. 138, pp. 80–88, April 1991.

[135] H. Helmken and M. Vanderhill, "Very low grazing angle radar backscatter from the ocean surface," in *IEEE International Radar Conference*, pp. 181–188, May 1990.

[136] H. Helmken, "Low-grazing-angle radar backscatter from the ocean surface," *IEE Proceedings F (Radar and Signal Processing)*, vol. 137, pp. 113–117, April 1990.

[137] I. Antipov, "Analysis of sea clutter data," Tech. Rep. DSTO-TR-0647, Tactical Surveillance Systems Division, Electronics and Surveillance Research Laboratory, Defense Science and Technology Organization, November 2001.

[138] I. Antipov, "Statistical analysis of northern Australian coastline sea clutter data," Tech. Rep. DSTO-TR-1236, Surveillance Systems Division, Electronics and Surveillance Research Laboratory, Defense Science and Technology Organization, November 2001.

[139] J. Carretero-Moya, J. Gismero-Menoyo, A. Blanco-del Campo, and A. Asensio-Lopez, "Statistical analysis of a high-resolution sea-clutter database," *IEEE Transactions on Geoscience and Remote Sensing*, vol. 48, pp. 2024–2037, April 2010.

[140] J. Tang and Z. Zhu, "Compound Gaussian process and its derived processes [radar clutter]," in *Proceedings of the IEEE Aerospace and Electronics Conference*, vol. 2, pp. 1074–1079, July 1997.

[141] S. Watts, "Radar detection prediction in sea clutter using the compound K-distribution model," *IEE Proceedings F (Communications, Radar and Signal Processing)*, vol. 132, pp. 613–620, December 1985.

[142] D. Schleher, "Radar detection in Weibull clutter," *IEEE Transactions on Aerospace and Electronic Systems*, vol. AES-12, pp. 736–743, November 1976.

[143] D. Shnidman, "Radar detection in clutter," *IEEE Transactions on Aerospace and Electronic Systems*, vol. 41, pp. 1056–1067, July 2005.

[144] V. Anastassopoulos, G. A. Lampropoulos, A. Drosopoulos, and M. Rey, "High resolution radar clutter statistics," *IEEE Transactions on Aerospace and Electronic Systems*, vol. 35, pp. 43–60, January 1999.

[145] G. Weinberg, "Assessing Pareto fit to high-resolution high-grazing-angle sea clutter," *Electronics Letters*, vol. 47, pp. 516–517, April 2011.

[146] L. Rosenberg and S. Bocquet, "The Pareto distribution for high grazing angle sea-clutter," in *IEEE International Geoscience and Remote Sensing Symposium (IGARSS)*, pp. 4209–4212, July 2013.

[147] M. Farshchian and F. Posner, "The Pareto distribution for low grazing angle and high resolution X-band sea clutter," in *IEEE Radar Conference*, pp. 789–793, May 2010.

[148] D. Walker, "Doppler modelling of radar sea clutter," *IEE Proceedings of Radar, Sonar and Navigation*, vol. 148, pp. 73–80, April 2001.

[149] D. Walker, "Experimentally motivated model for low grazing angle radar Doppler spectra of the sea surface," *IEE Proceedings of Radar, Sonar and Navigation*, vol. 147, pp. 114–120, June 2000.

[150] R. Miller, "Variability in spectra of low-grazing angle sea clutter returns, NATO," in *Proceedings of SET Symposium on Low Grazing Angle Clutter: Its Characterisation, Measurement and Application*, 2000.

[151] S. Watts, "Radar detection prediction in K-distributed sea clutter and thermal noise," *IEEE Transactions on Aerospace and Electronic Systems*, vol. AES-23, pp. 40–45, January 1987.

[152] E. Kelly, "An adaptive detection algorithm," *IEEE Transactions on Aerospace and Electronic Systems*, vol. AES-22, pp. 115–127, March 1986.

[153] K. Sangston, F. Gini, and M. Greco, "Coherent radar target detection in heavy-tailed compound-Gaussian clutter," *IEEE Transactions on Aerospace and Electronic Systems*, vol. 48, pp. 64–77, January 2012.

[154] K. Sangston, F. Gini, M. Greco, and A. Farina, "Structures for radar detection in compound Gaussian clutter," *IEEE Transactions on Aerospace and Electronic Systems*, vol. 35, pp. 445–458, April 1999.

[155] L. Roy and R. Raja Kumar, "A GLRT detector in partially correlated texture based compound-Gaussian clutter," in *National Conference on Communications (NCC)*, pp. 1–5, January 2010.

[156] E. Conte, A. De Maio, and G. Ricci, "Covariance matrix estimation for adaptive CFAR detection in compound-Gaussian clutter," *IEEE Transactions on Aerospace and Electronic Systems*, vol. 38, pp. 415–426, April 2002.

[157] E. Conte, A. De Maio, and G. Ricci, "Estimation of the covariance matrix for adaptive CFAR detection in compound-Gaussian clutter," in *Proceedings of IEEE International Symposium on Information Theory*, p. 84, 2000.

[158] J. Wang, A. Dogandzic, and A. Nehorai, "Maximum likelihood estimation of compound-Gaussian clutter and target parameters," *IEEE Transactions on Signal Processing*, vol. 54, pp. 3884–3898, October 2006.

[159] F. Gini, G. Giannakis, M. Greco, and G. Zhou, "Time-averaged subspace methods for radar clutter texture retrieval," *IEEE Transactions on Signal Processing*, vol. 49, pp. 1886–1898, September 2001.

[160] R. M. Gray, "Toeplitz and circulant matrices: A review," *Foundations and Trends in Communications and Information Theory*, vol. 2, no. 3, pp. 155–239, 2006.

[161] A. Drosopoulos, "Description of the OHGR database," Tech. Rep. 94-14, Defence Research Establishment, Ottawa, December 1994.

[162] F. Gini, M. V. Greco, A. Farina, and P. Lombardo, "Optimum and mismatched detection against K-distributed plus Gaussian clutter," *IEEE Transactions on Aerospace and Electronic Systems*, vol. 34, pp. 860–876, 1998.

[163] Y. Li, W. Moran, S. Sira, A. Papandreou-Suppappola, and D. Morrell, "Adaptive waveform design in rapidly-varying radar scenes," in *Waveform Diversity and Design Workshop*, pp. 263–267, February 2009.

[164] Y. Li, W. Moran, S. P. Sira, A. Papandreou-Suppappola, and D. Morrell, "Monte-Carlo based estimation methods for rapidly-varying sea clutter," in *Digital Signal Processing Workshop*, pp. 256–261, January 2009.

[165] Y. Li, *Dynamic Waveform Design for Sensor Systems with Novel Estimation of Sensing Environment Characteristics*. PhD thesis, Arizona State University, May 2010.

[166] K. Werner, M. Jansson, and P. Stoica, "On estimation of covariance matrices with Kronecker product structure," *IEEE Transactions on Signal Processing*, vol. 56, pp. 478–491, February 2008.

[167] M. Jansson, P. Wirfalt, K. Werner, and B. Ottersten, "ML estimation of covariance matrices with Kronecker and persymmetric structure," in *Digital Signal Processing Workshop and 5th IEEE Signal Processing Education Workshop*, pp. 298–301, January 2009.

[168] P. Wirfalt and M. Jansson, "On Kronecker and linearly structured covariance matrix estimation," *IEEE Transactions on Signal Processing*, vol. 62, pp. 1536–1547, March 2014.

[169] C. F. Van Loan and N. Pitsianis, "Approximation with Kronecker products," in *Linear Algebra for Large Scale and Real Time Applications* (M. S. Moonen, G. H. Golub, and B. L. de Moor, eds.), pp. 293–314, Springer, 2nd ed., 2000.

[170] M. G. Genton, "Separable approximations of space-time covariance matrices," *Environmetrics*, vol. 18, no. 7, pp. 681–695, 2007.

[171] C. F. Van Loan, "The ubiquitous Kronecker product," *J. Comp. Applied Mathematics*, vol. 123, pp. 85–100, 2000.

[172] G. H. Golub and C. F. Van Loan, *Matrix Computations.* Johns Hopkins University Press, 2013.

[173] N. Lu and D. L. Zimmerman, "On likelihood-based inference for a separable covariance matrix," Tech. Rep. 337, Department of Statistics and Actuarial Science, University of Iowa, December 2004.

[174] P. Dutilleul, "The MLE algorithm for the matrix normal distribution," *Journal of Statistical Computation and Simulation*, vol. 64, no. 2, pp. 105–123, 1999.

[175] M. Ulmke, "Improved GMTI-tracking using road-maps and topographic information," in *Proceedings of SPIE*, vol. 5204, pp. 143–154, 2003.

[176] L. Miao, J. Zhang, C. Chakrabarti, and A. Papandreou-Suppappola, "A new parallel implementation for particle filters and its application to adaptive waveform design," in *IEEE Workshop on Signal Processing Systems*, pp. 19–24, 2010.

[177] T. Tsiligkaridis and A. Hero, "Covariance estimation in high dimensions via Kronecker product expansions," *IEEE Transactions on Signal Processing*, vol. 61, pp. 5347–5360, November 2013.

[178] S. Bidon, O. Besson, and J.-Y. Tourneret, "Characterization of clutter heterogeneity and estimation of its covariance matrix," in *IEEE Radar Conference*, pp. 1–6, May 2008.

[179] O. Besson, J.-Y. Tourneret, and S. Bidon, "Bayesian estimation of covariance matrices in non-homogeneous environments," in *IEEE International Conference on Acoustics, Speech and Signal Processing*, vol. 3, pp. 1037–1040, April 2007.

[180] J. Guerci and E. Baranoski, "Knowledge-aided adaptive radar at DARPA: an overview," *IEEE Signal Processing Magazine*, vol. 23, pp. 41–50, January 2006.

[181] J. Zhang, Q. Ding, S. Kay, A. Papandreou-Suppappola, and M. Rangaswamy, "Agile multi-modal tracking with dependent measurements," in *Asilomar Conference on Signals, Systems and Computers*, pp. 1653–1657, 2010.

APPENDIX A

PROPERTIES OF KRONECKER PRODUCT

Property 1: Given four matrices $\mathbf{X}_1$, $\mathbf{X}_2$, $\mathbf{X}_3$, and $\mathbf{X}_4$ with dimensions $(L \times M)$, $(M \times N)$, $(P \times Q)$, and $(Q \times R)$, respectively, the product of two matrices in KP form can be written as

$$(\mathbf{X}_1 \otimes \mathbf{X}_3)(\mathbf{X}_2 \otimes \mathbf{X}_4) = \mathbf{X}_1\mathbf{X}_2 \otimes \mathbf{X}_3\mathbf{X}_4. \tag{A.1}$$

The dimension of the product matrix is $(LP \times NR)$.

Property 2: If an $(L \times P)$ matrix $\mathbf{U}$ can be decomposed into three matrices $\mathbf{X}_1$, $\mathbf{D}$, and $\mathbf{X}_2$ with dimensions $(L \times M)$, $(M \times N)$ and $(N \times P)$, respectively, then the matrix $\mathbf{U}$ can be vectorized into an $(LP \times 1)$ vector using the KP property

$$\text{if } \ \mathbf{U} = \mathbf{X}_1\mathbf{D}\mathbf{X}_2, \quad \text{then } \ \text{vec}(\mathbf{U}) = (\mathbf{X}_2^{\mathtt{H}} \otimes \mathbf{X}_1)\text{vec}(\mathbf{D}) \tag{A.2}$$

where vec($\mathbf{U}$) is the vector obtained by stacking all the columns of matrix $\mathbf{U}$.

Property 3: The trace of a KP matrix is the product of the trace of individual matrices,

$$\text{tr}(\mathbf{U} \otimes \mathbf{V}) = \text{tr}(\mathbf{U})\text{tr}(\mathbf{V}). \tag{A.3}$$

Property 4: Given two square matrices $\mathbf{U}$ and $\mathbf{V}$ with dimensions $(M \times M)$ and $(N \times N)$ respectively, the determinant of the KP of these matrices can be written as

$$|\mathbf{U} \otimes \mathbf{V}| = |\mathbf{U}|^N |\mathbf{V}|^M. \tag{A.4}$$

Property 5: Given two square and invertible matrices $\mathbf{U}$ and $\mathbf{V}$ with dimensions $(M \times M)$ and $(N \times N)$ respectively, the inverse of the KP of these matrices is the KP of the inverse matrices $\mathbf{U}^{-1}$ and $\mathbf{V}^{-1}$,

$$(\mathbf{U} \otimes \mathbf{V})^{-1} = (\mathbf{U}^{-1} \otimes \mathbf{V}^{-1}). \tag{A.5}$$